Analysis of Widespread Fatigue Damage In Aerospace Structures
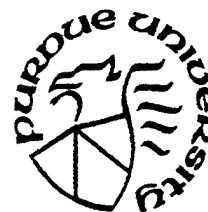
Final Report

for

Air Force Office of Scientific Research
Grant Number F49620-98-1-0293

prepared by

A. F. Grandt, Jr., T. N. Farris,
and B. H. Hillberry

February 1999

19990316 107

School of Aeronautics and Astronautics
1282 Grissom Hall
Purdue University
W. Lafayette, IN 47907-1282
Telephone: (317) 494-5117
Fax: (317) 494-0307

REPORT DOCUMENTATION PAGE

0076

Public reporting burden for this collection of information is estimated to average 1 hour per response, including the time for revie
the data needed, and completing and reviewing this collection of information. Send comments regarding this burden estimate o
reducing this burden to Washington Headquarters Services, Directorate for Information Operations and Reports, 1215 Jefferson
Management and Budget, Paperwork Reduction Project (0704-0188), Washington, DC 20503

1. AGENCY USE ONLY (Leave blank)	2. REPORT DATE February 1999	3. REPORT TYPE AND DATES COVERED Final report for 15 Feb 98 – 30 Nov 98

4. TITLE AND SUBTITLE
Analysis of Widespread Fatigue Damage in Aerospace Structures

5. FUNDING NUMBERS
Grant No. F49620-98-1-0293

6. AUTHOR(S)
A. F. Grandt, Jr., T. N. Farris, B. M. Hillberry

7. PERFORMING ORGANIZATION NAME(S) AND ADDRESS(ES)

School of Aeronautics and Astronautics
1282 Grissom Hall
Purdue University
W. Lafayette, Indiana 47907-1282

School of Mechanical Engineering
Purdue University
W. Lafayette, IN 47907

8. PERFORMING ORGANIZATION REPORT NUMBER

9. SPONSORING / MONITORING AGENCY NAME(S) AND ADDRESS(ES)

AFOSR/NA
801 North Randolph Street
Room 732
Arlington, VA 22203-1977

POC: Major Brian Sanders

10. SPONSORING / MONITORING AGENCY REPORT NUMBER

11. SUPPLEMENTARY NOTES

12a. DISTRIBUTION / AVAILABILITY STATEMENT
Approved for public release; distribution unlimited

12b. DISTRIBUTION CODE

13. ABSTRACT *(Maximum 200 Words)*

This report summarizes research dealing with analyzing the effects of widespread fatigue damage on aircraft structural integrity. Results are described for determining how cracks nucleate by corrosion, fatigue, or fretting fatigue, and once formed, grow, coalesce and lead to final fracture. The research is conducted in the context of the aging aircraft issue, which focuses on determining procedures for ensuring the continued safety of aircraft that operate beyond their original design lifetimes.

14. SUBJECT TERMS widespread fatigue damage, fretting, corrosion			15. NUMBER OF PAGES 160
			16. PRICE CODE

17. SECURITY CLASSIFICATION OF REPORT Unclassified	18. SECURITY CLASSIFICATION OF THIS PAGE Unclassified	19. SECURITY CLASSIFICATION OF ABSTRACT Unclassified	20. LIMITATION OF ABSTRACT

NSN 7540-01-280-5500

Standard Form 298 (Rev. 2-89)
Prescribed by ANSI Std. Z39-18
298-102

FOREWORD

This is the final report of research conducted on Air Force Office of Scientific Research Grant No. F49620-98-1-0293, "Analysis of Widespread Fatigue Damage in Aerospace Structures." This grant began on February 15, 1998, and was concluded on November 30, 1998. Professors A. F. Grandt, Jr. and T. N. Farris from the Purdue School of Aeronautics and Astronautics and Professor B. M. Hillberry from the School of Mechanical Engineering were the Principal Investigators. Major Brian Sanders was the AFOSR program manager. These faculty were assisted by graduate students from the Purdue Schools of Engineering.

1.0 INTRODUCTION

1.1 Objectives

The objective of this grant was to solve fundamental problems that limit the safe operation of aircraft beyond their original design or current economic lifetimes. The general objectives are summarized as follows.

- Characterization of initial and service induced damage and mechanisms that lead to crack formation through corrosion, fatigue, and fretting at joints.

- Determination of how cracks, once formed, grow through corrosion and fatigue, with emphasis on the development of crack interaction and fracture criteria for multiple-site-damage.

1.2 Research Personnel

The research program was conducted by a team of three faculty aided by graduate students from the Purdue University School of Aeronautics and Astronautics and the School of Mechanical Engineering. The faculty and students involved in this effort are summarized below.

1.2.1 Faculty

Alten F. (Skip) Grandt, Jr. (Principal Investigator) Professor, School of Aeronautics and Astronautics, 1282 Grissom Hall, Purdue University, West Lafayette, IN 47907-1282, Tel: (765) 494-5141, Fax: (765) 494-0307, e-mail: grandt@ecn.purdue.edu. **Topics:** fatigue, fracture mechanics, multiple-site damage, residual strength, corrosion.

Thomas N. Farris (Co-Investigator), Professor and Head, School of Aeronautics and Astronautics, 1282 Grissom Hall, Purdue University, West Lafayette, IN 47907-1282, Tel: (765) 494-5134, Fax: (765) 494-0307, e-mail: farrist@ecn.purdue.edu. **Topics:** tribology, fretting fatigue, fracture mechanics, boundary elements.

Ben M. Hillberry (Co-Investigator), Professor, School of Mechanical Engineering, 1288 Mechanical Engineering Building, Purdue University, West Lafayette, IN 47907-1288, Tel: (765) 494-5721, Fax: (765) 494-0539, email: hillberr@ecn.purdue.edu. **Topics:** fatigue, fracture, crack formation, statistical and probabilistic modeling.

2.2.2 Students

The following graduate students were involved in this research. (Note some students were also supported from other sources, effectively leveraging AFOSR support on the project.)

School of Aeronautics and Astronautics

Patrick J. Golden, Murthy Haradanahalli, Ganapathy Harish, Pamela McVeigh, Matthew Szolwinski, Jason N. Scheuring, Hsing-Liang Wang

School of Mechanical Engineering

Beth DeBartolo, Karl Gruenberg, Peter Laz, Monty Moshier, John Zamber

2.0 ACCOMPLISHMENTS

The research accomplishments are discussed in the following publications resulting from this research grant. Some of these papers are reproduced as Appendix A to this report.

2.1 List of Publications and Presentations

1. H. L. Wang and A. F. Grandt, Jr., "Fatigue Analysis of Multiple Site Damage in Lap Joint Specimens," *Fatigue and Fracture Mechanics: 30th Volume,* ASTM Special Technical Publication (in press).

2. G. H. Bray, R. J. Bucci, M. Kulak, C. J. Warren, A. F. Grandt, Jr., P. J. Golden, and D. G. Sexton, "Benefits of Improved Fuselage Skin Sheet Alloy 2524-T3 in Multi-Site Damage Scenarios," Proceedings of The Second Joint NASA/FAA/DoD Conference on Aging Aircraft, Williamsburg, Virginia, August 31-September 3, 1998. Also published in *Light Metal Age,* Vol. 56, Nos. 11, 12, December 1998, pp. 20 –28.

3. G. H. Bray, R. J. Bucci, P. J. Golden, and A. F. Grandt, Jr., "Effect of Prior Corrosion on Fatigue Performance of Toughness Improved Fuselage Skin Sheet Alloy 2524-T3," AGARD Applied Vehicle Technology Panel Workshop 2 on Fatigue in the Presence of Corrosion, October 7-8, 1998, Corfu, Greece.

4. H. L. Wang and A. F. Grandt, Jr., "Monte Carlo Analysis of Widespread Fatigue Damage in Lap Joints," 1998 USAF Structural Integrity Program Conference," San Antonio, Texas, December 1-3, 1998.

5. A. F. Grandt, Jr. and H. L. Wang, "Analysis of Widespread Fatigue Damage in Lap Joints," Paper Number 99GCRAM-56, 1999 SAE General, Corporate & Regional Aviation Meeting & Exposition, Wichita KS, April 20-22, 1999.

6. J. N. Scheuring and A. F. Grandt, Jr., "A Fracture Mechanics Based Approach to Quantifying Corrosion Damage," Paper Number 99GCRAM-59, 1999 SAE General, Corporate & Regional Aviation Meeting & Exposition, Wichita KS, April 20-22, 1999.

7. J. E. Zamber and B. M. Hillberry, "A Probabilistic Approach to Predicting Fatigue Lives of Corroded 2024-T3," Proceedings 39th AIAA/ASME/ASCE/AHS/ASC Structures, Structural Dynamics and Materials Conference, paper AIAA-98-2054, pp 2976-2984, Long Beach, CA, April 1998.

8. K. M. Gruenberg, B.A. Craig and B. M. Hillberry, "A Probabilistic Method for Predicting the Variability in Fatigue Behavior of 7075-T6 Aluminum," Proceedings 39th AIAA/ASME/ASCE/AHS/ASC Structures, Structural Dynamics and Materials Conference, paper AIAA-98-2055, pp 2055-2965, Long Beach, CA, April 1998.

9. M. Moshier and B. M. Hillberry, "The Effect of Compressive Residual Stress on Crack Growth Modeling," 1998 USAF Aircraft Structural Integrity Program Conference, 1-3

December 1998, San Antonio, Texas.

10. B. M. Hillberry and J. E. Zamber, "Remaining Fatigue Life of 2024-T3 Aluminum with pitting Corrosion Damage," 1998 USAF Aircraft Structural Integrity Program Conference, 1-3 December 1998, San Antonio, Texas.

11. E. A. DeBartolo and B. M. Hillberry, "Characterization of Fatigue Crack Nucleation Sites in 2024-T-3 Aluminum Alloy," accepted for presentation at FATIGUE '99: The Seventh International Fatigue Conference, 8-12 June 1999, Beijing, P. R. China.

12. P .J. Laz, B. A. Craig, S. M. Rohrbaugh and B. M. Hillberry, "The Development of a Total Fatigue Life Approach Accounting for Nucleation and Propagation," accepted for presentation at FATIGUE '99: The Seventh International Fatigue Conference, 8-12 June 1999, Beijing, P. R. China.

13. B. M. Hillberry, P. J. Laz, K. M. Gruenberg, E. A. DeBartolo, and B. A. Craig, "Inherent Material Behavior and Widespread Fatigue," FATIGUE '99: The Seventh International Fatigue Conference, 8-12 June 1999, Beijing, P. R. China.

14. H. L. Wang, "Evaluation of Multiple Site Damage in Lap Joint Specimens," Ph. D. Thesis, School of Aeronautics and Astronautics, Purdue University, December 1998.

15. M.P. Szolwinski and T.N. Farris, ``Linking Riveting Process Parameters to the Fatigue Performance of Riveted Aircraft Structures,'' *Proc. 40th AIAA/ASME/ASCE/ASC Structures, Structural Dynamics, and Materials Conf.*, In-Press, St Louis, MO, April

16. G. Harish and T.N. Farris, ``An Integrated Approach for Prediction of Fretting Crack Nucleation in Riveted Lap Joints,'' *40th AIAA/ASME/ASCE/ASC Structures, Structural Dynamics, and Materials Conf.*, In-Press, St Louis, MO, April 1999.

17. P.A. McVeigh and T. N. Farris, ``Analysis of Surface Stresses and Stress Intensity Factors Present During Fretting Fatigue,'' *Proc. 40th AIAA/ASME/ASCE/ASC Structures, Structural Dynamics, and Materials Conf.*, In-Press, St Louis, MO, April 1999.

18. Harish, G. and Farris, T.N., ``Shell Modeling of Fretting in Riveted Lapjoints,'' *AIAA Journal,* **36** (6) pp 1087-1093 (1998).

19. M.P. Szolwinski and T.N. Farris, ``Observation, Analysis and Prediction of Fretting Fatigue in 2024-T351 Aluminum Alloy,'' *Wear,* **221**(1), pp 24-36 (1998).

20. T.N. Farris, M.P. Szolwinski and G. Harish, ``Fretting in Aerospace Structures and Materials," *ASTM STP 1367, Fretting Fatigue: Current Technologies and Practices,*D.W. Hoeppner, V. Chandrasekaran and C.B. Elliot, Eds, Submitted.

APPENDIX A
REPRINTS OF TECHNICAL PAPERS

The following papers describe results from this research grant and are reproduced here in the following section.

- H. L. Wang and A. F. Grandt, Jr., "Fatigue Analysis of Multiple Site Damage in Lap Joint Specimens," *Fatigue and Fracture Mechanics: 30th Volume,* ASTM Special Technical Publication (in press).

- G. H. Bray, R. J. Bucci, M. Kulak, C. J. Warren, A. F. Grandt, Jr., P. J. Golden, and D. G. Sexton, "Benefits of Improved Fuselage Skin Sheet Alloy 2524-T3 in Multi-Site Damage Scenarios," Proceedings of The Second Joint NASA/FAA/DoD Conference on Aging Aircraft, Williamsburg, Virginia, August 31-September 3, 1998. Also published in *Light Metal Age,* Vol. 56, Nos. 11, 12, December 1998, pp. 20 –28.

- G. H. Bray, R. J. Bucci, P. J. Golden, and A. F. Grandt, Jr., "Effect of Prior Corrosion on Fatigue Performance of Toughness Improved Fuselage Skin Sheet Alloy 2524-T3," AGARD Applied Vehicle Technology Panel Workshop 2 on Fatigue in the Presence of Corrosion, October 7-8, 1998, Corfu, Greece.

- H. L. Wang and A. F. Grandt, Jr., "Monte Carlo Analysis of Widespread Fatigue Damage in Lap Joints," 1998 USAF Structural Integrity Program Conference," San Antonio, Texas, December 1-3, 1998.

- A. F. Grandt, Jr. and H. L. Wang, "Analysis of Widespread Fatigue Damage in Lap Joints," Paper Number 99GCRAM-56, 1999 SAE General, Corporate & Regional Aviation Meeting & Exposition, Wichita KS, April 20-22, 1999.

- J. N. Scheuring and A. F. Grandt, Jr., "A Fracture Mechanics Based Approach to Quantifying Corrosion Damage," Paper Number 99GCRAM-59, 1999 SAE General, Corporate & Regional Aviation Meeting & Exposition, Wichita KS, April 20-22, 1999.

- J. E. Zamber and B. M. Hillberry, "A Probabilistic Approach to Predicting Fatigue Lives of Corroded 2024-T3," Proceedings 39th AIAA/ASME/ASCE/AHS/ASC Structures, Structural Dynamics and Materials Conference, paper AIAA-98-2054, pp 2976-2984, Long Beach, CA, April 1998.

- K. M. Gruenberg, B. A. Craig and B. M. Hillberry, "A Probabilistic Method for Predicting the Variability in Fatigue Behavior of 7075-T6 Aluminum," Proceedings 39th AIAA/ASME/ASCE/AHS/ASC Structures, Structural Dynamics and Materials Conference, paper AIAA-98-2055, pp 2055-2965, Long Beach, CA, April 1998.

- E. A. DeBartolo and B. M. Hillberry, "Characterization of Fatigue Crack Nucleation Sites in 2024-T-3 Aluminum Alloy," accepted for presentation at FATIGUE '99: The

Seventh International Fatigue Conference, 8-12 June 1999, Beijing, P. R. China.

- P. J. Laz, B. A. Craig, S. M. Rohrbaugh and B. M. Hillberry, "The Development of a Total Fatigue Life Approach Accounting for Nucleation and Propagation," accepted for presentation at FATIGUE '99: The Seventh International Fatigue Conference, 8-12 June 1999, Beijing, P. R. China.

- B. M. Hillberry, P. J. Laz, K. M. Gruenberg, E. A. DeBartolo, and B. A. Craig, "Inherent Material Behavior and Widespread Fatigue," FATIGUE '99: The Seventh International Fatigue Conference, 8-12 June 1999, Beijing, P. R. China.

- Harish, G. and Farris, T.N., ``Shell Modeling of Fretting in Riveted Lapjoints,'' *AIAA Journal,* **36** (6) pp 1087-1093 (1998).

- M.P. Szolwinski and T.N. Farris, ``Observation, Analysis and Prediction of Fretting Fatigue in 2024-T351 Aluminum Alloy,'' *Wear,* **221**(1), pp 24-36 (1998).

Hsing-Ling Wang[1], and Alten F. Grandt, Jr.[2]

FATIGUE ANALYSIS OF MULTIPLE SITE DAMAGE IN LAP JOINT SPECIMENS

ABSTRACT: This paper describes research to determine the influence of multiple-site damage on the fatigue life of lap joint specimens. Multiple-site damage is an important concern in aging aircraft, and deals with determining failure conditions for multiple crack configurations. The goal of this paper is to determine the fatigue life for a mechanically fastened joint with multiple fatigue cracks located along one row of rivet holes. A life prediction model for the fatigue life is evaluated with the results of several pre-cracked specimens tested to failure under constant amplitude loading. Predictions for the growth and coalescence of individual cracks in specimens with various initial crack configurations and applied stress levels agree well with the experimental results.

KEYWORDS: Lap joints, load transfer mechanism, hole expansion, rivets, multiple site damage, fatigue crack propagation, life prediction.

The multiple site damage (MSD) issue [1-7] deals with assuring structural integrity after extended periods of service when many small cracks have formed at multiple locations. The MSD problem is of particular concern in lap joint structure where the many fastener holes provide likely locations for MSD to form, propagate, coalesce, and finally lead to catastrophic failure. Predicting failure involves complicated analysis of load transfer through the fasteners [3,7-11], residual stresses from rivet installation [12], interface contact [7,8], bending due to fuselage curvature [13,14], and biaxial loading [15]. One must also consider crack formation at the fastener holes [15],

---

[1] Graduate Research Assistant;
[2] Professor, School of Aeronautics and Astronautics, 1282 Grissom Hall, Purdue University, West Lafayette, IN 47907-1282.

crack propagation, interaction between adjacent crack tips [2-7,16], and residual strength criteria to reach the final life prediction [2-7].

This paper demonstrates analysis procedures developed to evaluate MSD in single lap joint structure. The approach includes formulating a load transfer model that considers MSD in the lap joint, determination of stresses associated with rivet installation and bending, and computation of stress intensity factors. Residual strength and fatigue crack growth lives are then computed for the joint. The analysis procedure is experimentally evaluated with a set of fatigue tests. The particular experiments discussed here involve 2.29 mm thick 2024-T3 aluminum sheets joined with three rows of eight 4.76 mm diameter countersunk aluminum rivets. As discussed later, the rivets are installed with a force controlled riveting process that results in 1.15 % hole expansion. Five such specimens are precracked along one row of holes to simulate MSD, and then cycled to failure under constant amplitude loading. A fracture mechanics analysis is then used to predict the growth, coalescence, and final fracture resulting from the initial MSD in the lap joint.

Analysis

This sections briefly summarizes the procedure used to determine the stress intensity factors and subsequent fatigue life of a lap joint that contains MSD. Further details of the analysis procedure are given in Reference 7.

Load Transfer Analysis for a Riveted Lap Joint

The analysis begins with an elastic load transfer solution proposed by Barrois [17] to determine the force applied by individual fasteners in a mechanical joint. There are two assumptions in this model. First, beam theory is used to determine the deformation of a rivet lying on elastic foundation, and second, there is no interference or clearance between the rivet and the foundation contact surfaces. The load transferred by two adjacent rivets can be determined by considering displacement compatibility associated with changes in the dimensions δ and Λ shown in Fig. 1.
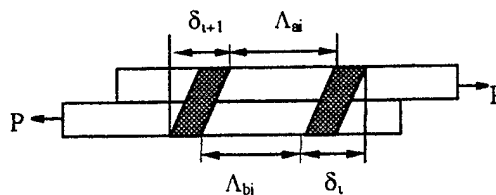

FIG. 1—Displacement compatibility of two adjacent rivets.

$$\delta_i - \delta_{i+1} = \Lambda_{ai} - \Lambda_{bi} \qquad (1)$$

Two boundary conditions are used to account for two extremely different deflections on the contact surface between the rivet head and panels. One approach is to assume a perfectly clamped rivet head, and the other is to assume a pinned head that allows rotations at this location. These two boundary conditions induce different fastener flexibilities and result in different rivet load transfer ratios. The benefit of the Barrois analysis over other empirical load transfer models is that it provides an analytical method to extend load transfer calculations to more complicated structural geometries and different types of rivet heads (including countersinks). Several empirical load transfer solutions [*11*] for an uncracked lap joint are compared with the Barrios model in Fig. 2. This particular case is for a three row, single lap joint with equal sheet thicknesses, and a rivet/panel stiffness ratio (E_{rivet}/E_{panel}) of 3. Note that all of the empirical load transfer ratios for this case are encompassed by the two extreme boundary conditions considered in the Barrois model. Load transfer experiments conducted with "neat fit" pins indicate that the Barrois model gives good results for the pinned end condition [7].
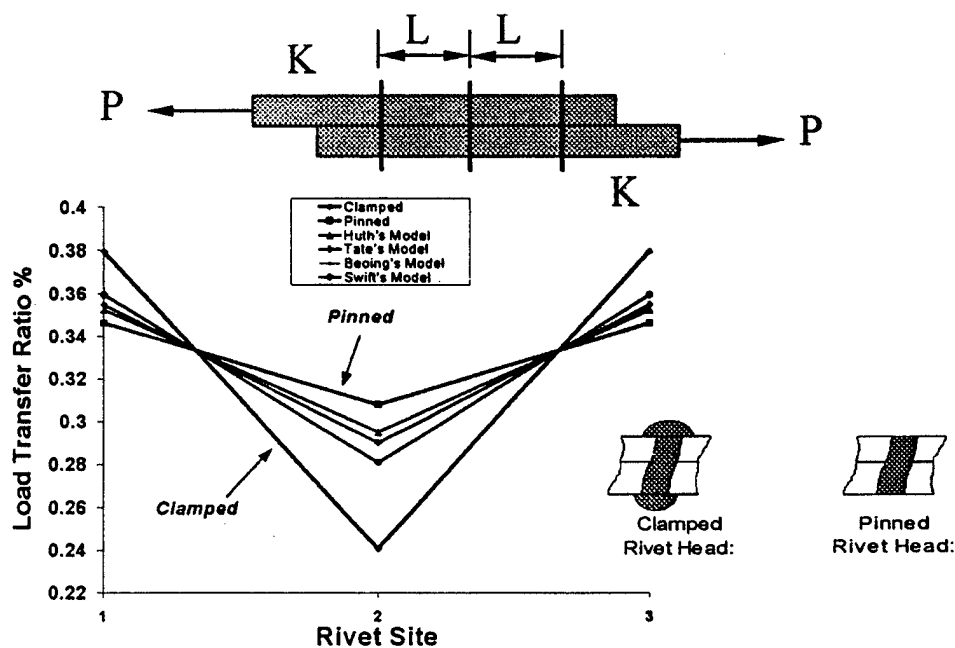

FIG. 2—*Load transfer ratio (elastic solution) and boundary conditions*

The relative displacement terms, δ_i, given in Eq. 1 are based on an analytic solution for a beam on an elastic foundation, and do not allow interference or clearance between the rivet and the elastic foundation contact surfaces. In reality, installation of practical countersink rivets involves interference fit during the rivet squeezing process, and creates plastic deformation that invalidates the elastic assumptions. In order to apply the Barrois analysis to the interference fit countersunk fasteners employed in the experimental program, the joint flexibility was determined experimentally with the setup described below.

Single lap joint specimens with a single rivet (Fig. 3) were tested, and an extensometer (MTS Model 632.11B-20) was used to obtain the load-deflection curve across the joint. The relatively long (102 mm) gage length was selected to minimize bending effects in the single lap joint. Four different squeeze forces were used to install the rivets (17.80 KN, 15.58 KN, 13.35 KN and 11.13 KN) in order to determine the influence of fastener interference. (As discussed later, hole expansion was experimentally related to the rivet installation squeeze force.) In addition, the displacement was measured on both sides of replicate specimens (**front side** with countersunk head and **rear side** with driven head) to ensure that consistent behavior was obtained from the load-displacement tests. The specimens were loaded in tension in a 90 KN (20 kip) servo-hydraulic MTS test machine until the force-displacement curve slightly exceeded yield, and then the specimen was unloaded. The specimen was then reloaded and unloaded ten more times in the elastic regime. The average slope of the deflection-force curves is the joint flexibility, and is reported in Table 1 for the four rivet squeeze forces. Note that joint flexibility initially decreases as the squeeze force is increased (and the lap faces are held more tightly together), resulting in a stiffer joint. The flexibility increases again, however, for large squeeze forces, indicating that there is an optimum value of squeeze force with respect to joint stiffness. Similar behavior has been reported in Ref. 18.
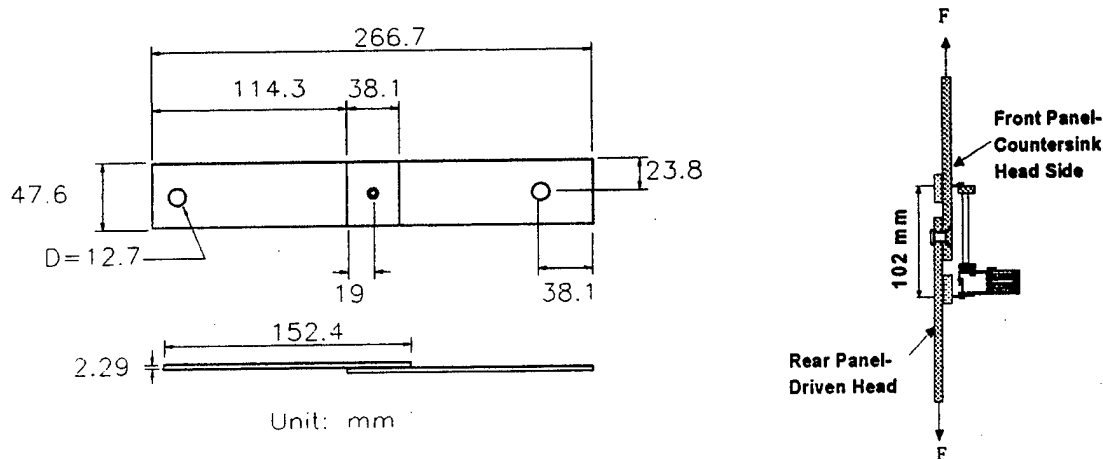
FIG. 3—*Setup for joint flexibility measurement.*

TABLE 1—*Joint Flexibility versus deformed rivet head.*

Rivet Squeeze Force		D/D_0	Joint Flexibility, *(JF)* mm/MN
KN	Kip		
17.80	4.0	1.186	54.39
15.58	3.5	1.257	53.94
13.35	3.0	1.321	52.80
11.13	2.5	1.386	58.11

A parametric study for a 3-row, countersunk, single lap joint structure was conducted to determine the influence of squeeze force on load transfer. For higher rivet squeezing forces, the plastic deformation becomes more severe and the joint flexibility is smaller (less flexible). It is, therefore, plausible that more load can be transferred from this "tighter" clamping condition. Fig. 4 shows the load transfer ratios for rivet rows installed with different rivet squeeze forces. As shown by case I, if rivets in all three rows are squeezed with the same force (15.58 KN = 3.5 kip), the top and the bottom rivet rows transfer the same load, while the middle row carries less force. Case II considers different squeeze forces for all three rows, with the top row installed with the largest force (15.58 KN = 3.5 kip) and the middle with the smallest force (11.13 KN = 2.5 kip). Note that in this example the load transfer ratio for the top row increases, while the middle row decreases. If, as in case III, the middle row rivets are installed with the highest squeeze force and the top row has the lowest installation force, the changes in load transfer ratios are reversed from case II.
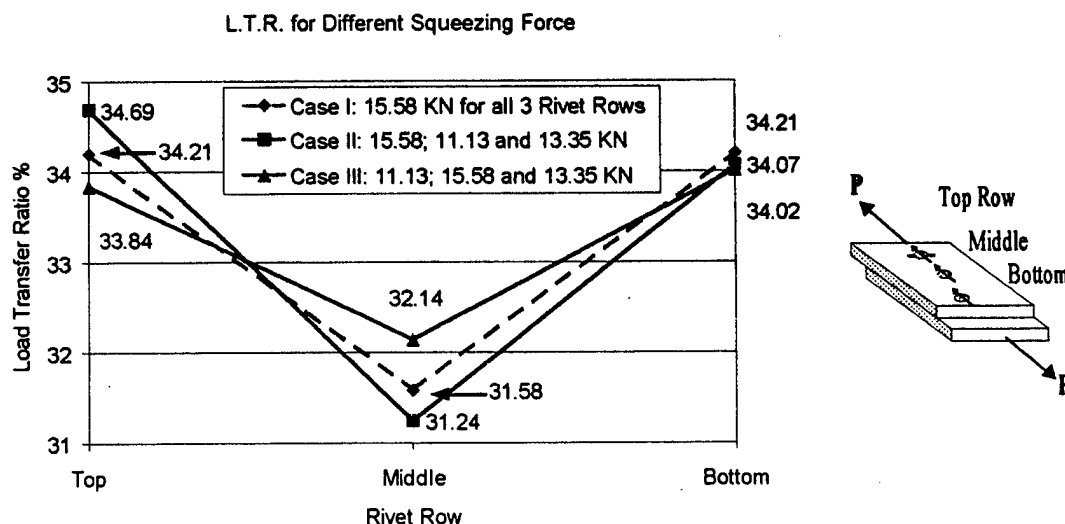

FIG. 4—Load transfer ratio for a 3-row riveted joint

Another load transfer issue is associated with the growth of cracks at various fastener holes. As these cracks grow, the structural compliance will increase (i.e. become less stiff), inducing additional displacement in the joint. This effect can cause load shedding from cracked to uncracked rows of rivets, and change the load transfer mechanism. In order to analyze this load shedding effect, the displacement compatibility given by Eq 1 can be rewritten as

$$\delta_i - \delta_{i+1} = \Lambda_{ai} - \Lambda_{bi} - \delta_{due\_to\_crack} \qquad (2)$$

Here $\delta_{due\_to\_crack}$ is the product of the applied force P and the structural compliance C for the cracked member. The structural compliance is a function of the load transfer ratio, the stress intensity factor, and geometry [4,7,19]. The SIF solutions used here are from [20], and employ the solutions for a plate with a row of through-cracked holes (case TCO5) and for a crack at an offset hole in a plate (case TC03). Reference 7 presents example results for the change in load transfer associated with crack growth, and provides more details about the calculations.

Stress Intensity Factor For Interference Fit Rivets

Interference fit fasteners are often used to increase fatigue life since hole expansion produces residual stresses that delay fatigue crack formation and growth. As discussed later, interference fit can also affect the load transfer in a riveted joint. Two interference fit models proposed by Rich and Impellizzeri [12] and by Hsu and Forman [21] are used for this study. The major difference between the Rich-Impellizzeri and the Hsu-Forman stress analyses is that the former assumes elastic-perfectly plastic material behavior, while the latter applies work hardening plasticity. Comparison of residual stresses predicted by these two models for various interference levels are given in Ref. 7.

Residual stresses created by the interference fit can reduce the effective hoop stress at the fastener hole and cause significant improvement in fatigue life. Cathey and Grandt [22] showed that stress intensity factors obtained by a relatively simple weight function method could be used to obtain reasonable fatigue crack growth lives for open, cold-worked holes in 7075-T6 aluminum specimens. The SIF K_R due to the residual stresses can be calculated from a tabulated weight function [23] if the uncracked stress distribution is known. The total SIF K_{tot} associated with load transfer and the interference-fit plasticity analysis of the riveted structure is given by superposition as

$$K_{tot} = K_{by-pass\ loading} + K_{pin-loading} \pm K_R \qquad (3)$$

Here the $K_{by\text{-}pass\ loading}$ and the $K_{pin\text{-}loading}$ terms are the stress intensity factors from Reference 20 for the by-pass and pin-loading cases, and employ the load transfer analysis described previously. The +/- K_R term in Eq 3 adds or subtracts the interference fit SIF depending on whether the residual stress field is tension or compression. Thus, when the interference fit results in compressive residual stresses, the SIF due to remote loading is reduced, and crack formation and propagation are delayed. Example calculations for these stress intensity factors are reported in Ref. 7.

An experimental program was conducted to determine the appropriate hole expansion for the installed rivets employed for the present work. Once the interference fit level is established, the plastic deformation and the compressive stress around the rivet hole can be estimated, and stress intensity factors computed by Eq. 3. A controlled squeeze force riveting procedure was employed here to ensure consistent quality of the

riveted specimens [18]. Since inconsistent installation will effect the level of interference fit and corresponding stress field around the rivet holes, force-controlled riveting processes are commonly recommended for aviation manufacturing [18,24-25]. The current work employed a controlled squeeze-force rivet apparatus based on a 22 KN (5 kip) MTS testing system.

Hole expansion measurements were performed on the specimen shown in Fig. 5. Here three rows of 9 rivets were used to join two 2.29 mm (0.09 in) thick 2024-T3 aluminum sheets. The distance between holes and free edges was 5 times the 4.87 mm (0.192 in) rivet diameter to avoid interaction during the riveting process. The countersunk rivets (100° flush head) were made from 2117 aluminum alloy, had a shank diameter $D_0 = 4.76$ mm (0.187 in), and had the following identification number: MS20426-AD-6-6 [25]. Four different squeezing forces were examined (11.13 KN, 13.35 KN, 15.58 KN and 17.80 KN), with all 27 rivets in a given specimen installed with the same squeeze force.
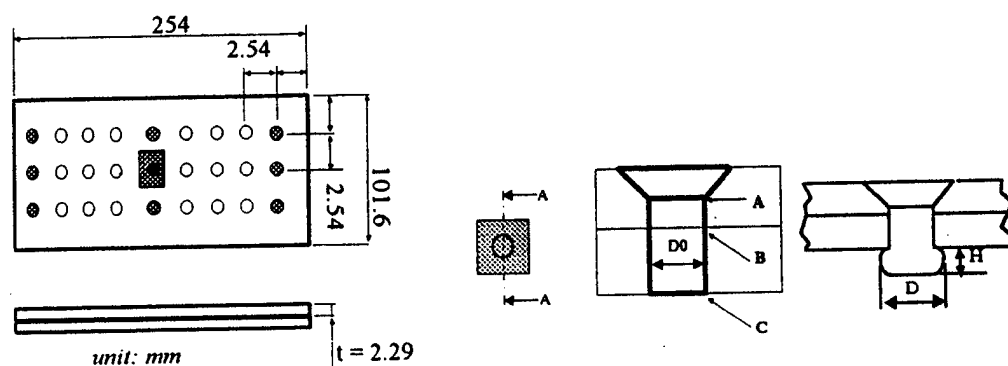

FIG 5—Specimen setup for hole expansion measurement (dimension in mm).

Nine of the twenty-seven installed rivets were cut from each assembly, sectioned, carefully polished, and measured to determine the expansion diameters at three locations [7]. Table 2 and Fig. 6 give results for the average expansion D measured at the three locations shown in Fig. 5 - A: the root of countersink head, B: the interference between two plates and C: driven head. Note that the expansion level increases with the applied rivet squeeze force.

TABLE 2—Deformed rivet diameter and height versus squeezing force

Squeezing Force KN	Kip	D, mm	Std. Dev. mm	D/D$_0$	H, mm	Std. Dev. mm
17.80	4.0	6.6	0.00127	1.386	2.48	0.00194
15.58	3.5	6.29	0.00141	1.321	2.69	0.00199
13.35	3.0	5.99	0.00153	1.257	3.00	0.00248
11.13	2.5	5.65	0.00115	1.186	3.33	0.00278

Hole Expansion Measurement

Hole Expansion (mm) = 8.11 e-9 x (Sqeeze Force) -3.858 e-5
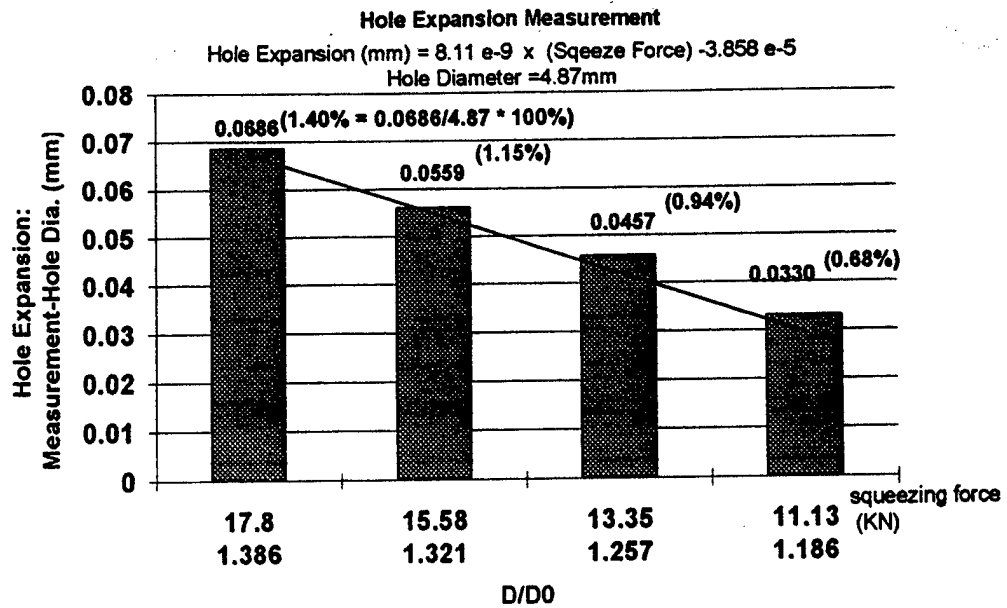
Hole Diameter =4.87mm

FIG. 6 —Hole expansion measurements as a function of rivet squeeze force

Secondary Bending Effect

Secondary bending considerations also play a role for SIF calculations in single-lap joint specimens. A bending stress calculation proposed by Schijve [26] is given by Eq. 4 in the form of an estimated bending ratio k.

$$k = \frac{\sigma_{bend}}{\sigma_{remote}} = \frac{6}{t_1} \times \frac{e - T_2 \dfrac{\beta}{\alpha_2}}{1 + \dfrac{\alpha_1}{\alpha_2}\dfrac{T_2}{T_1}}$$

(4)

Here, as shown in Fig. 7,

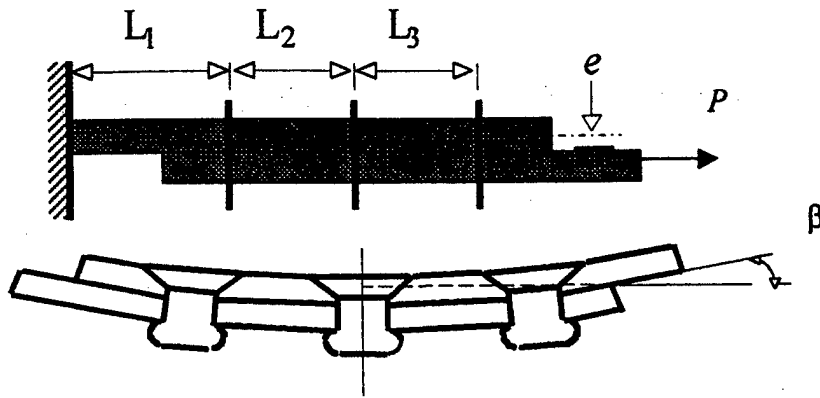|	
t_1	= plate thickness, mm,
e	= eccentricity of two jointed plates,
β	= rivet rotational angle,
P	= Remote load, KN,
E_i , I_i	= Young's modulus and moment of inertia of ith plate,
α_i	= $P/(E_i I_i)$,
L_i	= the distance between the rivet to the boundary or the spacing between the rivets, mm,
T_i	= Tanh($\alpha_i L_i$)

FIG. 7—Schematic representation of the secondary bending (rivet rotation) model.

With the aid of Eq 4, the bending stress σ_{bend} can be calculated, and the SIF due to secondary bending can be estimated by the following equations [14].

$$K_{bend} = \beta_{ben} k \sigma_{remote} \sqrt{\pi a_{eff}} \tag{5}$$

$$\beta_{ben} = 0.39 \times \left(1.0 + 0.16 \left(\frac{a_{eff}}{W_{eff}} \right)^2 \right) with \, v = 0.3$$

Here W_{eff} is the hole spacing and $2a_{eff}$ is an effective crack length that includes the hole diameter and radial crack lengths. Rewriting Eq 3, the total SIF for a single lap joint specimen is:

$$K_{tot} = K_{by-pass\ loading} + K_{pin-loading} \pm K_R + K_{bend} \tag{6}$$

Failure Criteria

While several failure criteria have been proposed for the MSD problem, this research employs the net section yield and Swift's ligament yield criteria [1]. The net section yield criterion states that failure will occur when the failure load P_{Cnet} causes the net section stress to equal or exceed the tensile yield stress (σ_{ys}). This condition may be expressed as follows:

$$P_{Cnet} = \sigma_{ys}(W - nD - n_{MSD}a_{avg.} - 2a_{lead})t$$
$$= \sigma_{ys}W_{net}t \tag{7}$$

Here W is the panel width, n is the total number of rivet holes, D is the average rivet hole diameter, n_{MSD} is the number of MSD cracks, a_{avg}, is the average crack length, a_L is the half-crack length of the central lead crack, and t is the panel thickness.

The Swift ligament yield failure criterion [1] states that the failure occurs when the plastic zones of two approaching crack tips "touch" each other as shown schematically in Fig. 8. This failure load, P_{CLY}, is given by Eq 8.

$$P_{CLY} = \sigma_{ys}tW_{net}\sqrt{\left[\frac{2b}{(a_{MSD}\beta^2{}_h\beta^2{}_{iMSD} + a_{lead}\beta^2{}_{ilead})}\right]} \tag{8}$$

In Eq 8, W_{net} is the net width of the specimen, defined in Eq 7, a_{MSD} and a_{lead} are the two approaching MSD and lead crack lengths, β_{ilead} and β_{iMSD} are the Kamei-Yokobori [16] interaction factor for two approaching cracks, β_h is the TC05 SIF solution [20], and b is the crack tip separation shown in Fig. 8.
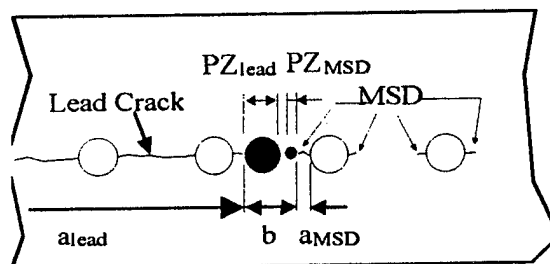

FIG.8—Schematic of the ligament yield criterion proposed by T. Swift [1]

Fatigue Tests of Lap Joint Specimens and Life Predictions

Five lap joint fatigue tests were conducted to evaluate the ability to predict the growth and coalescence of MSD cracks. The single lap specimens were joined by three rows of eight countersunk rivets as shown in Fig. 9. All specimens were pre-cracked along the top rivet row where experience (and the load transfer model) indicates the most severe cracking occurs. The specimens were then tested under constant amplitude loading, and the growth, coalescence, and final fracture resulting from individual cracks was recorded, and compared with the numerical analysis.

All specimens were made from 2.29 mm (0.09 in) thick 2024-T3 bare aluminum alloy loaded in the T-L rolling direction. Specimen preparation consisted of two steps. First, 812 mm long by 406 mm (32 x 16 in) wide panels were constructed with a "dogbone" test section that was 228.6 mm (9in) wide. A single row of eight 3.97 mm (5/32 in) diameter holes were then drilled in these specimens, and a jeweler's saw (blade thickness = 0.33 mm = 0.013 in) was used to cut a pair of small notches on the opposite sides of each hole (average length = 0.381 mm 0.015 in). The two outside holes were not notched, however, since it is known that more load is taken by rivets located near free edges than by other rivets in wide lap joint specimens [18,27], and it was desired to prevent premature failure at those locations. The panels were then cyclically loaded to develop cracks at the saw-cuts. This precracking was conducted at a frequency of 5 Hz, and employed a load shedding procedure that ended when the SIF for the longest crack tip reached 6.6 $Mpa\sqrt{m}$ (6 ksi√in). The lengths of these cyclic MSD cracks ranged from 4.57 mm (0.18 in) to zero (including the sawcut).
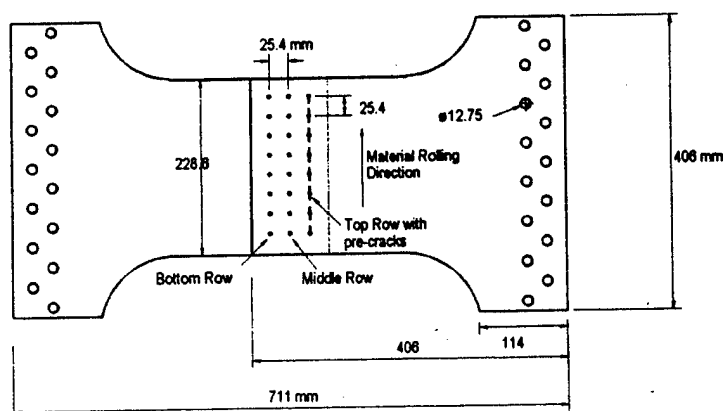

FIG. 9—Schematic of single lap joint specimen

The next step was to cut each panel in half, leaving one member of each pair with the precracked row of holes. These two halves were then drilled to the desired 8 × 3 rivet hole pattern, reamed to a final hole diameter of 4.85 mm (0.191 in), and countersunk on one side. This final drill and ream removed the initial saw cuts, leaving only small fatigue cracks in one panel at the initial row of holes. Finally, 4.76 mm (0.187 in) diameter countersunk rivets (MS20426-AD-6-6) were installed with a fixed 15.58 KN (3.5 kip) squeeze force. Since the specimens were riveted after pre-cracking, some of the shorter cracks were contained within the residual stress field formed during the rivet crimping procedure. In addition, portions of some cracks were removed by the countersinking, leaving an internal crack that was hidden from view by the rivet head. The average radial pre-cracks were typically on the order of 0.34 mm to 1.12 mm (0.0134 – 0.044 in) long, and emanated from both sides of the countersunk rivet holes. The average MSD pre-crack lengths and the applied fatigue loads are summarized in Table 3 for the five experiments reported here.

Comparison of Analysis and Experiment

Cyclic extension of all MSD cracks resulting from the R = 0.05 constant amplitude fatigue loading were measured by means of a travelling microscope, and were recorded as a function of elapsed cycles. Fatigue crack growth lives were then computed by a fracture mechanics based algorithm that incrementally grows individual cracks based on their current stress intensity factor and the fatigue crack growth rate behavior for the test materials. (See Ref. 7 for the fatigue crack growth properties of the 2024-T3 material tested here.) The initial growth, coalescence, and final fracture is predicted in this manner, and the algorithm has been quite successful in predicting fatigue lives for other MSD specimens that contain open holes in stiffened and unstiffened panels [2,4-6]. The predictive algorithm was modified in the present case to include the stress intensity factor and load transfer solutions described previously for the lap joint configuration. Since the current life prediction model is based on through-cracked stress intensity factor solutions, and does not consider three-dimensional effects associated with part-through cracks or the countersink, the average hole diameter and through-crack length were used as input for the MSD life prediction program.

As mentioned previously, some of the small precracks were hidden under the rivet heads or contained in the plastic zone around the installed rivet and did not immediately grow, resulting in a period of "crack retardation." (The measured delay cycles are listed in Table 3.) Note that specimen Slap#5 exhibited significant delay, and the observed fatigue crack growth period is relatively long compared to Slap#1 and #4 which were also tested at the same 55.1 Mpa (8 ksi) cyclic stress level (note, however, that the average MSD size was smaller for this specimen). Since the algorithm assumes MSD cracks at all hole locations, and a few of the smaller precracks were removed following the final ream and countersink, it was decided to assume a small 0.127 mm (0.005 in) crack length at those locations. Fig. 10 plots crack tip position versus elapsed cycles for SLap #4 (see Ref. 7 for similar plots for the other specimens), and Fig. 11 summarizes the measured and predicted fatigue crack growth lives for all five lap joint tests. The average difference between the measured and predicted lives for these 5 fatigue tests is 15%, varying between 8.0 % and 27.4%.

Table 3—Summary of test specimen initial conditions and failure data.

Test Specimen ID	Avg. Crack Length (mm)	Max Applied Stress KN	Ksi	Total Life / Prediction Life (Cycles)	Delayed Cycles	Diff.%
Slap #1	0.98	55.1	8	99,143/ 126,281	56,000	27.4 %
Slap #2	1.00	96.5	14	9,028/ 7,801	0	13.6 %
Slap #3	0.34	68.9	10	50,489/ 42,629	10,000	15.6 %
Slap #4	1.12	55.1	8	97,655/ 109,266	40,000	11.9 %
Slap #5	0.82	55.1	8	160,024/ 147,350	70,000	8.0 %

As indicated previously, the initial fatigue crack growth was "retarded" by two mechanisms- the clamping pressure between the cracked plates, and plasticity-induced compressive stress around the rivet holes. If the crack lengths are long enough, or the applied remote stress is large enough, the cracks will propagate immediately upon applied cyclic loading, and the life prediction agrees well with the experimental results. Specimen SLap#2, for example, contained relatively short precracks, but was tested to the largest applied cyclic stress (96.5 Mpa = 14 ksi), and the cracks began growing immediately, without a delay period. The predicted and measured lives agreed within 14 % for this case. In the other tests, it was necessary to start computations after the cracks were observed to begin growing in the fatigue test in order to obtain a reasonable fatigue life. The experimental data do indicate, however, that it is possible to obtain excellent life predictions once the cracks have started to grow. Thus, the load transfer analysis and stress intensity factor solutions developed for the lap joint problem give reasonable crack growth lives when the crack retardation effect is experimentally accounted for. Continuing research is focusing on developing techniques to predict the delay period for analysis purposes.
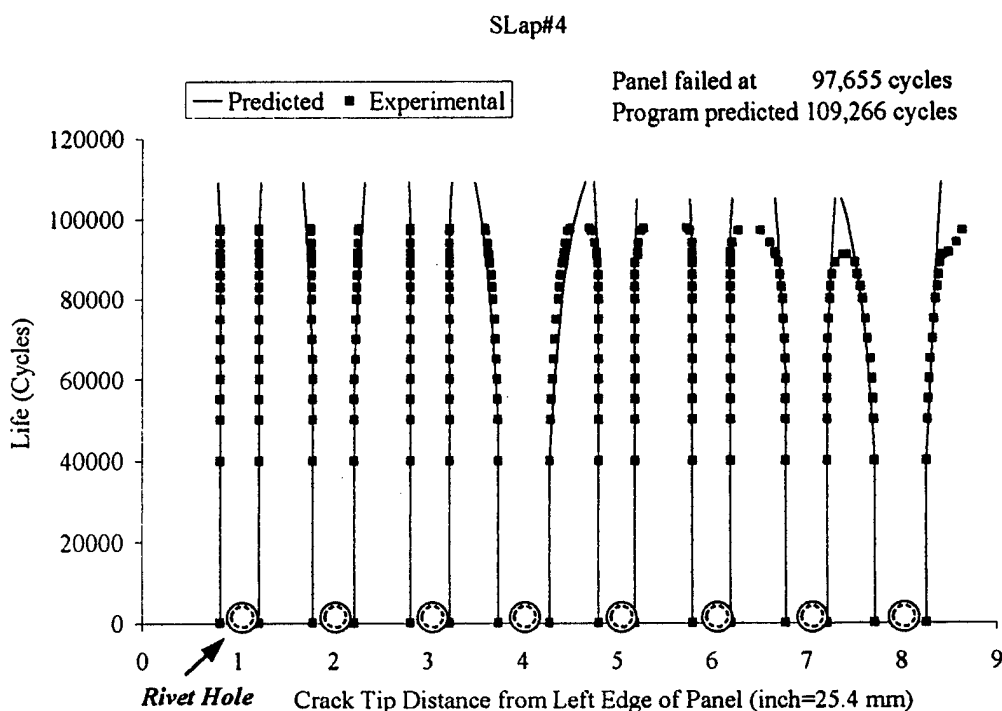
SLap#4

FIG. 10 —Comparison of experimental and predicted fatigue crack propagation for a single lap joint specimen SLap #4 (3 rows of 8 rivets) tested at a cyclic stress level of 55.1Mpa (8 Ksi) (the size of rivet hole is not to scale).
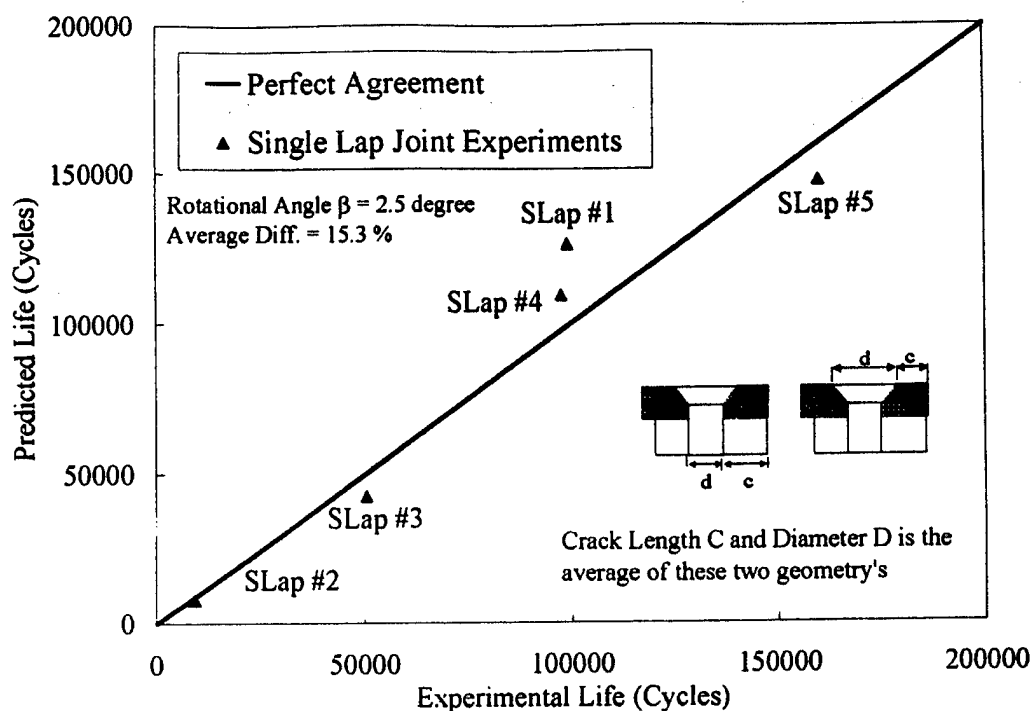
FIG. 11— Measured and predicted fatigue panel failure lives for tests

References

[1]   Swift, T., "Widespread Fatigue Damage Monitoring Issues and Concern," The 5th International Conference on Structural Airworthiness of New and Aging Aircraft, Hamburg, Germany, June 16-18, 1993.

[2]   Moukawsher, E.J., Grandt, A.F., Jr., and Neussl, M.A. "Fatigue Life of Panels With Multiple Site Damage," Journal of Aircraft, Vol. 33, No. 5, September-October 1996, pp. 1003-1013.

[3]   Wang, H.L., Buhler, K., and Grandt, A.F., Jr. "Evaluation of Multiple Site Damage in Lap Joint Specimens," Proceedings of the 1995 USAF Structural Integrity Program Conference, ASIP Volume 1, August 1996, pp.21-38.

[4]   Heinimann, M.B. and Grandt, A.F., Jr., "Analysis of Stiffened Panel with Multiple Site Damage", 1996 USAF Structural Integrity Program Conference, San Antonio, Texas, December 3-5, 1996.

[5]   Grandt, A.F., Jr., Sexton, D.G., Golden, P.J., Bray, G.H., Bucci, R.J., and Kulak, M., "A Comparison of 2024-T3 and 2524-T3 Aluminum Alloys under Multi-Site Damage Scenarios," ICAF 97 Fatigue in New and Aging Aircraft, Volume II, Poster Papers, Editors: R. Cook and P. Poole, Proceedings of the 19th ICAF Symposium, International Committee on Aeronautical Fatigue, 18-20 June 1997, Edinburgh, Scotland, pp. 659-669.

[6]   Heinimann, M.B., and Grandt, A.F., Jr., "Fatigue Analysis of Stiffened Panels with Multiple Site Damage," First Joint DoD/FAA/NASA Conference on Aging Aircraft, Ogden, Utah, 8-10 July 1997

[7]   Wang, H.L., "Evaluation of Multiple Site Damage in Lap Joint Specimens," Ph.D. Thesis, School of Aeronautics and Astronautics, Purdue University, West Lafayette, IN, August, 1998.

[8]   Beuth, J.L., Hutchinson, J.W., "Fracture Analysis of Multiple Site Cracking in Fuselage Lap Joints," Durability of Metal Aircraft Structures, Proceeding International Workshop on Structural Integrity of Aging Airplane, Atlanta, GA, 31 March- 2 April, 1992, Atlanta Technology Publications, 1992.

[9]   Beuth, J.L., Hutchinson, J.W., "Fracture Analysis of Multi-Site Cracking in Fuselage Lap Joints," Computational Mechanics, 1994, 13, pp.315-331.

[10]   Lee, Eun U., "Effect of Load Transfer on Fatigue of Mechanically Fastened Metallic Joints," Fatigue in Mechanically Fastened Composite and Metallic Joints, ASTM STP 927, ASTM, Philadelphia, 1986, pp.95-117.

[11]   Huth, Heimo "Influence of Fastener Flexibility on the Prediction of Load Transfer and Fatigue Life for Multiple-Row Joints," Fatigue in Mechanically Fastened Composite and Metallic Joints, ASTM STP 927, ASTM, Philadelphia, 1986, pp.221-250.

[12]   Rich, D.L., Impellizzeri, L.F., " Fatigue Analysis of Cold-Worked and Interference Fit Fastener Holes", Cyclic Stress-Strain and Plastic Deformation Aspects of Fatigue Crack Growth, ASTM STP 637, ASTM, Philadelphia, 1977, pp.153-175.

[13]   Singh, R., Park, J.H., Atluri, S.N., "Growth of Multiple Cracks and Their Linkup in a Fuselage Lap Joint," AIAA Journal, Vol. 32, No. 11, November 1994, pp.2261-2268.

[14]   Sampath, S., Broek, D., "Estimation of Requirements of Inspection Intervals for Panels Susceptible to Multiple Site Damage", Structural Integrity of Aging Airplanes, Springer-Verlag, Berlin, Heidelberg, 1991, pp.339-389.

[15]   Vleiger, H., "Results of Uniaxial and Biaxial Tests on Riveted Fuselage Lap Joint Specimens", Presented at the FAA/NASA International Symposium on Advanced Structural Integrity Methods for Airframe Durability and Damage Tolerance, May 4-6, 1994, Hampton, VA.

[16]   Kamei, A., Yokobori, T., "Two Collinear Asymmetrical Elastic Cracks," Report of the Research Institute for Strength and Fracture of Materials, Tohoku University, Vol. 10, Section 1-4, pp.41-42, December 1974.

[17]   Barrois, W., "Stress and Displacements Due to Load Transfer by Fasteners in Structural Assemblies," Engineering Fracture Mechanics, 1978, Vol. 10, pp.115-176.

[18]   Muller, Richard P.G., "An Experimental and Analytical Investigation on the Fatigue Behavior of Fuselage Riveted Lap Joints- The significant of the rivet squeeze force and a comparison of 2024-T3 and Glare 3," Ph.D. Dissertation, Delft University of Technology, Faculty of Aerospace Engineering Structures and Materials Laboratory, The Netherlands.

[19]   Grandt, A.F., Jr. and Sinclair, G.M., "Stress Intensity Factors for Surface Cracks in Bending, " Stress Analysis and Growth of Cracks, Proceedings of the 1971 National Symposium on Fracture Mechanics, Part I, ASTM STP 513, ASTM, Philadelphia, 1972, pp.37-58.

[20]   Fatigue Crack Growth Computer Program "NASA/FLAGRO" Version 2.0, Appendix C, December 1992.

[21]   Hsu, Y.C., Forman, R.G., "Elastic-Plastic Analysis of an Infinite Sheet Having a Circular Hole Under Pressure," Journal of Applied Mechanics, June 1975, pp.347-352.

[22]   Cathey, W.H., Grandt, A.F., Jr., "Fracture Mechanics Consideration of Residual Stresses Introduced by Coldworking Fastener Holes," Journal of Engineering Materials and Technology, January 1980, Vol. 102, pp.85-91.

[23] Kullgren, T.E., Grandt, A.F., Jr.," Tabulated Stress Intensity Factor Solutions for Flawed Fastener Holes," Engineering Fracture Mechanics Vol. 18, No. 2, 1983, pp. 435-451.

[24] Standard Aircraft Handbook, 5th Edition. Edited by Larry Reithmaier, Originally Compiled and Edited by Stuart Leavell and Stanley Bungay, TAB/AERO, Division of McGraw-Hill, Inc. Blue Ridge Summit, PA 17294-0850.

[25] Military Handbook, Metallic Materials and Elements for Aerospace Vehicle Structures, MIL-HDBK-5G, November 1 1994.

[26] Schijve, J., "Some Elementary Calculations on Secondary Bending in Simple Lap Joints," NLR TR 72036 U, 1972.

[27] Newman, J.C., Jr., Harris, C.E., James M.A., Shivakumar, K.N., "Fatigue-Life Prediction of Riveted Lap-Splice Joints Using Small-Crack Theory", ICAF 97 Fatigue in New and Aging Aircraft, Volume I, Poster Papers, Editors: R. Cook and P. Poole, Proceedings of the 19th ICAF Symposium, International Committee on Aeronautical Fatigue, 18-20 June 1997, Edinburgh, Scotland, pp. 523-552.

BENEFITS OF IMPROVED FUSELAGE SKIN SHEET ALLOY 2524-T3 IN MULTI-SITE DAMAGE SCENARIOS

Gary H. Bray, Robert J. Bucci, Michael Kulak and Charles J. Warren
Aluminum Company of America
Alcoa Center, PA 15069 USA
Telephone: (724) 337-5727
FAX: (724) 337-5436
gary.bray@alcoa.com

Alten F. Grandt, Jr., Patrick J. Golden and Darren G. Sexton
School of Aeronautics and Astronautics
Purdue University
West Lafayette, IN 47907 USA

ABSTRACT

This paper quantifies the improved resistance to the consequences of multi-site damage (MSD) that can develop in older aircraft provided by new Alcoa aluminum fuselage skin sheet alloy 2524-T3. Results from three types of tests are presented for 2524-T3 and the incumbent fuselage skin sheet alloy 2024-T3: (1) residual strength tests to assess the effect of multi-site damage on residual strength of unstiffened and stiffened flat panels; (2) fatigue tests on unstiffened flat panels to assess the effects of multi-site damage on fatigue life; and (3) fatigue tests on multi-hole coupons with and without prior corrosion to evaluate the resistance of each alloy to naturally occurring MSD. The results indicate that alloy 2524 offers improved structural damage tolerance in the presence of MSD due to its superior fatigue crack growth resistance and fracture toughness and is more resistant to MSD from corrosion in bare sheet form. The residual strength of 2524 panels containing a lead crack with MSD at adjacent holes was 8.8 to 10.4% higher than 2024 panels and the average fatigue life 27 to 45% longer depending on MSD flaw size. The two alloys had equivalent resistance to MSD from fatigue alone but the mean flaw areas following corrosion and fatigue were 18% smaller in bare 2524 than in bare 2024 and the corroded area alone 32% smaller. Potential advantages of the improved damage tolerance of 2524-T3 to aircraft manufacturer/operators are weight savings, lower operating costs, easier inspectability and increased safety.

1. INTRODUCTION

The service life of an airframe can potentially introduce multi-site damage (MSD) states such as widespread fatigue and/or corrosion that may imperil the structural integrity of the aircraft. The inspection intervals set by standard residual strength and damage tolerant design are normally directed at the presence of a single crack, but may be inadequate in the presence of MSD. It is well known, for example, that small fatigue cracks ahead of a larger lead crack can significantly reduce the residual strength and fatigue life normally associated with the lead crack [1-5]. This realization and the desire for reliable, longer lasting aircraft with lower maintenance costs have given rise to requirements that non-pristine or aging structure be accounted for in design and maintenance strategies. This philosophical shift has created demand for affordable replacement materials that cannot only resist the occurrence of multi-site damage, but which offer improved structural damage tolerance when MSD is present.

An excellent example of one such material is new aluminum alloy 2524-T3 (formerly C188-T3) developed by Alcoa. Currently used in the Boeing 777 aircraft, 2524-T3 was designed for fuselage skin sheet as a replacement for 2024-T3, the industry standard since the DC-3. As shown in Table 1, 2524-T3 has superior fatigue crack growth resistance and plane stress fracture toughness (Kc) in comparison to 2024-T3 while maintaining equivalent tensile properties. Boeing utilized the improvements of 2524 in fracture toughness and fatigue crack growth resistance to obtain weight savings and reduced manufacturing costs in new structure over incumbent alloy 2024 design [6-8]. The goal of the present study described in this paper is to quantify the beneficial effects of the improved damage tolerance provided by 2524-T3 over 2024-T3 once MSD is already present and to compare the resistance of both alloys to the onset of MSD from fatigue alone and in combination with corrosion.

TABLE 1. TYPICAL MECHANICAL PROPERTIES OF ALCLAD 2524-T3 AND 2024-T3 ALUMINUM ALLOYS (LT DIRECTION)

Alloy	Thickness (inch)	TYS (ksi)	UTS (ksi)	Kc^a (ksi√in)	da/dN@ ΔK=30 (inch/cycle)[b]
2524-T3	0.032-0.062	44	61	158	9.0E-05
	0.063-0.128	45	64		
	0.129-0.249	44	64		
2024-T3	0.032-0.062	43	62	128	2.7E-04
	0.063-0.128	45	65		
	0.129-0.249	45	65		

[a] M(T) specimen, T-L orientation, W=16 in., 2ao= 4 in.

[b] T-L orientation, R=0.1, relative humidity > 90%

2. EXPERIMENTAL PROCEDURES

2.1 TEST MATERIALS

The 2024-T3 and 2524-T3 materials used in this study were purchased commercially in the form of 0.050-inch thick alclad and 0.100-inch thick bare sheet. The strength and plane stress fracture toughness (Kc) properties measured in these materials are shown in Table 2. Fatigue crack growth curves for the 0.050-inch alclad sheet are shown in Figure 1.

TABLE 2. MECHANICAL PROPERTIES OF MATERIALS IN THIS STUDY (LT DIRECTION)

Alloy	Thickness (in.)	TYS (ksi)	UTS (ksi)	Elong. (%)	Kc (ksi√inch)[a]
Alclad 2524-T3	0.050	43.6	60.3	20.5	150
Alclad 2024-T3	0.050	43.6	61.9	18.5	136
Bare 2524-T3	0.100	44.9	68.0	24.0	149
Bare 2024-T3	0.100	45.8	69.5	21.2	136

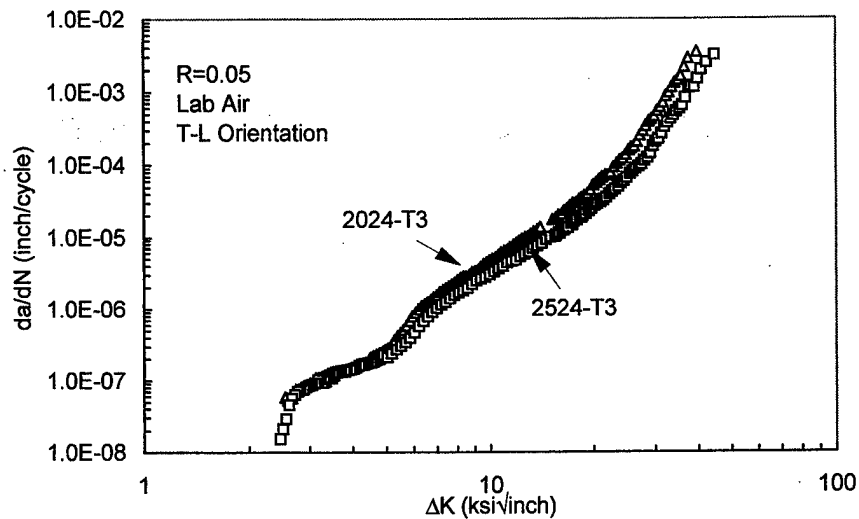[a] M(T) specimen, T-L orientation, W=16 in., 2ao= 4 in.

Figure 1. Fatigue crack growth curves for alclad 2524-T3 and 2024-T3 sheet in this study.

2.2 MSD RESIDUAL STRENGTH TESTS

The goal of these tests was to determine how the residual strength of each alloy is influenced by small flaws (MSD) ahead of a lead crack. The lead crack is intended to model accidental damage or a large fatigue crack from a rogue flaw, while the small MSD is representative of widespread fatigue or corrosion which could develop in older aircraft. Tests were performed on both unstiffened and stiffened flat panels of 0.050-inch alclad sheet. The unstiffened panels were 16 inches wide by 40 inches long with a 21-inch long uniform-width test section. The panels contained a central row of open holes oriented perpendicular to the applied tensile stress. The holes were 5/32 inch diameter and were spaced 1.0 inch apart on center. A 4.4-inch long lead crack was formed by sawing the ligament between the five central holes and then introducing 0.10-inch long EDM notches at the end of this slot. The configuration of the stiffened panels was identical except that two stiffeners 0.080 thick by 1.25 wide by 26.25 inches long of 7050-T76 sheet were attached to the panel by 3/16 diameter rivets spaced 0.75 inch apart. The stiffeners were attached parallel to the panel length and spaced 9 inches apart with the lead crack centrally located between them. Small through-thickness MSD flaws were introduced by EDM on each side of the remaining open holes in the plane of the lead crack. The unstiffened panels contained MSD flaw sizes of either zero, 0.05, 0.10, or 0.15 inch and the stiffened panels contained flaw sizes of either 0.05 or 0.10 inch. All cracks were oriented in the T-L orientation relative to the parent sheet. The panels were pulled to failure in remote tension under displacement control. Extension of the lead crack was obtained as a function of applied load during stable crack growth. Link-ups between the lead crack and the cracks emanating from the MSD flaws were also recorded visually with the aid of an optical microscope.

2.3 MSD PANEL FATIGUE TESTS

The goal of these tests was to determine how fatigue life of each alloy is influenced by small flaws (MSD) ahead of a lead crack. Tests were performed on unstiffened panels of 0.050-inch alclad sheet. The panels were 9 inches wide by 21 inches long with a 14-inch long uniform-width test section. These panels also contained a single row of 5/32-inch diameter holes spaced 1.0 inch apart oriented

3

perpendicular to the applied tensile stress. A 1.36-inch long lead crack was created by sawing the ligament between the two central holes and introducing a 0.10 inch long EDM slot at the end of the two holes. Small through-thickness MSD flaws of either zero, 0.05 or 0.10 inch were introduced by EDM on each side of the remaining open holes in the plane of the lead crack. All cracks were again oriented in the T-L orientation. The panels were cycled to failure using a maximum gross stress of 8.56 ksi and a stress ratio of R=0.05. The position of each crack tip including the lead and MSD flaws was recorded as a function of elapsed cycles with a traveling microscope.

2.3 MULTI-HOLE FATIGUE COUPON TESTS

The goal of these tests was to compare the size and frequency of naturally occurring MSD in 2524 and 2024 sheet resulting from fatigue alone or in combination with corrosion. Multi-hole fatigue tests were conducted on three material/conditions; (1) pristine 0.050-inch thick alclad sheet; (2) pristine 0.100-inch thick bare sheet; and (3) 0.100-inch thick bare sheet with prior corrosion. The multi-hole coupons were 6.25 inches wide by 24 inches long and contained four rows of six holes (24 total) at mid-length. The length dimension was in the long transverse (LT) direction of the parent sheet. The hole diameter was 5/32 inch and the hole spacing was 1.0 inch on center. The holes were drilled and deburred but not reamed. The pristine alclad and pristine bare coupons were then fatigue tested without any additional preparation. Three pristine alclad coupons of each alloy were fatigued 150000 cycles at maximum remote stress of 14.9 ksi and two pristine bare coupons 200000 cycles at a maximum remote stress of 14 ksi. Coupons for the bare corroded condition were exposed 24 h in sodium chloride/hydrogen peroxide solution prepared in accordance with ASTM G110. Previous work on 2024 indicates the fatigue performance following this method of corrosion is similar to that following one year seacoast exposure. Three coupons of each alloy were then fatigued 100000 cycles at a maximum stress of 10 ksi. The stress ratio in all tests was R=0.05. The specific number of cycles applied to each condition was approximately two-thirds to three-fourths of the lifetime of specimens tested to failures.

Following fatigue cycling to the specified number of cycles, each hole (24 per coupon) was broken open and examined for possible fatigue cracks and in the case of the bare corroded coupons for corrosion damage. To break open each hole, a 1-inch square coupon of material containing the hole was excised from the panel. Notches were cut in the square piece perpendicular to the direction of loading in the plane of likely crack growth. Then each specimen was pulled to failure in a tensile test machine to expose any cracks. The total number of potential cracks in each alloy was 96 for the pristine bare condition (2 specimens x 2 per hole) and 144 (3 specimens) for the pristine alclad and corroded bare condition. All holes were examined using an optical microscope at magnifications up to 70x. Depth and area measurements were made of all observed cracks. The accuracy of the optical measurement technique was verified by examining a portion of the fracture surfaces in a scanning electron microscope. For the pristine conditions, the observed crack shapes were converted to an equivalent quarter-circular corner crack using a stress intensity matching method similar to Luzar and Hug [9]. This enabled cracks of various aspect ratios to be fairly compared. For the bare corroded condition, this method was not practical due to the complexity and irregularity of the combined corrosion and fatigue damage. Instead the area of corrosion, area of fatigue and total damage area were measured and compared.

3. EXPERIMENTAL RESULTS AND DISCUSSION

3.1 RESIDUAL STRENGTH WITH MSD

The results of the residual strength tests on unstiffened and stiffened panels with MSD are given in Table 3. In the unstiffened panels, rapid failure occurred upon link-up of the lead crack and MSD at the adjacent fastener hole with the exception of the panels with no MSD which exhibited first link-up while

exhibiting stable crack extension. In the stiffened panels, rapid failure was preceded by link-up between the lead crack and MSD at the adjacent fastener hole and link-up between the resulting crack and MSD at the second fastener hole. In both cases the lead cracks were observed to extend stably at approximately 70% to 80% of the maximum load while the MSD cracks did not extend until very close to specimen failure at approximately 95% of maximum load. A comparison of stiffened panel behavior in the two alloys is illustrated by plots of applied remote stress versus lead crack length for the 0.05-inch MSD flaw size in Figure 2. Residual strength as a function of MSD flaw size for the stiffened and unstiffened panels are shown graphically in Figure 3. While the presence of small MSD in the holes ahead of a lead crack reduced the residual strength in both alloys, 2524 continues to have superior residual strength relative to 2024 when MSD is present. The percentage improvement in 2524 over 2024 was 8.8 to 10.4% in the unstiffened panels and 9.3 to 10% in the stiffened panels depending on MSD flaw size. Thus, when viewed as a replacement for 2024-T3, alloy 2524-T3 gives a significant increase in the margin of safety for multi-site damage scenarios.

TABLE 3. RESIDUAL STRENGTH TEST RESULTS FROM UNSTIFFENED AND STIFFENED
2524-T3 AND 2024-T3 PANELS WITH MSD

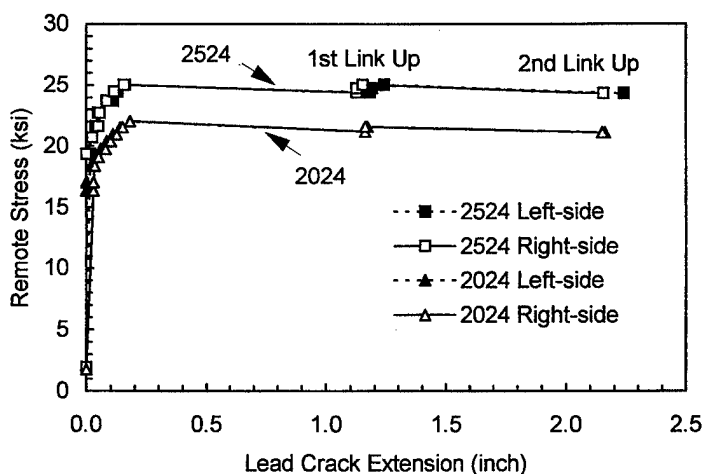| Specimen Type	MSD Size (inch)	Event	Remote Stress (ksi)		Improvement (%)
			2024-T3	2524-T3	
Unstiffened	None	Failure	26.83	29.19	8.8
	0.05	Failure	23.47	25.80	9.9
	0.10	Failure	21.96	24.04	9.5
	0.15	Failure	19.47	21.50	10.4
Stiffened	0.05	1st Link Up	22.20	25.00	11.2
		2nd Link Up	21.63	24.87	13.0
		Failure	26.81	29.57	9.3
	0.10	1st Link Up	21.38	23.79	10.1
		2nd Link Up	21.13	23.24	9.1
		Failure	25.25	28.05	10.0

Figure 2. Results of residual strength tests on stiffened panels comparing response of 2524-T3 and 2024-T3 alclad sheet with 0.05 inch MSD.
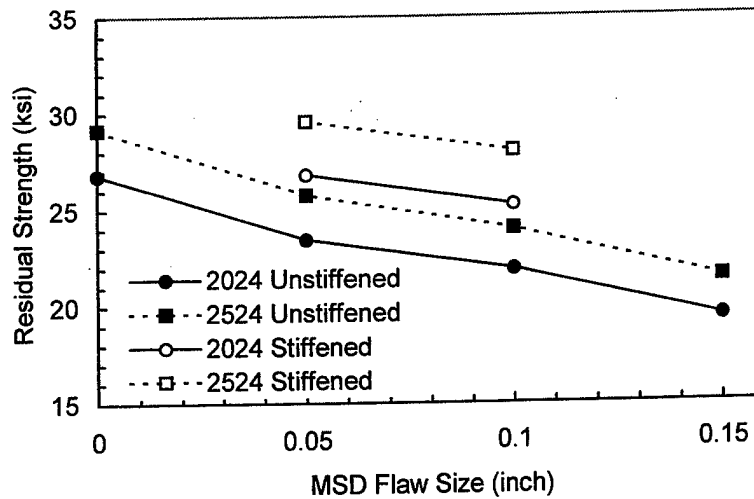
Figure 3. Comparison of residual strengths for 2524-T3 and 2024-T3 alclad sheet in unstiffened and stiffened panels versus MSD flaw size.

3.2 FATIGUE LIFE WITH MSD

The results of the fatigue tests on unstiffened panels are summarized in Table 4. In the two panels of each alloy with no MSD, fatigue cracks quickly formed at the tips of the lead crack and propagated to failure. Fatigue cracks were not observed to initiate in the row of open holes until these holes were intersected by the lead crack. The lead crack stopped momentarily at the open holes until fatigue initiated on the opposite side. In the three panels of each alloy with MSD, fatigue cracks initiated from the MSD flaws in the row of open holes after 20 to 25% of the total lifetime and propagated until overtaken by the lead crack. A crack propagation diagram comparing the position of the lead and MSD cracks as a function of elapsed cycles in 2524 and 2024 is shown in Figure 4 for the 0.05-inch MSD flaw size. Fatigue life for each alloy as a function of MSD flaw size is shown graphically in Figure 5. As anticipated, the fatigue life decreases with increasing MSD flaw size in both alloys. However, for any given flaw size, the lives of the 2524 panels are 27 to 45% longer than corresponding 2024 panel as a consequence of the superior fatigue crack growth resistance of alloy 2524.

TABLE 4. FATIGUE TESTS RESULTS FROM UNSTIFFENED 2524-T3
AND 2024-T3 PANELS WITH MSD

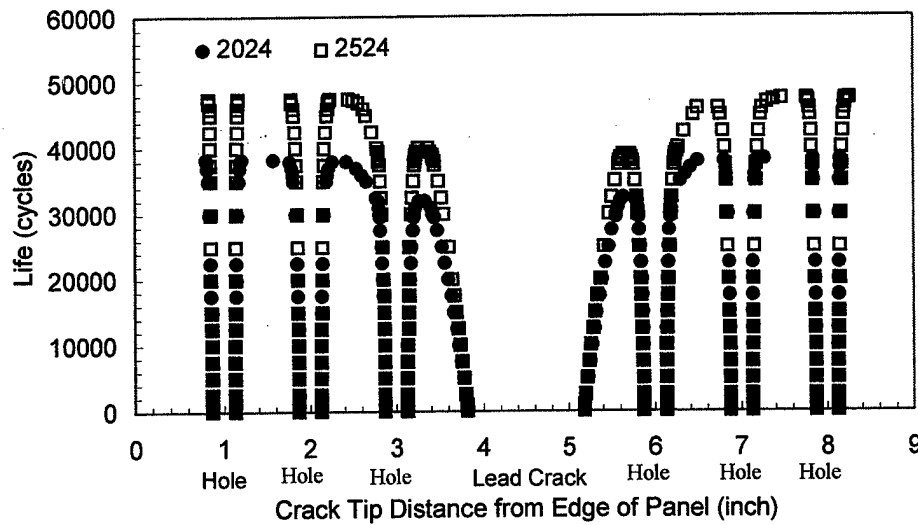| MSD Size (inch)	Lifetime to Failure (cycles)		Average Improvement (%)
	2024-T3	2524-T3	
None	90141	115392	28.6
	75725	97980	
0.05	38379	47577	26.9
	38256	49693	
0.10	26616	38593	45.0

Figure 4. Comparison of fatigue crack propagation diagrams for unstiffened panels of 2524-T3 and 2024-T3 alclad sheet with 0.05 inch MSD.
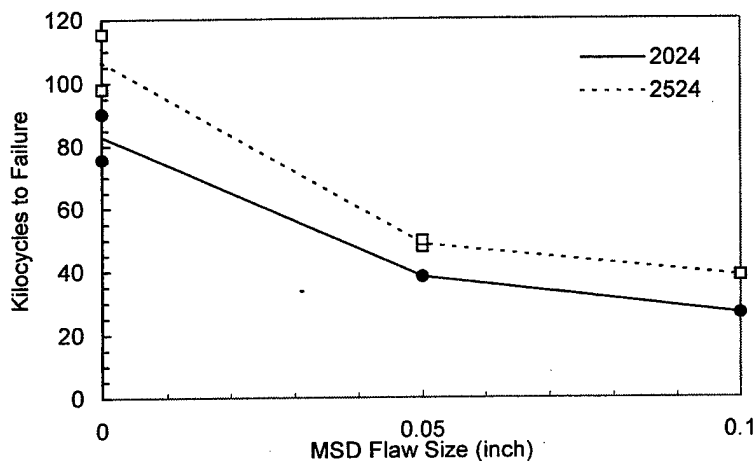

Figure 5. Comparison of fatigue life for 2524-T3 and 2024-T3 alclad sheet in unstiffened panels versus MSD flaw size.

3.3 MSD FROM FATIGUE AND CORROSION

Descriptive statistics from the pristine alclad and pristine bare multi-hole coupons are given in Table 5. In the pristine alclad condition, about 20% of the potential 144 sites exhibited fatigue cracks in both alloys. Typical of alclad sheet, nearly all the fatigue cracks initiated in the softer clad layer instead of the core material. In the pristine bare condition, only about 3% of the potential 96 sites exhibited fatigue cracks. The far greater percentage of initiating sites in the clad material than in the bare material indicates that clad material is more prone to the formation of MSD from fatigue alone. However, the purpose of the clad layer is to protect the core material from corrosion. Therefore, it is likely that any advantage bare material provides with respect to resistance to MSD from fatigue may be lost in the presence of corrosion which is prevalent on aging aircraft. The mean of the equivalent quarter circular corner crack sizes obtained by stress intensity matching was about 13% greater in 2524 than in 2024.

7

The means include only those sites containing a crack. Confidence intervals at the 95% level were calculated for the difference in means between alclad 2524 and 2024 and this difference was determined to be statistically insignificant [10]. The scarcity of initiation sites in the bare material made such a calculation meaningless. It was initially expected that 2524 would have smaller equivalent crack sizes due to its improved fatigue crack growth resistance. However, the advantage of 2524 over 2024 is typically greater at medium and high ΔK than it is at low ΔK present at the early stage of crack growth. For the specific lots of 2524 and 2024 used in this study there was very little difference in fatigue crack growth (FCG) resistance at low ΔK (see Figure 2). The results of the panel fatigue tests and multi-hole coupon tests taken together indicate that while the improved FCG resistance in 2524 relative to 2024 yields a significant improvement in fatigue life when MSD flaws are already present, it does not significantly effect the resistance to the formation of MSD from fatigue because of the different portions of the FCG curve involved in the early and later stages of crack growth.

TABLE 5. DESCRIPTIVE STATISTICS FOR PRISTINE MULTI-HOLE FATIGUE COUPONS OF ALCLAD AND BARE 2524-T3 AND 2024-T3 SHEET

| | Clad 0.050 inch thick Fatigued 150000 cycles at 14.9 ksi | | | Bare 0.100 inch thick Fatigued 200000 cycles at 14.0 ksi | | |
	2024-T3	2524-T3	Diff.	2024-T3	2524-T3	Diff.
No. Cracks/No. Sites	33/144	31/144	-2/144	2/96	3/96	+1/96
Mean (inch)[a]	0.0113	0.0128	+13.2%	0.0107	0.0121	+13.1%
St. Dev. (inch)	0.0089	0.0074	-16.8%	0.006	0.0052	-13.3%

[a] Mean crack size for equivalent quarter circular corner crack.

Descriptive statistics from the bare corroded multi-hole specimens are given in Table 6. Of the potential 144 sites, corrosion was observed at 99% of the sites and fatigue at 97% of the sites in the 2024 specimens compared to 92% and 83% of the sites, respectively, in the 2524 specimens. Typically, fatigue emanated at corrosion pits along the bore of the hole. The mean values of the areas from corrosion, fatigue and total damage for each alloy and 95% confidence intervals for the mean are shown in Figure 6. On average, the area of corrosion was 32% less in 2524 than in 2024. This was a consequence of the pits in 2524 being, in general, less deep and separated by uncorroded material while those in 2024 were deeper and partially or fully coalesced. These same characteristics were observed in a previous study by Bray et al. [11]comparing the smooth fatigue performance of bare 2524 and 2024 with prior corrosion. In that study, these characteristics were attributed to the much lower number density of constituent particles in 2524 relative to 2024. Pitting at the smaller constituent particles abundant in 2024 is believed to link up or coalesce the larger pits formed at the larger particles. The mean area of fatigue was 5% greater in 2524. Again, it was expected that the fatigue area would be less in 2524 because of its improved FCG resistance and because the starting flaw (i.e., the area of corrosion) was smaller. However, as already discussed the FCG resistance at low ΔK in the specific lots used in this study were not significantly different. Also, most of the fatigue area in 2524 is between the non-coalesced pits while in 2024 this material has already been corroded away. Since the pits in 2524 are not coalesced and not as deep the fatigue cracks may be experiencing greater stress intensification from the hole than in 2024. On average, the total area of corrosion plus fatigue at each hole was 18% less and the maximum depth of attack 16% less in 2524 than in 2024. Confidence intervals at the 95% level were calculated for the difference in means for corrosion, fatigue and total damage areas [10]. The difference in means between 2524 and 2024 was statistically significant for corrosion area and total damage area but not for fatigue area.

TABLE 6. DESCRIPTIVE STATISTICS FOR CORRODED MULTI-HOLE FATIGUE COUPONS OF BARE 2524-T3 AND 2024-T3 SHEET

Metric	2024-T3	2524-T3	% Difference
Number of Sites (144 possible)			
With Corrosion	142	133	-6%
With Fatigue	140	127	-9%
With Corrosion and Fatigue	138	120	-1%
Mean Value			
Maximum Depth (mm)	0.81	0.68	-16%
Corrosion Area (sq. mm)	0.94	0.64	-32%
Fatigue Area (sq. mm)	0.56	0.59	+5%
Total Area (sq mm)	1.50	1.23	-18%
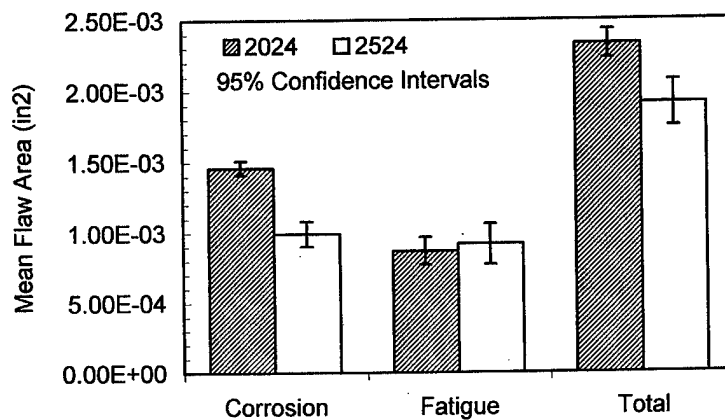
Figure 6. Comparison of mean values of area from corrosion, fatigue and total damage in corroded 2524-T3 and 2024-T3 bare sheet.

CONCLUSIONS

The results of this study indicate that alloy 2524-T3 sheet offers significant advantages in structural damage tolerance relative to incumbent alloy 2024-T3 in fuselage skin sheet applications, both in new aircraft and in multi-site damage scenarios that might be found in aging aircraft. The results show that 2524 offers not only improved structural damage tolerance relative to 2024 due to its superior fatigue crack growth resistance and fracture toughness but is also more resistant to MSD from corrosion in bare sheet form. Potential advantages of 2524-T3 to aircraft manufacturer/operators are an increase in allowable stress (weight savings), increase in inspection interval (lower operating costs), easier inspectability (larger crack sizes can be tolerated) and increase in safety (reduced risk of failure).

ACKNOWLEDGMENTS

REFERENCES

1. Mar, J.W., "Structural Integrity of Aging Airplanes: A Perspective," Structural Integrity of Aging Airplanes, S.N. Atluri, S.G. Sampath, P. Tong, Eds. Springer-Verlag, 1991, pp. 241-273.

2. Swift, T., "Widespread Fatigue Damage Monitoring Issues and Concerns," FAA/NASA International Symposium on Advanced Structural Integrity Methods for Airframe Durability and Damage Tolerance, NASA Conference Publication 3274, Part 2, C.E. Harris, Ed., Sept. 1994, pp. 829-870.

3. Moukawsher, E.J., Heinimann, M.B, and Grandt, A.F., Jr., "Residual Strength of Panels with Multiple Site Damage," Journal of Aircraft, Vol. 33, No. 5, 1996, pp. 1014-1021.

4. Moukawsher, E.J., Grandt, A.F., Jr., and Neussl, M.A., Fatigue Life of Panels with Multiple Site Damage," Journal of Aircraft, Vol. 33, No. 5, 1996, pp. 1003-1013.

5. Heinimann, M.B., and Grandt, A.F., Jr., "Analysis of Stiffened Panels with Multiple Site Damage," Proc. Of 1996 USAF Structural Integrity Program Conference, San Antonio, TX, Dec. 3-5, 1996.

6. Hyatt, M.V. and Axter, S.E., "Aluminum Alloy Development for Subsonic and Supersonic Aircraft," Science and Engineering of Light Metals (RASELM '91), Japan Institute of Light Metals, October 1991, pp. 273-280.

7. Staley, J.T., "Aluminum Alloys for Subsonic Aircraft," Aerospace Thermal Structures and Materials for a New Era, University of Virginia Thermal Structures Conference (2nd), Charlottesville, VA, Oct. 19, 1994, pp. 343-358.

8. McGuire, J. and Varanasi, R., "Boeing Structural Design and Technology Improvements," Airliner, April-June 1996, pp. 12-19.

9. Luzar, J., Hug, A., "Lower Wing Disassembly and Inspection Results of Two High Time USAF B707 Aircraft," presented at USAF Structural Integrity Program Conference, San Antonio, TX, Dec. 1996.

10. Golden, P.J., A Comparison of Fatigue Crack Initiation at Holes in 2024-T3 and 2524-T3 Aluminum Alloys," M.S. Thesis, School of Aeronautics and Astronautics, Purdue University, 1997.

11. Bray, G.H., Bucci, R.J., Colvin, E.L., and Kulak, M., "Effect of Prior Corrosion on the S/N Fatigue Performance of Aluminum Sheet Alloys," Effects of the Environment on the Initiation of Crack Growth, ASTM STP 1298, W.A. Van der Sluys, R.S. Piascik, and R. Zawierucha, Eds., American Society for Testing and Materials, 1997.

EFFECT OF PRIOR CORROSION ON FATIGUE PERFORMANCE
OF TOUGHNESS IMPROVED FUSELAGE SKIN SHEET ALLOY 2524-T3

G.H. Bray
R.J. Bucci
Aluminum Company of America
Alcoa Center, PA 15069 USA

P.J. Golden
A. F. Grandt
School of Aeronautics and Astronautics
Purdue University
West Lafayette, IN 47907 USA

SUMMARY
Aviation industry demand for continuous safety improvement in the face of trends toward increasing service life of aircraft and cost control necessitates stronger prevention and control measures to avoid the likelihood of structural failures linked to multi-site damage (MSD) involving corrosion and fatigue. New materials with improved damage tolerance attributes can improve the margin of safety in the presence of MSD. An excellent example of one such material is new aluminum alloy 2524 (formerly C188). In this study, the effect of prior pitting corrosion on the S/N fatigue performance of thin ($\leq$ 3.17 mm) 2524-T3 and 2024-T3 bare sheet was evaluated in a two part study. First, smooth axial fatigue specimens were corroded by accelerated methods to approximate 1yr seacoast exposure and then fatigue tested in lab air. The fatigue strength of 2524 was approximately 10% greater and the lifetime to failure 30 to 45% longer than that of 2024. Second, panels containing 24 open holes were similarly corroded and then fatigued in lab air for 100,000 cycles. The mean flaw areas following corrosion and fatigue were 18% smaller in 2524 and the corroded area alone 32% smaller. The results of this study indicate that thin, bare 2524 sheet is more resistant to MSD from pitting corrosion than thin, bare 2024 sheet. Alloy 2524 also offers improved structural damage tolerance in the presence of MSD due to its superior fatigue crack growth resistance and fracture toughness.

1. INTRODUCTION
The economic necessity to extend the operating lifetimes of both new and existing aircraft has given rise to new requirements that non-pristine or aging structure be accounted for in design and maintenance strategies. Explicit in these requirements is the upgrading of prevention/control measures to counter the potential emergence of a multi-site damage state, that in the presence of a larger rogue crack could imperil the structure's damage tolerance capability. As a result, corrosion is no longer viewed primarily as a maintenance issue, but as a potential threat to aircraft safety when combined with fatigue. This shift creates demand for affordable, replacement materials that not only can resist the occurrence of multi-site damage (MSD) from corrosion or other sources, but which also offer improved structural damage tolerance with MSD present.

An excellent example of one such material is new aluminum alloy 2524 developed to have improved fracture toughness and fatigue crack growth resistance relative to incumbent alloy 2024. Typical mechanical properties of 2524 and 2024 are compared in Table 1. The results of a separate study (Ref. 1) to quantify the improved resistance of 2524 to the consequences of MSD are shown in Fig. 1. The residual strength of 2524 panels containing a lead crack with MSD at adjacent holes was 9 to 10.5% higher than 2024 panels (Fig. 1a) and the fatigue life 27 to 45% longer (Fig. 1b) depending on MSD flaw size.

The objective of the present study was to determine if 2524 is more resistant than 2024 to MSD resulting from corrosion. The two alloys possess equivalent tensile (Table 1) and S/N fatigue properties (Fig. 2) when tested in an uncorroded condition. The classical rating systems of evaluating corrosion performance also rate both alloys as being nominally equivalent (Table 2). However, recent work by Wei et al. (Ref. 2) and Chen et al. (Refs. 3 and 4) indicates fatigue initiation resistance is degraded by pitting at large, second phase particles commonly referred to as constituent particles. Since 2524 has a significantly lower density of constituent particles as a result of compositional and processing improvements, it was hypothesized that the S/N fatigue performance of bare 2524 would be superior to that of 2024 in a precorroded condition.

2. EXPERIMENTAL PROCEDURES

2.1 Part I- Smooth Axial Fatigue with Prior Corrosion
Two thicknesses of clad 2024-T3 and 2524-T3 sheet, 1.60 mm and 3.17 mm, fabricated by Alcoa Davenport Works were procured for Part I of this study. Since these materials were clad and the desired test condition was bare, the cladding was removed by machining prior to testing. The final thicknesses after removal of the cladding were 1.37 mm and 2.54 mm, respectively. The materials will be referred to by their nominal thickness, 1.60 mm and 3.17 mm, for designation purposes. The morphology of constituent particles on the L-ST plane was examined using optical metallography. This plane was normal to the direction of loading in the fatigue tests. In addition, the number of particles and their areal size were measured with automated optical image analysis for the 3.17-mm sheet only. The sample area was 2.525 sq. mm. The minimum particle size that could be resolved was 2 sq. μm.

Smooth, sheet-type S/N fatigue specimens were machined in the long-transverse (LT) direction, seven per alloy from the 1.60 mm-sheet and thirteen per alloy from the 3.17-mm sheet. A smooth geometry was selected instead of a notched one because it samples a larger volume of material. The specimen had a gage length of 31.7 mm and a gage width of 12.7 mm. The tool marks from removal of the cladding were eliminated by wet sanding the specimen faces in the length direction with 600 grit paper. The specimens were corroded by 24 h exposure to sodium chloride/hydrogen peroxide solution prepared in accordance with ASTM G110. A comparison with seacoast data indicated the fatigue performance of 2024 sheet after 24 h exposure in sodium chloride/hydrogen peroxide is similar to that obtained after one year exposure to a seacoast environment. Both the faces and edges were exposed in the gage section of the specimens. The faces correspond to the L-LT plane and the edges to the LT-ST plane.

One corroded specimen from each of the materials was cross-sectioned on a random L-ST plane and examined using optical metallography to determine the mode of corrosion attack. To characterize the severity of attack in the 3.17 mm-sheet, the number and depth of the corrosion features on the perimeter of the random plane were quantified by automated optical image analysis. The minimum depth of corrosion attack that could be resolved was approximately 12 µm. This information was also used to estimate the area loss due to corrosion.

The remaining corroded specimens were tested in laboratory air using a stress ratio of R=0.1. Duplicate specimens for each material were tested to failure at three stress levels, 172, 207 and 241 MPa, in order to define the S/N fatigue curve in the neighborhood of 100,000 cycles. The load applied to achieve a given stress level was based on the nominal specimen dimensions prior to corrosion. For the 3.17-mm sheet, four additional specimens were tested for each alloy at the intermediate stress level to better determine the variability in lifetime. Six failed specimens per thickness and alloy were examined in a scanning electron microscope (SEM) to determine primary initiating feature(s) and their sizes. The number of secondary cracks were also counted for the 3.17-mm sheet.

2.2 Part II- Multi-Hole Fatigue with Prior Corrosion
Bare 2024-T3 and 2524-T3 sheet, 2.54 mm thick, was procured for Phase II of this study. Panels 160 mm wide by 610 mm long containing four rows of six holes (24 total) at mid-length were machined from each alloy. The length dimension was in the long transverse (LT) direction of the parent sheet. The diameter of the holes was 4.0 mm and the hole spacing or pitch was 25.4 mm. The panels were corroded by 24 h exposure to sodium chloride/hydrogen peroxide solution prepared in accordance with ASTM G110. Three panels of each alloy were then fatigued at a gross stress of 69 MPa for 100,000 cycles in laboratory air at a stress ratio of 0.05. One panel of 2524 and two panels of 2024 were tested to failure.

Following fatigue cycling, each hole (72 total per alloy) was broken open and examined to determine the area of fatigue and corrosion. To break open each hole, a 25 mm square coupon of material containing the hole was excised from the panel. Notches were cut in the square piece perpendicular to the direction of loading in the plane of likely crack growth. Then each specimen was pulled to failure in a tensile test machine to expose the crack surfaces. The exposed cracks were examined and area measurements made using an optical microscope at magnifications up to 70x to determine the area of fatigue and corrosion. A portion of the fracture surfaces were examined in a scanning electron microscope to verify the accuracy of the optical measurement technique.

3. EXPERIMENTAL RESULTS

3.1 Part I- Smooth Axial Fatigue with Prior Corrosion
Optical metallography revealed that 2524 had significantly fewer constituent particles than 2024 in both sheet thicknesses as expected. The distribution of particle sizes obtained from the 3.17-mm sheet (Fig. 3) revealed that 2524 had fewer particles over the entire size range, but that the greatest difference between the two alloys was in the size range of 25 sq. µm and less. The overall density of particles was 800/sq. mm in 2524 compared to 2290/sq. mm in 2024.

The type of corrosion attack in all materials was predominantly pitting corrosion (Fig. 4). The pits on the specimen faces (L-LT plane) were hemispherical in shape, while those on the specimen edges (LT-ST) plane were elongated. It was not determined whether the pitting was associated with the constituent particles,

but the work of Wei et al. (Ref. 2) and Chen et al. (Refs. 3 and 4) suggest this is probably the case. The distribution of pit depths obtained in the 3.17-mm sheet is shown in Fig. 5. The average density of resolvable pits (12 µm) on the specimen perimeter was 2.5/mm in 2524 compared to 3.2/mm in 2024. The density of smaller pits (<12 µm deep) may have been significantly greater in 2024, but these would be less likely to act as fatigue initiation sites. The area loss due to corrosion in the 1.60-mm sheet was estimated to be 4.6% for 2024 and 4.0% for 2524, while that in the 3.17-mm sheet was estimated to be 1.1 and 0.9%, respectively.

A Box-Cox equation (Ref. 5) was fit to the individual fatigue test results to obtain stress-life (S/N) curves for precorroded 2524 and 2024 (Fig. 6). The lifetime at each stress level and the fatigue strength at 100,000 cycles obtained from the Box-Cox fit are given in Table 3. The fatigue performance of precorroded 2524 was superior to that of 2024. For both thicknesses, the lifetime to failure of precorroded 2524 was 30 to 45% longer than that of precorroded 2024 depending on stress level, and the fatigue strength at 100,000 cycles approximately 21 MPa or 10% higher. Prior corrosion reduced the fatigue strength of both alloys approximately 140 MPa relative to the typical smooth ($K_t=1$) fatigue strength of 345 MPa for bare, uncorroded material (Ref. 6).

SEM fractography revealed that the largest or primary fatigue cracks originated on the specimen edges in all specimens examined. The edges correspond to the through-thickness orientation (LT-ST plane) which is representative of the surfaces of a fastener hole or splice edge. Fatigue cracking typically initiated at 4 to 8 pits and then coalesced to form a common crack front. Generally, the pits in 2524 were elongated and separated by uncorroded material, while those in 2024 were partially or fully coalesced (Fig. 7). The maximum depth of corrosion attack in the primary origin area varied significantly from specimen to specimen but on average was similar in the two alloys for the 1.60-mm sheet, while in the 3.17-mm sheet, 2524 exhibited shallower attack than 2024 (Table 4). The fracture surfaces exhibited many secondary cracks on both the faces and edges, each typically containing multiple pit initiation sites. The number of secondary cracks in the 3.17-mm sheet also varied significantly from specimen to specimen, but on average was slightly less in 2524.

3.1 Part II- Multi-Hole Fatigue with Prior Corrosion
The descriptive statistics from the examination of the broken open holes from the multi-hole specimens are given in Table 5. The areal measurements for each alloy have also been represented graphically by use of histograms in Fig. 8. Of the potential 144 sites (72 holes times two sides), corrosion was observed at 99% of the sites and fatigue at 97% of the sites in the 2024 specimens compared to 92% and 83% of the sites, respectively, in the 2524 specimens. The broken open holes revealed pitting corrosion and fatigue emanating from the bore of the holes very similar in appearance to that observed at the edges of the smooth specimen (see Fig. 7). Generally, the pits in 2524 were less deep and separated by uncorroded material while those in 2024 were deeper and partially or fully coalesced. As a result of these differences, the area of corrosion at each hole was on average 32% less in 2524 than in 2024. The distribution of corrosion area for all holes is compared in the histogram in Fig. 8a. It was anticipated that the fatigue area might also be smaller in 2524 since the starting flaw (i.e., the area of corrosion) was smaller in 2524 and its fatigue crack growth resistance is higher. This was not the case as seen in Table 5 and Fig. 8b possibly for several reasons. First, most of the fatigue area in 2524 is between the non-coalesced pits while in 2024 this material has already been corroded away. Second, because the pits are not

coalesced and the corrosion area is smaller in 2524, the fatigue cracks are experiencing greater stress intensification from the hole than in 2024. Third, the improvement in fatigue crack growth resistance of 2524 over 2024 is much greater at high ΔK than at the low ΔK present at the early stage of fatigue crack growth. On average, the total area of corrosion plus fatigue at each hole was 18% less and the maximum depth of attack 16% less in 2524 than in 2024 as seen in Table 5 and 8c.

Confidence intervals were calculated at the 95% level to determine the statistical significance of the differences in mean values of the area from corrosion, fatigue and total damage for 2524 and 2024 were statistically significant. The mean and confidence intervals are shown in Fig. 9. The differences between the two materials was calculated to be statistically significant for the corroded area and total area only. The difference in the fatigue area was calculated to be insignificant. The confidence intervals indicate that it can be stated with 95% confidence that the mean corrosion area of 2024 is 24 to 40% greater than that of 2524 and the total area of corrosion plus fatigue in 2024 is 8 to 28% greater than that of 2524.

The two 2024 specimens fatigued to failure had lifetimes of 204,300 and 151,200 compared to a lifetime of 263,000 in the 2524 specimen, an improvement of 22% and 42%, respectively. The improvement in 2524 is consistent with that observed in the smooth specimen results.

4. DISCUSSION

The results of this study indicate that thin, bare 2524 sheet is more resistant to the formation of MSD from pitting corrosion than thin, bare 2024 sheet. In Part I of this study, the smooth fatigue strength of corroded 2524 was approximately 10% greater and the lifetime to failure 30 to 45% longer than that of corroded 2024 depending on stress level. In Part II, the mean flaw area at open holes was 20% less in 2524 than in 2024 following corrosion and fatigue to 100,000 cycles. Alloy 2524 also offers improved structural damage tolerance in the presence of MSD due to its superior fatigue crack growth resistance and fracture toughness.

In a previous paper (Ref. 7) the factors contributing to the improved smooth fatigue performance of corroded 2524 relative to corroded 2024 were analyzed. Possible contributing factors were: (1) less cross-sectional area loss; (2) a less damaging configuration of initiating features (i.e., pits); and (3) and better fatigue crack growth resistance. The results of this analysis indicated that less than 5% of the life improvement was due to less cross-sectional area loss in 2524, its better fatigue crack growth resistance was responsible for 50 to 75% of the life improvement, and a less damaging configuration of initiating pits in 2524 was responsible for the remaining 20 to 45% of the lifetime.

The configuration of initiating pits was less damaging not because of far fewer pits in 2524 as first anticipated but because the shape of the pits was less damaging with respect to their depth and/or their aspect ratio. Based on the work of Wei et al. (Ref. 2) and Chen et al. (Refs. 3 and 4) which indicates that pits primarily form at large, second phase particles, it was anticipated that 2524 would have far fewer pits, since its particle density is only about a third of that in 2024. However, while the density of resolvable pits (>12 μm) measured in Part I (see Fig. 5) was less in 2524, the difference was not as large as expected. One possible explanation is that pits of resolvable depth were mainly associated with the larger particles in the upper tail of the size distribution where the difference between the two alloys was not as great (see Fig. 3). The number of smaller pits (<12 μm deep) may have been significantly greater in 2024, but these would be

less likely to serve as fatigue initiation sites. As a result, the average number of secondary cracks and the total number of initiation sites (see Table 4) was not significantly different in the two alloys.

However, in both Parts I and II, the pits in 2024 were observed to be typically deeper and/or wider at their base (i.e., lower aspect ratio) than those in 2524 due to pit coalescence in the former. A possible explanation for this behavior consistent with the observations of Chen et al. (Refs. 3 and 4) is that pitting at the smaller particles abundant in 2024 (see Fig. 3) are acting to link up or coalesce the larger pits. The analysis performed in the previous paper (Ref. 7) showed that pit depth and aspect ratio of the initiating pits can affect fatigue lifetime just as significantly as the number of initiating features as seen in Fig. 10. Thus, it appears that while the lower density of constituent particles of 2524 relative to 2024 did not result in fewer fatigue initiating pits as anticipated, it did result in the shape of these initiating pits being less damaging to fatigue performance.

While the observed improvement in 2524 with respect to 2024 is believed to be correct and plausible mechanisms for this improvement have been identified, it should be recognized that the test data is limited in scope with respect to the number of lots tested (3 each alloy) and are therefore insufficient to reliably quantify the magnitude of the performance improvement. It should also be noted that the improvement was observed for the case of pitting corrosion in thin, bare sheet only. Pitting corrosion is typically observed in 2X24-T3X products less than approximately 2 mm in thickness which can be quenched rapidly enough to be resistant to intergranular (IG) corrosion. As product thickness increases, the attack typically changes from pitting to a mixture of pitting and IG corrosion to primarily IG corrosion (Ref. 8). The corrosion behavior of both alloys can also vary considerably from lot-to-lot particularly in the intermediate thickness range where the mode of corrosion is mixed. Therefore, the relative performance of the two alloys may vary from lot to lot and in the presence of other forms of corrosion. However, the fatigue crack growth resistance and fracture toughness of 2524 sheet is expected to exceed that of 2024 sheet in nearly all cases. Thus, when multi-site damage (MSD) is present in the form of corrosion or any other form, alloy 2524 has an inherent advantage over 2024 (see Fig. 1).

The results of this study also point out the need to develop and standardize new metrics for assessing the combined effects of fatigue and corrosion. With respect to classical rating systems of fatigue and corrosion, 2524 and 2024 are nominally equivalent (see Table 2 and Fig. 2). However, the results of this study indicates that the fatigue performance of thin, bare 2524 sheet after corrosion is superior to that of 2024. One approach for discriminating such differences would be to determine the equivalent initial flaw size (EIFS) for corrosion damage. The EIFS approach has been applied to pores and microfeatures in aluminum alloy 7050 by Magnusen et al. (Ref. 9) and to corrosion damage in 2124 and 7050 by Perez (Ref. 10). Basically, in this approach, the equivalent corner or through-crack dimensions which gives the same lifetime as a corroded specimen is obtained through fatigue crack growth analysis. The better performance of an improved alloy like 2524 would be recognized by a smaller equivalent initial flaw size (EIFS) than that from a poorer performing alloy such as 2024. Before widespread use of such a rating system would be possible, protocols for corrosion exposure, crack growth analysis, test specimens, number of lots and thicknesses required to achieve representative and statistically meaningful comparisons, etc. would need to be agreed upon and standardized.

Because of the potential threat to aircraft safety from MSD resulting from the combination of corrosion and fatigue, it is recommended that similar information be generated for older incumbent alloys such as 7075 and newer alloys such as 7055 which are intended to replace them. Such information would be useful not only to designers of new aircraft but also to those selecting alloys for retrofit applications on existing aging aircraft. More fundamental studies on the role of constituent particles and their influence on the severity or corrosion features with respect to their number size and shape should also be performed since insight from such studies would be useful to alloy developers.

5. CONCLUSIONS

The results of this study indicate that thin, bare 2524-T3 sheet is more resistant to multi-site damage (MSD) from pitting corrosion than thin, bare 2024-T3 sheet. In smooth fatigue specimens with prior corrosion, the fatigue strength of 2524 was approximately 10% greater and the lifetime to failure 30 to 45% longer than that of 2024. In open hole specimens, the mean flaw areas following corrosion and fatigue were 18% smaller in 2524 than in 2024 and the corroded area alone 32% smaller. The improvements in 2524 are due to a less damaging configuration of fatigue initiating pits believed to result from a much lower density of constituent particles. The better resistance of 2524 to MSD could be particularly beneficial in small aircraft where the use of thin, bare sheet is common. 2524 also offers improved structural damage tolerance in the presence of MSD due to its superior fatigue crack growth resistance and fracture toughness.

This study points out the need to develop new, standardized metrics and a rating system for assessing the ability of an alloy with respect to the combined effects of corrosion and fatigue. A reasonable approach for ranking alloys in this regard would be to determine the equivalent initial flaw size (EIFS) for corrosion damage. It is also recommended that similar studies be performed on pairs of older incumbent alloys and the newer alloys intended to replace them. Such information would be useful to both designers of new aircraft and for those selecting alloys for retrofit applications on existing aging aircraft.

REFERENCES

1. Grandt, A.F et al., "A Comparison of 2024-T3 and 2524-T3 Aluminium Alloys Under Multi-Site Damage Scenarios," *ICAF '97 Fatigue in New and Ageing Aircraft, Vol. II*, R. Cook and P. Poole, Eds., Engineering Materials Advisory Services, Ltd, UK, 1997, pp. 659-669.

2. Wei, R.P, Gao, M. and Harlow, D.G., "Pitting Corrosion in Aluminum Alloys: Experimentation and Modeling," Presentation at Air Force 3rd Aging Aircraft Conference, Wright-Patterson Air Force Base, September 1995.

3. Chen, G.S et al., "Corrosion and Corrosion Fatigue of Airframe Aluminum Alloys," *FAA/NASA International Symposium on Advanced Structural Integrity Methods for Airframe Durability and Damage Tolerance*, NASA Conference Publication 3274, Part 2, September 1994, pp. 157-173

4. Chen, G.S., Gao, M. and Wei, R.P., "Micro-Constituents Induced Pitting Corrosion in a 2024-T3 Aluminum Alloy," *Corrosion*, Vol. 52, No. 1, January 1996, pp. 8-15.

5. Hinkle, A.J. and Emptage, M.R., "Analysis of Fatigue Life Data Using the Box-Cox Transformation," *Fatigue and Fracture of Engineering Materials and Structures*, Vol. 14, No. 5, 1991, pp. 591-600.

6. *Metallic Materials and Elements for Aerospace Vehicle Structures*, Mil-Hdbk-5G, 1994.

7. Bray, G.H. et al., "Effect of Prior Corrosion on the S/N Fatigue Performance of Aluminum Sheet Alloys 2024-T3 and 2524-T3, *Effects of the Environment on the Initiation of Crack Growth, ASTM STP 1298*, W.A. Van Der Sluys, R.S. Piascik, and R. Zawierucha, Eds., American Society for Testing and Materials, 1997, pp. 89-103.

8. *Aluminum: Properties and Physical Metallurgy*, J. Hatch, ed., American Society for Metals, 1984, p. 167-169.

9. Magnusen, P.E. et al., "Final Report: The Role of Microstructure on the Fatigue Durability of Aluminum Aircraft Alloys," ONR Contract N00014-91-C-0128, November 1995.

10. Perez, R., "Corrosion/Fatigue Metrics," *ICAF '97 Fatigue in New and Ageing Aircraft, Vol. I*, R. Cook and P. Poole, Eds., Engineering Materials Advisory Services, Ltd, UK, 1997, pp. 215-225.

Table 1. Typical mechanical properties for 2524-T3 and 2024-T3 sheet in the long-transverse direction.

Alloy	Condition	UTS MPa	TYS MPa	Elong. %	Kc[a] MPa$\sqrt{m}$	da/dN @ ΔK=33[b] m/cycle
2524-T3	Clad	455	310	18	174	2.3E-06
	Bare	462	317	18	---	---
2024-T3	Clad	455	310	18	141	7.0E-06
	Bare	462	317	18	---	---

[a] M(T) specimen, T-L orientation, W=406 mm, $2a_0$= 102 mm tested per ASTM B646.

[b] T-L orientation, tested per ASTM E647 under constant ΔK conditions, R=0.1, relative humidity> 90%.

Table 2. Corrosion performance of several lots of bare 2524-T3 and 2024-T3 sheet.

Alloy	Thickness mm	EXCO[a] 48 h	EXCO[a] 96 h	MASTMAASIS[b] 2 week	MASTMAASIS[b] 4 week	Type of Attack[c]
2524-T3	0.81	P	P	P	P	P
	3.17	EA	EB	P	EB	IG
	6.32	EA	EB	P	EC	IG
2024-T3	1.02	P	EA	P	EA	P+IG[d]
	2.54	EA	EA	P	EA	P+IG[d]
	6.32	EA	EA	EA	EA	IG

[a] Tested at mid-thickness (t/2) per ASTM G34.

[b] Tested at mid-thickness (t/2) per ASTM G85, Annex A.2 (dry bottom).

[c] Tested per ASTM G110.

[d] Pitting with slight IG attack.

Table 3. Comparison of S/N fatigue performance of bare 2524-T3 and 2024-T3 sheet with prior corrosion [a].

Thickness mm	Alloy	Lifetime at Smax= 172 MPa	Lifetime at Smax= 207 MPa	Lifetime at Smax= 241 MPa	Smax at 10^5 cycles
1.60	2024	171800	82000	47900	196
	2524	221900	115000	70200	216
	% Improved	+29%	+40%	+46%	+10%
3.17	2024	197500	96400	57000	205
	2524	252600	135000	83500	228
	%Improved	+28%	+40%	+47%	+11%

[a] Smooth specimen tested in lab air after 24 h in NaCl/H_2O_2 solution (ASTM G110), R=0.1.

Table 4. Maximum depth of corrosion attack in primary origin area and number of secondary cracks on plane of failure.

Thickness mm	Alloy	Max. Depth of Attack, mm Range[a]	Max. Depth of Attack, mm Average[a]	No. Secondary Cracks Range[a]	No. Secondary Cracks Average[a]
1.60	2524	0.267-0.521	0.367	---	---
	2024	0.259-0.648	0.374	---	---
3.17	2524	0.292-0.632	0.416	5-26	15
	2024	0.439-0.681	0.550	6-28	16

[a] Range and average of six specimens from each thickness and alloy.

Table 5. Descriptive statistics for flaws in multi-hole specimens after corrosion and fatigue.

Metric	2024-T3	2524-T3	% Difference
Number of Sites (144 possible)			
With Corrosion	142	133	-6%
With Fatigue	140	127	-9%
With Corrosion and Fatigue	121	120	-1%
Mean Value			
Maximum Depth (mm)	0.81	0.68	-16%
Corrosion Area (sq. mm)	0.94	0.64	-32%
Fatigue Area (sq. mm)	0.56	0.59	+5%
Total Area (sq mm)	1.50	1.23	-18%
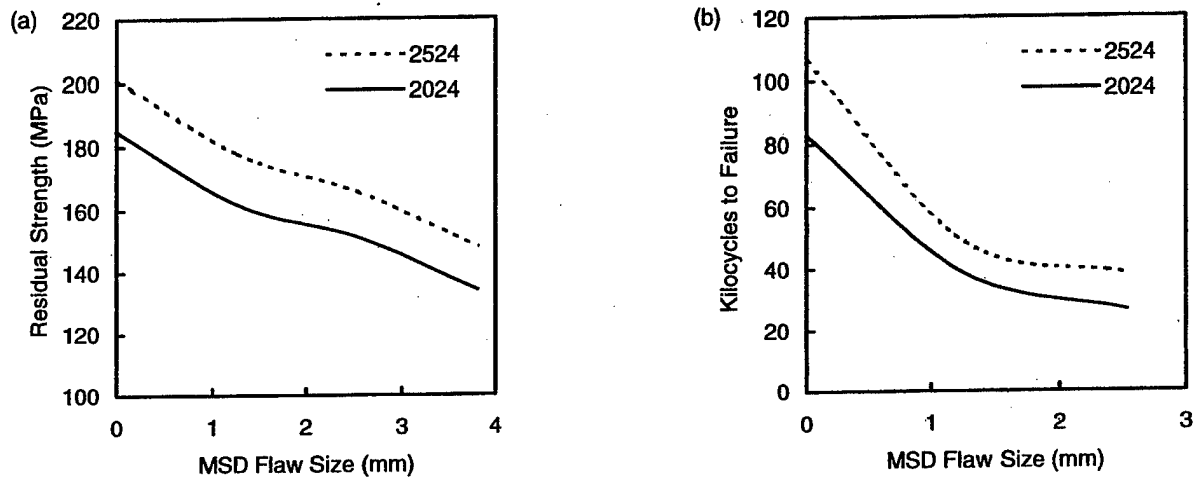
Figure 1. A comparison of (a) residual strength and (b) fatigue life in alloy 2524-T3 and 2024-T3 sheet with multi-site damage (MSD) present *after Grandt et al. (Ref. 1)*.
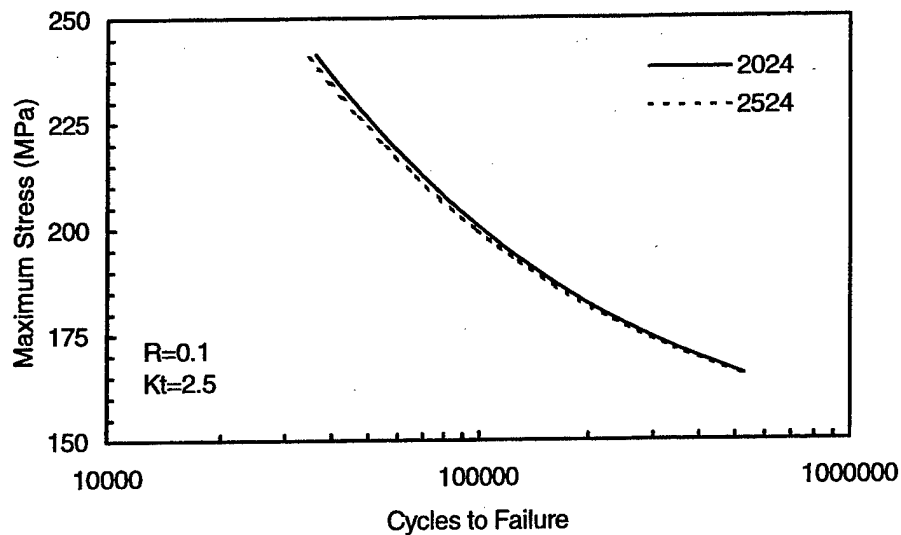
Figure 2. Comparison of S/N fatigue performance of bare 2424-T3 and 2024-T3 sheet in an uncorroded condition.
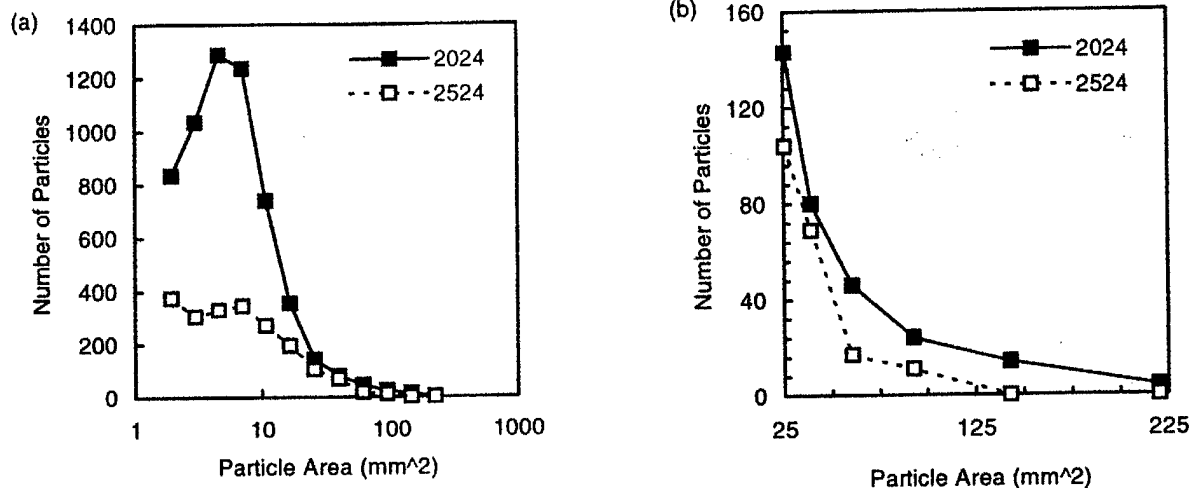
Figure 3. Histograms comparing (a) entire distribution and (b) upper tail of the distribution of particle sizes in 3.17-mm thick 2524-T3 and 2024-T3 sheet.
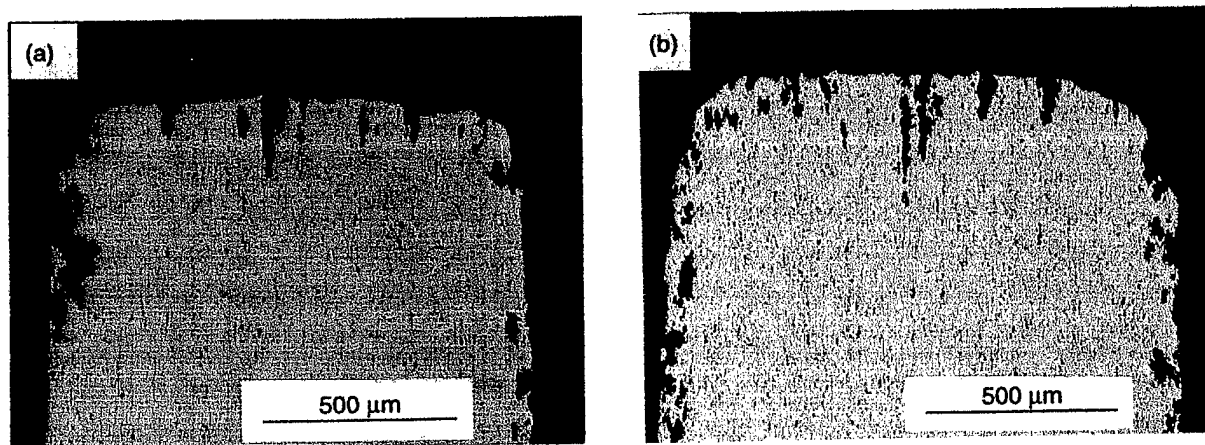
Figure 4. Optical micrographs of random plane showing pitting corrosion in bare 1.60-mm thick (a) 2524-T3 and (b) 2024-T3 sheet after 24h exposure to $NaCl/H_2O_2$ solution.
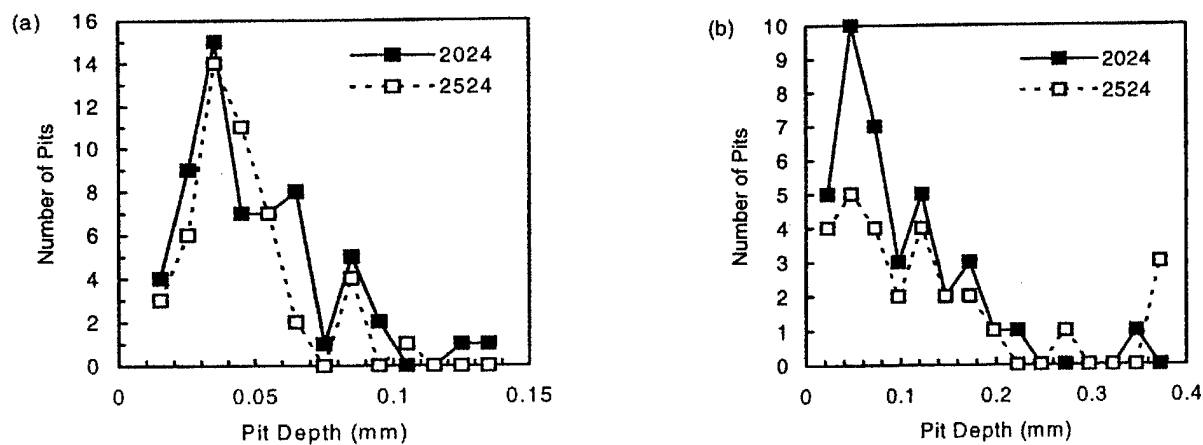
Figure 5. Histograms comparing distribution of pit depths (after 24 h in $NaCl/H_2O_2$) on random plane (L-ST) of 3.17-mm thick 2524-T3 and 2024-T3 sheet for (a) specimen faces and (b) specimen edges.
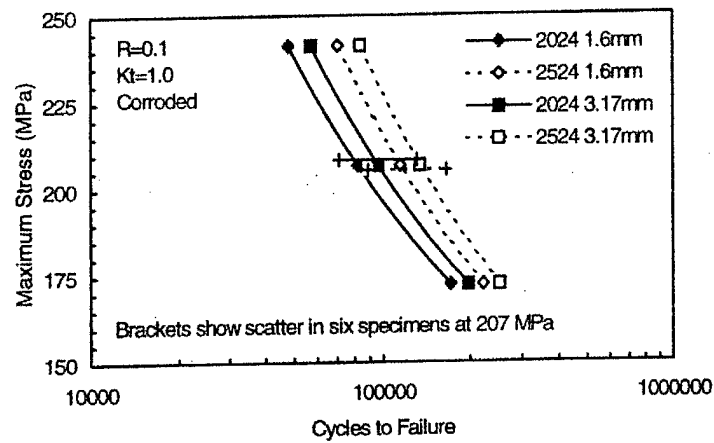
Figure 6. Stress-life fatigue curves for bare 2524-T3 and 2024-T3 sheet with prior corrosion (24h in NaCl/H_2O_2).
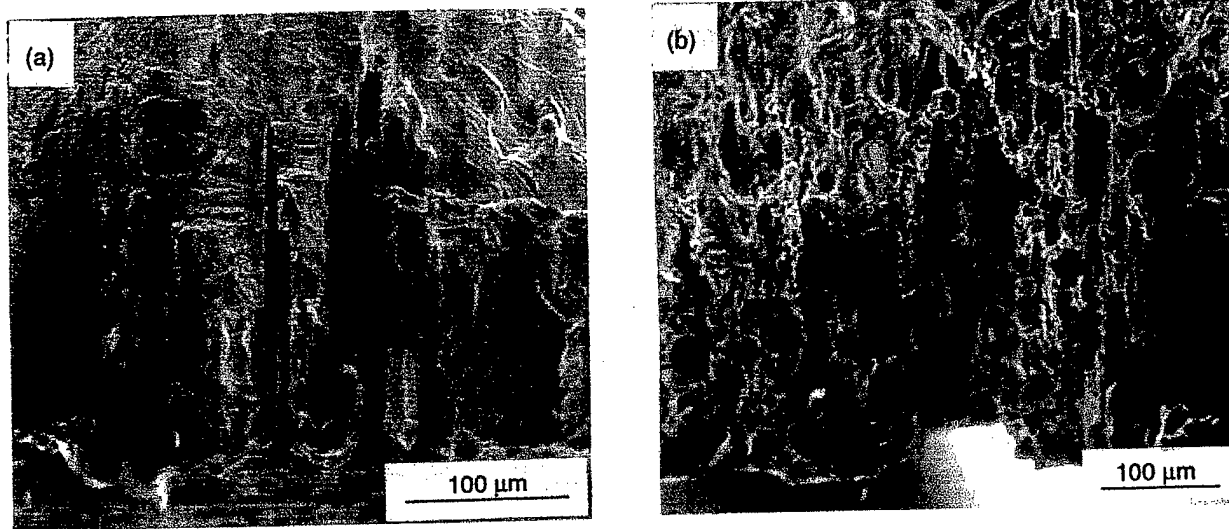
Figure 7. SEM fractographs from 3.17-mm thick sheet showing typical primary origin area on specimen edge in (a) 2524-T3 and (b) 2024-T3 sheet.
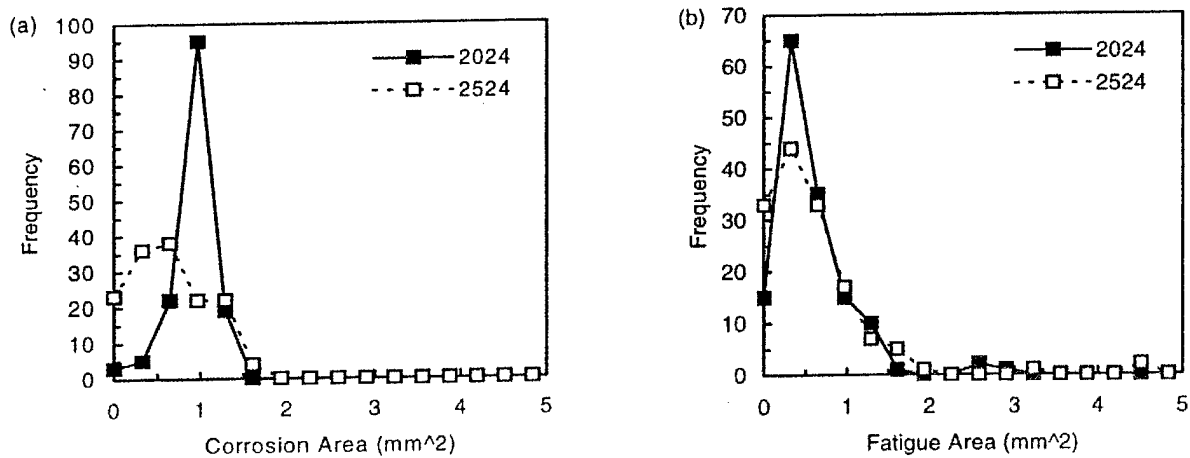
Figure 8. Histograms from 2.54-mm thick corroded and fatigued multi-hole specimens comparing: (a) area of corrosion, (b) area of fatigue (continued next page)
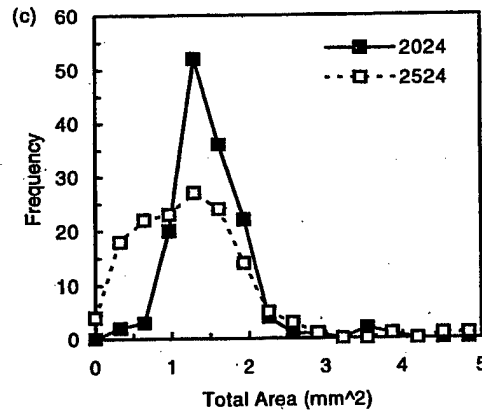
Figure 8 (continued). (c) total area of fatigue and corrosion.
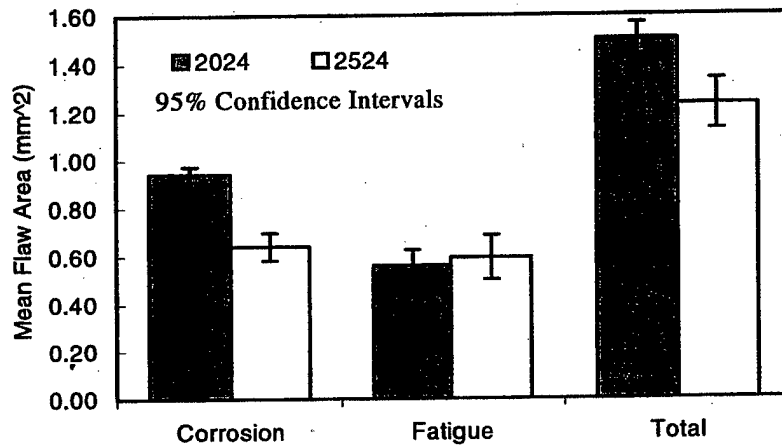
Figure 9. Comparison of mean values of area from corrosion, fatigue, and total damage from 2.54-mm thick multi-hole specimens (144 holes total) of 2524-T3 and 2024-T3 sheet.
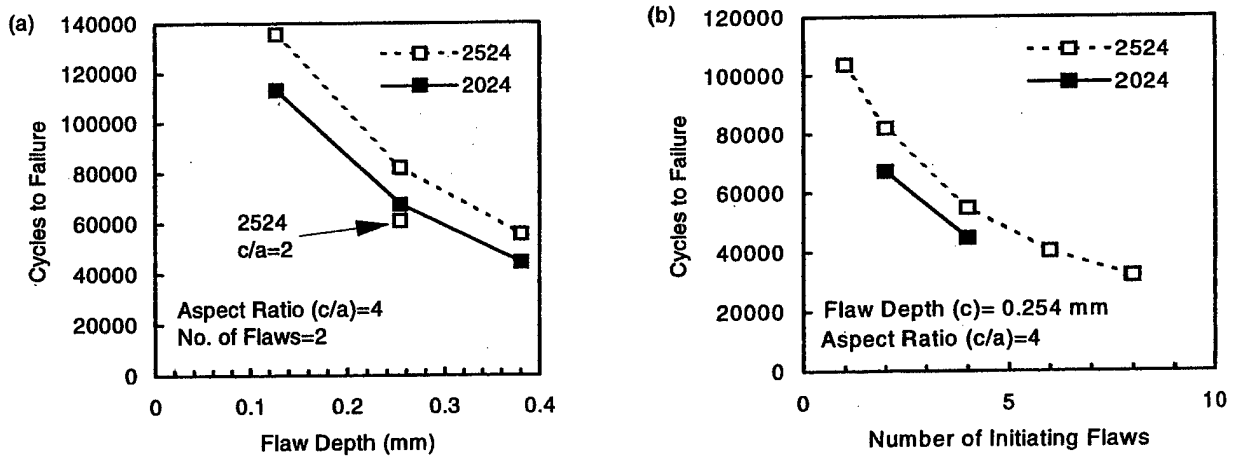
Figure 10. Results of crack growth analysis showing effect of (a) flaw depth and aspect ratio, and (b) number of initiating flaws on propagation lifetime *after Bray et al. (Ref. 7)*.

Monte Carlo Analysis of Widespread Fatigue Damage in Lap Joints

By

H.-L. Wang[1] and A. F. Grandt, Jr.[2*]

[1]Graduate Research Assistant and [2] Professor,
School of Aeronautics and Astronautics, 1282 Grissom Hall, Purdue University,
West Lafayette, IN 47907-1282

1. ABSTRACT

The goal of this paper is to describe research directed toward analyzing the influence of widespread fatigue damage (WFD) in lap joints. The particular objective is to determine when WFD could degrade the residual strength of joints that contain various combinations of lead cracks and small WFD. This issue is of interest for older aircraft that could have developed widespread cracking during service. A deterministic model is described to compute fatigue crack growth and residual strength of riveted lap joint panels. The numerical analysis determines load transfer through the various fastener rows, residual stresses associated with rivet installation (i.e. interference fit), and the growth of lead and small WFD cracks located along one row of rivets. Fatigue crack growth tests conducted to evaluate the WFD model are summarized, and indicate that good agreement is obtained between experimental and numerical results. Monte Carlo simulations are then performed to determine the influence of statistical variability on various analysis parameters. In particular, a wide panel containing 3 rows of 30 rivets is modeled, and the variation in residual strength is determined as a function of elapsed cycles. The initial WFD is based on statistical crack size distributions obtained from a recent teardown inspection of retired B-707 aircraft, while the variation in fastener interference (and its subsequent effect on rivet stress fields) is based on measurements from specimens that contain large numbers of installed rivets. Monte Carlo simulations (1000 runs) are performed to determine the statistical degradation in residual strength (i.e. probability of failure) as the WFD extends by fatigue. The influence of both rivet installation (i.e. fastener interference) and initial WFD size on fatigue life and residual strength are

presented, and indicate the relative influence of these parameters on structural integrity.

2. INTRODUCTION

The longer a load-bearing structure is operated, the more likely it is to develop structural damage that may lead to a component replacement or an unscheduled repair. To ensure the safety of aircraft structure, an efficient and reliable inspection method and maintenance strategy should be issued periodically before structural strength degrades to an unacceptable level. Clearly, a systematic evaluation for overall safety management of aircraft structures requires appropriate life predictions. This approach should take into account the probability of flaw occurrence, damage deterioration properties, inspection intervals, human factors, cost benefits, and replacement and repair methodology. [1]

A deterministic widespread fatigue damage (WFD) life prediction model, which has successfully predicted the WFD behavior for five single lap joint specimens, is used here to grow multiple cracks in a mechanical joint [2,3]. The goal is to investigate the effect of WFD on the life prediction of a single lap joint through a stochastic approach that evaluates statistical inputs, such as <u>initial crack size</u> and <u>interference fit levels</u>.

3. STOCHASTIC PARAMETERS

3.1 Equivalent Initial Flaw Size (EIFS)

Rivet hole quality is usually determined by the manufacturing process, material properties and the usage environment [4,5]. The initial fatigue quality (IFQ) characterizes the initial state of a structure with respect to initial flaws in a part, component, or airframe prior to service [6]. The IFQ is represented by an equivalent initial flaw size distribution (EIFSD). The EIFSD for specific teardown fractographic data from a lower wing skin structure of two retired B707 aircraft [7,8], is derived here by a back-extrapolation methodology- "stochastic crack growth approach" (SCGA) proposed by Yang et. al. [9]. The SCGA has been a successful analytical tool for determining the EIFSD and was utilized in assuring design requirement of aircraft durability.

3.1.1 Crack Data from Teardown Inspection

The first step in the current analysis was to obtain an EIFSD that is representative of an aging aircraft. To this end, fractographic fatigue crack data were acquired from two E-8C Joint STARS B707 lower wing skin structures [7,8]. Crack indications were found in 2,631 fastener holes through a 20X optical microscope, and a small sampling of crack indications were examined to characterize the through thickness cracks. The stress intensity factor for each cracking site was calculated and an equivalent single corner crack size was derived for an assumed analytical shape. The histogram and accumulated crack occurrences are plotted in Figure 1. The crack growth for a typical lower wing stringer-S8, shown in Figure 2, is calculated from the spectrum analysis of E-8C WS360 lower wing skin mission profiles [8]. The spectrum loading of E-8C is reduced by 10.5% from relative life data of an E-8A lower wing structure supplied by Grumman Aircraft Co. The E-8C spectrum loading applies Wheeler's crack growth retardation model with a factor of 0.80, which is based on analysis/test experience from prior C/KC-135 programs [8]. All the crack sizes are for an assumed equivalent single corner crack shape. Figure 3 plots the crack growth rate versus crack length. The detailed calculation and crack growth rate model are given in Reference 8. A three-parameter Weibull cumulative distribution function (CDF) [10,11] was used here to estimate a typical fatigue cracking distribution. This model has the following mathematical expression.

$$F\left(a; x_u, \eta, \phi\right) = \exp\left\{-\left[\frac{\ln\left(x_u/a\right)}{\phi}\right]^{\eta}\right\}$$

(1)

Here x_u is the upper bound of crack population; ϕ is the shape parameter and η is the exponent of function. The three parameters for the crack population shown in Figure 1 are $X_u = 0.6773$ inches, $\phi = 5.589$ and $\eta = 1.8376$.

3.1.2 EIFS Calculation- Backward Stochastic Crack Growth Approach (SCGA)

Since the crack occurrence data given in Figure 1 were obtained from a retired aircraft, it was decided to grow this distribution back in time to obtain an EIFSD that was more representative of new structure. A stochastic model for fatigue crack propagation proposed by Yang et. al. [9,11] in 1985 was used for this purpose. The general form of this model is:

$$\frac{da(t)}{dt} = L(\Delta K, a, K, R, S) \tag{2}$$

where $a(t)$ = crack size, L is a non-negative function, ΔK is the stress intensity factor range, K is the stress intensity factor, R is the stress ratio, and S is the maximum applied stress. From fractographic data for aluminum fastener holes subjected to a spectrum loading history [5], such as bomber or fighter spectra, the crack growth rate can be expressed as:

$$\frac{da(t)}{dt} = XQa^b(t) \tag{3}$$

where X is a non-negative random process with the median value equal to unity. Extensive fractographic data (Reference 5) provided basic evidence that Equation 3 is capable of estimating fatigue crack propagation well in the small crack size region (0.004" to 0.07") under bomber and fighter loading spectra [6]. Taking the logarithm of both sides of Equation 3, one obtains:

$$Y = bU + q + Z \tag{4}$$

where

$$Y = \log\frac{da(t)}{dt}, \; U = \log a(t), \; q = \log Q, \; Z = \log X \tag{5}$$

The linear relationship for the log crack growth rate Y to the log crack size U, shown in Figure 3, is derived by a 5-point incremental polynomial method. The good linear correlation between crack growth rate and crack length indicates the effectiveness of Equation 3. The term $Z = \log X$ is a random variable from a normal distribution with zero mean (The mean of X is 1), and a standard deviation σ_z is estimated from the linear regression relation from Equation 4:

$$\mu_y = b \times U + q \tag{6}$$

$$\sigma_y = \sigma_z \tag{7}$$

The parameter Z in Equation 4 includes all the variation of b and Q, and therefore, controls the rate of crack growth deduced from the testing data (Figure 2). For example, a curve with a 95 percentile represents the case that 95% of the cracks grow faster than the rate of this crack growth curve. A parametric study

(using an equivalent initial crack size = 0.003 inches) shows that a 99.9 percentile curve can comprise all the variation in estimating the crack growth rates from the population. Therefore, a 99.9 percentile crack growth rate curve, as a master crack growth rate curve for fractographic data, is used to back-extrapolate the EIFS distribution at time zero (Figure 4).

3.1.3 EIFS Distribution Calculation Based on SCGA

The stochastic crack growth approach is shown schematically in Figure 5, and is described below. Equation 3 can be integrated to yield the crack size $a(t)$ as a function of flight hour t,

$$a(t) = \frac{a(0)}{\left[1 - XcQta^c(0)\right]^{1/c}} \tag{8}$$

in which $a(0)$ is the initial crack size and

$$c = b - 1 \tag{9}$$

where b is shown in Equation 3. Let Z_γ be the γ percentile of the normal random variable Z and,

$$\gamma\% = P[Z > z_\gamma] = 1 - \Phi\left(\frac{z_\gamma}{\sigma_z}\right) \tag{10}$$

or, conversely,

$$z_\gamma = \sigma_z \Phi^{-1}\left(1 - \gamma\%\right) \tag{11}$$

in which $\Phi(\ )$ is the standardized normal distribution function and $\Phi^{-1}(\ )$ is the corresponding inverse function. Then, the γ percentile of the normal random variable X, denoted by X_γ, is given by

$$X_\gamma = 10^{z_\gamma} \tag{12}$$

Therefore, the EIFS $a(0)$, from Equation 8 at service time $t=0$, can be expressed as:

$$a(0) = \frac{a_\gamma(t)}{\left[1 - X_\gamma c Q t a_\gamma{}^c(t)\right]^{1/c}} \tag{13}$$

where $a_\gamma(t)$ is the crack length distribution (from the fractographic data of a torn-down structure) at service time $= t$. The EIFS for the lower wing skin at stringer S8 for the aging Boeing 707 aircraft is plotted in Figure 6. Again, the EIFS data points can still be fit by a three-parameter Weibull distribution function. These three parameters are $X_u = 0.00941$ inches, $\phi = 1.8012$, and $\eta = 0.9323$. Remember that $X_u = 0.00941$ inches is the upper limit for the EIFS distribution, and a median crack size for this particular lower wing skin structure is 0.003 inches which suitably meets the requirement of small crack region assumption for Equation 3 (0.004~0.07 inches). Table 1 lists the Weibull distribution function parameters for both fractographic data and the extrapolated EIFS. A cut-off crack size of 0.001 inches is applied as a lower limit of the EIFS distribution.

3.2 Interference Fit Levels

Another stochastic parameter investigated here is the fastener interference fit level. The interference fit is due to the plastic expansion of the rivet hole during the riveting process, and results in a compressive residual stress that is beneficial in improving the fatigue life of a riveted structure [12-18]. The residual compression can decrease the probability of crack occurrence (POCO) to propagate to critical sizes by reduction of the stress concentration effect around the rivet hole [19]. Air-pressurized rivet guns are widely utilized in current aircraft industry. This conventional rivet tool is fast, and has relatively low manufacture cost, but the riveting quality is very hard to control.

The goal in this section is to find a suitable distribution for the hole expansion level obtained by using a rivet gun. A pair of 4 inch wide by 10 inch long 0.09 inches thick 2024-T3 aluminum panels were joined by 3 rows of nine 2117 aluminum, 100° countersink rivets (identification number: MS20426-AD-6-6) with an air-pressurized rivet gun. Hole expansion levels for 27 installed rivets were measured following the procedure described in Reference 2. The original hole diameters for 54 rivet holes (27 for each panel) were measured and the histogram for the hole diameter measurements are shown in Figure 7. The hole expansion levels shown in Figure 8 are the average expansion at three locations-the root of countersink head, the interface between two panels, and the corner of driven head. A log-normal distribution with mean $\mu = 0.445$ and standard deviation $\sigma = 1.0223$ (equivalent to 2.06% of average hole expansion level and

σ=1.09%) gives a primitive estimate for the distribution of experimental measurements from rivet gun process. The choice of such a distribution function is that the 'negative' hole expansion is not allowed physically. The hole expansion levels from 18 measurements out of 27 rivets are shown in Figure 8. A cut-off hole expansion level of 0.5% was picked as a lower limit since, according to Hsu-Forman residual stress analysis [2,20], the rivet hole is assumed to be elastically deformed within 0.5% of hole expansion.

3.3 Monte Carlo Simulation of Fatigue Life

Monte Carlo simulation is a statistical data process which handles statistical parameters with different distributions through a deterministic approach. The use of Monte Carlo simulation can basically eliminate the cost of building and operating expensive equipment, and, in addition, reduces the time required for a direct solution [21]. Two stochastic parameters- Equivalent initial flaw size (EIFS) distribution and interference fit level- are investigated here as two random variables in Monte Carlo simulations for the fatigue life of a lap joint with a deterministic WFD life prediction model. A minimum number of trials are tested to ensure the majority of percentiles of failure life within a reasonable accuracy, with acceptable computational time. A thousand trials, proven to be a sufficient number, were selected and performed throughout the simulation [10]. The six Monte Carlo simulation cases examined here consisted of combinations of fixed/ varied interference fit level and EIFSD at rivet holes. The outcome for those simulations will be discussed as the individual/ interaction effect of these two parameters are presented.

3.3.1 Methodology

A 30 inch wide, single lap joint made of 0.09 inch thick 2024-T3 aluminum sheets joined by three rows of thirty 2117 aluminum countersink rivets (MS 20426) was modeled here. Only the top row of 30 rivet holes contains initial damage which is randomly picked from the EIFS distribution (Figure 6), and these cracks are forced to propagate during fatigue loading. The typical, maximum stress experienced at a typical lower wing skin location in a commercial aircraft is approximately 11 ksi. An 11 ksi constant amplitude loading history with R=0.05 was utilized in the current simulation. The simulation matrix is given in Table 2 and the specification of each case is stated below.

Case I: One crack size is randomly picked from the EIFS distribution (Figure 6). This crack size is applied at both sides of each rivet hole (symmetric crack sizes are the same at all 30 rivet holes). Interference fit level is fixed at 1.15% for all rivet holes.

Case II: 30 crack sizes are randomly picked from EIFS distribution. A different crack size is assigned to both sides of each rivet hole (symmetric cracks at each hole). Interference fit level is fixed at 1.15% or 2.06% for all rivet holes.

  Case II-a: Fixed hole expansion level at 1.15% due to low squeeze force.
  Case II-b: Fixed hole expansion level at 2.06% due to high squeeze force.

Case III: 60 crack sizes are randomly picked from EIFS distribution, and are assigned to both sides of each hole, resulting in unsymmetric cracks at each rivet hole. Interference fit level is fixed at 1.15% for all rivet holes.

Case IV: Random crack sizes same as case I. Interference fit level at each hole is randomly picked from the hole expansion distribution (Figure 8) at each rivet hole.

Case V: Random crack sizes same as case II. Interference fit level at each hole is randomly picked from the hole expansion distribution at each rivet hole.

  Case V-a: Random hole expansion level with $\mu = 2.06\%$ and $\sigma = 1.09\%$ (1 standard deviation).
  Case V-b: Random hole expansion level with $\mu = 2.06\%$ and $\sigma = 0.55\%$ (median variation).
  Case V-c: Random hole expansion level with $\mu = 2.06\%$ and $\sigma = 0.0\%$ (No variation).

Case VI: Random crack sizes same as case III. Interference fit level at each hole is randomly picked from the hole expansion distribution at each rivet hole.

3.3.2 Summary and Discussion of the Monte Carlo Simulations

For each case, 1000 trials are completed and the fatigue lives versus frequency of failure (FOF) or cumulative probability of failure (CPOF) are plotted in Figures 9 to 12. Summary and discussion of the Monte Carlo simulations follows below.

1. Figure 9 shows the simulation results for the first three cases. Figure 10 shows more details for Cases II-a and III. From Figure 10, the shape and distribution of CPOF for these two cases are almost the same. Case III has a higher CPOF at the given failure life than the Case II-a, i.e. Case III has an average shorter failure life than Case II-a. These shorter lives are due to the fact that Case III has higher possibility of containing larger WFD cracks (60 randomly picked crack sizes) than in Case II-a. However, the CPOF of these two cases have similar distribution shapes as shown in Figure 10. This is because that the order of crack lengths, within the population of 0.001 inch to 0.00941 inches, is so small that the difference in fatigue life distribution for both cases is not significant.

2. The distribution of CPOF for Case I is flatter and wider spread than the other two cases (Figure 9). This result is reasonable since the panel life is mainly dominated by long cracks, and Case I has less possibility in containing larger WFD cracks than Case II-a and III. All three cases are under the condition of fixed interference fit level at 1.15%.

3. Figure 11 compares the effect of two different squeeze forces on the fatigue life distribution for Case II-a and Case II-b. As expect, the higher the squeeze force, the longer the fatigue life, since the residual compressive stress region becomes larger due to the higher interference fit level. The larger compressive residual stress can reduce the crack tip SIF more effectively, increasing the fatigue life. The interference fit level of 2.06% corresponds to high squeeze force, while the 1.15% interference fit level is due to a lower squeeze force.

4. From summary 1, Cases II-a and III give similar simulation results. Therefore, only the results for the <u>symmetric crack size at both sides of rivet hole</u> case IV and V are discussed below.

5. The interference fit level due to the rivet gun process is assumed log-normally distributed with a mean value of 2.06% and a standard deviation of 1.09%. Figure 12 shows the simulation outcome for Cases IV-a and V. Not surprisingly, Case V-a has a higher CPOF than Case IV due to the greater possibility of long crack occurrence. The FOF spreads widely from 75,000 cycles through 1,000,000 cycles, which results from a larger variation in hole expansion levels- i.e. a poorer, less consistent riveting quality. The lowest fatigue life of 75,000 cycles results from the occurrence of longest EIFS

(0.00941"), which dominates the failure of the structure, with cut-off hole expansion level at 0.5%.

6. Figure 13 shows the effect of hole expansion variation on failure life (Case V-a, –b and -c). The CPOF curve with no variation case (i.e. fixed hole expansion at 2.06% with 0% variation: Case V-c) shows that the failure lives are highly compact within the range of 110,000 cycles to 170,000 cycles. As the variation increases, i.e. larger hole expansion distribution levels due to less consistent riveting quality, the range of FOF stretches out because the formation of larger residual compressive stress at higher hole expansion levels increases the fatigue life.

7. Figure 14 shows that the flatter the bell-shape distribution of rivet gun riveting process is, the larger the portion of population at both tail parts occurs. At lower end, for example, the variation curve for Case V-a has a higher possibility of small hole expansion levels occurrence than the variation curve for Case V-b. As a result, the CPOF for Case V-a is higher than for Case V-b. (indicating a higher possibility of structural failure) On the other hand, a higher possibility of large hole expansion levels for Case V-a at the other end reduces the CPOF than for the Case V-b does (at the lower hole expansion level).

8. The degradation in residual strength (i.e. probability of failure) as the WFD extends by fatigue was also studied through the Monte Carlo simulations. The residual strength of the riveted joint versus elapsed fatigue cycles is shown in Figure 15. (Fixed hole expansion level = 2.06%) The 95 percentile curve stands for the case that 95 % of 1,000 trials have equal or lower residual strength at given fatigue life. Therefore, a smaller percentile curve indicates more severe residual strength degradation or faster crack propagation rate in a riveted lap joint structure. Figure 15 illustrates that the residual strength of the aircraft structure is not a deterministic quantity but, rather, a statistical distributed quantity. If the hole expansion variation increases (from Case V -c to Case V -a), as shown in Figure 16 and Table 3, the distribution in failure life widens with larger variation in hole expansion level (the 95 percentile curve moves to right-hand side as the variation increases.) However, the 5 percentile curves of failure at different hole expansion level variations are very closed to one another. This comes from the fact the population (69% within one standard deviation) of this bell-shape, normal distribution falls around the mean value of the total population. The residual strength here is governed and predicted by Net-section yielding failure criteria [22-25] without lead crack presence.

9. Another WFD issue of concern to structural integrity is the residual strength degradation due to foreign object damage (such as engine burst, bird strike, battle damage, etc.). A lead crack, with linkup length (1.1918 inches + WFD lengths of two link-up holes) of two adjacent rivet holes, is imposed onto the structure at different service lives. Figure 17 demonstrates the residual strength degradation if the lead crack is formed after 10,000 cycles, 30,000 cycles or 50,000 cycles during the total service life of 106,415 fatigue cycles for a riveted lap structure (which is the mean fatigue life for Case V -a.) As the lead crack is introduced during the service life, the residual strength drops as the net-section area that can sustain the applied force becomes smaller. The residual strength degrades as the lead crack propagates towards to adjacent WFD. As the lead crack grows longer, the residual strength predicted by the Ligament Yielding Criteria [26] suppresses the net-section yielding criteria and the failure soon takes place as the lead crack rapidly links up with the approaching WFD. The calculation indicates that, whenever the formation of lead crack is presented, the residual strength reduces very quickly and the remained life is less than 10,000 cycles for the cases examined.

4. SUMMARY AND DISCUSSION

A summary of the results is given in the following section.

1. The EIFS examined here is based on fractographic data from the lower wing skins of two retired Boeing 707 aircraft. A three-parameter Weibull distribution function well describes the inspected crack sizes and EIFS distribution.

2. The stochastic crack growth approach (SCGA) is shown to be an effective method to extrapolate the crack size distribution to service time $t = 0$ as long as the crack size distribution, from tear-down fractographic data or non-destructive evaluation (NDE) method, at service time $t = t_f$ is known.

3. The interference fit level distribution associated with rivet gun riveting process is assumed to be a log-normal distribution with a mean value of 2.06% and standard deviation of 1.09% as found from experimental measurements. Since only 18 samples were examined, however, more samples need to be done to full understand the statistical property of this distribution. The rivet gun riveting process inevitably causes wider spread in

hole expansion levels which results from various sources of error such as manufacture process (rivet hole drilling process), installation process (operational time, riveting force) and human error (operational error, misalignment between lap area/ rivets, air-pressure levels and instrumental precision, etc.) More hole expansion measurements and finite element analysis are suggested to further investigate interference fit levels and residual compressive stress field calculations.

4. The EIFS is an artificial crack size distribution at service time = 0. The influence of riveting quality (reflected as the interference fit) on the EIFS distribution is included into the Stochastic Crack Growth Approach (SCGA) since the crack growth rate was supplied by Grumman Aircraft Co. This crack growth information was calculated from a spectrum analysis of E-8A WS 360 mission profiles which applied the Wheeler's crack growth retardation model. However, since the Grumman analysis [7,9] did not provide the initial hole expansion levels, the influence of interference fit on EIFS distribution can not be solely investigated. (It is because the variation in crack growth rate has been fitted by adjusting the factors either in the retardation model or in SCGA) In addition, other types of joints, such as countersink/universal rivet joint or bolted joint, which might lead to different levels of hole expansion, should also be studied.

The Monte Carlo simulation results suggest:

♦ High interference fit level increases the fatigue life more than low interference fit level.

♦ The fatigue lives for the symmetric and unsymmetric crack sizes (Case II and Case III) have similar distribution and the same order of lives. This is because the EIFS ranges from 0.001" to 0.00941", where the influence on failure lives is not so significant.

♦ Comparison between simulations for fixed (zero variation) and variable interference fit levels lead to two suggestions. First, riveting quality is a dominant variable in determining the fatigue life of a joint structure. Second, inconsistent riveting process leads to a dispersed fatigue life distribution, which is a potential threat in the evaluation of structural safety concern.

♦ Again, achieving consistent riveting process is an important factor concerning the safety of lap joint structure.

5. ACKNOWLEDGEMENTS

REFERENCES:

1. P. W. Hovey, Berens and D. A. Skinn, "Risk Analysis for Aging Aircraft Fleets", Volume 1- Analysis, WL-TR-91-3066, University of Dayton, Research Institute, October 1991.

2. H. L. Wang, "Evaluation of Multiple Site Damage in Lap Joint Specimens," Ph.D. Thesis, School of Aeronautics and Astronautics, Purdue University, West Lafayette, IN, December 1998.

3. H. L. Wang and A.F. Grandt, Jr., "Fatigue analysis of Multiple Site Damage in Lap Joint Specimens", 30th National Symposium on Fatigue and Fracture Mechanics, ASTM, June 23-25, 1998

4. J. P. Gallagher, F. J. Glessler, A. P. Berens, R. M. Engle, Jr. "USAF Damage Tolerant Design Handbook: Guidelines for the Analysis and Design of Damage Tolerant Aircraft Structures," AFWAL-TR-82-3073, May 1984.

5. "Fastener Hole Quality", AFFDL-TR-78-206, Volume I, II, Structures Design Department, General Dynamics Fort Worth Division, Fort Worth, Texas 76101, December 1978.

6. J. N. Yang, S. D. Manning, J. L. Rudd, M. E. Artley, and J. W. Lincoln, "Stochastic Approach for Predicting Functional Impairment of Metallic Airframes," 28th Structures, Structural Dynamics and Materials Conference- Part I, 1987, pp. 215-223.

7. J. Luzar and A. Hug, "Lower Wing Disassembly and Inspection Results of Two High Time USAF B707 Aircraft," Proceedings of the 1996 USAF Structural Integrity Program Conference, Volume 1, WL-TR-97-4054, June 1997, pages 509 - 528.

8. "Fracture Mechanics/ Crack Growth Analysis and Data Reduction of Teardown/ Inspection Results," Typical Lower Wing Stringers S7, S8 and S9 Inboard of WS 360 Splice B707-300C. Attachment A to Boeing Letter Y-7WH8-JPF-96-041, 1996.

9. J. N. Yang, W. H. Hsi, S.D. Manning, and J.L. Rudd, Journal of Aircraft, Vol. 22, No. 2, September 1985, pp. 810-817.

10. S. M. Rohrbaugh, B. M. Hillberry, and D. Ruff, "A Probabilistic Fatigue Analysis of Multiple Site Damage: Influence of the Number of Fastener Holes", ICAF '95 International committee on Aeronautical Fatigue 18th Symposium, Melbourne, Australia, May 3-5, 1995.

11. S. D. Manning and J. N. Yang, "Advanced Durability Analysis, Volume II- Analytical Predictions, Test Results and Analytical Correlations," AFWAL-TR-86-3017, February 27, 1989.

12. J. Y. Mann and G. S. Jost, "Stress Fields Associated with Interference Fitted and Cold-Expanded Holes", Metals Forum Vol. 6, No. 1, 1983.

13. N. Slundarraj, B. Dattaguru and T. S. Ramamurthy, "Analysis of a Double Shear Lap Joint with Interference Fit Pin", Computer & Structures, Vol. 55, No. 2, pp. 357-363, 1995.
14. H. Armen, Alvin Levy, and H. L. Eidinoff, "Elastic-Plastic Behavior of Coldworked Holes", Journal of Aircraft, Vol. 21, No. 3, March 1984.
15. L. R. Hall, R. C. Shah, and W. L. Engstrom, "Fracture and Fatigue Crack Growth Behavior of Surface Flaws and Flaws Originating at Fastener Holes," Air Force Flight Dynamics Laboratory, WPAFB, AFFDL-TR-74-47, Vol. 1, May 1974.
16. G. J. Petrak and R. P. Stewart, "Retardation of Cracks Emanating from Fastener Holes," Engineering Fracture Mechanics, Vol. 6, 1974, pp. 275-282.
17. J. H. Crews, Jr., "An Elastoplastic Analysis of a Uniaxially Loaded Sheet with an Interference Bolt," NASA Tech. Note D-7748, October 1974.
18. D. L. Rich, L. F. Impellizzeri, " Fatigue Analysis of Cold-Worked and Interference Fit Fastener Holes", Cyclic Stress-Strain and Plastic Deformation Aspects of Fatigue Crack Growth, ASTM STP 637, American Society for Testing and Materials, 1977, pp. 153-175.
19. G. S. Wang, "A Statistical Multi-site Fatigue Damage Analysis Model", Fatigue Fracture Engineering Material Structure , Vol. 18, No. 2, pp.257-272, 1995.
20. Y. C. Hsu, R. G. Forman, "Elastic-Plastic Analysis of an Infinite Sheet Having a Circular Hole Under Pressure", Journal of Applied Mechanics, June 1975, pp. 347-352.
21. R. A. Johnson, "Miller & Freund's Probability & Statistics for Engineers," 5th edition, Prentice Hall, Englewood Cliffs, New Jersey 07632, 1994.
22. E.J. Moukawsher, A.F. Grandt, Jr., and M.A. Neussl "Fatigue Life of Panels With Multiple Site Damage," Journal of Aircraft, Vol. 33, No. 5, September-October 1996, pp. 1003-1013.
23. E. J. Moukawsher, "Fatigue Life and Residual Strength of Panels with Multiple Site Damage," M. S. Thesis, School of Aeronautics and Astronautics, Purdue University, West Lafayette, IN, May 1993.
24. M. B. Heinimann, "Analysis of Stiffened Panel with Multiple Site Damage", Ph.D. Thesis, School of Aeronautics and Astronautics, Purdue University, West Lafayette, IN, May 1997.
25. D. G. Sexton, "Comparison of the Fatigue Damage Resistance and Residual Strength of 2024-T3 and 2524-T3 Panels Containing Multiple Site Damage", Master Thesis, School of Aeronautics and Astronautics, Purdue University, West Lafayette, IN, August, 1997.
26. T. Swift, "Widespread Fatigue Damage Monitoring Issues and Concern," The 5th International Conference on Structural Airworthiness of New and Aging Aircraft, Hamburg, Germany, June 16-18, 1993.

Table 1 Three Parameter of Weibull Distribution Function Derived from Fractographic Data and EIFS

	Equivalent Single Corner Crack Size (Figure 1)	EIFS (Figure 6)
X_u	0.6773 inch	0.00941 inch
ϕ	5.589	1.8012
η	1.8376	0.9323

Table 2 Test Matrix for Monte Carlo Simulation

30 rivet holes	EIFS distribution (Figure 6)	Hole Expansion Levels (Figure 8)
Case I	One crack size is randomly picked, and is assumed to occur at both sides of all 30 rivet holes.	Fixed hole expansion level (_1.15%_) at all 30 rivet holes:
Case II	30 crack sizes are randomly picked, and one crack size is assigned to both sides of the 30 rivet holes. (_symmetric_ crack size at a rivet hole)	a. 1.15% Hole expansion level (low squeeze force) b. 2.06% Hole expansion level (high squeeze force)
Case III	60 crack sizes are randomly picked. Different crack size assigned at each side of a rivet hole. (_unsymmetrical_ crack size at a rivet hole)	
Case IV	Same as Case I.	Varied hole expansion levels randomly picked from the log-normal distribution. _μ =0.445 , σ = 1.0223, (equivilent to a mean expansion of 2.06% with a std. of 1.09%)_
Case V	Same as Case II.	a. μ = 2.06%; σ = 1.09 % b. μ = 2.06%; σ = 0.55 % c. μ = 2.06%; σ = 0.0 %
Case VI	Same as Case III.	

Table 3 Failure Life at Different Hole Expansion Levels for Different Percentile Population.

Fatigue Life @ Certain Percentile (Cycles)	Case V -a $\sigma = 1.09\%$	Case V -b $\sigma = 0.55\%$	Case V -c $\sigma = 0.0\%$
5 %	77,609	78,259	111,932
50 %	106,415	122,350	127,505
95 %	813,737	407,424	140,500

Equivalent Single Corner Crack Size
B707-100,321 lower wing skin. S8
Reference: Joe Luzar and Anthony Hug, - Presented at the 1996 USAF Structural Integrity Program Conference, San Antonio, Texas, 3-5 December 1996

◇ Cumulative %

□ Frequency of Crack Occurence

X_u = 0.6773"

ϕ = 5.589

η = 1.8376
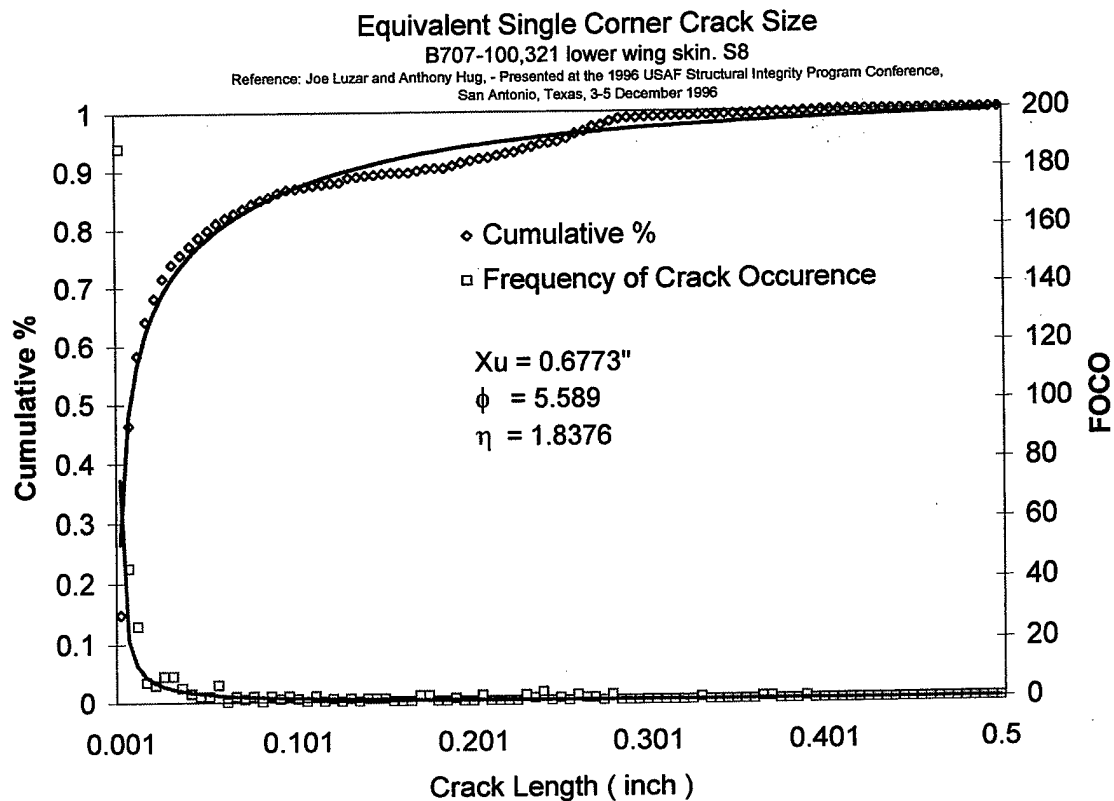
Figure 1 Frequency of Crack Occurrence and Cumulative Percentage of Crack Sizes [7].

Stringer S8, E8C;
load factor = 0.895; Wheeler Retardation Factor = 0.80

— Crack Length v.s. Flight Hours
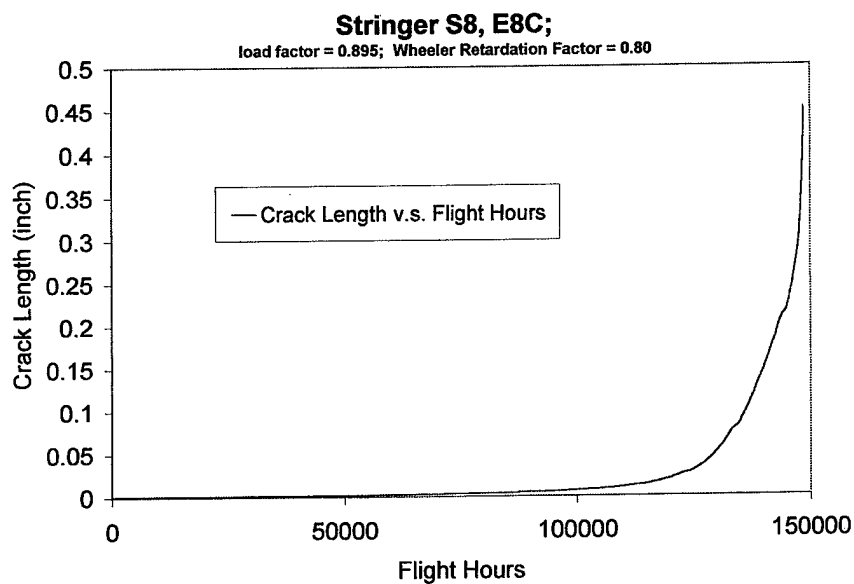
Figure 2 Predicted Crack Length versus Flight Hours [8].

S8 Stringer; E8C;
Load Factor = 0.895; Wheeler Retardation Factor = 0.80
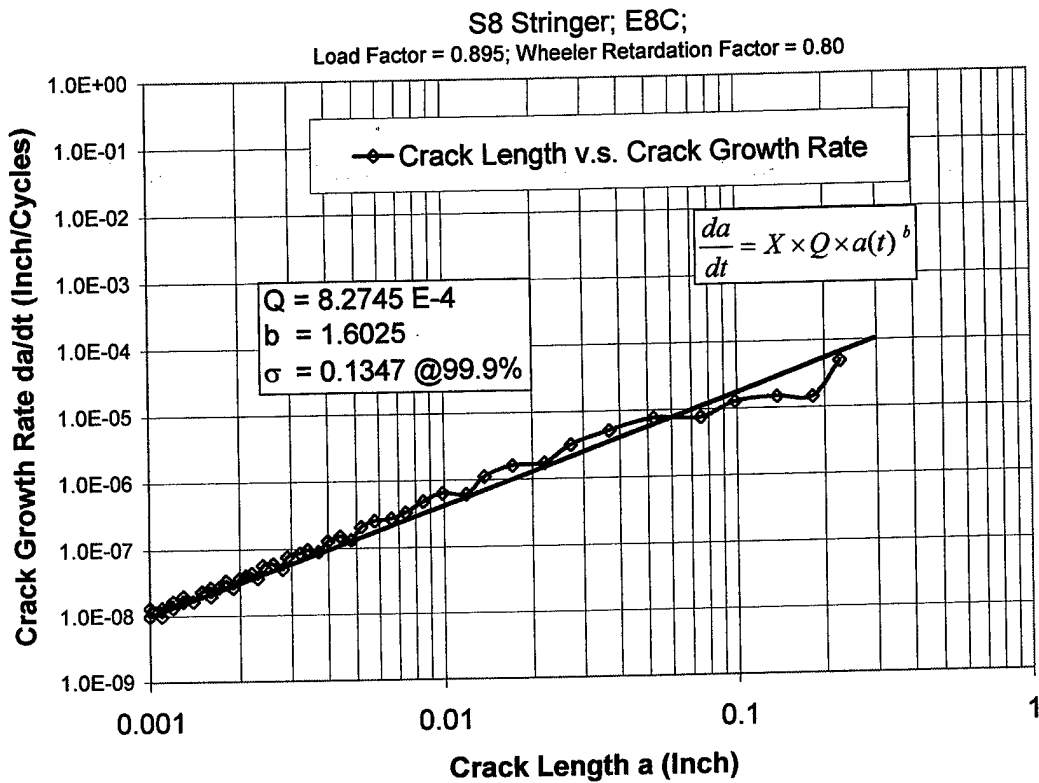
Figure 3 Crack Growth Rate versus Crack Length.

Percentile of Crack Growth Rate v.s. E8C;
load factor = 0.895; Wheeler Retardation Factor = 0.80
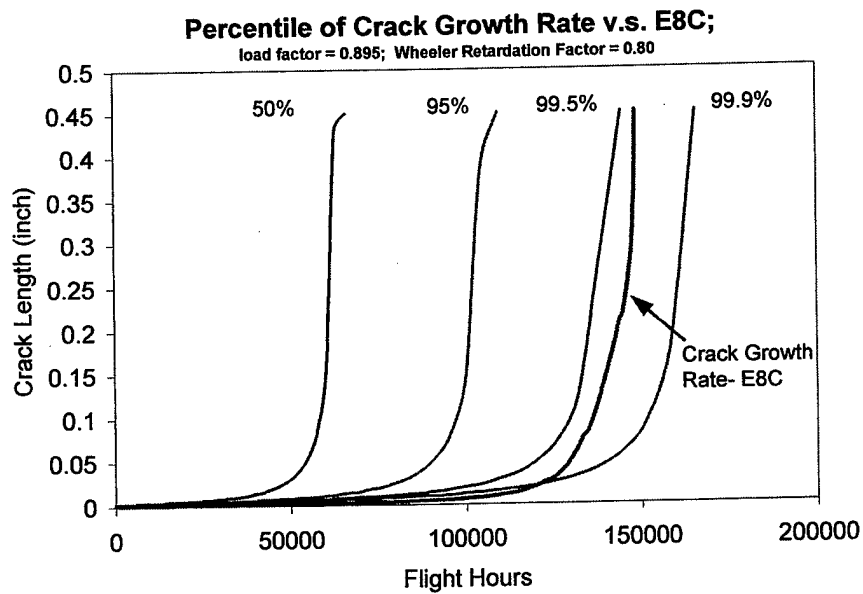
Figure 4 Percentiles of Crack Size as a Function of Service Time Based on Statistical Model for B707 Lower Wing Skin Data Set.
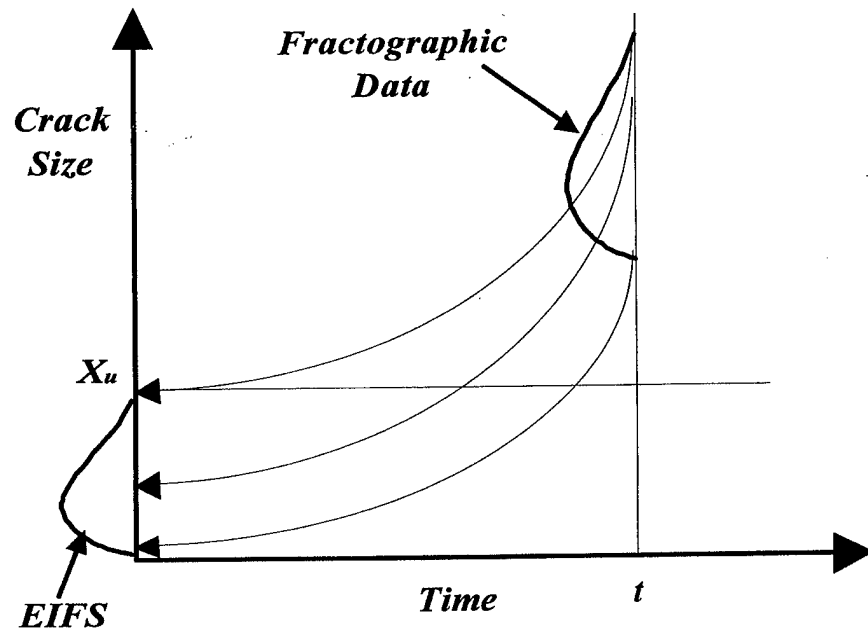
Figure 5 Schematic Representation of Stochastic Approach Used to Grow Final Crack
Distribution Back in Time.

EIFS

reference: "Stochastic Crack Propagation in Fastener Holes", J.N. Yang et al., J. aircraft, Vol. 22, No
2, September 1985

◇ Cumulative %

□ Frequency of Crack Occurrence (FOCO)

Xu = 0.00941"
φ = 1.8012
η = 0.9323
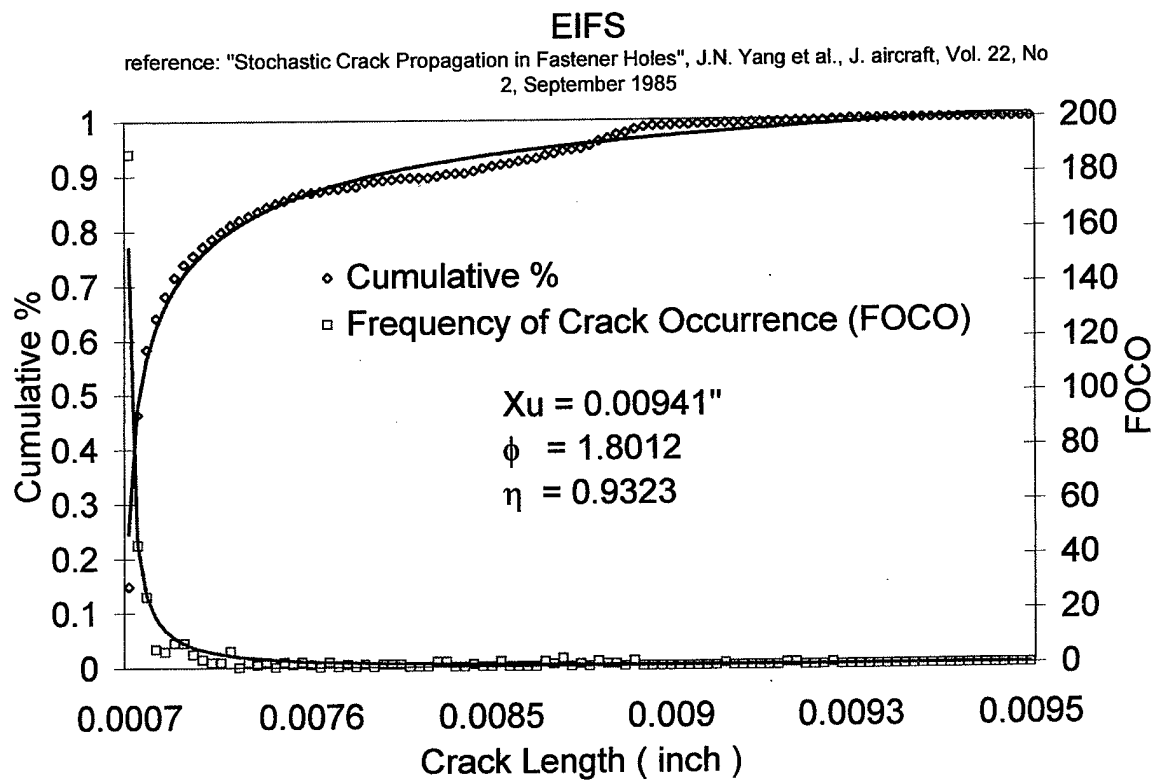
Figure 6 EIFS Distribution of Boeing 707 Lower Wing Skin, Stringer S8 with E8C
Spectra Loading

μ=0.19182"
σ=0.00033"

0.189   0.190   0.191   0.192   0.193   0.194   0.195

Original Hole Diameter (inches)
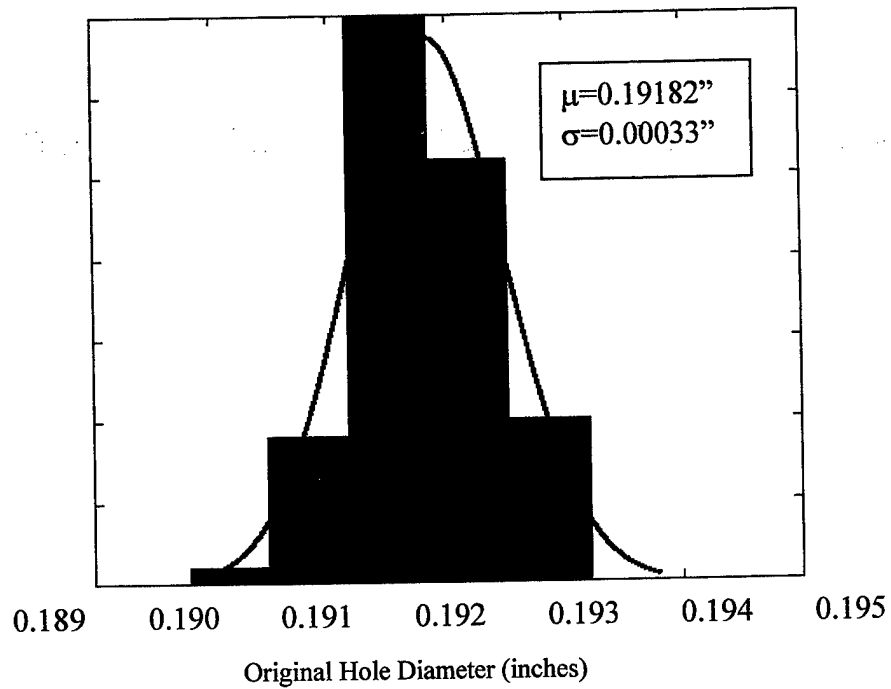
Figure 7 Histogram of Hole Diameter Measurements (54 Samples).

μ = 2.06 %

σ = 1.09 %

Cut-off at 0.5%

0.1   1   10   100

Hole Expansion Level   %
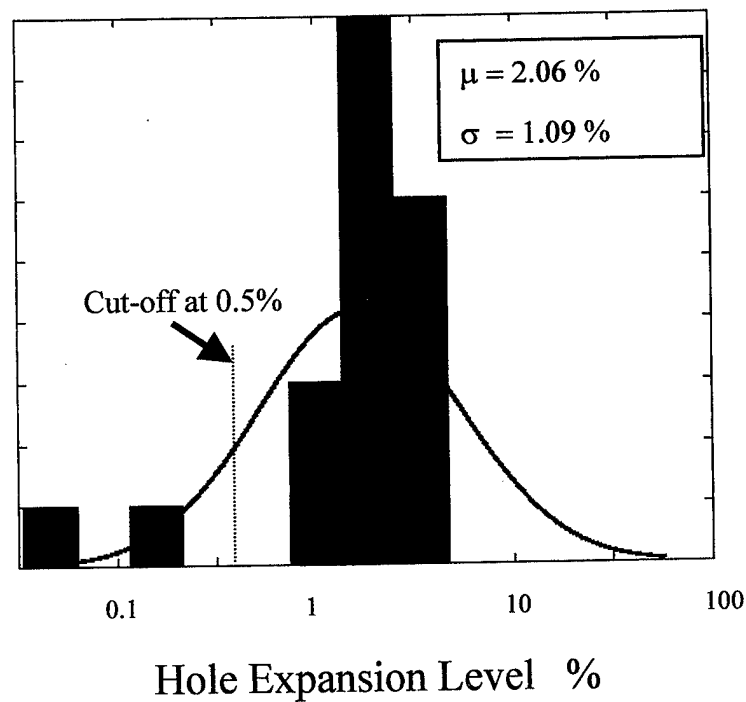
Figure 8 Histogram of Hole Expansion Measurements (18 Samples) of a Single Lap
Specimen Manufactured from a Rivet Gun (Log-Normal Plot)
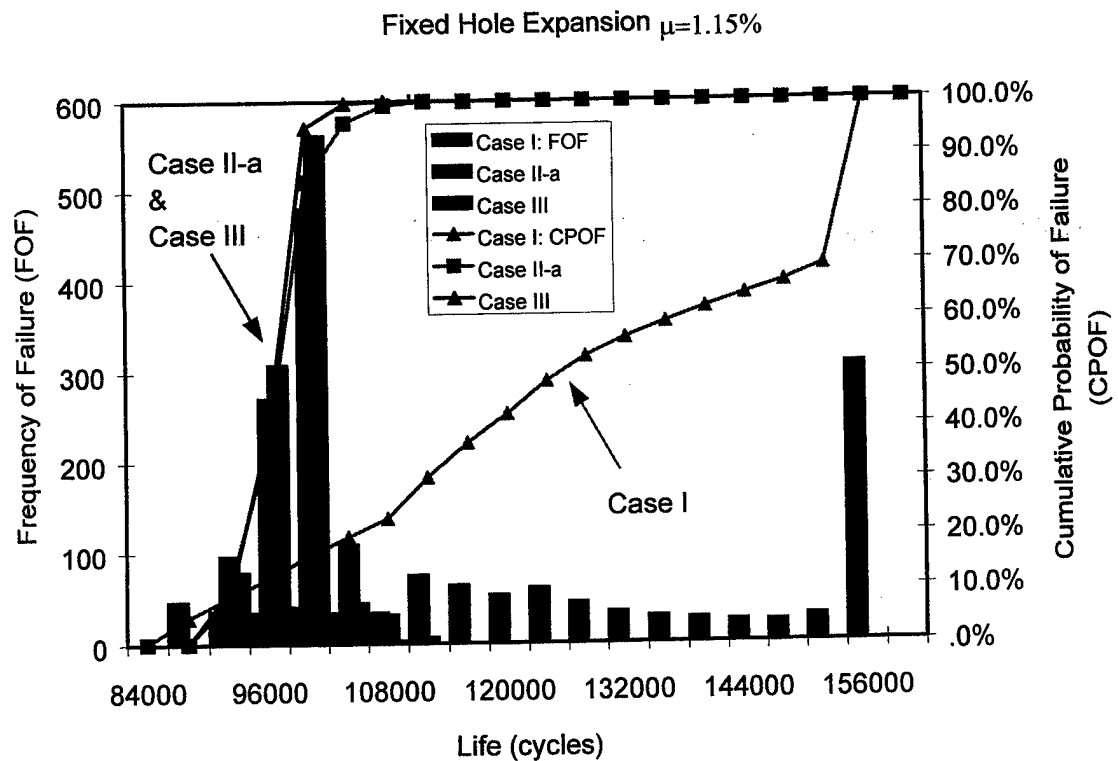
Figure 9 Plot of the Fatigue Lives of Three Cases- I, II-a and III, for the MSD Panel with Fixed Hole Expansion Levels- 1.15%
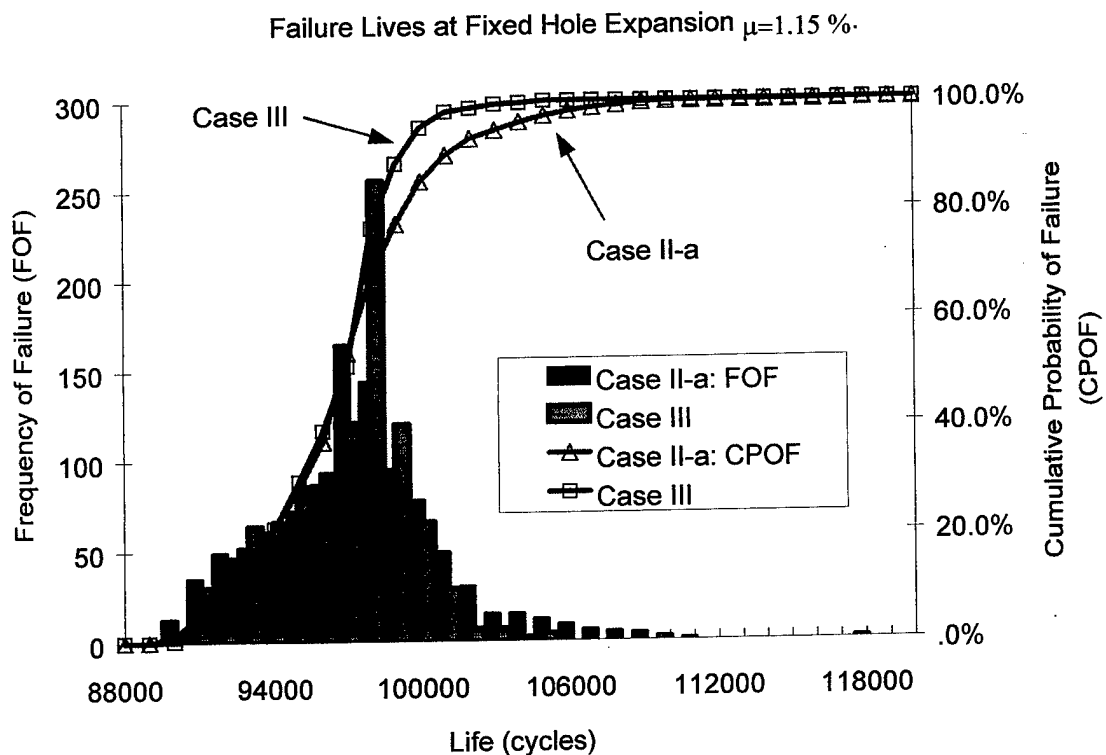
Figure 10 Plot of the Fatigue Lives of Cases- II-a and III, for the MSD Panel with Fixed Hole Expansion Levels- 1.15%

Failure Lives at Different Squeezing Forces.
Case II-a: Fixed Hole Expansion $\mu=1.15\%$
Case II-b: Fixed Hole Expansion $\mu=2.06\%$
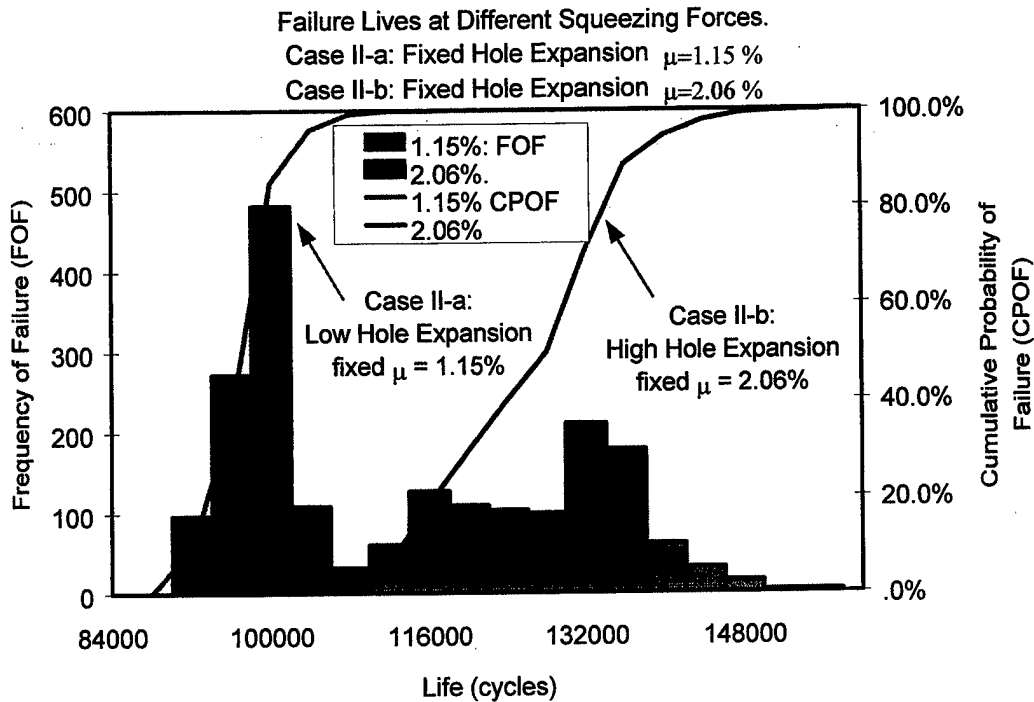
Figure 11 Comparison of the Fatigue Lives between High/ Low Hole Expansion Levels-
2.06% versus 1.15%

Failure Lives for Varied Hole Expansion Levels.
$\mu=2.06\%$ $\sigma=1.09\%$
Case IV: Equal Crack Length for 30 Rivet Holes
Case V: Symmetric Crack Length at Both Sides of a Rivet Hole
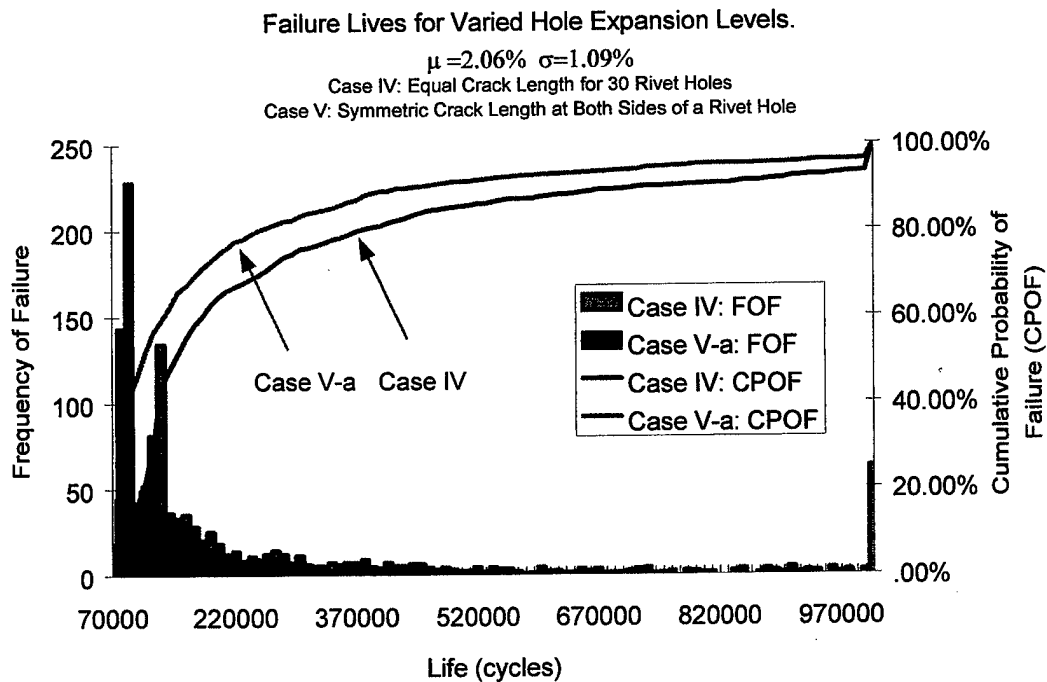
Figure 12 Comparison of the Fatigue Lives between Case IV and V-a

Case V: Random Hole Expansion Level;
Symmetric Crack Size at Both Sides of a Rivet Hole
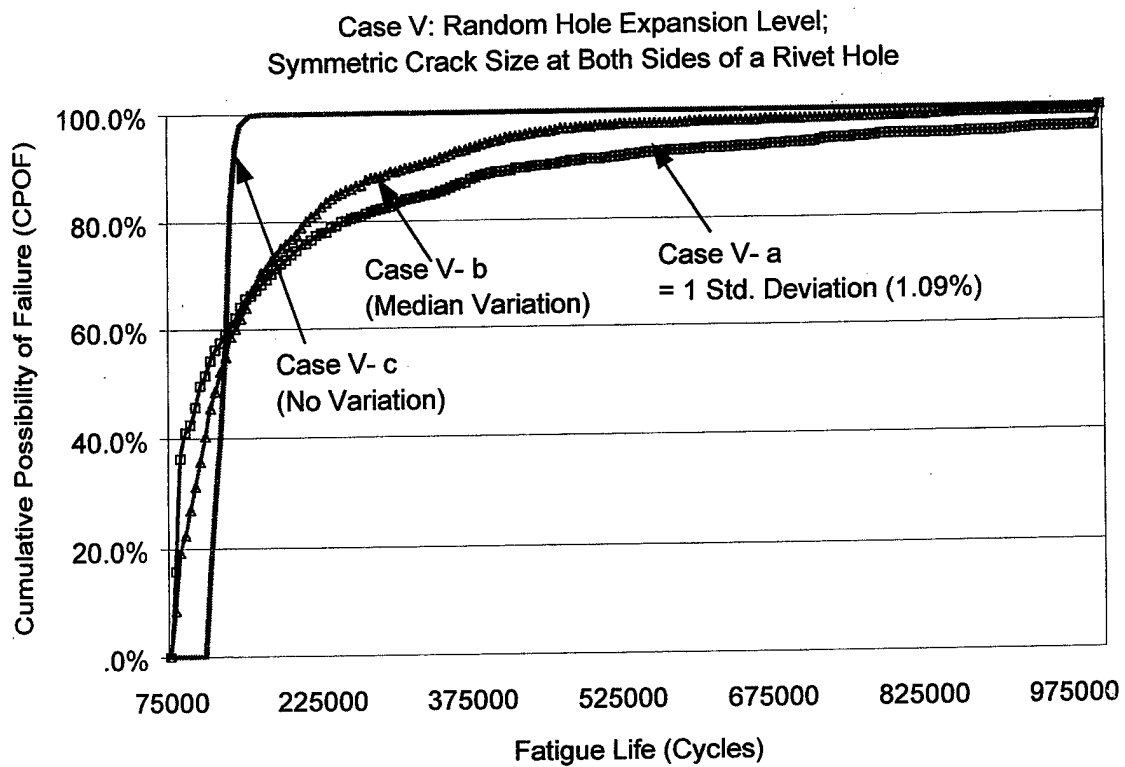
Figure 13 Variation in Hole Expansion Levels versus Fatigue Lives (Case V-a, b and c)
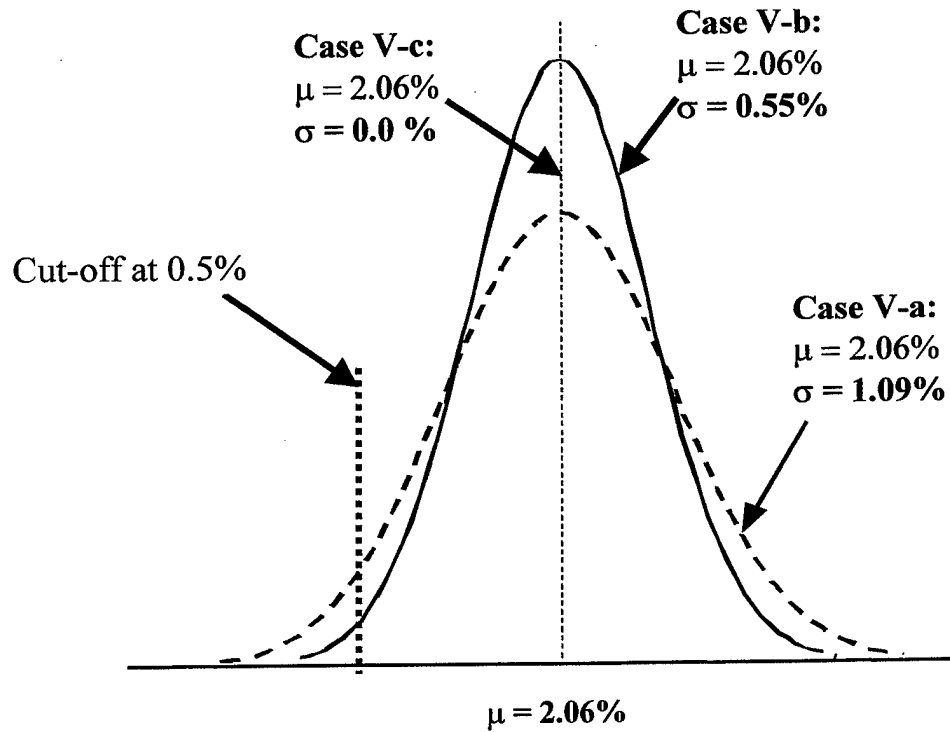
Figure 14 Log-Normal Distribution of Rivet Gun Riveting Process at Different Variation
Levels
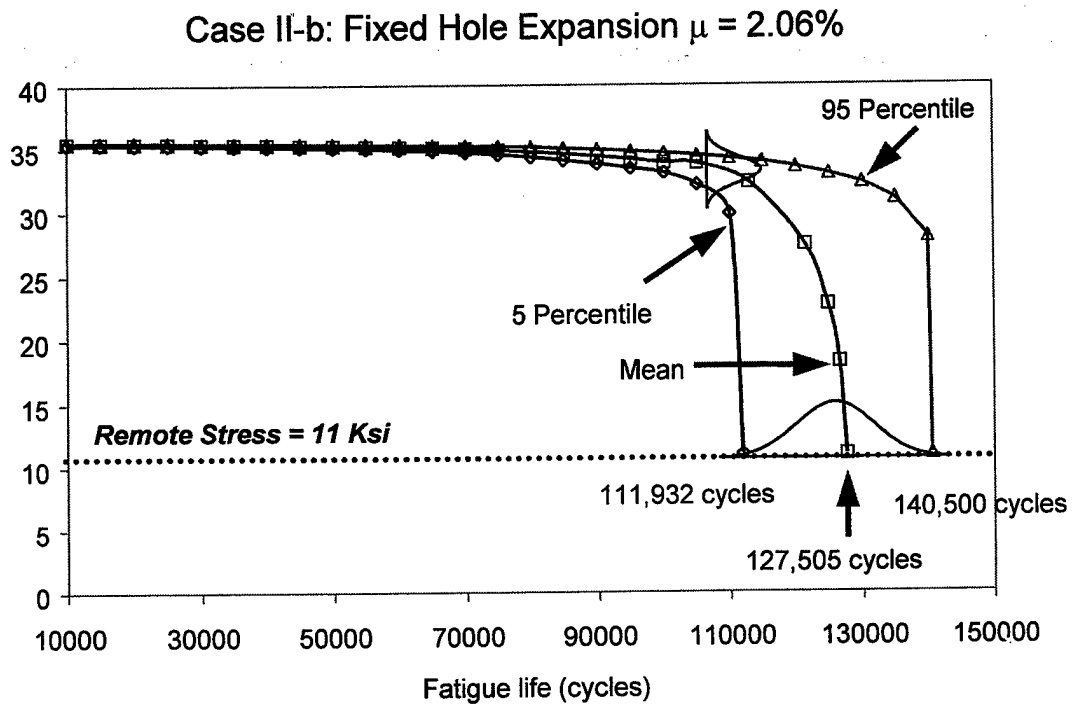
Figure 15 Distribution in Residual Strength for a Riveted Lap Joint. (1,000 Trials, with hole expansion level fixed at 2.06%, random symmetric initial crack sizes at all 30 holes.)
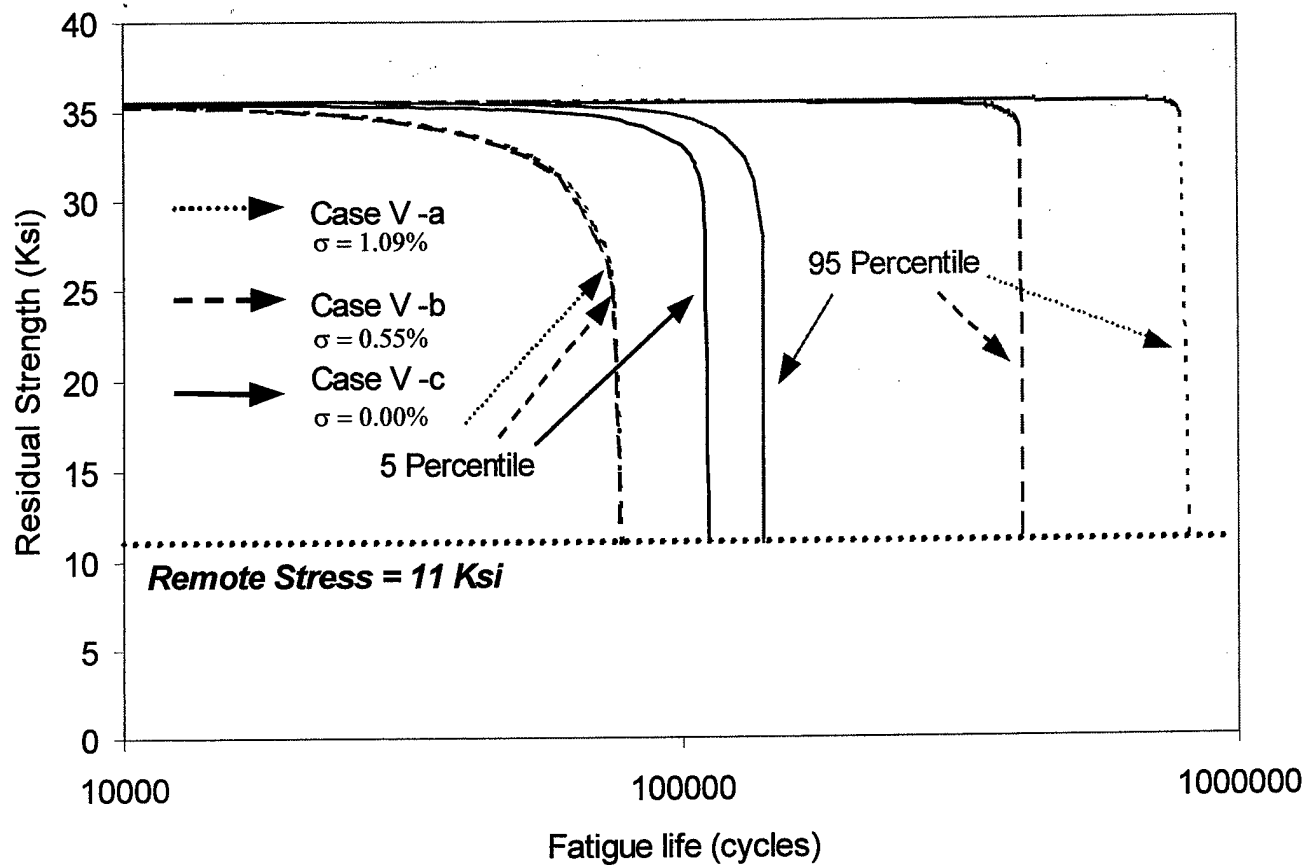
Figure 16 Distribution in Residual Strength for a Riveted Lap Joint. (Random Variation in Symmetric Initial Crack Sizes, with Three Different Hole Expansion Level Variations-MSD without Lead Crack)
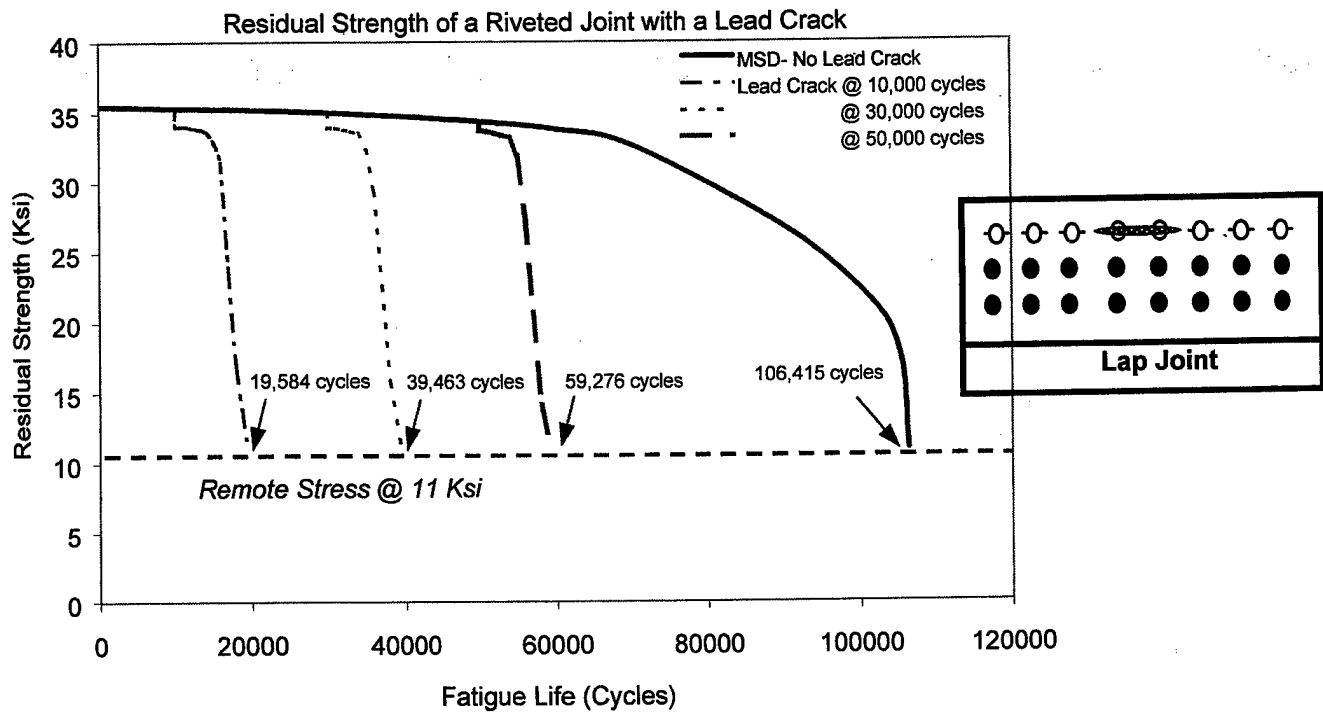
Figure 17 Residual Strength of a Riveted Lap Joint. (Case V-a, MSD with a Lead Crack at Different Fatigue Lives)

Analysis of Widespread Fatigue Damage in Lap Joints

A. F. Grandt, Jr. and H. L. Wang
School of Aeronautics and Astronautics, Purdue University, W. Lafayette, IN 47907-1282

ABSTRACT

This paper describes research to analyze widespread fatigue damage in lap joints. The particular objective is to determine when large numbers of small cracks could degrade the joint strength to an unacceptable level. A deterministic model is described to compute fatigue crack growth and residual strength of riveted panels that contain multiple cracks. Fatigue crack growth tests conducted to evaluate the predictive model are summarized, and indicate good agreement between experimental and numerical results. Monte Carlo simulations are then performed to determine the influence of statistical variability on various analysis parameters.

INTRODUCTION

As shown in Figure 1, widespread fatigue damage (WFD) occurs when large numbers of small cracks develop at repeated structural details and compromise the discrete source residual strength provided by stiffeners and other damage tolerance structural features [1-2]. The classic example of this problem is the 1988 Aloha Airlines incident where small fatigue cracks developed along a row of fastener holes, coalesced, and jumped across adjacent stiffeners, failing a large section of fuselage skin in a B-737 aircraft [2]. This incident clearly demonstrated the deleterious effects of WFD, and has led to much research on this problem. The particular concerns deal with determining the size of small cracks that compromize lead crack residual strength, and the time when those cracks occur [2].

The authors and their colleagues are developing models to predict the nucleation and propagation of widespread fatigue damage (WFD) that forms at material inhomogeneities, corrosion damage, or from fretting fatigue [3-13]. The predictive scheme is based on a deterministic analysis [3, 6, 8] for the growth, coalescence, and final fracture resulting from various combinations of small cracks and large lead cracks that occur along a row of holes in a flat sheet (see Figure 1). The multi-degree-of-freedom model allows individual cracks to grow independently, until interacting and linking up with adjacent cracks, or until growing into an uncracked hole (i.e., a "crack stopper"). The algorithm also employs a notch fatigue analysis to predict crack nucleation at pristine holes, or to continue growing cracks which are momentarily stopped at the holes.

Numerical predictions for lead and WFD fatigue crack growth [3, 8, 10-11] are compared with test results for both stiffened and unstiffened specimens in Figure 2. Note that the current WFD model does an excellent job of predicting fatigue life for these open hole tests.

Figure 1 Schematic representation of a large lead crack and small WFD cracks in a stiffened panel.
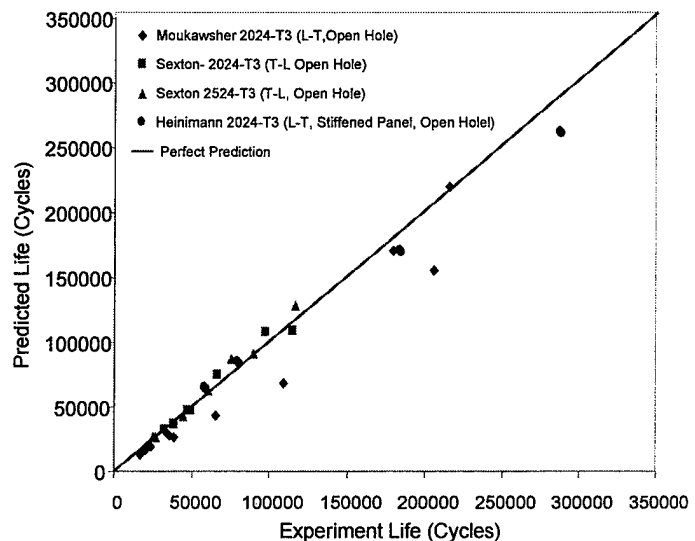

Figure 2 Comparison of predicted and measured fatigue lives for stiffened and unstiffened panels with combinations of large lead and small WFD cracks.

Residual strength tests [4-5, 7, 11] have also been conducted with both stiffened and unstiffened panels that contain WFD and lead cracks in order to evaluate various residual strength criteria proposed for the widespread fatigue damage problem. Although one objective of stiffeners is to arrest lead cracks before they can completely sever the panel, it is possible for the crack arrest capability to be defeated by small WFD that occurs on the opposite side of the stiffener. Figure 3 [7] summarize tests with stiffened 2024-T3 aluminum panels, and confirms that the residual strength of stiffened panels with relatively large lead cracks (4.5 – 6.0 inch long) can be significantly reduced when small WFD cracks (0.05 ≤ average length ≤ 0.15 inch) exist on the opposite side of the stiffener.
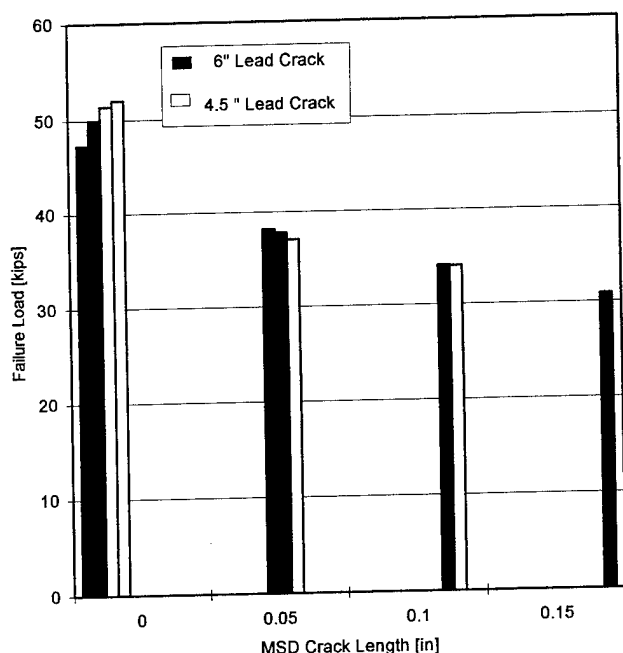
Figure 3   Reduction in lead crack residual strength caused by multiple site damage (MSD) in 15 inch wide stiffened 2024-T3 aluminum panels [7].

LAP JOINTS

The preceding section summarized results for widespread fatigue damage that occurs along a row of open holes in stiffened or unstiffened panels. A more practical problem, however, deals with lap joint structure where the holes are filled with fasteners that transfer load from one member to another. Predicting failure in this case involves complicated analysis of load transfer through the fasteners, residual stresses from rivet installation, interface contact between joined surfaces, and bending effects. This section summarizes analysis procedures developed to evaluate widespread fatigue cracking in lap joints. The approach includes formulating

a load transfer model that considers WFD in the lap joint, determination of stresses associated with rivet installation and bending, and computation of stress intensity factors. Residual strength and fatigue crack growth lives are then computed for the joint.

LOAD TRANSFER ANALYSIS FOR RIVETED JOINT

The analysis begins with an elastic load transfer solution proposed by Barrois [14] to determine the force applied by individual fasteners in a mechanical joint. There are two assumptions in this model. First, beam theory determines the deformation of a rivet lying on elastic foundation, and second, there is no interference or clearance between the rivet and the foundation contact surfaces. Two boundary conditions are used to account for two extremely different deflections on the contact surface between the rivet head and panels: (1) assume a perfectly clamped rivet head, or (2) assume a pinned head that allows rotations at this location. These two boundary conditions induce different fastener flexibilities and result in different load transfer ratios. Several empirical load transfer solutions [15] for an uncracked lap joint are compared with the Barrios model in Fig. 4 This particular case is for a three row, single lap join with equal sheet thicknesses, and a rivet/panel stiffness ratio of 3. Note that all of the empirical load transfe ratios for this case are encompassed by the two extreme boundary conditions considered in the Barrois mode Load transfer experiments conducted with "neat fit" pin indicate that the Barrois model gives good results for the pinned end condition [16].
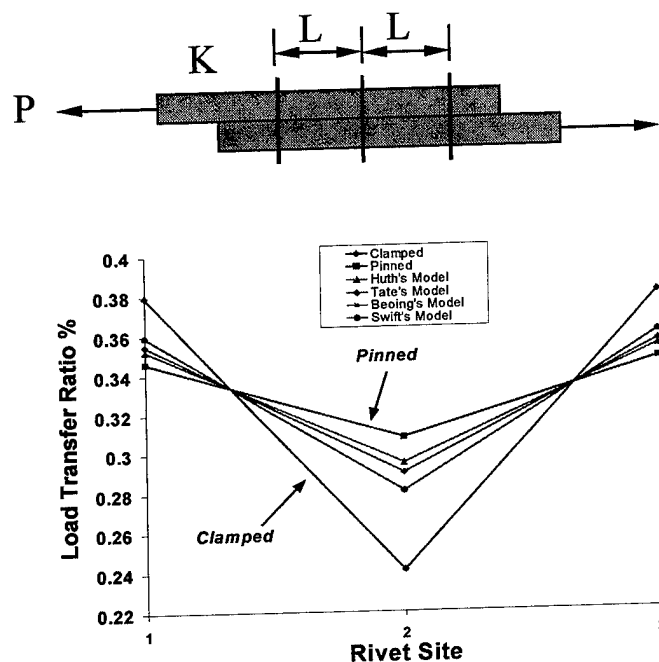

Figure 4   Comparison of load transfer ratio determine by Barrois model with other empirical solutio for a three-row lap joint.

The benefit of the Barrois analysis is that it provides an analytical method to extend load transfer calculations to more complicated joints configurations and rivet heads (including countersinks). The approach is however, based on an analytic solution for a beam on an elastic foundation, and does not allow interference or clearance between the rivet and the elastic foundation contact surfaces. Actual rivet installation involves interference fit and plastic deformation that invalidates the elastic assumptions. In order to apply the Barrois analysis to the interference fit countersunk fasteners employed in the experimental program, the joint flexibility was determined experimentally with the setup described in References 12 and 16.

Another load transfer issue occurs when the cracks grow and increase the structural compliance, leading to additional displacement in the joint. This effect can cause load shedding from cracked to uncracked rows of rivets, and change the load transfer mechanism. In order to analyze this load shedding effect, the additional compliance associated with crack growth was determined, and incorporated into the load transfer model. Reference 16 presents example results for the change in load transfer associated with crack growth, and provides more details about the calculations.

STRESS INTENSITY FACTORS

In order to predict crack growth, one must have stress intensity factor (K) solutions that account for load transfer, interference fit, and secondary bending effects in the joint. The current analysis employs load transfer K solutions given in Reference 17, where the stress intensity factor is broken into components caused by the by-pass loading and the load transferred through the fastener (pin-loading). The load transfer model described above is used to obtain the appropriate by-pass and pin-loading for the joint.

Interference fit fasteners are often used to increase fatigue life since hole expansion produces residual stresses that delay fatigue crack formation and growth. Interference fit can also affect the load transfer in a riveted joint. Two interference fit models proposed by Rich and Impellizzeri [18] and by Hsu and Forman [19] are used for this study. The major difference between the Rich-Impellizzeri and the Hsu-Forman stress analyses is that the former assumes elastic-perfectly plastic material behavior, while the latter applies work hardening plasticity. Comparison of residual stresses predicted by these two models for various interference levels are given in Reference 16.

Residual stresses created by interference fit can reduce the effective hoop stress at the fastener hole and cause significant improvement in fatigue life. Cathey and Grandt [20] showed that stress intensity factors obtained by a relatively simple weight function method could be used to obtain reasonable fatigue crack growth lives for open, cold-worked holes in 7075-T6 aluminum specimens. The stress intensity factor due to the

residual stresses can be calculated from a tabulated weight function [21] if the uncracked stress distribution is known. The total stress intensity factor K_{tot} associated with load transfer and the interference-fit plasticity analysis of the riveted structure is given by superposition as

$$K_{tot} = K_{by-pass\,loading} + K_{pin-loading} \pm K_R \quad (1)$$

Here the $K_{by-pass}$ loading and the $K_{pin-loading}$ terms are the stress intensity factors from Reference 17 for the by-pass and pin-loading cases, and employ the load transfer analysis described previously. The +/- K_R term in Equation 1 adds or subtracts the interference fit K depending on whether the residual stress field is tension or compression. Thus, when the interference fit results in compressive residual stresses, the K due to remote loading is reduced, and crack formation and propagation are delayed. Example calculations for these stress intensity factors are reported in Reference 16.

An experimental program was conducted to determine the appropriate hole expansion for the installed rivets employed for the present work [12, 16]. Once the interference fit level is established, the plastic deformation and the compressive stress around the rivet hole can be estimated, and stress intensity factors computed by Equation 1. Since inconsistent rivet installation will affect the level of interference fit and corresponding stress field around the rivet holes, a controlled squeeze force riveting procedure was employed here to ensure consistent quality of the riveted specimens [12, 16]. This riveting procedure involved squeezing the rivets on a test machine to a preset installation force.

Secondary bending considerations also play a role for K calculations in single-lap joint specimens. A bending stress calculation proposed by Schijve [22] was used estimate the bending stresses, and a corresponding adjustment was made to the stress intensity factor solution in order to account for secondary bending [16]. The total SIF for a single lap joint specimen is:

$$K_{tot} = K_{by-pass\,loading} + K_{pin-loading} \pm K_R + K_{bend} \quad (2)$$

FAILURE CRITERIA

While several failure criteria have been proposed for the WFD problem, this research employs the net section yield and Swift's ligament yield criterion [2]. The net section yield criterion states that failure will occur when the net section stress equals or exceeds the tensile yield stress. The Swift ligament yield failure criterion states that the failure occurs when the plastic zones of two approaching crack tips "touch" each other as shown schematically in Figure 5. Although this failure criterion may not be valid for all multiple crack configurations, it is relatively easy to apply for engineering applications, and

has been shown to give reasonable results for the types of problems considered here [4-5, 7].
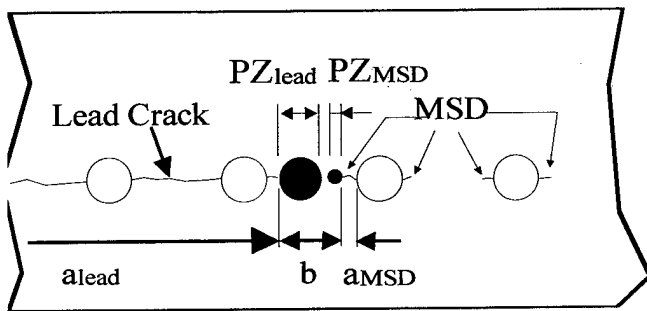

Figure 5 *Schematic representation of the Swift [2] ligament yield failure criterion for widespread fatigue damage.*

EXPERIMENTAL EVALUATION OF ANALYSIS

This section summarizes a test program to evaluate the ability to predict the growth and coalescence of WFD cracks in lap joints.

FATIGUE TESTS

Five constant amplitude fatigue tests were conducted with the single lap specimen shown in Figure 6. All specimens were made from 2.29 mm (0.09 in) thick 2024-T3 bare aluminum loaded in the T-L rolling direction. Specimen preparation consisted of two steps. First, 812 mm long by 406 mm (32 x 16 in) wide panels were constructed with a "dogbone" test section that was 228.6 mm (9in) wide. A single row of eight 3.97 mm (5/32 in) diameter holes were then drilled in these specimens, and a jeweler's saw (blade thickness = 0.33 mm = 0.013 in) was used to cut a pair of small notches on the opposite sides of each hole (average length = 0.381 mm = 0.015 in). The two outside holes were not notched, however, since it is known that more load is taken by rivets located near free edges than by other rivets in wide lap joint specimens [23-24], and it was desired to prevent premature failure at those locations. The panels were then precracked in fatigue following a load shedding procedure that ended when K for the longest crack tip reached 6.6 $Mpa\sqrt{m}$ (6 ksi$\sqrt{in}$). The lengths of these cracks ranged from 4.57 mm (0.18 in) to zero (including the sawcut).

Next, each panel was cut in half, leaving one member of each pair with the precracked row of holes. These two halves were then drilled to the desired 8 x 3 rivet hole pattern, reamed to a final hole diameter of 4.85 mm (0.191 in), and countersunk on one side. This final drill and ream removed the initial saw cuts, leaving only small fatigue cracks in one panel at the initial row of holes. Finally, 4.76 mm (0.187 in) diameter countersunk rivets (MS20426-AD-6-6) were installed with a fixed

15.58 KN (3.5 kip) squeeze force. The average radial pre-cracks were typically on the order of 0.34 mm to 1.12 mm (0.0134 – 0.044 in) long, and emanated from both sides of the countersunk rivet holes. The average pre-crack lengths and the applied fatigue loads are summarized in Table 1 for the five experiments reported here. (Reference 12 gives more details of the experimental program.)
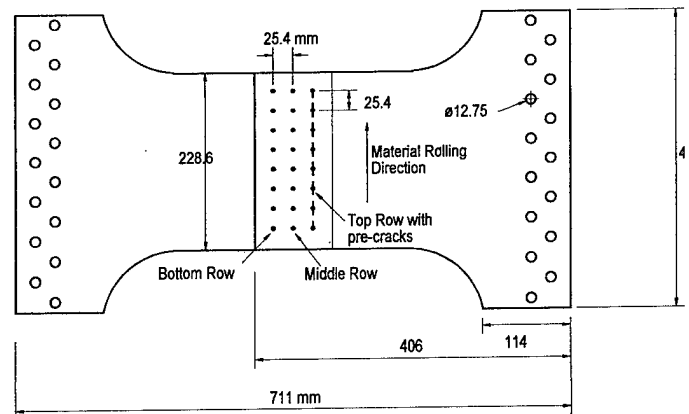

Figure 6 *Lap joint test specimen.*

COMPARISON OF ANALYSIS AND EXPERIMENT

Growth of all cracks resulting from the R = 0.05 constant amplitude fatigue loading were measured with a travelling microscope and recorded as a function of elapsed cycles. Fatigue crack growth was then computed by the fracture mechanics based algorithm (modified in the present case to include the stress intensity factor and load transfer solutions developed for the lap joint configuration). Figure 7 compares measured and predicted crack tip position versus elapsed cycles for specimen SLap #4, while similar plots for the other tests are given in Reference 16. Since the current life prediction model does not consider three-dimensional effects associated with part-through cracks or the countersink, the average hole diameter and through-crack length were used as input for the life prediction program.

Some of the small precracks were hidden under the rivet heads or contained in the plastic zone around the installed rivet and did not immediately grow, resulting in a period of "crack retardation." (These measured delay cycles are listed in Table 1.) If the crack lengths are long enough, or the applied stress is large enough, however, the cracks will propagate immediately upon applied cyclic loading. Specimen SLap#2, for example, contained relatively short precracks, but was tested to the largest applied cyclic stress (96.5 Mpa = 14 ksi), and the cracks began growing immediately, without a delay period. The predicted and measured lives agreed within 14 % for this case. In the other tests, it was necessary to start computations after the cracks were observed to begin growing in the fatigue test in order to obtain a reasonable fatigue life.

SLap#4

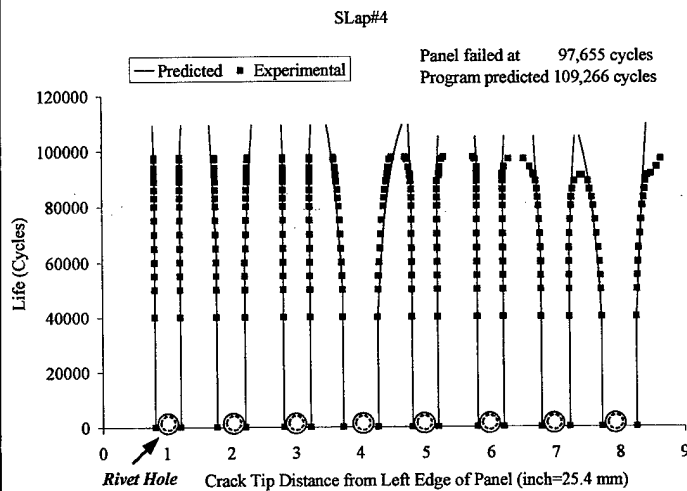Panel failed at 97,655 cycles
Program predicted 109,266 cycles

Figure 7 Comparison of experimental and predicted
fatigue crack propagation for a single lap joint
specimen SLap #4 (3 rows of 8 rivets) tested
at a cyclic stress level of 55.1Mpa (8 Ksi) (the
size of rivet hole is not to scale).

Figure 8 summarizes the measured and predicted
fatigue crack growth lives for all five lap joint tests. The
average difference between the measured and predicted
lives for these 5 fatigue tests is 15%, varying between
8.0 % and 27.4% Since these experimental data
indicate that it is possible to obtain excellent life
predictions once all WFD cracks have started to grow,
one may conclude that the load transfer analysis and
stress intensity factor solutions developed for the lap
joint problem are reasonably accurate. Reference 16
describes additional research to handle the situation
when the initial crack sizes are hidden by the rivet
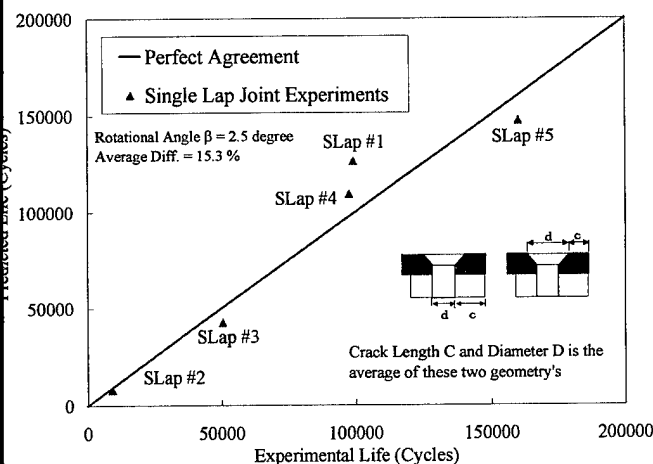heads, or are retarded by the rivet installation stresses.

Figure 8 Summary of predicted and measured fatigue
crack growth lives for lap joint fatigue tests.

MONTE CARLO SIMULATIONS

Although the basic WFD analysis is deterministic in
nature, fatigue usually demonstrates significant
variability. This "scatter" is due to many sources,
including specimen quality, material variability, applied
loading, etc. Thus, Monte Carlo calculations are used
here to determine the variation in life (or probability of
fracture) resulting from uncertainty in input parameters
such as initial crack size, material properties, or fastener
fit. Reference 25 describes prior Monte Carlo
simulations for a wide plate with open holes that contain
WFD, and incorporated statistical variations in the initial
crack size and in fatigue crack growth properties to
obtain distributions in fatigue life. This section describes
a more recent application [13, 16] of this probabilistic
approach to analyze multiple site damage in a lap joint.

These calculations considered a 31 inch wide single lap
joint with three rows of thirty 5/32 inch diameter rivets.
The specimen was subjected to a constant amplitude (R
= 0.05) peak cyclic stress of 76 Mpa (11 ksi). The
statistical input variables include initial flaw size
distributions and variability in interference fit associated
with rivet installation. One row of fasteners was assumed
to contain WFD cracks randomly selected from an
equivalent initial flaw size (EIFS) distribution obtained
from a recent tear-down of retired B-707 aircraft
conducted for the USAF E-8C Joint STARS program
[26]. The variation in fastener interference (and its
subsequent effect on rivet stress fields) was based on
measurements from specimens that contained large
numbers of rivets installed with a conventional rivet gun
[16]. Monte Carlo simulations (1000 runs) were
performed to determine the influence of both rivet
installation (i.e. fastener interference) and initial WFD on
fatigue life.

Figures 9 - 10 show the variability in residual strength
degradation as a function of elapsed cycles as the WFD
cracks grow (fracture occurs when the residual strength
drops to the 11 ksi peak cyclic stress). The mean, 95th
and 5th percentile variations in residual strength are
shown in Figures 9 – 10. Figure 9 is for a case when the
rivet interference was assumed to be constant, and the
initial WFD at the top row of rivet holes were randomly
selected for the B-707 EIFS distribution (see References
13 and 16 for additional details of the EIFS distribution
and the rivet interference measurements). Figure 10
presents a case where both the initial WFD cracks and
the fastener interference level were allowed to vary
randomly. Note that these calculations indicate
significant variation in the effect of WFD on residual
strength. (Several other cases are discussed in
References 13 and 16.)

Although the above examples use equivalent initial flaw
size distributions obtained from tear-down inspections,
the EIFS data could also be based on models that
estimate WFD caused by material inhomogeneities [27],
pre-corroded material state [10], fretting [9-10], or on the
results of nondestructive inspection capability (i.e.

probability of detection curves). One of the main goals for such probabilistic studies would be to determine the most critical parameters and/or those that induce the most variability in life, and, thus, help fleet managers focus on the most critical aspects of the WFD problem.
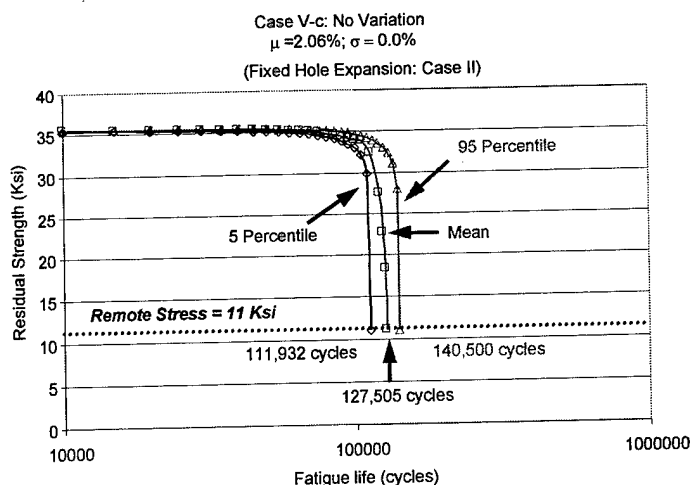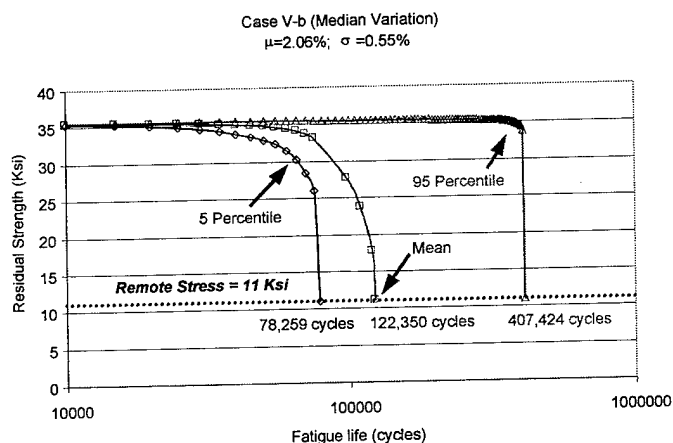
Case V-c: No Variation
μ =2.06%; σ = 0.0%
(Fixed Hole Expansion: Case II)

Figure 9 Monte Carlo simulations for the distribution in residual strength of a riveted lap joint. The hole expansion level is fixed at 2.06% and randomly selected initial WFD cracks are located along the top rivet row.

Case V-b (Median Variation)
μ=2.06%; σ =0.55%

Figure 10 Monte Carlo simulations for the distribution in residual strength of a riveted lap joint. The hole expansion level and the initial WFD cracks are randomly selected from experimentally measured statistical distributions.

CONCLUSION

This paper summarizes fracture mechanics analyses developed to analyze the significance of widespread fatigue damage in lap joints. The numerical solutions involve calculation of load transfer and stress intensity factors for cracks that develop around holes that contain interference fit rivets. Fatigue crack growth and coalescence leading to final fracture is then computed. Comparision between numerical and experimental results suggests that the analysis procedures may be expected to yield reasonable fatigue lives. Having established confidence in the deterministic analsysis, Monte Carlo simulations were then performed to explore the signficance of variablity in intitial crack size and fastener interference. These preliminary results indicate that rivet quality, as reflected by the variation in interference fit, has a significant influcence of fatigue life.

ACKNOWLEDGMENTS

CONTACT

A. F. Grandt, Jr. is a Professor and H. L. Wang a recent Ph. D. graduate from the Purdue University School of Aeronautics and Astronautics. A. F. Grandt, Jr. may be reached at the following address: 1282 Grissom Hall, Purdue University, W. Lafayette, IN 47907-1282, USA. His email address is: grandt@ecn.purdue.edu

REFERENCES

1. *Aging of U.S. Air Force Aircraft*, Final Report, Committee on Aging of U.S. Air Force Aircraft, National Materials Advisory Board, National Research Council, Publication NMAB-488-2, National Academy Press, 1997.
2. T. Swift, "Widespread Fatigue Damage Monitoring Issues and Concerns," The 5th International Conference of Structural Airworthiness of New and Aging Aircraft, Hamburg, Germany, June 16-18, 1993.
3. E. J. Moukawsher, A. F. Grandt, Jr. and M. A. Neuss, "Fatigue Life of Panels with Multiple Site Damage, *Journal of Aircraft*, Vol. 33, No. 5, September-October 1996, pp 1003-1013.
4. E. J. Moukawsher, M. Heinimann, and A. F. Grandt, Jr "Residual Strength of Panels with Multiple Site Damage, *Journal of Aircraft*, Vol. 33, No. 5, September-October 1996, pp 1014-1021.
5. M. C. Cherry, S. Mall, and M. B. Heinimann, and A. F Grandt, Jr., "Residual Strength of Unstiffened Aluminum Panels with Multiple Site Damage," *Engineering Fracture Mechanics*, Vol. 57, No. 6, 1997, pp. 701-713.
6. H. L. Wang, K. Buhler, and A. F. Grandt, Jr., "Evaluation of Multiple Site Damage in Lap Joint Specimens," Proc. of 1995 USAF Structural Integrity Program Conference, Sa

Antonio, Texas, November 28-30, 1995, Technical Report WL-TR-96-4093, August 1996, Materials Directorate, Wright Laboratory, WPAFB OH, edited by G. K. Waggoner, J. W. Lincoln, and J. L. Rudd , Vol. I, pp 21-38.

7. M. B. Heinimann and A. F. Grandt, Jr., Analysis of Stiffened Panels with Multiple Site Damage," Proc. of 1996 USAF Structural Integrity Program Conference, WL-TR-97-4055, Wright Laboratory, WPAFB, OH, June 1997, pp 655-682.

8. M. B. Heinimann and A. F. Grandt, Jr., "Fatigue Analysis of Stiffened Panels with Multiple Site Damage," First Joint DoD/FAA/NASA Conference on Aging Aircraft, Ogden, Utah, 8-10 July 1997, to appear in Conference Proceedings (43 pages).

9. T. N. Farris, A. F. Grandt, Jr., G. Harish, P. McVeigh, M. Szolwinski, and H. L. Wang, "Fretting Fatigue Crack Nucleation and Propagation in Structural Joints," Proceedings, Air Force 4th Aging Aircraft Conference, USAF Academy, Colorado, July 9-11, 1996, pp 141-165.

10. A. F. Grandt, Jr., T. N. Farris and B. M. Hillberry, "Analysis of the Formation and Propagation of Widespread Fatigue Damage," ICAF 97, Fatigue in New and Aging Aircraft, Vol. I, Proceedings of the 19th Symposium of the International Committee on Aeronautical Fatigue, Edinburgh, 18 - 20 June 1997, pages 115-133.

11. A. F. Grandt, Jr., D. Sexton, P. Golden, G. H. Bray, R. J. Bucci, and M. Kulak, "A Comparison of 2024-T3 and 2524-T3 Aluminum Alloys Under Widespread Damage Scenarios," ICAF 97, Fatigue in New and Aging Aircraft, Vol. II, Proceedings of the 19th Symposium of the International Committee on Aeronautical Fatigue, Edinburgh, 18 - 20 June 1997, pages 659-669.

12. H. L. Wang and A. F. Grandt, Jr., "Fatigue Analysis of Multiple Site Damage in Lap Joint Specimens," Fatigue and Fracture Mechanics 30th Volume, ASTM STP 1360 (in press).

13. H. L. Wang and A. F. Grandt, Jr., "Monte Carlo Analysis of Widespread Fatigue Damage in Lap Joints," Proc. 1998 USAF Structural Integrity Program Conference, San Antonio, TX, December 1998 (in press).

14. W. Barrois, "Stress and Displacements Due to Load Transfer by Fasteners in Structural Assemblies," Engineering Fracture Mechanics, 1978, Vol. 10, pp.115-176.

15. H. Huth, "Influence of Fastener Flexibility on the Prediction of Load Transfer and Fatigue Life for Multiple-Row Joints," Fatigue in Mechanically Fastened Composite and Metallic Joints, ASTM STP 927, ASTM, Philadelphia, 1986, pp.221-250.

16. H. L. Wang, "Evaluation of Multiple Site Damage in Lap Joint Specimens," Ph.D. Thesis, School of Aeronautics and Astronautics, Purdue University, West Lafayette, IN, December, 1998.

17. Fatigue Crack Growth Computer Program "NASA/FLAGRO" Version 2.0, Appendix C, December 1992.

18. D. L. Rich and L. F. Impellizzeri, " Fatigue Analysis of Cold-Worked and Interference Fit Fastener Holes", Cyclic Stress-Strain and Plastic Deformation Aspects of Fatigue Crack Growth, ASTM STP 637, ASTM, Philadelphia, 1977, pp.153-175.

19. Y. C. Hsu and R. G. Forman, "Elastic-Plastic Analysis of an Infinite Sheet Having a Circular Hole Under Pressure," Journal of Applied Mechanics, June 1975, pp.347-352.

20. W. H. Cathey and A. F. Grandt, Jr., "Fracture Mechanics Consideration of Residual Stresses Introduced by Coldworking Fastener Holes," Journal of Engineering Materials and Technology, January 1980, Vol. 102, pp.85-91.

21. A. F. Grandt, Jr., and T. E. Kullgren, "Tabulated Stress Intensity Factor Solutions for Flawed Fastener Holes," Engineering Fracture Mechanics Vol. 18, No. 2, 1983, pp. 435-451.

22. J. Schijve, "Some Elementary Calculations on Secondary Bending in Simple Lap Joints," NLR TR 72036 U, 1972.

23. R. P. G. Mueller, "An Experimental and Analytical Investigation on the Fatigue Behavior of Fuselage Riveted Lap Joints – The Significance of the Rivet Squeeze Force, and a Comparison of 2024-T3 and Glare 3," Ph. D. Dissertation, Delft University of Technology, Facultyof Aerospace Engineering Structures and Materials laboratory, The Netherlands, 1995.

24. J. C. Newman, Jr., C. E. Harris, M. A. James, and K. N. Shivakumar, "Fatigue-Life Prediction of Riveted Lap-Splice Joints Using Small-Crack Theory," ICAF 97, Fatigue in New and Ageing Aircraft, Volume I, Proceedings of the 19th Symposium of the International Committee on Aeronautical Fatigue, Edinburgh, 18 - 20 June 1997, pages 523 – 552.

25. S. M. Rohrbaugh, B. M. Hillberry, and B. P. McCabe, and A. F. Grandt, Jr., "A Probabilistic Fatigue Analysis of Multiple Site Damage," Proceedings of FAA/NASA International Symposium on Advanced Structural Integrity Methods for Airframe Durability and Damage Tolerance, Hampton, VA, May 4-6, 1994, NASA Conference Publication 3274, Part 2, C.F. Harris, Ed., pp. 635-652, September 1994.

26. J. Luzar and A. Hug, "Lower Wing Disassembly and Inspection Results of Two High Time USAF B707 Aircraft," presented at the 1996 USAF Structural Integrity Program Conference, San Antonio, Texas, 3-5 December 1996.

27. A. F. Grandt, Jr. and A. J. Hinkle, "Predicting the Influence of Initial Material Quality on Fatigue Life," Proceedings of 17th International Committee on Aeronautical Fatigue Symposium on Durability and Structural Reliability of Airframes," ICAF 93, Stockholm, Sweden, June 9-11, 1993.

Table 1 Summary of test specimen initial conditions and failure data.

Test Specimen ID	Avg. Crack Length (mm)	Max Applied Stress		Total Life / Prediction Life (Cycles)	Delayed Cycles	Diff.%
		MPa	Ksi			
Slap #1	0.98	55.1	8	99,143/ 126,281	56,000	27.4 %
Slap #2	1.00	96.5	14	9,028/ 7,801	0	13.6 %
Slap #3	0.34	68.9	10	50,489/ 42,629	10,000	15.6 %
Slap #4	1.12	55.1	8	97,655/ 109,266	40,000	11.9 %
Slap #5	0.82	55.1	8	160,024/ 147,350	70,000	8.0 %

Fracture Mechanics Based Approach for Quantifying Corrosion Damage

Jason N. Scheuring and Alten F. Grandt
Purdue University

ABSTRACT

The objective of this project is to quantify structural degradation due to corrosion through a fracture mechanics based approach. The metric parameters employed are Equivalent Initial Flaw Size and general material loss. Another objective is to correlate a measurable property to the amount of structural durability damage from corrosion, ideally through current NDE technology, with eddy-current as the primary choice. The approach is comprised by the following areas: corroding aluminum alloys, evaluation of the corrosion through techniques such as surface roughness and eddy current, cyclic testing, calculation of corrosion metric, and, correlation between corrosion metric and physically measurable properties.

INTRODUCTION

In today's era of fiscal restraint, procurement of new aircraft is a less viable option than in the past. This financial limitation affects the military, airframers, and the airline industries. Current commercial and military aircraft, especially large transports, are being asked to fly well beyond their initial estimated design lifetimes.[1-6] This phenomenon has been recognized since the late 1980's, but brought to the forefront by the Aloha accident in 1988.[3] An example of this aging aircraft phenomenon is the military tanker C/KC-135. The C/KC-135 fleet, which is on average at least 35 years old, is expected to fly until the year 2040, well beyond their initial design lifetimes.[7]

In response to this ever-increasing problem, both the military and industry have carried out numerous studies and evaluations of problems that will present themselves due to the continued operation of aging aircraft. From these multitudes of studies, it can be concluded that two major problems need to be investigated if today's aircraft are to continue to operate safely; namely multiple site damage and corrosion. In the commercial aircraft genre, multiple site damage seems to be the limiting factor, as aircraft are now asked to accumulate excessive flight cycles.[3] Since some military aircraft are now expected to have lifetime on the order of 70-80 years, annual flight hour restrictions are imposed. Corrosion, however, accrues with calendar time regardless of the number of flight cycles.[5] The nature of the corrosion problem is even more pronounced when considering that the high strength aluminum alloys of the 1950's and 1960's, chosen primarily for their strength, are not particularly corrosion resistant. The crux of this paper will focus on some of the corrosion related problems.

While corrosion has seldom been the cause of major catastrophes, its detrimental nature on aircraft safety cannot be denied.[5] In general, it is believed that corrosion is detrimental to the life of transport aircraft. The durability problems that corrosion creates are numerous. Examples are: an increase in stress due to uniform thickness loss, pits acting as initiation sites, and an increase in bending stress from pillowing in lap joints.[8] Additionally, there have been studies that show corrosion can have adverse effects on basic material such as fatigue crack growth rate and stress-life properties when compared to virgin material properties.[9,10] Another problem in dealing with corrosion is the exhaustive number of combinations of material and environment.[11]

Detection of corrosion is the first step in treatment of the degradation problem. One of the most economical ways to determine if a structure has corrosion present is to utilize some form of non-destructive evaluation (NDE). Some of the more common, accepted NDE tools are ultrasound, eddy current, and D-Sight. This paper will focus on the use of eddy current as the primary NDE tool.

The quantification of the corrosion damage, however, is very subjective in nature. In this industry, it behooves one to err on the side of conservatism when dealing with a corroded component or airframe. This conservatism, however, can lead to an unnecessary waste of materials, structures, labor, and financial resources. This leads one to believe that a more substantial corrosion quantification method is necessary for continued operation of aging aircraft in a safe, and economic,

manner. It would be desirable that this method be easily implemented in actual applications, not merely a laboratory exercise.

One example of how material has been characterized in the past is with the utilization of the Equivalent Initial Flaw Size (EIFS). In the 1980s, utilization of the EIFS was performed at ALCOA to compare the quality of some of their aluminum alloys.[12] In this concept, a specimen is tested to failure, and an EIFS is backcalculated as the initial crack size that would have led to failure in the given test period. A higher quality material would be expected to have a longer life, and, thus a smaller EIFS than that of a lower quality alloy. Yang and Manning have shown that it is possible to translate EIFS from one geometry to another, useful for translating results of coupon tests to more complex geometries.[13] These concepts show promise as a useful tools in determining material quality, even for specimens subjected to corrosion damage.

OBJECTIVES

The principal objective of this project is to ascertain the severity of a corroded structure quantitatively by employing a fracture mechanics based approach. The methodology employs the use of bulk material properties, Equivalent Initial Flaw Size and a general load loss carrying capability thru material loss, to determine the state of a material subjected to a degrading processes. The motivation is to remove the subjectivity of the owner/operator in measuring the structural degradation of a structure subjected to a detrimental corrosion process.

There are several perceived needs for this project. One is in quantification of corroded structures found during normal maintenance operations. In this scenario, quantification of the severity of the structural damage can be assessed in a more deterministic manner. Another need deals with the necessity of cataloging degraded material into a database of materials and components that have been removed from service. Utilization of such a database could possibly help in the maintenance of a fleet in a more economical and safe fashion.

APPROACH

There are several steps that will have to be performed throughout the project. These steps can be broken down into several major components: corrosion, quantification, and correlation. These will now be explained in further detail.

The first step in the approach is to corrode the material. The material can be corroded either through natural or artificial means, the only requirement being that there is a reduction in the durability of the structure. Since data from actual aircraft components is limited, artificially corroded specimens will be utilized as a primary source of data. A variety of artificial corrosion processes will be utilized. For the most part, the corrosion will be in the form of pitting, intergranular, or exfoliation corrosion. These types of corrosion run from localized damage, pitting, to general uniform damage, exfoliation.

The damage state properties that will characterize the structural degradation are local stress concentrators and general load loss capability. To quantify the local stress concentrators associated with the corroded components, EIFS will be computed and used in a variety of life predictions. General load loss carrying capability will be modeled primarily through uniform thickness loss of material due to corrosive processes. It is believed that these parameters, EIFS and thickness loss, are able to characterize the majority of corrosion damage for the numerous material/environment combinations. It is also believed that through the use of these parameters, structural durability will be able to be determined for a component level structures from coupon level tests. Figure 1 illustrates some typical structural levels that can be used in these types of material and structural degradation studies; smooth coupon, notched coupon, component, and complete structure.

The final aspect of the approach is the correlation of the structural degradation to a measurable quantity that is not inherently subjective, such as a visual inspection. Both destructive and non-destructive inspection techniques will be assessed. The techniques employed are those that are available with current technology or are new applications of current methods. Examples of current technologies include visual inspection, eddy-current, surface roughness measurements, and electrochemical measurements.

SPECIMEN DESIGN AND TESTING

The aluminum alloys that are prevalent in aging aircraft were chosen primarily for their static and fatigue strength but not, however, for their corrosion resistance. The work performed to date has been with 0.088-inch nominal thickness 2024-T3 bare aluminum alloy. It is desired to also carry out additional testing and evaluation utilizing a 7xxx series alloy, most likely 7075-T6 or 7178-T6 due to their prevalent nature older large transport aircraft.

There are several geometries that are employed throughout the project. The three main geometries are illustrated schematically in Figure 1. Depicted schematically are a smooth unnotched specimen (SUN), notched specimen with a simple hole in the center (NN), a multiple site damage specimen (MSD), and a structural level aircraft. The MSD geometry has yet to be finalized, but will be similar to other MSD work in this area. The gage surface area for the SUN specimen is nominally 0.5 inches by 2.0 inches while the gage area for the NN specimen is approximately 1.0 inch by 2.0 inches. The purpose behind using a variety of specimens will be explained shortly. To date numerous specimens of the first two varieties have been utilized. In a previous study, 28 SUN specimens were tested in a variety of corrosion states; no corrosion, exfoliation,

pitting, and a variety of surface preparations. Specimens corroded to date by this author are listed in Table 1. To date, 199 specimens have been corroded while 124 have been tested to failure.

Specimen preparation plays an important role in the corroding processes described below. It is desired that the preparation process be as non-varying as possible from specimen to specimen and from geometry to geometry. Or, if not repeatable, at least distinguishable via a measurement such as surface roughness. After the specimens have been machined, they are wet sanded with 600-grit sandpaper on all surfaces in the gage area. The specimens are then coated outside the gage area with either a chemical resistant paint or low melting point plastic in order to prevent material degradation in the grip area, thus preventing unwanted grip failure.

The specimens were cyclically tested to failure after being corroded and characterized with various techniques, described below. One of the main concerns in testing was the amount of bending that is present in the system. To minimize the bending affects that arise from the load train and the specimen itself, Wood's metal grips were employed for each fatigue test.

CORROSION

Naturally occurring corrosion from aged aircraft would be the most acceptable form of material to exploit for the test program, as it would be indicative of the actual corrosion levels present on today's aging aircraft. However, a limited supply of usable, naturally corroded material is available for evaluation. In addition, naturally corroded material is highly variable, providing little control for the development of new analysis tools or methodologies. Hence, artificially corroded specimens are the prime source of degraded material.

Several forms of artificial corrosion are employed in this study. To accrue localized corrosion damage, ASTM G44 Alternate Immersion testing was utilized. The current system is highlighted by a ferris wheel that rotates 60 degrees every 10 minutes.[14] By immersing the specimens in a standard 3.5% sodium chloride solution for 10 minutes out of each hour, pits initiate, grow, and coalesce on the exposed surface of the specimens. To date, the experimental corrosion chamber has been utilized for runs lasting from 6 days to 2 months in duration, with longer times resulting in increased material degradation. Examples of this process are depicted in Figure 2; note that the specimens have been chemically cleaned of their corrosion products via ASTM G1 standard cleaning procedures. Shown in the figure are specimens that have had 6, 21, and 42 days exposure time in the corrosion chamber.

The methods that will be employed for uniform material loss will be one of two methods. The first is the ASTM G34 EXCO test.[15] In the EXCO test, the specimen is left submerged in a standard solution on the order of 4 to 96 hours. The resulting corrosion is primarily intergranular and/or exfoliation-like in nature. The second procedure that is employed frequently for developing uniform corrosion is ASTM B236 CASS salt fog spray corrosion process.[10] This process has been utilized in several corrosion programs in industry. [10] It is thought that 24 hours of exposure to this salt fog spray simulates one year of naturally occurring coastal corrosion.

CORROSION METRICS

The goal of this portion of the project is to develop a metric that will allow one to ascertain the status of material that has been degraded by corrosion. Some desired characteristics of this metric would be that it is independent of stress loading, stress ratio, and stress concentration factor. [16] Thus, one would prefer that the results of the metric are not completely specific for a given structure/loading combination, i.e. results should be easily transferable from geometry to geometry. It is also desirable that the metric provide results that are consistent with actual observations from corroded aircraft structures. The combination of parameters that are employed as a corrosion quality metric in this study are the Equivalent Initial Flaw Size and general thickness loss combination.

Equivalent Initial Flaw Sizes (EIFS) can be calculated for any specimen that has been tested to a given number of cycles if the final crack length is known. Thus, one would expect that a specimen that has been damaged, either physically or chemically, would have a larger EIFS than an undamaged specimen. Similarly, one would expect that different levels of degradation would lead to different EIFS's for comparable geometries and stress histories. One of the objectives of the EIFS calculations is to be able to perform coupon level tests that predict the performance of more complex structures.

For the given specimen geometries in Table 1, there are a variety of flaw geometries that can be utilized. For the SUN specimen, either a corner crack, a surface crack, or a multi-crack combination of the previous are used. For the notched specimen, surface or corner cracks are employed, either symmetrical or unsymmetrical cases. For an MSD geometry, either a thru crack, corner crack, or a surface crack along the bore of the hole are employed. An example of EIFS calculations is depicted in Figure 3. In this case, the experimental failure life was used to calculate the EIFS. The EIFS geometry in this case is a corner crack. Note that there are 3 levels of corrosion and 3 remote loadings present for the 108 SUN specimens. As can be seen from the figure, there are distinct differences for the various corrosion exposure times, with longer exposure times giving rise to larger EIFS. The data is also presented in Figure 4 in histogram form where the EIFS parameter "a", initial crack length, is presented as for the three pitting corrosion exposure times, 6, 21, and 42 days. Similar plots have been obtained for surface crack and embedded crack geometries.

In a similar vein as the EIFS concept is the concept of stochastic fatigue crack growth rate. It has been brought forward by Manning and Yang, that fatigue crack growth may be variable in nature rather than completely deterministic.[17] Consequently, one can also back-calculate an EIFS or EIFS distribution with the variable fatigue crack growth rate.

CORROSION CORRELATION

One of the goals of this project is to relate the corrosion metric to an easily accessible property. NDE techniques offer the most promise in this area due to their accepted nature in the aircraft industry. Forays were made using a variety of techniques. Visual inspection, with a digital application, was employed and showed some promise. A brief attempt was made to measure the corrosion rate using electrochemical means, but no discernable trends were observed in this study. Immersion ultrasound was employed to facilitate whole field measurements, but current equipment available did not have enough resolution in order to obtain working results.

Surface roughness measurements show some promise for use in this area, but primarily as a cataloging tool. Harmsworth [19] demonstrated that there is a relation between surface roughness and cycles to failure. The thrust of the work in this area seeks to employ surface roughness as a similar parameter, but also as an indicator of why specimens subjected to similar corrosion exposure times and stress loadings fail at different cycle counts. Eddy current was used as the main technique for the corrosion correlation method.

EDDY CURRENT

Eddy current is a proven NDE technology that is employed throughout the aircraft industry. It is adept at many NDE tasks. It can be utilized in flaw detection, thickness measurements, alloy sorting, and coating thickness measurements. The system employed in this study is a Nortec19e Single Frequency Eddy Current system from the Staveley Company.

Eddy current was utilized for two different purposes in this study. First and foremost was its ability to accurately measure thickness for aircraft quality aluminum alloys. The precision of the measurement is dependent on the probe used and the accuracy of the calibration. For this project, thickness was on the order of 0.088 inches; hence, it was desired to have an accuracy of ±0.001 inches or better. A calibration block with steps of approximately 0.0005 inches was made and then measured to the nearest ±0.0001 inches with a high precision micrometer. Thickness measurements were then performed on the pre-corrosion machined specimens, corroded specimens with corrosion products intact, and corroded specimens with the corrosion products removed. Figure 5 illustrates examples of the output taken in this process. Shown are a calibration block measurement, a thickness measurement from a corroded specimen with corrosion products intact, and the same specimen in an uncorroded portion of the sample. These measurements depict the general load loss carrying capability due to general material loss. Figure 6 compares the pre and post corroded specimen's thickness' for 40 notched specimens (NN) corroded for 7, 21, and 42 days, as measured by the eddy current method. Figure 7 illustrates similar results in terms of a stress increase due to a general reduction in cross sectional area for the different corrosion exposure times for all 75 NN specimens. As illustrated, for 7, 21, and 42 days of exposure there is an average increase in the remote stress of 0.93%, 1.53%, and 2.19%, respectively (corresponding to thickness losses of 0.95%, 1.49%, and 2.14% for these specimens).

The second rational for employing eddy current was its ability to measure lift-off. Lift-off is schematically illustrated in Figure 8. Lift-off is commonly used to measure paint or coating thickness. Lift-off is simply the distance between the probe and the desired material. For a perfectly flat surface, as the probe is brought into contact with the material, its lift-off measurement goes to zero. In general, unless determining a coating thickness, lift-off is often undesirable for most measurements. In this case, however, it provides useful information about the amount of damage present on a specimen's surface. Also illustrated in Figure 8 are the calibration setup and example of specimens with different surface conditions. For highly corroded materials, it is expected that lift-off will be larger for a variety of reasons. One is the increased surface roughness while another is the increase in the volume of corrosion products that arise from longer exposure times.[9] Lift-off measurements are made with and without the corrosion products on the specimens in the hopes that one, or both measurements, would provide a correlation to the amount of corrosion present. An example of how lift-off can be related to structural degradation is depicted in Figure 9. In this figure the average, and standard deviation, lift-off for SUN specimens, which have been corroded for 6, 21, and 42 days, are illustrated. In this set of measurements, the corrosion products have been removed, leaving only the degraded surface. Illustrated in Figure 10 is the same lift-off data as a function of cycles to failure, corrosion level, and remote stress level. As can be seen from the figure, the lift-off data for the 6, 21, and 42 day corrosion levels clearly illustrate an observable trend in which the lift-off for a specified exposure time are nearly constant.

Figure 11 illustrates the same EIFS as a function of lift-off for the SUN geometry as Figure 10. In this case, the corner crack geometry is used. As can be seen in the figure, the longer corrosion exposure times have larger EIFS and lift-off measurements, as one would expect. Note the increase in scatter for the longer exposure times.

Figure 12 is similar in nature to Figure 9, but in this case, the specimens have not been cleaned of their corrosion products. Note that the lift-off for specimens with corrosion products removed are an order of magnitude smaller than those with the corrosion products intact.

Shown Figure 12 are notched specimens with 7, 21, and 42 days of exposure to pitting corrosion. Again, there is a marked difference between the levels of corrosion exposure duration. The lift-off is again nearly constant for a given corrosion exposure time, and the longer corrosion exposure time gives rise to larger lift-off.

CONCLUSIONS

The principal goal of this project is to determine the severity of structural degradation when a component is subjected to corrosion quantitatively with a fracture mechanics based approach. The motivation for this project is to remove the subjectivity in interpreting the amount of damage a structure accumulates due to corrosion. There are two main perceived needs for this process. One is in quantification of corroded structures found during normal maintenance operations. In this scenario, assessment of the structural damage can be performed in a more deterministic manner. Another need deals with the necessity of cataloging degraded components in a database.
• 2024-T3 aluminum alloys have been corroded via ASTM G44, resulting in localized corrosion damage.
• EIFS, in conjunction with general load loss capability, seems to provide an acceptable corrosion metric for objectively quantifying corrosion degradation.
• EIFS have been utilized to compare specimens with different levels of corrosion while subjected to the same stress loads.
• Existing eddy current technology provides a technique for correlating the aforementioned corrosion metric parameter through the measurable properties of thickness and lift-off.

FUTURE WORK

Enumerated here is the planned future work for completion of this project. This list represents the work that is currently being performed.
• Finish testing and evaluating the notched specimens, in the same manner as previous smooth unnotched specimens.
• Determine an MSD geometry for use and the number of specimens to evaluate.
• Expand the types of artificial corrosion employed to include a uniform thickness loss corrosion, either EXCO or CASS corrosion methods.
• Diversify the types of materials to include a 7xxx series aluminum, either 7075-T6 or 7178-T6.
• Incorporate the process of translating EIFS from one geometry to another.

CONTACT

Jason Scheuring: scheurin@ecn.purdue.edu
1282 Grissom Hall
West Lafayette, IN 47907-1282
http://roger.ecn.purdue.edu/~scheurin
ph: (765) 494-1378 or (765) 494-5159

Prof. Alten F. Grandt: grandt@ecn.purdue.edu
1282 Grissom Hall
West Lafayette, IN 47907-1282
http://aae.www.ecn.purdue.edu/AAE/Faculty/Grandt
ph:(765) 494-5141

REFERENCES

1. Wilson, J. R., and B. Rek, " Caring for the Elderly Jet," *Interavia Aerospace Review*, p. 1177-1179, December 1989.
2. Groner, D. J., "US Air Force Aging Aircraft Corrosion," *Structures Division Current Awareness* Bulletin, Aerospace Structures Information and Analysis Center, Spring 1997.
3. Murphy, E. E. (Ed), "Aging Aircraft: Too Old To Fly?" *IEEE Spectrum*, p. 28-31, June 1989.
4. Goranson, U. G, and M. Miller, "Aging Jet Transport Structural Evaluation Programs," *Presented at the 15th Symposium of the International Committee on Aeronautical Fatigue*, Jerusalem, Israel, June 21-23, 1989.
5. Lincoln, J. W., "Aging Aircraft – USAF Experience and Actions," *Presented at the 19th Symposium of the International Committee on Aeronautical Fatigue*, Edinburg, U.K., June 16-20, 1997.
6. Anonymous, "The U.S. Airline Industry: Coping with an Aging Fleet", *Aerospace Engineering*, p. 13-17, January 1990.
7. Jones, W. F., "Air Force Aging Aircraft Basic Research Program," *USAF Corrosion/Fatigue Planning Meeting*, Wright-Patterson AFB, Ohio, February 8, 1995.
8. Bellinger, N. C., and J. P. Komorowski, "Corrosion Pillowing Stresses in Fuselage Lap Joints," National Research Council Canada Institute for Aerospace Research, May 10 , 1996.
9. Koch, G. H., and T. H. Bieri, "Effect of Corrosion on Fatigue Crack Propagation in Aluminum Alloy 2024-T3," *1993 USAF Structural Integrity Program*, San Antonio, Texas, December 1993.
10. Bray, G. H., R. J. Bucci, E. L. Colvin, and M. Kulak, "Effect of Prior Corrosion on the S/N Fatigue Performance of Aluminum Sheet Alloys 2024-T3 and 2524-T3," *Effects of the Environment on the Initiation of Crack Growth, ASTM STP 1298*, 1997.
11. Fontana, M. G., **Corrosion Engineering**, Corrosion Engineering, McGraw-Hill Inc., 3rd edition, 1986.
12. Anonymous, "Initial Material Quality: A Need," *Aerospace Engineering*, vol. 8, no. 5, p. 32-37, May 1988.
13. Yang, J. N., S. D. Manning, J. L. Rudd, and R. M. Bader, "Investigation of Mechanistic-Based Equivalent Initial Flaw Size Approach," *ICAF '95 International Committee on Aeronautical Fatigue, 18th Symposium*, Melbourne, Australia, May 3-5, 1995.

14. ASTM G44-94, "Standard Practices for Evaluating Stress Corrosion Cracking Resistance of Metals and Alloys by Alternate Immersion in 3.5% Sodium Chloride Solution", *1995 Annual Book of ASTM Standards*, sec. 3, vol. 2, p. 172-175, 1995.
15. ASTM G34-90, "Standard Test Method for Exfoliation Corrosion Susceptibility in 2XXX and 7XXX Series Aluminum Alloys (EXCO Test)", *1995 Annual Book of ASTM Standards*, sec. 3, vol. 2, p. 129-134, 1995.
16. Brooks, C., S. Prost-Domasky, and K. Honeycutt," Determining the Initial Quality State for Materials," *Presented at 1998 USAF Aircraft Structural Integrity Program Conference*, San Antonio, Texas, December 1-3, 1998.
17. Yang, J. N. and S. D. Manning, "A Simple Second Order Approximation for Stochastic Crack Growth Analysis," *Engineering Fracture Mechanics*, vol. 53, no. 5, p. 677-686, 1996.
18. Yang J. N., and S. D. Manning, "Stochastic Crack Growth Analysis Methodologies for Metallic Structures," *Engineering Fracture Mechanics*, vol. 37, no. 5, p.1105-1124, 1990.
19. Harmsworth, C. L., ASD Technical Report 61-121, Wright Laboratory, July 1961.

TABLES & FIGURES

Table 1. Test matrix of corroded specimens from 2024-T3 bare aluminum alloys. Corrosion performed using ASTM G34 [14] Alternate Immersion corrosion system. Different series indicate different calendar times to corrosion exposure. Example: 21 day P series were corroded at a different calendar time than the 21 day Q series.

Type	Series	Number of Specimens (corrosion level)			Applied Stress (ksi)
		6 days	21 days	42 days	
Smooth (SUN)	P	-	15	15	25, 35, 50
	Q	-	47	-	15, 25, 35, 50
	R	31	-	-	15, 25, 35, 50
Notched (NN)	S	12	12	11	15, 20
	T	12	16	12	15, 20
MSD	W	-	-	-	-
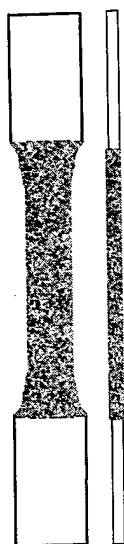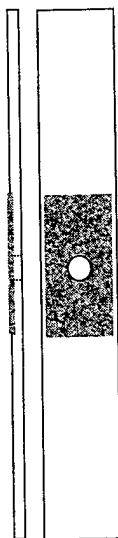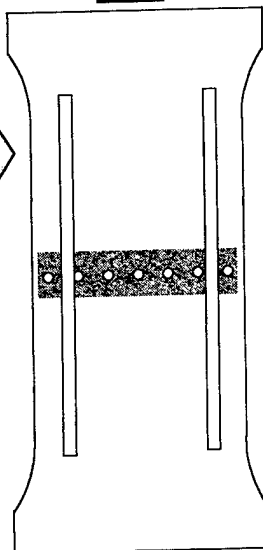
Smooth → Notched → MSD → Structure
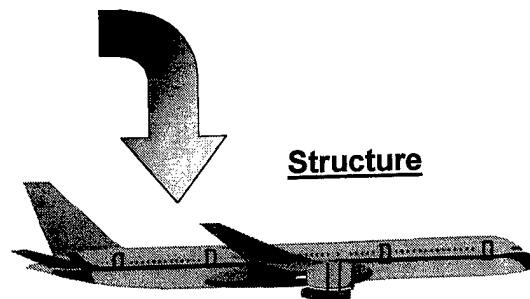
Figure 1. Typical structural Levels for corrosion project; smooth coupon, notched coupon, component, and whole structure. Corrosion depicted as darker areas in smooth, notched, and MSD specimens.

42 day   21 day   6 day

1.0 cm
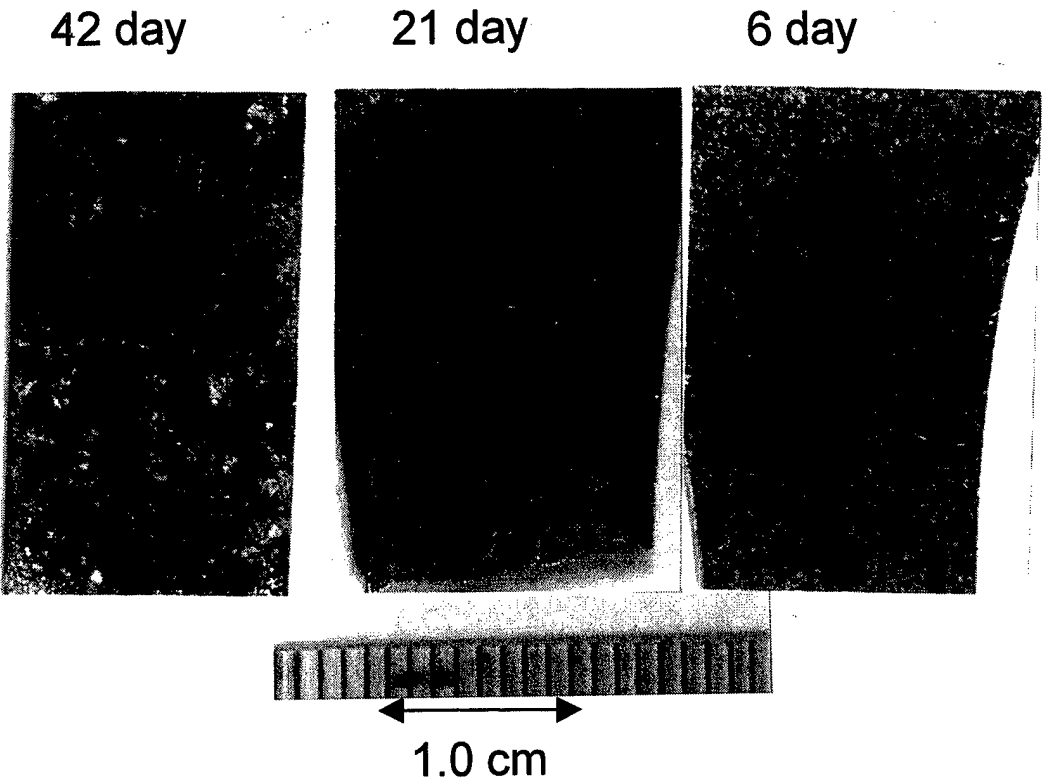
Figure 2. Examples of pitting corrosion for samples exposed to 6, 21, and 42 days of pitting corrosion in an ASTM G44 process. All specimens shown with the same magnification. Note the progression of pit size from lower to higher corrosion exposure time.
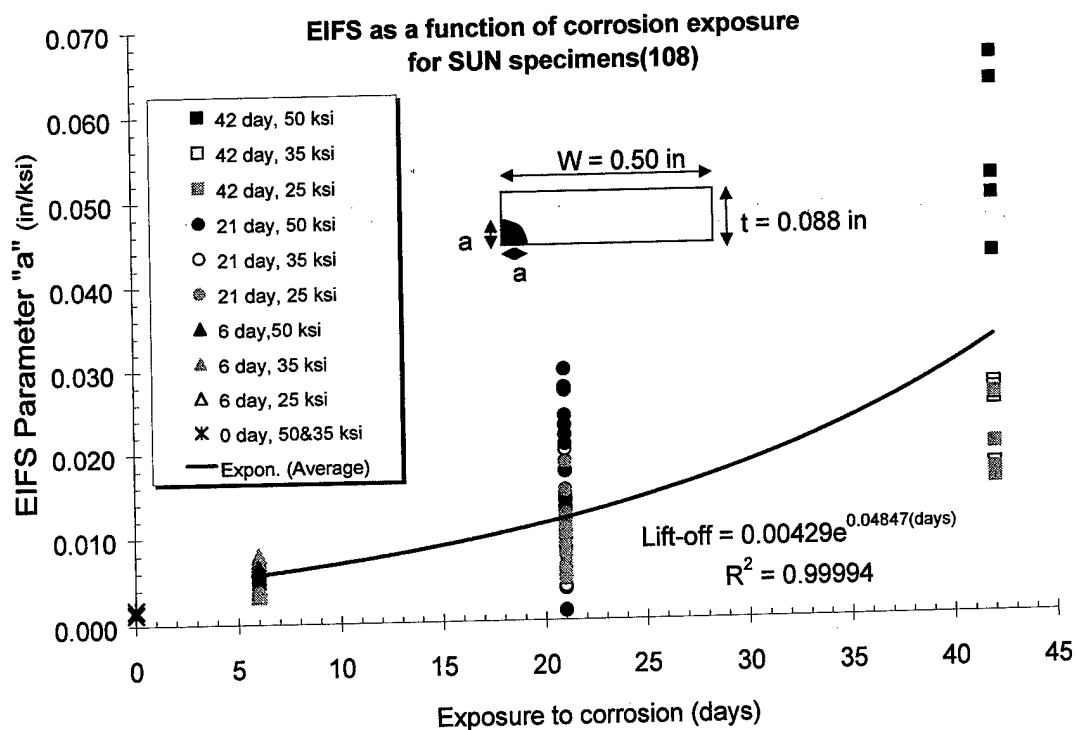
Figure 3. Equivalent Initial Flaw Size as a function of corrosion exposure time for 108 SUN specimens. Also depicted is the trend line for this set of data.
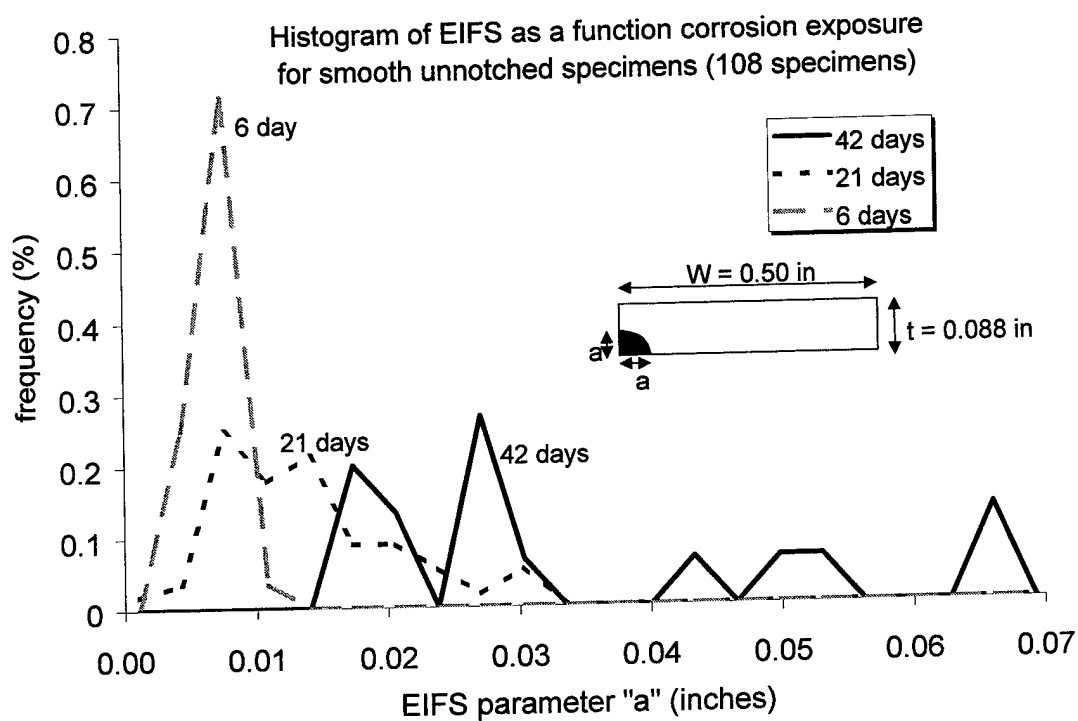
Figure 4. Histogram of EIFS for SUN specimens subjected to various corrosion levels. There are 15, 57, and 36 specimens with exposure times of 42, 21, and 6 days, respectively.
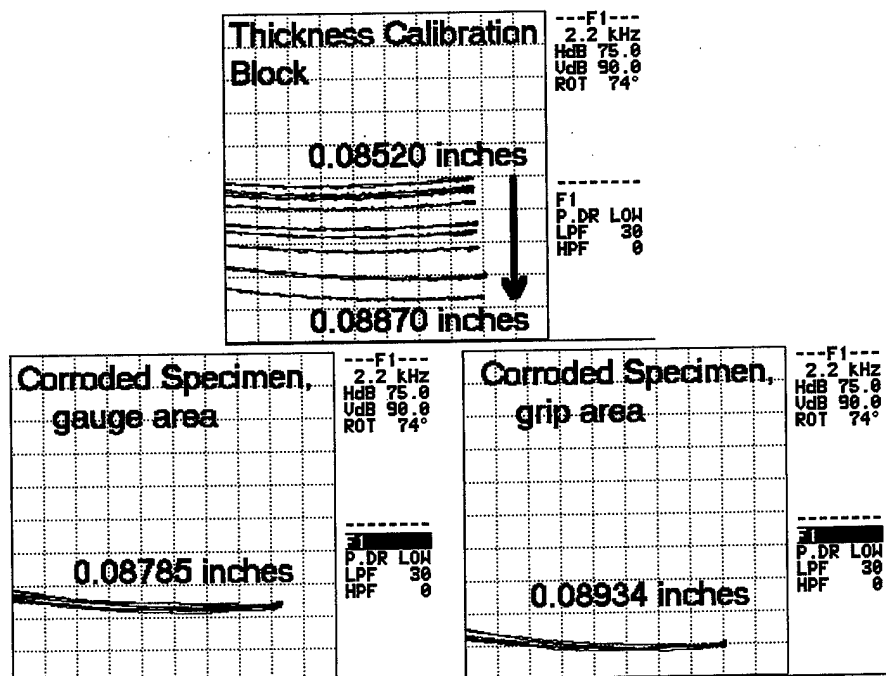
Figure 5. Thickness measurements from eddy current measurements for a notched specimen. Calibration block with approximately 0.0005 inch steps measured to +0.0001 inches.
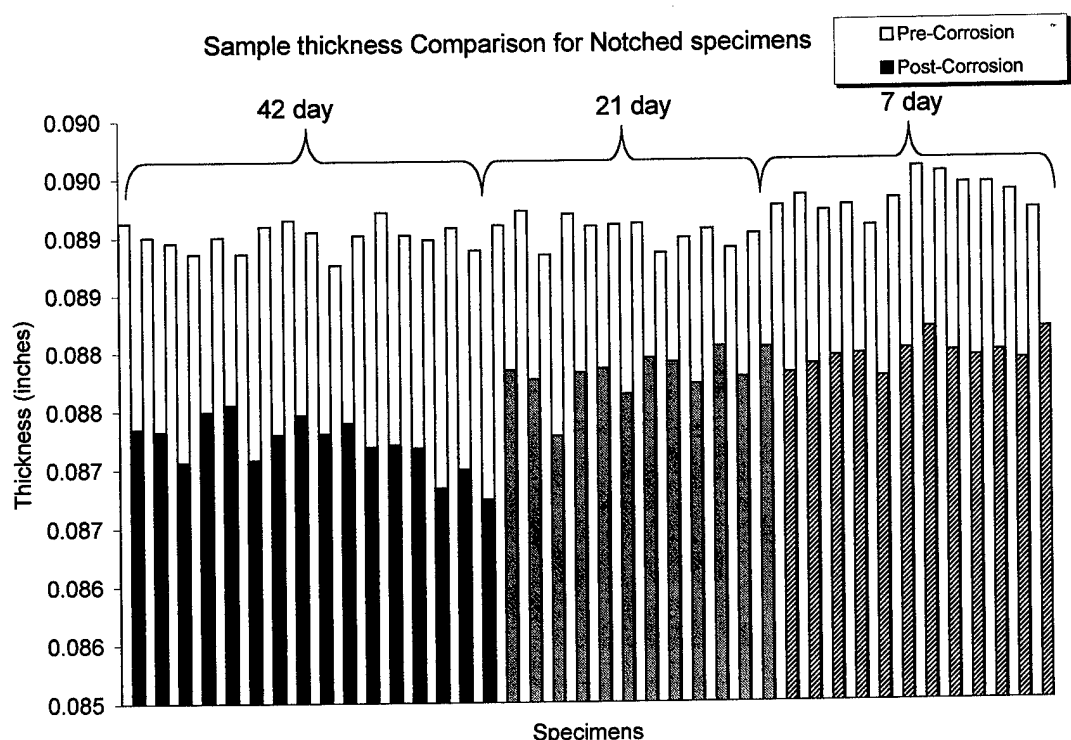
Figure 6. Thickness comparison before and after corrosion a NN set of specimens. Measurements made using eddy current. White indicates pre corrosion status while the black, gray, and striped indicate post corrosion thickness for 42, 21, and 7 days of corrosion exposure to ASTM G34.
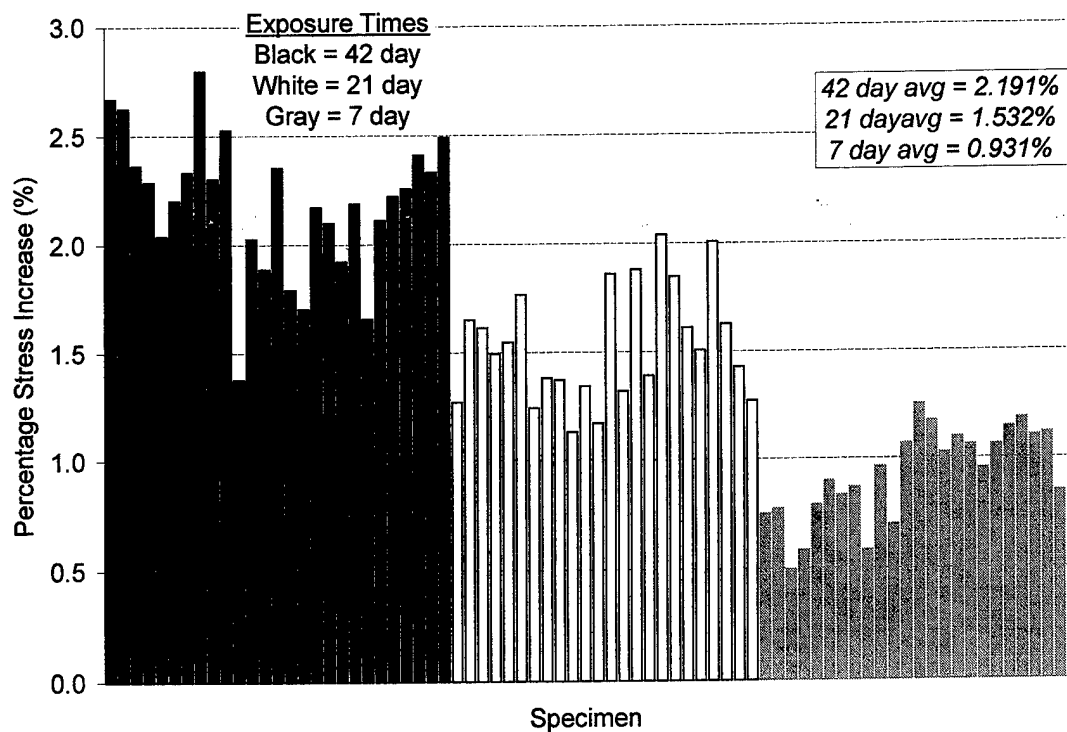
Figure 7. Stress increase due to thickness loss for all Notched specimens (NN). Measurements made with Staveley Nortec19e eddy current probe. Material loss due to corrosion exposure in alternate immersion system (ASTM G34).
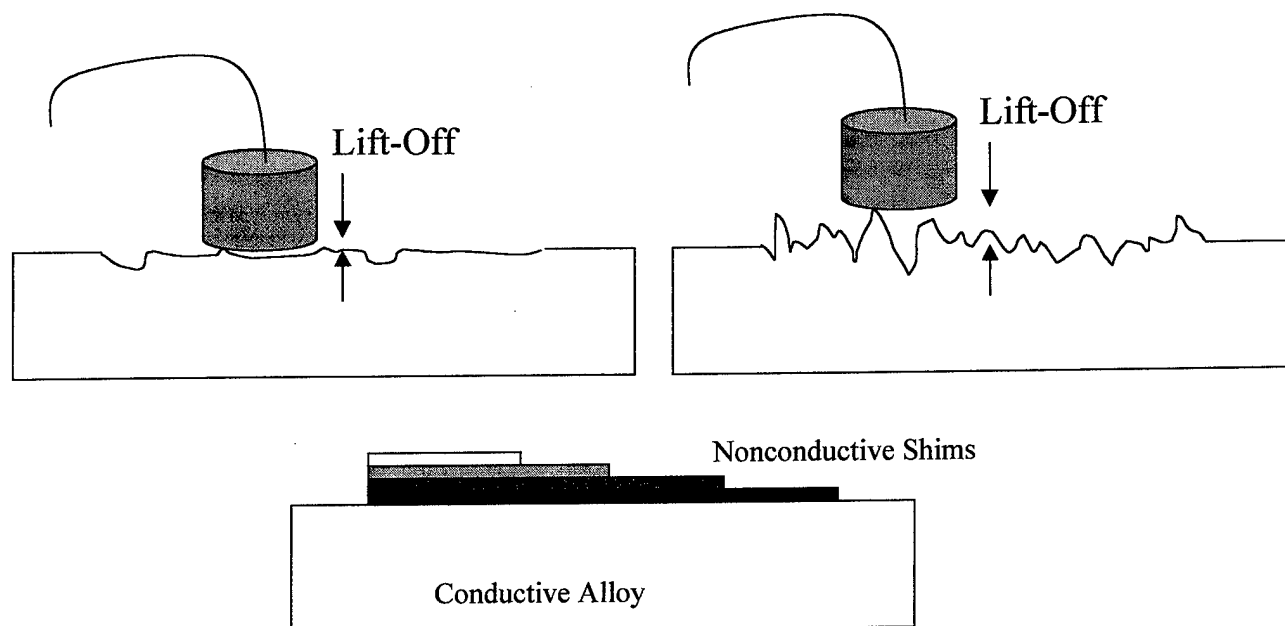
Figure 8. Lift-off for various corrosion exposure times. Also illustrated is lift-off calibration.
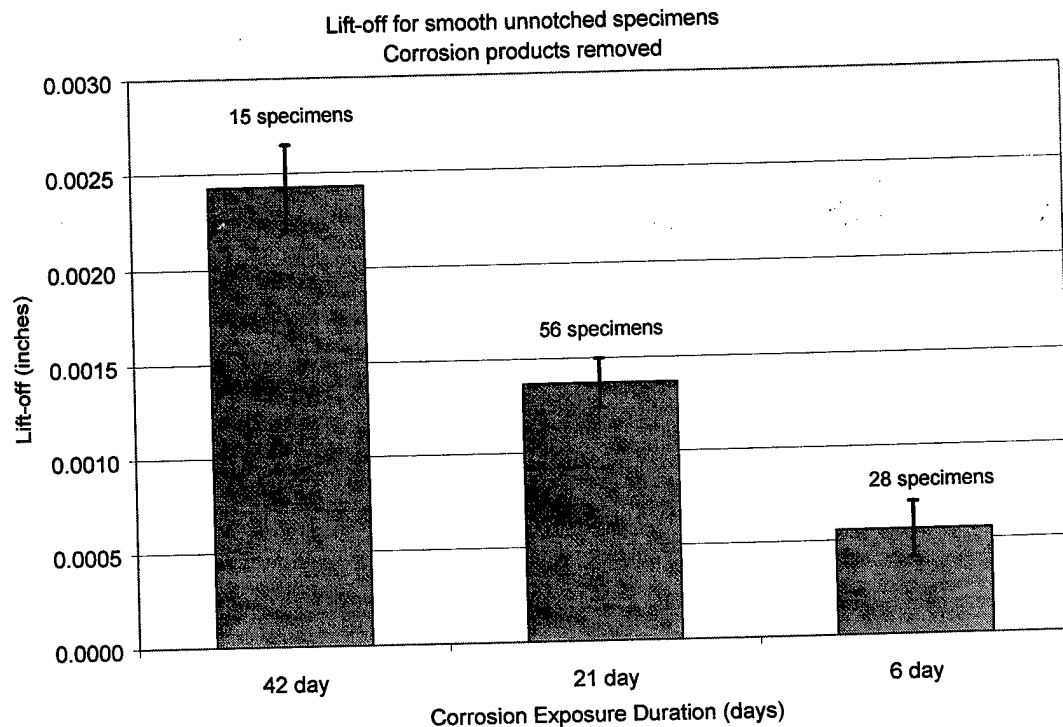
Figure 9. Lift-off for Smooth Unnotched specimen for various pitting corrosion exposures. Specimens have been cleaned of their corrosion products, only degraded aluminum alloy left. (scatterbars indicate ± one standard deviation)
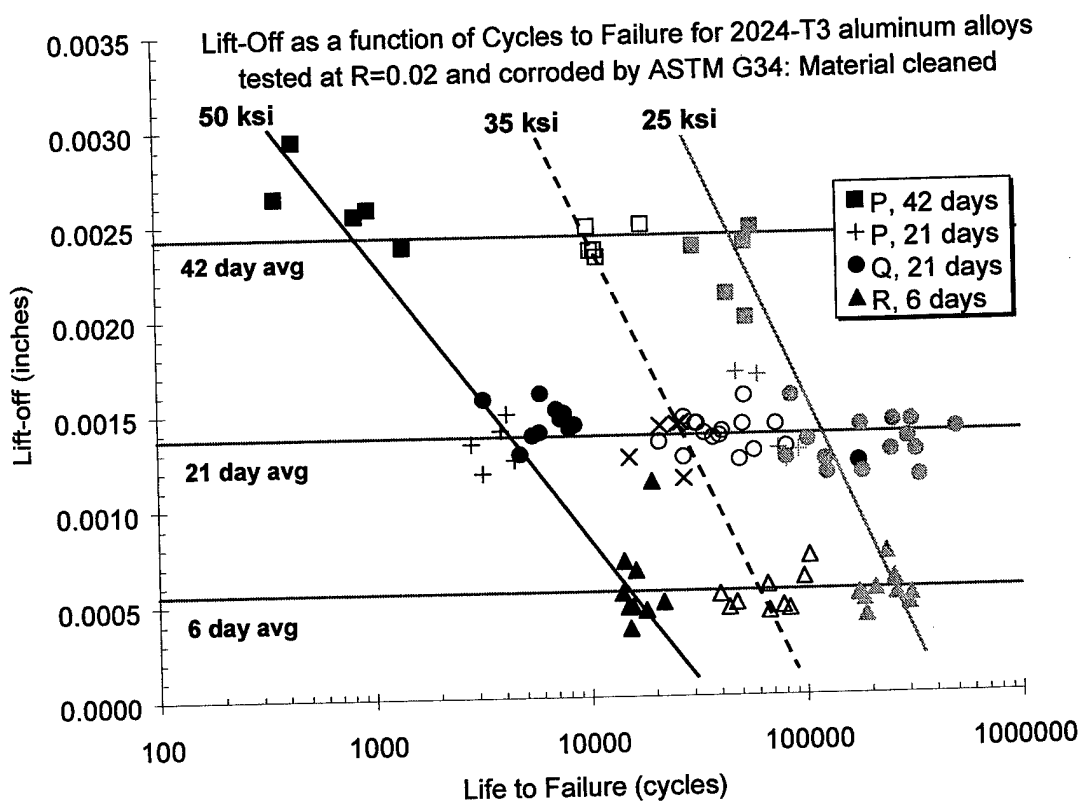
Figure 10. Lift-off for SUN corroded 2024-T3 specimens as a function of cycles to failure, applied loading, and corrosion exposure time. Note: specimens cleaned of corrosion products.
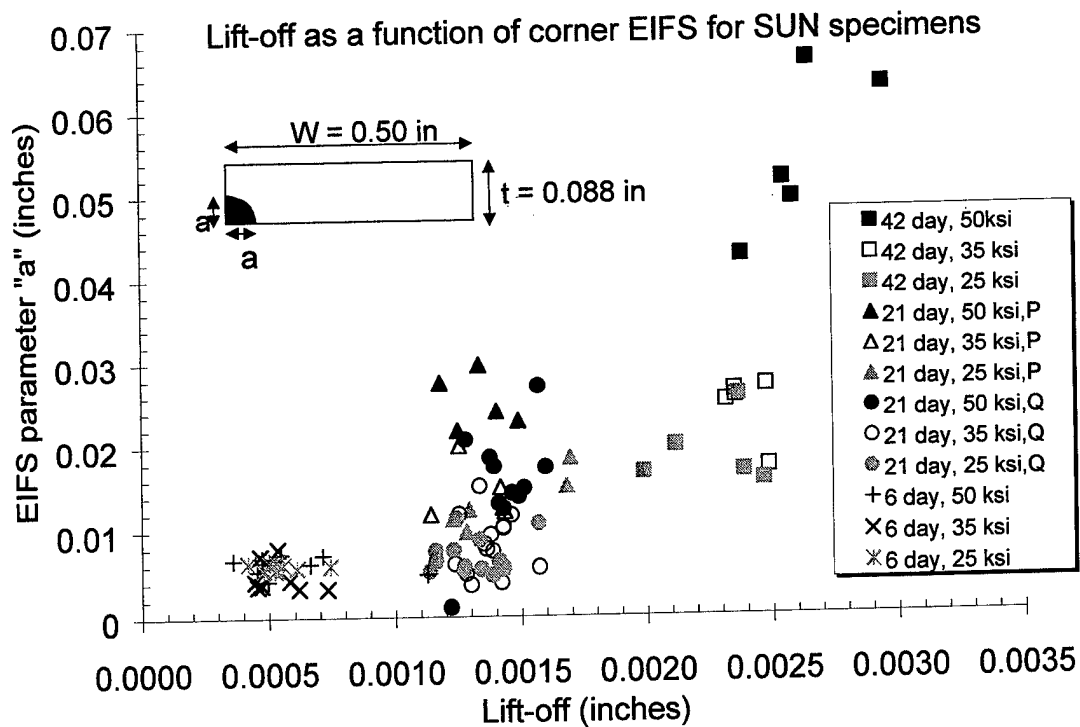
Figure 11. Lift-off as a function of EIFS for corroded specimens with no corrosion products intact.
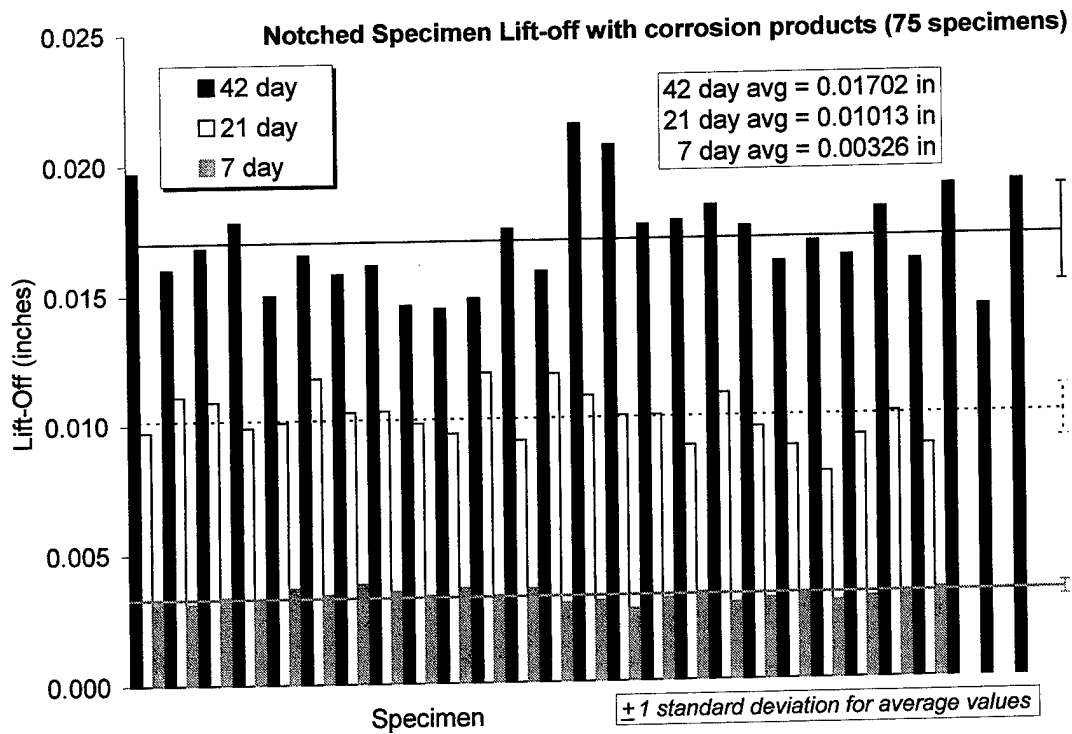
Figure 12. Lift-off for notched specimens that are corroded, but not cleaned of corrosion products for all NN specimens. Lift-off made using 1 MHz eddy current probe with Staveley Nortec19e.

A PROBABILISTIC APPROACH TO PREDICTING FATIGUE LIVES OF CORRODED 2024-T3

J.E. Zamber, B.M. Hillberry
Purdue University
West Lafayette, IN 47907

Abstract

The objective of this work was to develop a probabilistic approach to predict fatigue lives of corroded 2024-T3 aluminum tensile specimens. An experimental program was established to corrode fatigue specimens made of 2024-T3 sheet separately on the longitudinal-transverse (LT) and longitudinal-short (LS) metallurgical planes in a 3.5% sodium chloride solution for 6 and 8 days. The specimens were tested to fracture and the corrosion pits that nucleated fatigue cracks were analyzed with an electron microscope. Corroded material from the fractured specimens was polished on the short-transverse plane and the pits were viewed and photographed under a light microscope. The largest 10% of the collected pits were fit to extreme value distributions. These distributions were used in a Monte Carlo simulation where 1000 pit areas were selected, modeled as circular surface or corner cracks and treated as initial flaw sizes. Fatigue life predictions were made based on the initial flaw sizes from the Monte Carlo simulation and verified experimentally. Predicted cumulative distribution functions of fatigue life were within 22% of the experimental distribution for the LS specimens. The method predicted a reasonable distribution of fatigue lives for the 6 day LT specimens, but consistently under-predicted the experimental distribution of fatigue lives for the 8 day LT specimens.

I. Introduction

The replacement of worldwide aging aircraft fleets is unlikely due to the excessive cost. Therefore, to reliably operate older aircraft into the next century, additional knowledge of the mechanisms and predictive methodologies associated with corrosion and fatigue are required. When structural components are exposed to fatigue loading in a corrosive environment, fatigue crack formation and growth are often accelerated, resulting in premature failure. The structural aluminum alloy 2024-T3 has been the focus of several studies investigating the mechanisms and modeling of corrosion pitting. Chen et. al. [1] discovered that corrosion pitting of 2024-T3 in 0.5M NaCl was associated with micro-galvanic potential differences between constituent particles and the surrounding aluminum matrix. Further, Burynski [2] corroded

polished 2024-T3 aluminum coupons on the LT plane and collected SEM micrographs of the pitted LT surface. Analysis of the micrographs yielded corrosion pit area data, and the largest of these data were fit to extreme value distributions. Kondo and Wei [3] investigated the transition from pit growth to Mode I crack growth by fatigue testing open-hole specimens of 2024-T3 in 0.5M NaCl at room temperature. Among other things, the authors observed that fatigue cracks that led to failure usually nucleated from a single pit, and that the nucleating pits were typically among the largest pits observed.

The work presented here is an extension of the probabilistic method developed by Laz [4] and uses several of the methods and observations of the aforementioned corrosion studies. In this work, 2024-T3 aluminum tensile specimens were corroded in a 3.5% sodium chloride solution, and the resulting corrosion pitting damage was quantified and modeled as the initial damage state from which fatigue life predictions were made. These predictions were verified with an experimental program in which corroded tensile specimens were tested to fracture.

II. Materials and Methods

Fatigue Specimen Preparation

Standard 0.25 and 0.5 inch ASTM flat test specimens [5] were machined from 0.1 inch thick 2024-T3 aluminum sheet. The aluminum alloy used in this work was manufactured in 1976 and of the same lot as that tested by Virkler [6]. To insure surface finish uniformity, all LT and LS specimen surfaces were polished with 340, 400 and 600 grit papers, and polished with 4-8 micron and finally 1 micron diamond lapping compounds.

Because of documented differences in the severity of pitting between the metallurgical planes [1], the LT and LS planes were corroded separately for this work. 0.25 inch tensile specimens (LS specimens) were used in tests in which a 0.75 inch by 0.1 inch area of one LS edge was corroded and the other surfaces masked off. Similarly, 0.5 inch tensile specimens (LT specimens) were used for LT pitting tests where a 1.5 inch by 0.5 inch area of one of the LT surfaces was corroded while masking the other side and both edges. Masking of the surfaces was achieved with Tolber Miccro XP-2000 Stop-Off. A photograph of the

American Institute of Aeronautics and Astronautics

polished and Stop-Off coated LS and LT specimens is shown in Figure 1.

Corroding and Fatigue Testing

There are several methods available by which to corrode aluminum alloys for corrosion pitting studies. Among these are natural exposure, salt spray, immersion, and alternate immersion. Alternate immersion has been shown to accelerate corrosion pitting [7] and was selected as the method of corrosion for this work. Fatigue specimens were corroded in a 3.5% sodium chloride (NaCl) solution, using an alternate immersion machine that operated according to ASTM Standard G44-88 [7]. The alternate immersion corrosion process alternately immerses specimens in a solution of 3.5% NaCl, by weight, for ten minutes and then allows the specimens to dry for the remaining fifty minutes of the hour in a controlled environment. Several parameters were maintained according to the standard, among these: temperature, relative humidity and pH.
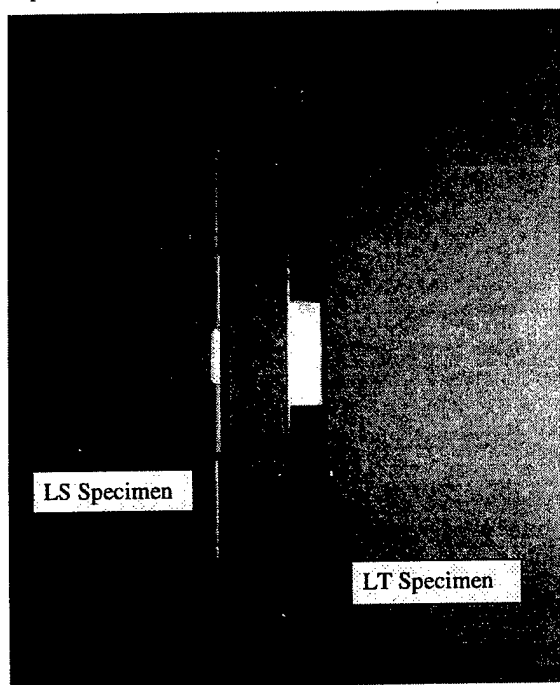
Figure 1: Polished and Stop-Off Coated LS and LT Fatigue Specimens

Nine LS and eight LT specimens were corroded in two separate batches for 6 days using identically prepared NaCl solutions. Nine LS and eight LT specimens were corroded together as a batch for 8 days. After corroding, products of corrosion were removed from each specimen's surface by rinsing with deionized water followed by immersion in a solution

made according to ASTM Standard G1-90 for cleaning corrosion products from aluminum alloys [8]. The cleaning solution was made by mixing 57.8 ml of 86.5% phosphoric acid with 20.0 g of chromium trioxide and enough deionized water to bring the total solution volume to 1.0 liter. The solution was heated to boiling and each specimen was immersed for 5 minutes, before rinsing in deionized water and finally with ethanol. All specimens were stored under vacuum until fatigue tested.

The corroded specimens were fatigue tested according to the test matrix in Table 1. Fatigue testing was performed using an MTS single axis load frame with hydraulic wedge grips and an Instron 8500 plus digital closed loop servohydraulic controller. Initially, all tests were to be conducted at a maximum stress of 220 MPa, a stress ratio of 0.1 and a frequency of 10 Hz. The 8 day corroded specimen maximum stress was reduced from 220 MPa to 200 MPa due to preliminary results indicating that cracking initiated from multiple nucleation sites. Corroded specimens were cycled until fracture.

Table 1: Fatigue Testing Matrix

Specimen Type	Number of Tests	S_{MAX} (MPa), R=0.1, f=10Hz
6 Day, LS	9	220
8 Day, LS	3	220
8 Day, LS	6	200
6 Day, LT	8	220
8 Day LT	2	220
8 Day LT	6	200

Corrosion Pit Quantification/Fracture Surface Analysis

Methods for corroding and quantifying corrosion pitting damage in 0.1 inch thick 2024-T3 sheet were developed. To insure that the corroded material used for pitting quantification had the same distribution of pit sizes as the fatigue specimens, corroded material was cut from corroded fatigue specimens after being tested to fracture. The corroded samples used for quantification purposes were mounted in Buhler Castoglass cold mount with the ST planes exposed. The ST planes were wet polished with 340, 400, and 600 grit papers, a 4-8 micron diamond paste, and finally a 0.01 micron chrome oxide solution. The polished surfaces revealed ST plane projections of the corrosion pits, that were viewed with a light microscope

outfitted with a Hitachi CCD camera. CCD images were digitized and saved using a Macintosh computer with a VideoSpigot video acquisition board. Due to differences in pit sizes, corrosion pits from the 6 day LS specimens were viewed at 800x, while all others were viewed at 256x.

ST plane projections of corrosion pit area, maximum depth and width data were collected through the analysis of the digitized images. The brightness and contrast of all images were identically adjusted to create binary images, wherein the pits were made black and the surroundings white. The particle analysis tool of the image analysis software IMIX [9] was used to count the total number of black pixels to determine pit area. Figure 2 contains a schematic representation of the collection procedure.
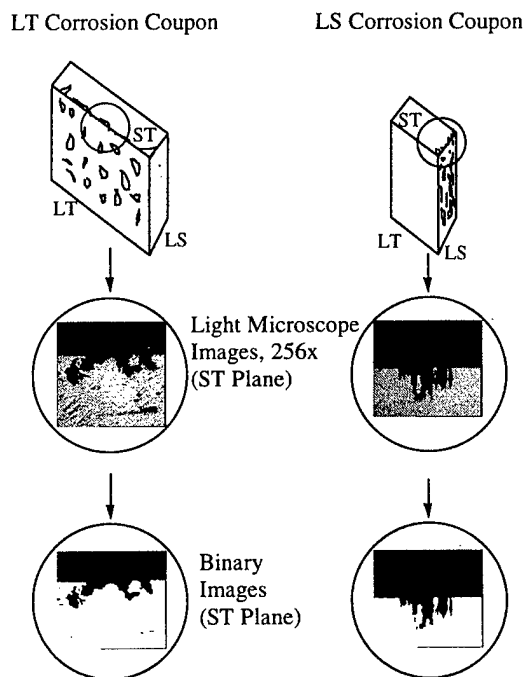
Figure 2: Schematic of Corrosion Pit Quantification Process for LT and LS Coupons

Pit area measurements were made through the analysis of environmental scanning electron microscope (ESEM) images taken of the fracture surfaces. Figure 3 contains an ESEM micrograph of the fracture surface of a 6 day corroded LT specimen showing, in the upper right corner, the corrosion pit that nucleated the critical fatigue crack. The nucleating pit was found by tracing the river-marks back to the pit. Another ESEM micrograph taken at higher magnification of the same fracture surface shows the nucleating corrosion pit outlined (Figure 4). Each nucleating pit was manually outlined and the area, maximum width and depth measured using the image analysis software NIH Image [10].
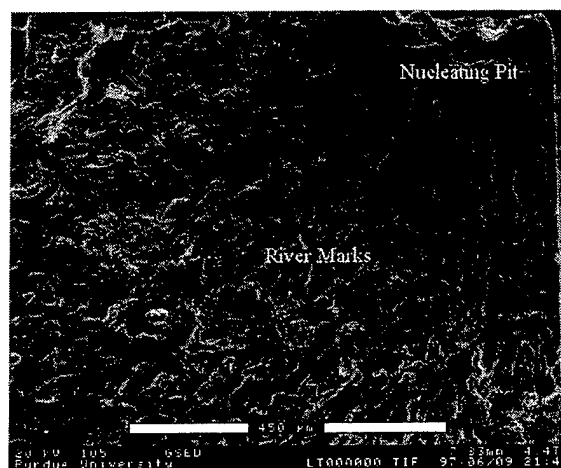
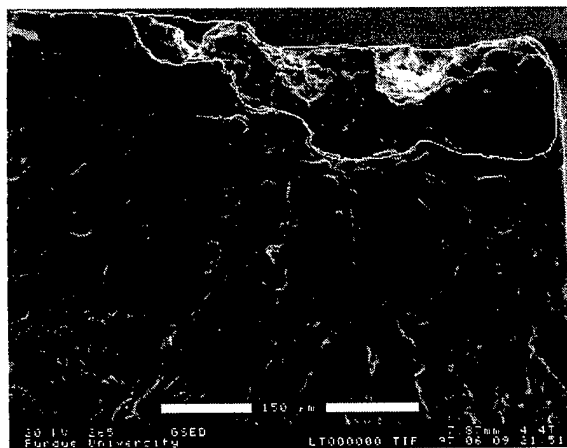Figure 3: ESEM Micrograph of the Nucleating Pit, 6 Day LT Specimen #1

Figure 4: ESEM Micrograph of the Nucleating Pit Outlined, 6 Day LT Specimen #1

III. Probabilistic Model

Assumptions

Assumptions used to simplify, understand and analyze a physical process are present in any modeling endeavor. The probabilistic model presented here was primarily based on the following assumptions:

1. Corrosion fatigue failures stem from a single pit.
2. The largest pits cause initiation and failure.
3. Corrosion pits may be regarded as an initial damage state.
4. Fatigue crack nucleating corrosion pits may be modeled as circular surface or corner cracks.
5. Cracks nucleate immediately with no initiation life.

Extreme Value Distributions

Burynski [2] has had success in modeling the largest corrosion pits with Type I extreme value (Gumbel) distributions, the cumulative distribution function of which is given in equation 1.

$$F_Y(y) = \exp[-\exp(-a(y-w))] \qquad (1)$$

where a and w are obtained from the observed data.

Gumbel distributions were fit to the largest ten percent of the ST plane projected corrosion pit area data from each data set. Fitting the distribution involved linearizing Equation 1 and performing a least squares fit with the experimental data to obtain the Gumbel distribution parameters (a and w). The Gumbel parameters and goodness of fit criteria were calculated and are listed in Table 2.

Table 2: Gumbel Fitting Parameters and Wellness of Fit Criteria

Data Set	Gumbel Coefficients		Wellness of Fit Parameters			
	a	w	r^2	F	n	$F crit$ 0.01
6 Day LS	0.00044	2237	0.92	338	31	7.59
8 Day LS	0.00044	11705	0.96	778	33	7.52
6 Day LT	0.00056	9161	0.92	426	39	7.37
8 Day LT	0.00050	11682	0.93	444	36	7.39

Cumulative distribution functions for each Gumbel fit were plotted with their respective experimental largest pit data sets in Figures 5 and 6 for the LS and LT corroded specimens, respectively.
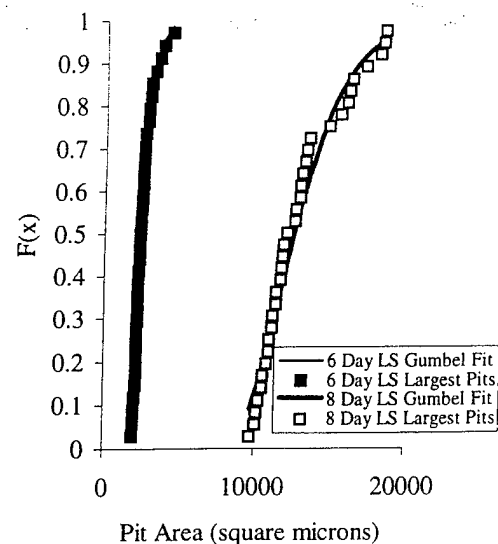

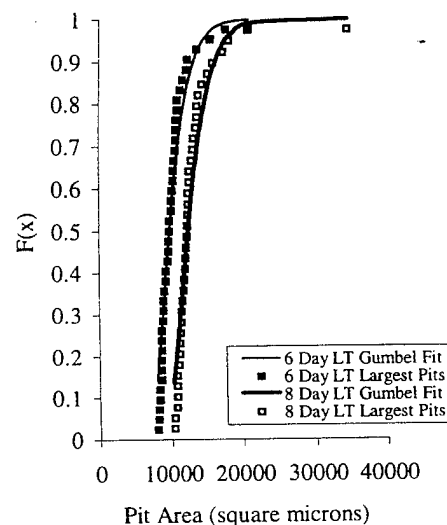Figure 5: Extreme Value Plots of Pit Area with Gumbel Fits, LS specimens

Figure 6: Extreme Value Plots of Pit Area with Gumbel Fits, LT Specimens

The Monte Carlo Simulation

The probabilistic model used a Monte Carlo simulation to select pit areas from the extreme value distributions. These areas were modeled as circular corner cracks in the ST plane. Using FASTRAN II, these initial cracks were grown to through thickness to simulate life to fracture. For each extreme value distribution, 1000 Monte Carlo trials were performed. A Monte Carlo simulation generates random numbers between 0 and 1, and selects the value from the CDF (in this case, pit area) that corresponds to the randomly generated number.

The Stress Intensity Factor Solution

Each pit area generated in the Monte Carlo simulation was modeled as a semicircle, and the radius (r) was calculated. The initial damage state corresponding to the randomly selected pit area was modeled as either a circular surface crack or a circular corner crack, each of radius r, using stress intensity factor solutions by Newman and Raju [11] for elliptical surface or corner cracks for the special case of circularity. The decision to use a corner crack versus a surface crack stress intensity factor solution was based on the type of crack that was experimentally favored. The stress intensity factor solutions for the surface and corner cracks are of the form given in Equations 2 and 3, respectively.

$$K_I = \frac{\sigma\sqrt{\pi b}}{E(k)} F_s\left(\frac{b}{a}, \frac{b}{t}, \frac{a}{W}, \phi\right) \qquad (2)$$

$$K_I = \frac{\sigma\sqrt{\pi b}}{E(k)} F_c\left(\frac{b}{a}, \frac{b}{t}, \phi\right) \qquad (3)$$

The process of modeling circular corner cracks from photographed semi-circular surface cracks is shown in the schematic representation of Figure 7.
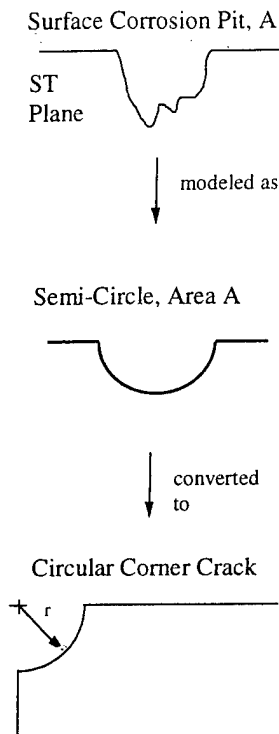

Figure 7: Schematic of Pit Modeling Procedure on the ST Plane

Physically, the model is based on the microstructure of the sheet material as defined by the rolling process during manufacture. This process elongates constituent particles in the rolling direction and presents elongated and flattened particles on the LT plane and cigar-shaped particles on the LS plane. Viewed from the ST plane, the particles near the edges appear semi-circular. When fatigue specimens are manufactured through milling and mechanical polishing operations, the projections of constituent particles on the LT and LS surfaces as viewed from the ST plane, will appear semi-circular except on the corners. The corners have particles that were partially polished away from both the LT and LS surfaces, and the projections on the ST plane appear quarter-circular. Since the constituent particles located at the corners were from the same distribution as those located on the surface, the corrosion pits formed at both positions should be of the same distribution. Therefore, the radii calculated from the assumed semi-circular surface pits should be roughly equal to the radii of the quarter circular corner pits, as schematically illustrated in Figure 8.
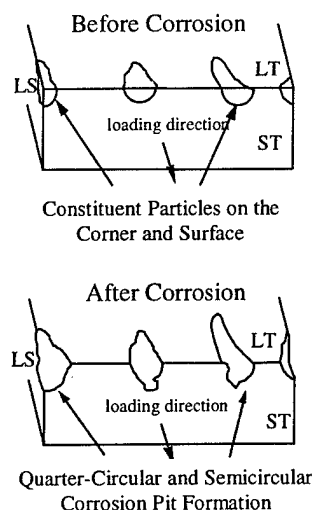
Before Corrosion

Constituent Particles on the
Corner and Surface

After Corrosion

Quarter-Circular and Semicircular
Corrosion Pit Formation

Figure 8: Schematic Illustrating Corner and Surface Pit Formation from Constituent Particles

Fatigue Life Predictions using FASTRAN II

FASTRAN II [12] is a life prediction code written by J.C. Newman, Jr. based on the crack closure concept and is used to predict crack growth versus cycles from an initial crack size to failure. FASTRAN II was used to predict life to fracture from an initial semi-circular corner crack of radius r calculated from the pit area selected in the Monte Carlo simulation. Predictions were made for the 1000 pit areas selected from the Monte Carlo simulation from each of the four extreme value distributions. To simulate life to fracture, FASTRAN II grew each crack until its length was equal to the specimen width.

IV. Results

Fatigue Testing Results

All 6 day LS and three of nine 8 day LS specimens were tested at a maximum stress of 220 MPa. Fatigue cracks nucleated from single pits in each 6 day LS specimen, and a typical nucleating 6 day LS pit is illustrated in Figure 9. Multiple nucleation sites were observed for 8 day LS specimens tested at 220 MPa. The maximum stress was reduced to 200 MPa for the remaining 8 day LS specimens which resulted in nucleation from single pits. Only experimental data from the 8 day LS specimens tested at a maximum stress of 200 MPa were used to validate the probabilistic model. All 6 day LT specimens were tested at a maximum stress of 220 MPa, and six of eight 8 day LT specimens were tested at a maximum stress of

200 MPa, again due to multiple nucleation sites observed when testing at a maximum stress of 220 MPa. A typical nucleating 6 day LT pit is illustrated in Figure 10. One 6 day and two 8 day LT specimens failed at the radii in uncorroded regions. Therefore, the experimental results from seven 6 day LT and four 8 day LT specimens were used to verify the probabilistic model.
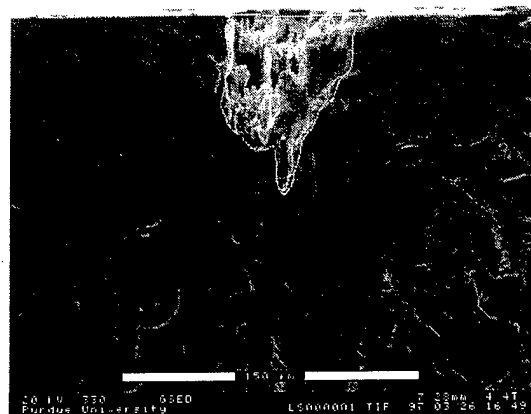

Figure 9: ESEM Micrograph of the Nucleating Pit for the 6 Day LS Specimen #3, (nucleating pit outlined)
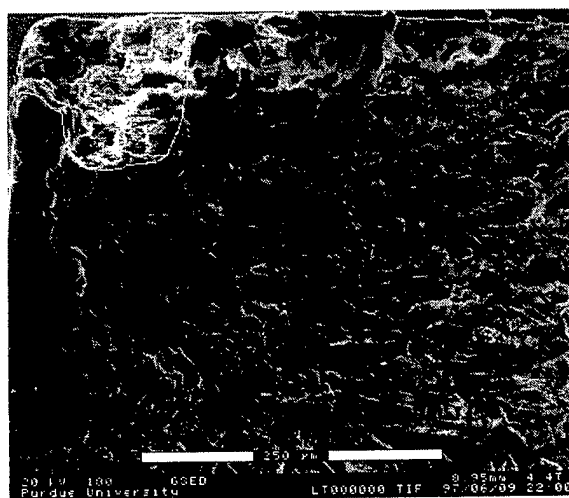

Figure 10: ESEM Micrograph of the Nucleating Pit Located at the Corner for the 6 Day LT Specimen, #3B, (nucleating pit outlined)

The average experimental life to fracture for the 6 and 8 day LS specimens was 267,322 cycles and 180,017 cycles, respectively. The average nucleating pit area for the 6 and 8 day LS specimens was 2,519 μm^2 and 24,262 μm^2, respectively. In every 6 and 8 day LS specimen, cracks nucleated from pits on the LS surface; corner crack formation was not observed. The

average experimental life to fracture for the 6 and 8 day LT specimens was 195,722 cycles and 373,515 cycles, respectively. The average nucleating pit area for the 6 and 8 day LT specimens was 13,295 μm^2 and 17,988 μm^2 respectively. In five of seven 6 day and all 8 day LT specimens, fatigue cracks nucleated from pitting at the corners; the two remaining 6 day LT specimens nucleated cracks from pits in close proximity to a corner.

Results of the Probabilistic Model

The probabilistic model used a Monte Carlo simulation that randomly selected 1000 pit areas from each of the extreme value distributions. These pit areas were modeled as circular corner cracks for the LT specimens and circular surface cracks for the LS specimens from which fatigue lives were predicted. The predicted and experimental fatigue life data were sorted according to longest lives and plotted as the predicted and experimental cumulative distribution functions illustrated in Figures 11 and 12 for the LS and LT specimens, respectively.
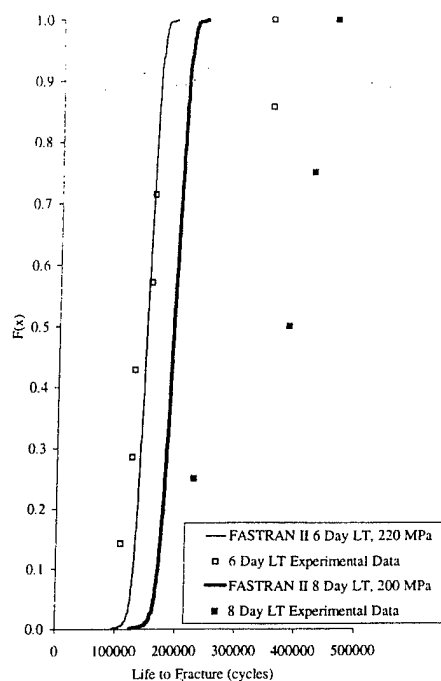

Figure 12: Predicted and Experimental Cumulative Distribution Functions of Life to Fracture for 6 and 8 Day LT Specimens

The probabilistic model predicted a distribution of fatigue lives within 19% and 22% of the experimental cumulative distributions for the 6 and 8 day LS specimens, respectively. In addition, the model predicted a distribution of fatigue lives for the 6 day LT specimens that was within 23% of five experimental points and within 55% of the two remaining experimental points that composed the 6 day LT experimental cumulative distribution of fatigue lives. Finally, the analytical CDF of life to fracture consistently under-predicted the experimental CDF for the 8 day LT specimens and was within 53% of the experimental CDF.

V. Discussion and Conclusion

Discussion of the Probabilistic Model

Overall, the probabilistic model predicted reasonable distributions of fatigue lives for the LS specimens and for the 6 day LT specimens. The predicted distribution of fatigue lives for the 8 day LT specimens was less accurate, and may be due to microstructural effects. It is hypothesized that the microstructure of the aluminum sheet and the aspect ratio of the 8 day LT pits may play a role in the discrepancies. Firstly, the 8 day LT nucleating pits

Figure 11: Predicted and Experimental Cumulative Distribution Functions of Life to Fracture for 6 and 8 Day LS Specimens

7

were mostly characterized by broad (in the transverse direction) and rounded looking pits as illustrated in the ESEM micrograph of the fracture surface of Figures 13. By contrast, most of the 6 day LT pits were less broad and more pointed as illustrated in Figure 14. The result of these differences in aspect ratio from the assumed initial circular crack is that more crack growth would be required in the short direction. When a crack grows in the short direction, it must propagate through flattened or pancake-like grains formed during the manufacture of the sheet material. Therefore, this crack growth in the short direction through the non-homogenous material may have reduced the rate of growth compared to what was predicted using the circular corner crack modeling of the nucleating pit and transverse crack growth data.
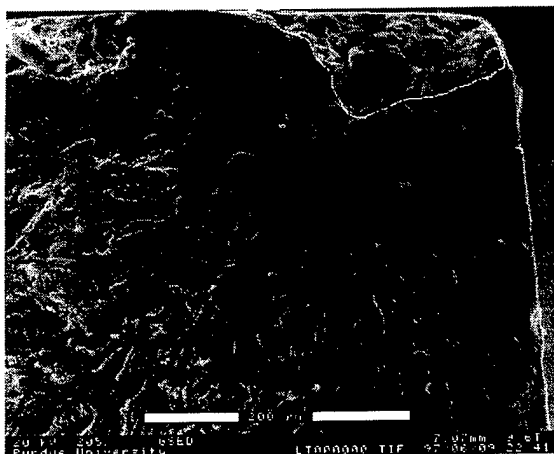
Figure 13: ESEM Micrograph of the Nucleating Pit for the 8 Day LT Specimen #7 (nucleating pit outlined)
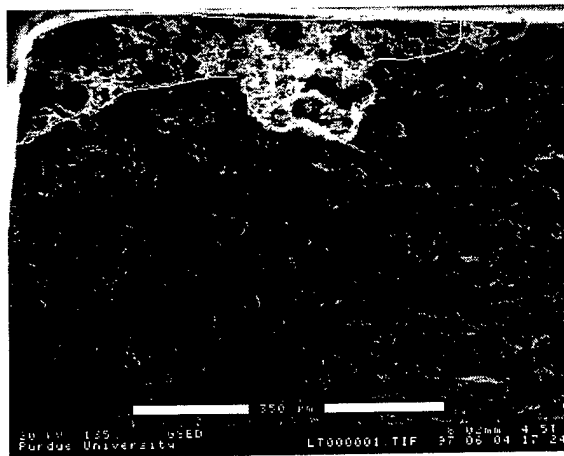

Figure 14: ESEM Micrograph of the Nucleating Pit for the 6 Day LT Specimen #6B (nucleating pit outlined)

Although the probabilistic model appears to generate reasonable distributions of fatigue lives, the inclusion of additional fatigue testing data may well shift or change the shape of the experimental cumulative distribution functions. Therefore, the claim that the model functions reasonably well is subject to the assumption that additional fatigue testing data would not greatly alter the experimental cumulative distribution functions. It is also important to note that the 6 day LS extreme value distribution of pit area from which the initial crack areas were selected using the Monte Carlo simulation did not include pit areas as small as two of those found to nucleate cracks in the 6 day LS experiments. The predicted cumulative distribution of fatigue lives reflects the assumption that all fatigue cracks would nucleate from pits consistent with the largest 10% measured. Therefore, were the two smaller pit areas included in the Gumbel distribution, the predicted cumulative distribution of fatigue lives would be shifted to the right, and would not match the experimental distribution as well for the 6 day LS CDF illustrated in Figure 11.

Conclusions

The most significant conclusions of this work are listed below:

1. The largest pit areas were well modeled by Type I extreme value distributions.
2. Except for two 6 day LS experiments, critical fatigue cracks nucleated from corrosion pits that were among the largest 10% of those measured.
3. Slower crack growth in the short direction may be a factor in the under-prediction of fatigue lives for two of the 6 day LT specimens and all of the 8 day LT specimens.
4. The probabilistic model predicts reasonably accurate distributions of fatigue lives for the LS specimens and the 6 day corroded LT specimens.

There are several limitations of this work worth discussing. Firstly, the relatively small sample sizes used in the extreme value distributions and in the experimental cumulative distribution functions prohibit a truly accurate verification of the probabilistic model. An increase in the sample size of corrosion pit areas used to fit the extreme value distribution would likely shift the extreme value distribution and cause a shift in the predicted cumulative distribution function of fatigue lives. Likewise, larger sets of experimental fatigue life data would likely shift and/or change the shape of the experimental cumulative distributions of fatigue lives.

VI. References

1. Chen, G.S., Gao, M., Harlow, D.C., and Wei, R.P. "Corrosion and Corrosion Fatigue of Airframe Aluminum Alloys." <u>FAA/NASA International Symposium on Advanced Structural Integrity Methods for Airframe Durability and Damage Tolerance.</u> NASA Conference Publication 3274, 1994, pp. 157-173.

2. Burynski, Raymond M. "Corrosion Response of a 2024-T3 Alloy in 0.5M NaCl Solution." M.S. Thesis. Lehigh University. 1994.

3. Kondo, Y., Wei, R.P. "Approach on Quantitative Evaluation of Corrosion Fatigue Initiation Condition." <u>Evaluation of Materials Performance in Severe Environments. Proceeding of International Conference</u>, The Iron ...d Steel Institute of Japan, Tokyo, Japan, 1989.

4. Laz, P.J. "A Probabilistic Approach to Predicting Fatigue Life for Crack Formation at Inclusions." M.S. Thesis. Purdue University. 1996.

5. ASTM G44-88 "Test Methods of Tension Testing of Materials." Volume 3.01, p.128.

6. Virkler, D.A. "The Statistical Nature of Fatigue Crack Propagation." M.S. Thesis. Purdue University. 1978.

7. ASTM G44-88 "Evaluating Stress corrosion Cracking Resistance of Metals and Alloys by Alternate Immersion in 3.5% Sodium Chloride Solution." Volume 3.02, 174-177.

8. ASTM G1-90 "Preparing, Cleaning, and Evaluating Corrosion Test Specimens" Volume 3.02, 39-45.

9. IMIX, v.7, Princeton, NJ: Princeton Gamma-Tech, 1994.

10. NIH Image, v.1.63, Washington D.C.: National Institute of Health, 1996.

11. Newman, J.C., Jr. And Raju, I.S. <u>Stress Intensity Factors Handbook, v.2</u>. Ed. Murakami, Y. Pergamon Press, 1987.

12. FASTRAN II: A Fatigue Crack Growth Structural Analysis Program. Hampton, VA. NASA Langley, 1992.

VII. Acknowledgements

AIAA-98-2055

A PROBABILISTIC METHOD FOR PREDICTING THE VARIABILITY IN FATIGUE BEHAVIOR OF 7075-T6 ALUMINUM

K. M. Gruenberg[*], B. A. Craig[†], and B. M. Hillberry[‡]
Purdue University
West Lafayette, IN 47907

ABSTRACT

This paper assesses the applicability of a probabilistic model to estimating fatigue life variability for 7075-T6 aluminum. The test specimens for the experimental program were 7075-T6 aluminum single edge notch tension specimens tested under constant amplitude loading (σ_{max} = 120 MPa, R = 0.01). The shortest observed fatigue life was 37,000 cycles and the longest 650,000 cycles. A plastic replication procedure was used to identify crack nucleation sites and monitor crack growth. The initiation sites were identified by examining the plastic replicas and the fracture surfaces of the failed specimens. In agreement with previous studies, the fatigue cracks formed in the center of the notch from material inclusions. For the prediction model, the distribution of inclusion sizes (0.2 μm^2-45 μm^2) within the material were used as the distribution of initial flaw sizes. It was assumed that the crack formation life was a small percentage of the total life, and thus life predictions were based entirely on crack propagation. The cumulative distributions for the fatigue lives from the experimental work and the numerical model were compared to assess the effectiveness of the model. While Experimental crack formation lives as long as 50-70% of the total life were observed in some of the tests, the model predicted failures well in the shorter life regime. The predicted lives were conservative, and in the shortest life region, the predictions were within 15% of the observed lives.

INTRODUCTION

One method that has been developed to address the variability in fatigue lives is a probabilistic approach[1]. This approach has been developed mainly from two observations in fatigue. First, fatigue studies have shown wide ranges of lifetimes within a given set of identical tests. Second, it has been observed that many fatigue failures have initiated at material inhomogeneities. Taking into account the inherent microstructural variability and other fatigue analysis concepts, like stress intensity factors, crack closure, and small crack effects, a method has been constructed to estimate the variability in fatigue life to failure. In addition, the method estimates this variability with reduced amounts of costly and time-consuming experimentation.

The main fracture mechanics concept used in fatigue analysis is the stress intensity factor, ΔK.

$$\Delta K = \Delta\sigma \cdot \sqrt{\pi a} \cdot \beta \qquad (1)$$

where $\Delta\sigma$ is the stress range, a is the crack length, and β is a function of component geometry.

In the last two decades, fatigue crack growth behavior in the low ΔK region has been closely examined. One result has been the concept that for any crack configuration for which the calculated ΔK is below a threshold (ΔK_{th}) the crack will not propagate[2-4].

It has been observed that cracks initiate very early in the fatigue life, occurring at a variety of material inhomogeneities[5-8]. For sheet materials, most of the porosity is eliminated during the rolling process. As a result, for a smooth surface of sheet material, the largest remaining defects are material inclusions[9-11].

Previous studies have shown that the fatigue behavior of many materials depends heavily on the microstructure[4,6,10,12,13,14]. These studies discuss the roles of material inclusions, material phases, grain orientation, and other microstructural characteristics that influence crack growth. It has been observed that all of these features provide more pronounced effects when the crack is "small."

Cracks have been observed to propagate such that the crack surfaces are perpendicular to the rolling direction. It has also been observed[10,15] that fatigue cracks quickly assume a semi-circular shape, a/c =1. From these observations, the projected area, A_i, of the initiating defect was converted to a semi-circular crack of radius r_i. This, coupled with the previous discussion about the different modes of crack initiation, can be used to develop a fatigue life prediction methodology that is based entirely on crack propagation.

Small cracks have been observed to grow faster than long cracks. Plasticity-induced closure reduces crack growth rates, however, small cracks have not

---

[*] Graduate Research Assistant, School of Mechanical Engineering
[†] Assistant Professor, Department of Statistics
[‡] Professor, School of Mechanical Engineering

1

developed any prior plastic deformation. The absence of closure effects for newly initiated cracks helped explain why low stress ratio loadings and compressive loadings resulted in faster crack growth rates than were predicted from long crack data[16].

It was discovered that cracks with different lengths, but the same ΔK, behaved differently[3,10,11]. The large difference between growth rates was attributed to crack length where the observed growth rates were much faster than those predicted from the available da/dN-ΔK relationships[3,5,9,10,14,16].

Laz[1], Newman et al.[5], Newman and Edwards[15], and Edwards and Newman[17] used a single edge notch tension (SENT) specimen to investigate the initiation and growth behavior of small cracks. This specimen design was initially chosen because it simulated the behavior of an open hole in an aircraft structure[15]. It was found that cracks nucleated in the center of the notch and in the middle 50% of the thickness.

Various investigations[5,14,15] have shown that there is an inherent nature about fatigue that produces varying fatigue lives for seemingly identical test configurations. Recently, investigators have made attempts to predict the variation in fatigue results[1,11,13]. In Laz' study[1] of 2024-T3 aluminum sheet, a probabilistic method was developed to predict the variability in fatigue lives based on microstructural variability. The probabilistic model was found to provide a good prediction of the experimental fatigue lives and the associated variability.

Laz' analysis implemented a Monte Carlo simulation to make analytical predictions of variability. A Monte Carlo simulation is a numerical method that is well-suited for generating a sample of results when the variables involved are related by complex mathematical equations. Also used in the analysis was FASTRAN II[18], a numerical crack growth model. This computer program, developed by Newman and referred to as "FASTRAN", incorporates the previously discussed theories of closure, small-crack effects, and da/dN-ΔK_{eff} relations. In the FASTRAN model, ΔK_{eff} is applied throughout the analysis, and the corresponding growth increment is calculated. In this study, as well as in Laz' study, FASTRAN was used to numerically grow the cracks to breakthrough.

MATERIALS AND METHODS

Aluminum 7075-T6 Sheet

The material used in this study was an aluminum Al-Zn-Mg alloy 7075-T6 in the form of 2.31 mm thick sheet. This previously untested panel was of the same lot as that tested by Edwards and Newman[17]. The da/dN-ΔK_{eff} data was developed by Newman et al.[5] for this material, and therefore, no measurements of crack growth rates were performed.

Large constituent particles on the order of 2-50 μm in size are formed during the processing of the sheet material. These particles are detrimental to the fatigue resistance of the alloy and actually act as fatigue crack formation sites[20].
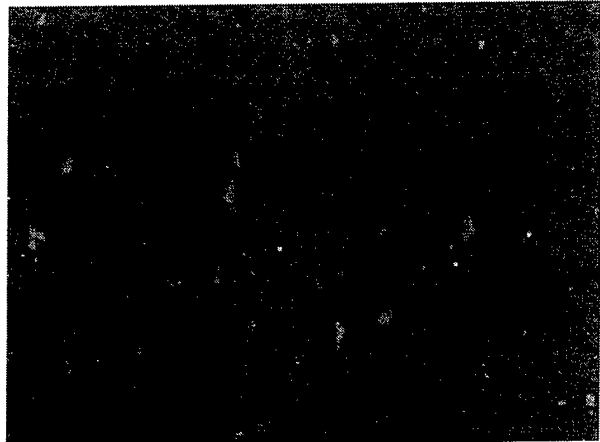

Figure 1: ESEM Image of ST Plane at 500X

Figure 1 shows the appearance of these larger particles on the ST plane of the 7075-T6 used in this study. The types of particles and precipitates formed in this alloy have nominal chemical compositions of $MgZn_2$, $Mg_3Zn_3Al_2$, Mg_2Si, Al_7Cu_2Fe, and Mg_5Al_3. Table 1 gives some of the mechanical properties of the 7075-T6 alloy[19].

Table 1: Mechanical Properties of 7075-T6[5,19]

	$S_{Y0.2\%}$, MPa	S_u, MPa	K_c, MPa-m$^{1/2}$
7075-T7	503	572	50

Experimental Testing

Test Specimens

A SENT specimen geometry was used for the experimental component of this investigation. The dimensions for the specimens are based on previous studies[1,5,15]: length = 216mm, width = 45mm, thickness = 2.235mm, and notch radius = 2.92mm. The single notch was used to localize the region within which cracks would initiate. Figure 2 shows the orientation of the metallurgical planes and the loading direction with respect to the specimen. Also shown in the figure is the orientation of the crack that forms in this type of specimen. Laz[1] and Murakami and Endo[21] observed that the ST plane is the most relevant plane for nucleation sites in this type of configuration.
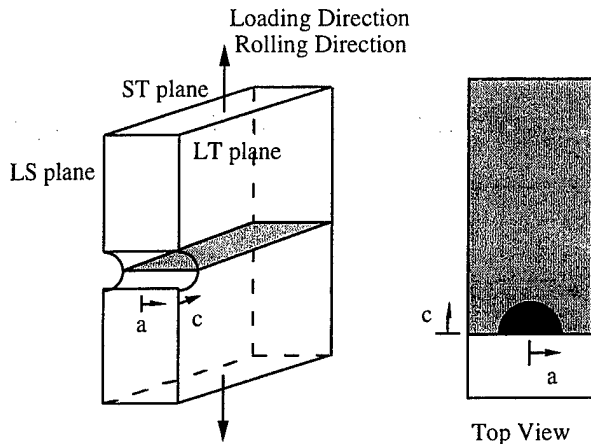
Figure 2: SENT Geometry and Orientation of Metallurgical Planes

Specimen Preparation

A total of 18 specimens were cut from one panel of the NASA material. To minimize the residual stresses, a series of decreasing depths of cut were used to machine the notch, followed by a chemical polishing procedure. The chemical polishing process[5] removed a uniform, thin layer of material from the specimen, approximately 40 μm from each surface. The polishing procedure removed any remaining scratches and helped reduce any remaining residual stresses. The testing dimensions were chosen so that the ΔK solution as developed by Newman would be applicable[5].

Test Conditions

The tests were run in laboratory air using a 10 Hz, constant amplitude sine wave. The maximum nominal stress applied was 120 MPa, and the minimum stress was 1.2 MPa so that the tests were run at a stress ratio, R, of 0.01. The load cycle was paused after predetermined cycle increments so that a replication procedure could be performed. To replicate the notch surface, the load cycling was stopped at the mean load, and the load was raised to 80% of the maximum load. A drop of high purity acetone was applied to the notch surface, and the acetyl cellulose film was lightly pressed into the notch. The acetone was allowed to set for a period of five minutes before the replica was removed. Replicas were examined at approximately 220X for the presence of cracks in the notch. At this magnification, a crack was detectable after it reached a length of about 20-40 μm. For each test the cycles to breakthrough, N_b, and the cycles to failure, N_f, were recorded.

The purpose of the replicas was to make a microscopic record of the notch surface throughout testing as well as to monitor crack growth. Each replica was stored so it could be examined in greater detail after testing. The replicas were examined in reverse order to help find the location and nature of the initial crack formation site.

Determination of ΔK_{th}

A value for ΔK_{th} was calculated from the experimental fatigue lives. Using the longest, finite experimental life, FASTRAN was used to determine the initial crack size, A_i corresponding to the threshold. However, there is still a possibility to observe a longer lifetime than those observed in this investigation. To address this possibility, the cumulative distribution value associated with the longest lifetime was taken to be the cumulative distribution value of the corresponding initial crack size, A_i. The threshold crack size, A_{th}, was determined by finding the appropriate crack size that matched the cumulative percentage based on the area distribution to the observed cumulative percentage for the longest, finite lifetime. The threshold area is used as a lower bound for initial areas in the probabilistic model, which will be discussed later. The assumption is that any initial crack with an area below the threshold value will not propagate.

PROBABILISTIC MODELING

Based on the observations and theories from the literature, several assumptions are incorporated into the probabilistic model:

- cracks form at particles at the center of the notch (0° from the ST plane)
- crack formation occurs in the middle of the specimen thickness
- cracks form as surface cracks and assume a semi-circular shape in the ST plane
- nucleating defect is assumed to be a flat crack
- the crack propagation path is parallel to the ST plane
- formation life is a small percentage of the total life and can be neglected

For the probabilistic model, particle areas were measured and fit to a 3-parameter log-normal distribution. The distribution was then used for two separate failure predictions. The first prediction used a Monte Carlo simulation to sample, from the estimated distribution of particle areas, 1000 initial crack sizes greater than the threshold area. These generated cracks were numerically grown to failure using FASTRAN. The second prediction used conditional probability to create a cumulative distribution for particle size and then took advantage of the one-to-one relation between particle area, A_i, and life to breakthrough, N_b to compile a cumulative distribution function (CDF) for fatigue lives. The Monte Carlo procedure, implemented in earlier work by Laz[1], produces an estimate of the exact CDF. The conditional probability procedure is an

improvement since it produces the exact CDF. Both procedures are used here to verify previous results.

Area Distribution Analysis

For particle analysis, two small coupons of sheet material were cut out of the larger panel from which the test specimens were made. The coupons were mounted in bakelite so that the short-transverse (ST) plane of the material, which is the plane of the resulting fatigue crack, was exposed. The ST surface was polished using 100, 320, 400, and 600 grit rotating sanding wheels. Two wet polishes, a 5 μm diamond paste and a 0.05 μm CrO₃ slurry, were used to achieve the final surface finish.

To document the particle area distribution, the mounted coupons were photographed using an environmental scanning electron microscope (ESEM). Twenty pictures of the ST plane were taken at a magnification of 500X. One such image is shown in Figure 1. The pictures were taken across the entire exposed area of the coupons so as to take a representative sample of the particle distribution. The particles in the plane perpendicular to the loading direction are the particles relevant to the initiating crack shapes[1,21]. The particles in the ST plane were analyzed because the ST plane is the plane perpendicular to the loading direction for this specimen and loading orientation.

An image analysis package, IMIX[22], was used to measure the area of each particle. Figure 3 shows the binary image corresponding to Figure 1. After calibration, the program converted the white pixels into particle areas. The image analysis resulted in measurement of 1282 particles from the total area examined which was a little more than 0.5 mm².

Figure 3: Black and White Image (of Figure 1) Used in Particle Analysis

As in Laz' analysis of 2024-T3, a 3-parameter log-normal distribution was fit to the distribution of particle areas. Equation 3 shows the general form of the density function of a 3-parameter log-normal distribution.

$$f(A) = \frac{1}{\sqrt{2\pi}(A-\theta)\sigma} \exp\left[-\frac{1}{2}\left(\frac{\ln(A-\theta)-\zeta}{\sigma}\right)^2\right] \quad (3)$$

where θ, σ, and ζ represent the threshold, shape, and scale parameters, respectively. To fit these parameters to the measured data, a process similar to that given in Johnson et al.[23] was followed. The value of θ was iteratively selected to find the best fitting set of three parameters for the estimated density function. The log-normal parameters θ, ζ, and σ were found to be 0.191 μm², -0.6772, and 1.8838, respectively.

To test the normality of the logarithms of particle area, a Kolmogorov D test was used. The observed Kolmogorov D statistic was 0.0418 and resulted in a p-value of < 0.01. This means that the calculated set of three parameters should be rejected as the true set of three parameters for the true distribution. However, if the log-area measurements are normalized to the standard normal variate via equation 4[24],

$$z = \frac{\ln(A-\theta)-\zeta}{\sigma} \quad (4)$$

the transformed variables have a mean of 0.0000180 and standard deviation of 0.999981. For the ideal standard normal distribution, the mean is 0.0 and standard deviation is 1.0. It is apparent that the normalized mean is nearly zero, and the standard deviation is approximately 1.0. With over 1200 observations, the Kolmogorov goodness of fit test is sensitive to very slight variations from normality, especially variations in the tails of the distribution. This appears to be the case here. Since the mean and standard deviation of the standardized variates are so close to what is expected, it is assumed that the estimated log-normal distribution explains the data adequately. Figure 4 shows the histogram of the particle distribution as well as the probability density function for the particle area. From this figure, it can be seen how well the 3-parameter log-normal distribution fits the observed particle areas.
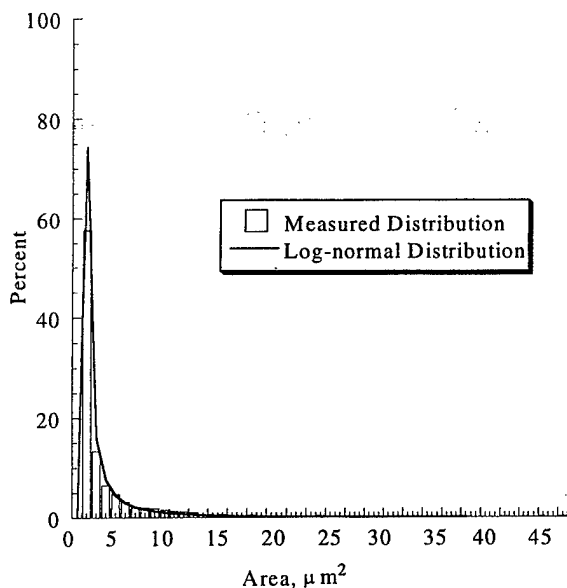
Figure 4: Histogram of Particle Areas on ST Plane

Monte Carlo Simulation

For this analysis, 1000 particles with areas above A_{th} were randomly chosen from the estimated log-normal distribution. A computer program, written in C, was used to accomplish the selection process. From the observations of Lankford[10] and Newman and Edwards[15] of crack shape, each generated A_i was converted to an equivalent-area semi-circular initial crack of radius r_i by use of equation 2. Each r_i was given to the numerical crack growth model FASTRAN.

To complete the Monte Carlo analysis, the 1000 generated fatigue lives were compiled to create a non-parametric CDF. Using a Kolmogorov test, a degree of fit between the experimental CDF and the numerical CDF for lives was calculated to measure the effectiveness of the predictions.

Conditional Probability

As mentioned earlier, the idea of a threshold initial area was used to bound the lower values of areas used in the numerical analysis. Since a propagating crack must already be at or above this threshold size, conditional probability calculations can be used to describe the remaining portion of the density function.

The concept of conditional probability implements relations between the probability of occurrence of events. The general formulation for conditional probability gives the probability that event X occurs given that event Y has already occurred. For the conditional probability,

$$P(X|Y) = \frac{P(X \cap Y)}{P(Y)} \qquad (5)$$

assuming $P(Y) \neq 0$. To create a CDF for N_b would require the calculation of the values in equation 6.

$$F(N_b) = P(N_b < N) \qquad (6)$$

The relationship between A_i and N_b (for a given crack shape) is one-to-one, and essentially, A_i is inversely proportional to N_b. Because A_i and N_b are inversely proportional, events of equation 6 are described as follows:

- Event X: the probability that the initial area is greater than a given value of A
- Event Y: the probability that the initial area is larger than A_{th}

Since event X always satisfies the condition of event Y, the probability of the intersection of X and Y is equivalent to the probability of X alone, and equations 5 and 6 are combined to give equation 7.

$$F(A) = \frac{P(x > A)}{P(x > A_{th})} \qquad (7)$$

Conditional probability analysis in this manner allows the values of area to be chosen in any region of the particle distribution. The particles do not have to be randomly chosen. In addition, this approach results in the exact CDF of fatigue life, whereas the CDF from the Monte Carlo procedure is an estimate of this CDF. Also, with the conditional approach, the tail regions can be examined more closely and sampling errors eliminated.

RESULTS

Experimental Program

Each test specimen from the experimental component of this test program provided four major pieces of data: cycles to crack formation, N_i, cycles to breakthrough, N_b, cycles to failure, N_f, and a series of plastic replicas

A summary of N_i, N_b, and N_f for all 18 tests is given in Table 2. The shortest life to breakthrough was 36,800 cycles, and the longest finite life was 650,000 cycles. One specimen failed in the gripping mechanism of the test machine at 600,000 cycles and was treated as a run-out, reducing the number of actual fatigue failures under scrutiny to 17. It can be mentioned that at 500,000 cycles no visible cracks were observed on the specimen that failed in the grips. As for N_f, regardless of the number of cycles to breakthrough, the number of cycles beyond breakthrough necessary to reach failure showed an average of 6045 cycles with a standard deviation 1144 cycles.

Table 2: Summary of Cycles to Crack Formation, Breakthrough, and Failure

Test	N_i	N_b	N_f
1	70000	108000	115566
2	170000	203000	209711
3	16000	50000	55015
4	(failed in grips)		*600000
5	100000	143000	147919
6	100000	155000	160795
7	1000	72000	77150
8	10000	42000	48272
9	35000	90000	93281
10	NA	105000	110443
11	>425000		650000
12	85000	130000	136170
13	7000	52000	58626
14	140000	170000	177400
15	85000	120000	127339
16	70000	95000	100876
17	7000	42700	49560
18	16000	36800	42501

Crack Formation Sites

For most of the specimens, examining the replicas in reverse order under an optical microscope enabled easy identification of the nucleating defect for most of the specimens. However, the initiation site was indiscernible for three specimens. From fractographic analysis, all the initiation sites were located, but the exact feature that initiated the crack was not evident for some specimens. The optical microscope and ESEM served as a cross-reference as well as a means to classify the nucleation site if one method was indeterminate. Using the combined results from the optical microscope and the ESEM images, 11 of the 17 critical flaws were found to nucleate at particles at or near the surface of the notch. Three cracks formed from a combined effect of either a pore and a particle or a void and a particle at or within 10-20 μm of the notch surface. The nucleation sites for the other three specimens were unable to be determined. The measured areas were converted to equivalent-area, semi-circular initial cracks, which were grown to failure using FASTRAN. The results of the FASTRAN predictions showed that the longest observed lives did not always correspond to the smallest initiating areas.

Figures 5-8 show ESEM images of two fracture surfaces and optical microscope digital images of the replicas from the corresponding two specimens. Figures 5 and 7 are ESEM images of the bottom fracture surface (which is contained in the ST plane) with the notch to the left side of each picture. Figures 6 and 8 are digital images of the replica surfaces where the ST plane is a horizontal line through the visible crack. Some of the replicas showed the crack soon after nucleation. These replicas exhibited the most easily identifiable initiation sites.
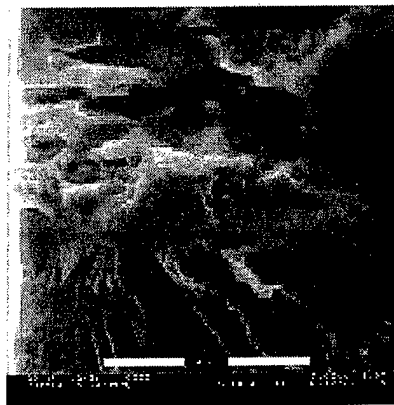

Figure 5: ESEM Image of Specimen 18 Fracture Surface

Figure 6: Digital Image of Replica From Specimen 18 After 16,000 Cycles

Figure 7: ESEM Image of Specimen 9 Fracture Surface

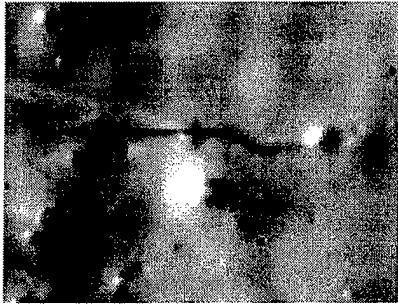American Institute of Aeronautics and Astronautics

Figure 8: Digital Image of Replica From Specimen 9 After 16,000 Cycles

From these images, the irregular shape of the nucleating particles can be observed. The images of the replicas show the presence of other, non-nucleating particles on the notch surface. Also visible in the replica images is how the cracks grew perpendicular to the loading direction soon after forming.

Three common results were observed in the specimens, in addition to most of the cracks initiating at inclusions:

- most cracks initiated in the middle 50% of thickness
- most cracks initiated 12° or less from the root of the notch
- one and only one initiation site was observed for all 17 finite life specimens

All the cracks initiated as surface cracks, and 13 out of 17 cracks initiated inside the middle 50% of the thickness. As far as position from the root of the notch, 13 out of 17 cracks initiated within ±12° of the root of the notch.

Threshold ΔK

From all the experimental testing, there were 18 measured fatigue lives under identical loading conditions. As mentioned earlier, one of these specimens was treated as a run-out. The remaining finite life test specimens reached breakthrough at or before 650,000 cycles. Two analyses were made of the threshold behavior for the 17 finite life specimens. For one analysis, the specimen that reached breakthrough at 203,000 cycles represented the lowest applied initial ΔK resulting in finite life. The FASTRAN results gave an initial crack size with radius of 6.062 μm. The corresponding initial ΔK was 1.3 MPa$\sqrt{m}$, as calculated using the equations for a semi-circular surface crack, and this value of ΔK is considered to be ΔK_{th} for this configuration. The results for the predicted CDFs with ΔK_{th} = 1.3 MPa$\sqrt{m}$ are shown in Figure 9. From the figure it can be seen that the predicted curve follows the experimental results quite well, and a more thorough discussion of this figure can be found in a later section. For the second analysis, the specimen that

reached breakthrough at 650,000 cycles represents the theoretically lowest applied initial ΔK. For this trial, the threshold crack size was an area with radius of 4.775 μm corresponding to a ΔK_{th} of 1.17 MPa$\sqrt{m}$. The results for the predicted CDFs with ΔK_{th} = 1.17 MPa$\sqrt{m}$ are shown in Figure 10. From the figure it can be seen that the predicted curve follows the experimental results quite well for the first few points, but becomes much more unconservative for longer lives. A more thorough discussion of this figure is found in a later section.

For purposes of this investigation, the ΔK_{th} determined from the longest lifetime was based on crack propagation and did not evaluate nucleation life. In the analysis where ΔK_{th} was determined to be 1.3 MPa$\sqrt{m}$, the failure at 650,000 cycles was treated as an incubation dominated lifetime. If the lifetime were adjusted for initiation life (>425,000 cycles for this specimen), the resulting life to breakthrough of 225,000 cycles would lie very close to the predicted curve of Figure 9.

Cycles For Crack Formation

Many of the test specimens did not exhibit visible crack formation early in fatigue life. Specifically, several specimens did not develop a visible crack until after 100,000 cycles. Yet most of these test samples sustained full fatigue failure at or before 203,000 cycles. This seems to indicate that there was an incubation life for some of these specimens. Though the model does not incorporate an incubation period, the fatigue lives of the experimental trials are within the distribution of lives predicted by the probabilistic model. The 650,000 cycle failure is outside the range of predictions based on ΔK_{th} = 1.3 MPa$\sqrt{m}$, but would be inside the range of predictions for the analysis where ΔK_{th} = 1.17 MPa$\sqrt{m}$. For the 6 specimens which failed at or before 70,000 cycles, the average initiation life was 15% of the life to breakthrough. For the other 10 specimens where initiation life was measured, the average initiation life was 68% of the life to breakthrough. An important result for consideration is that the specimen which failed at 650,000 cycles had a nucleation life greater than or equal to 425,000 cycles.

Probabilistic Analysis

Results from Both Numerical Techniques

In the Monte Carlo simulation, a total of 1000 particle sizes were generated from the estimated log-normal density function for the particle areas. The distribution of lives to breakthrough that resulted from the computer simulations formed one prediction for the

7

variability of fatigue lives. The second prediction is the distribution of lives to breakthrough from the conditional probability technique. For ΔK_{th} = 1.3 MPa$\sqrt{m}$ and ΔK_{th} = 1.17 MPa$\sqrt{m}$, the non-parametric CDF from the Monte Carlo predictions is shown by the solid line in Figure 10, and the conditional probability results are shown by the dashed line. As introduced earlier, the longest life predicted by the numerical analysis was the N_b that was used to estimate the threshold value for the SENT geometry at 120 MPa.
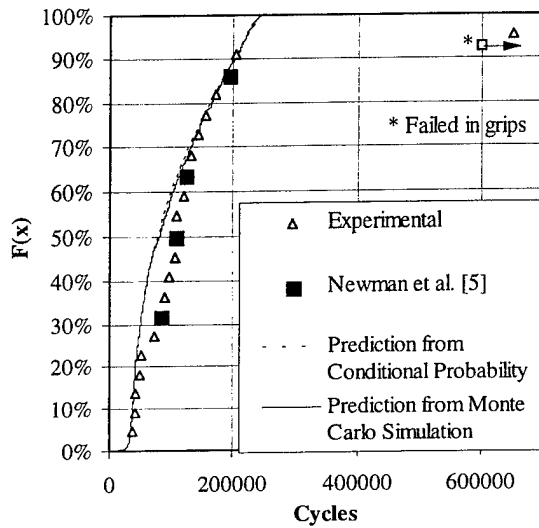
Figure 9: Combined CDFs for Cycles to Breakthrough with ΔK_{th} = 1.3 MPa$\sqrt{m}$

Comparison of Numerical and Experimental Results

The combined predicted and experimental results shown in Figures 9 and 10 include four experimental data points from Newman et al.[5]. In Newman's investigation of 7075-T6 aluminum, SENT specimens of nearly identical dimensions to those used in this study were tested. The four specimens tested by Newman were cycled at 120 MPa and a stress ratio of 0. Also, these specimens had the same stress concentration factor, K_T, at the notch as the specimens used in this investigation.

Figures 9 and 10 show the fatigue life to breakthrough results from both the numerical and experimental components of this investigation. One set of predicted fatigue lives, shown by the solid line, are the results of the Monte Carlo simulation. The second set of predicted lives, shown by the dashed line, are the results of the conditional probability technique. The experimental lives, N_b, were also compiled into a non-parametric CDF using an i/(N+1) formulation where i is the ordered number of the data point and N is the total number of data points (all studies), in this case 21.

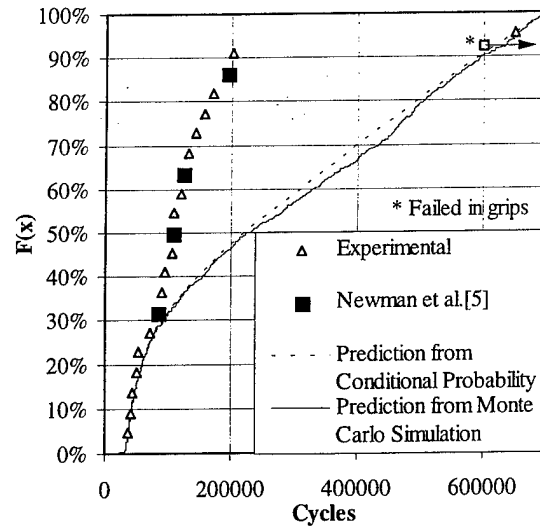Figure 10: Combined CDFs for Cycles to Breakthrough with ΔK_{th} = 1.17 MPa$\sqrt{m}$

From the figures, it is apparent that the Monte Carlo results are a good approximation for the cumulative distribution of lives to breakthrough from the conditional probability method. From Figure 9 where ΔK_{th} = 1.3 MPa$\sqrt{m}$, it is apparent that the two numerical predictions provide a good prediction of the shortest experimental fatigue lives. On the whole the numerical predictions make conservative predictions for the lives to breakthrough of the experimental trials. As for the overall distribution of lives, the ratio of observed life to predicted life ranged from 1.01 to 1.6. From Figure 10 where ΔK_{th} = 1.17 MPa$\sqrt{m}$, only the first few early failures are closely predicted. For this lower ΔK_{th}, the predictions overall are unconservative and the ratio of predicted life to observed life ranges from 1.01 at the shortest lifetimes to 3.0 at the longer lifetimes.

The Kolmogorov D test was utilized to compare the largest difference between the numerical CDF and the experimental CDF, where a statistical "rejection" would mean that the two distributions are different at a particular level of significance. For 20 degrees of freedom, the critical D statistic is 0.45 at an α level of 0.05 and 0.55 at an α level of 0.01. For the analysis corresponding to ΔK_{th} = 1.3 MPa$\sqrt{m}$, the observed value of the D statistic for these two CDFs was 0.246. This result indicates that there is no significant evidence to suggest these two CDFs are different at either significance level. For the analysis corresponding to ΔK_{th} = 1.17 MPa$\sqrt{m}$, the observed value of the D statistic for these two CDFs was 0.46 For the analysis using the ΔK_{th}, the observed test statistic is larger than the critical value for α = 0.05 and close to the critical value for α = 0.01. These results for the CDF where

8
American Institute of Aeronautics and Astronautics

ΔK_{th} = 1.17 MPa$\sqrt{m}$ mean that the curves come from different distributions at the 0.05 level and are almost rejected at the 0.01 level also.

DISCUSSION

Scatter In Fatigue Lives

Consistent with fatigue studies throughout the past, there was variability observed in the experimental fatigue lives within this experimental program. Within the finite N_b alone, there was over a 15:1 ratio of the longest life to the shortest life.

Crack Nucleation From Particles

Also consistent with previous fatigue studies, most of the cracks observed in the test specimens formed at particles (11 out of 17). This result is important information because it is one of the underlying assumptions of the probabilistic approach. The attempt to predict the variability in lifetimes is based on the variability of initial crack sizes.

Cracks Initiated From Largest Particles

For the eleven nucleation sites that could be identified as particles, the sizes of these particles (30-7200 μm^2) tended to be from the tail of the distribution that contained the largest particles. The tail of the distribution of particle areas results in the shortest fatigue life, which is the region of greatest interest. This may suggest that an extremal distribution might be a more appropriate choice to characterize the particle areas. Additionally, if the number and size of these largest particles can be reduced, there is good reason to expect that the resistance of the material to fatigue damage may be improved.

Best Agreement In Shortest Life Region

By examining Figures 9 and 10, it is apparent that there was good agreement between predicted and experimental lives in the shortest life region. From a design point of view, the shortest lives are the most critical. Better predictions for early fatigue failures can enable more reliable recommendations to be made for maintenance, safety schedules, and fatigue design in general. From this standpoint, the results of the probabilistic technique for the prediction of fatigue failure in 7075-T6 aluminum show a favorable degree of accuracy. For the overall distribution of lives where ΔK_{th} = 1.3 MPa$\sqrt{m}$, the ratio of observed life to predicted life ranged from 1.01 to 1.6. For the overall distribution of lives where ΔK_{th} = 1.17 MPa$\sqrt{m}$, the ratio of observed life to predicted life ranged from 0.333 to 1.01, and the predictions tended to be unconservative. From the results shown in Figures 9 and

10, it is apparent that the effectiveness of the probabilistic model is heavily dependent upon the value of ΔK_{th}, the crack growth rate characteristics of the material, and its crack nucleation behavior.

Modeling Assumptions

Most of the modeling assumptions were satisfied by the observed fatigue cracks. Cracks initiated as surface cracks, and the nominal crack propagation plane was perpendicular to the loading direction. The majority of the cracks initiated from particles in the center of the notch and in the middle of the sheet thickness. From the particle analysis the average aspect ratio was found to be 1.7 which is different from the semi-circular assumption where the aspect ratio should be 1. The shape of the initiation site and whether the initiation site is a hard particle, a debonded particle, or a cracked particle may affect the accuracy of the ΔK calculations.

Though most of the assumptions of the probabilistic method were satisfied for the 7075-T6, assuming a short nucleation life did not appear to be accurate for all of the specimens. One specimen, for example, showed no visible cracks until 140,000 cycles. For this specimen, the initiation life was about 2/3 of the total life of the specimen. Many of the other specimens exhibited considerable initiation lives as well. This result was not expected, at least in reference to Newman et al.[5] and Bowles and Schijve[25]. This observation suggests that the results of this probabilistic approach might be improved if a nucleation period is considered. Also, including a nucleation life may improve the overall performance of the probabilistic model, in addition to the characteristics of the nucleating particle.

The ΔK_{th} calculations made here are based entirely on crack propagation. Hence, treating the 650,000 cycle failure as a crack that initiated early in the loading history would be inaccurate since an initiation life of 425,000 cycles was observed. The discrepancy may need to be addressed by separating the effects of threshold behavior from the effects of an incubation life. The result of ignoring this discrepancy is realized in erroneous calculations of ΔK_{th}. Thus, including the specimen that showed an initiation life of 425,000 cycles would be an inaccurate assessment.

The use of acetone has been reported to increase the fatigue life of 7075-T6[5]. In the study by Newman, acetone was used in the replication procedure, but in contrast to some of the results reported here, short initiation lives were observed. Although longer fatigue lives from the use of acetone has not been fully explained, one suggestion is that the acetone removes any water vapor from the crack and effectively reduces environmental attack on the crack surfaces. Proposing the reduced environmental effect would follow from the

results observed by Gao et al.[26], where it was found that 7075-T651 plate showed slower crack growth rates under vacuum conditions than in humid air. However, Lankford[27] reports that 7075-T6 sheet shows the same average rate of crack extension in humid air as under vacuum conditions. Thus it is not clear what the effect of acetone is and how it may have influenced the results in this study, if at all.

CONCLUSIONS

The major conclusions drawn from this investigation are as follows:

1. The probabilistic model closely predicted the shorter fatigue lives.
2. Crack nucleation sites were particles.
3. Nucleating particles were from the large tail of the particle area distribution.
4. Cracks formed as surface cracks at the root of the notch and in the middle of the sheet thickness.
5. Nucleation lives were a significant portion of the total fatigue lives.
6. The irregular shape of many of the nucleating particles may affect the initial crack driving force.

The results of this investigation show that the effectiveness of the probabilistic model is dependent on the nucleation behavior of the material. From this perspective, adopting a nucleation analysis into the total prediction procedure may improve results.

REFERENCES

1. Laz, P., M. S. Thesis, Purdue University, 1996.

2. Turnbull, A., and DE LOS Rios, E. R., 1995, "Predicting Fatigue Life in Commercially Pure Aluminum Using a Short Crack growth Model," *Fatigue and Fracture of Engineering Materials and Structures*, Vol. 18, No. 12, pp. 1469-1481.

3. Newman, J. C., Jr., 1992, "Fracture Mechanics Parameters for Small Fatigue Cracks," *Small-Crack Test Methods, ASTM STP 1149*, J. Larsen and J. E. Allison, Eds., American Society for Testing and Materials, Philadelphia, pp. 6-33.

4. Turnbull, A., and DE LOS Rios, E. R., 1995, "The Effect of Grain Size on the Fatigue of Commercially Pure Aluminum," *Fatigue and Fracture of Engineering Materials and Structures*, Vol. 18, No. 12, pp. 1455-1467.

5. Newman, J. C., Jr., Wu, X. R., Venneri, S. L., Li, C. G., 1994, "Small-Crack Effects in High Strength Aluminum Alloys", *NASA/CAE Reference Publication 1309*.

6. Miller, K. J., 1982, "The Short Crack Problem," *Fatigue of Engineering Materials and Structures*, Vol. 5, No. 3, pp. 223-232.

7. Forsyth, P. J. E., 1969, *The Physical Basis of Metal Fatigue*.

8. Plumbridge, W. J., and Ryder, D. A., 1969, "The Metallography of Fatigue," *Metals Material Review 136*, Vol. 3, pp. 321.

9. Pearson, S., 1975, "Initiation of Fatigue Cracks in Commercial Aluminum Alloys and the Subsequent Propagation of Very Short Cracks," *Engineering Fracture Mechanics*, Vol. 7, pp. 235-247.

10. Lankford, J., 1982, "The Growth of Small Fatigue Cracks in 7075-T6 Aluminum," *Fatigue of Engineering Materials and Structures*, Vol. 5, No. 3, pp. 233-248.

11. Akiniwa, Y., Tanaka, K., Matsui, E., 1988, "The Growth of Small Fatigue Cracks in 7075-T6 Aluminum," *Materials Science and Engineering*, A104, pp. 105-115.

12. Navarro, A., and DE LOS Rios, E. R., 1988, "A Microstructurally-Short Fatigue Crack Growth Equation," *Fatigue and Fracture of Engineering Materials and Structures*, Vol. 11, No. 5, pp. 383-396.

13. Demulsant, X., and Mendez, J., 1995, "Microstructural Effects on Small Fatigue Crack Initiation and Growth in Ti6Al4V Alloys," *Fatigue and Fracture of Engineering Materials and Structures*, Vol. 18, No. 12, pp. 1483-1497.

14. Wu, X. J., and Akid, R., 1995, "Propagation Behavior of Short Fatigue Cracks in QN Steel," *Fatigue and Fracture of Engineering Materials and Structures*, Vol. 18, No. 4, pp. 443-454.

15. Newman, J. C., Jr., and Edwards, P. R., 1988, "Short-Crack Growth Behavior in an Aluminum Alloy - An AGARD Cooperative Test Programme," AGARD Report No. 732.

16. Newman, J. C., Jr., 1994, "A Review of Modeling Small-Crack Behavior and Fatigue-Life Predictions for Aluminum Alloys," *Fatigue and Fracture of Engineering Materials and Structures*, Vol. 17, No. 4, pp. 429-439.

17. Edwards, P. R., and Newman, J. C., Jr., 1990, "An AGARD Supplemental Test Programme on the Behavior of Short-Cracks Under Constant Amplitude and Aircraft Spectrum Loading," AGARD Report No. 767.

18. Newman, J. C., Jr., 1992, FASTRAN II Manual. NASA Technical Memorandum 104159.

19. American Society for Metals, 1990 Metals Handbook: *Properties and Selection: Nonferrous Alloys and Pure Metals,* 10th Edition, Vol. 4, pp. 70-73 and 114-117.

20. American Society for Metals, 1984, *Aluminum: Properties and Physical Metallurgy,* John E. Hatch, Ed.

21. Murakami, Y., and Endo, M., 1986, "Effects of Hardness and Crack Geometries on ΔK_{th} of Small Cracks Emanating from Small Defects," *The Behavior of Short Fatigue Cracks,* K. J. Miller and E. R. de los Rios, Eds., EGF Publication 1, Mechanical Engineering Publications, London, pp. 223-232.

22. IMIX Software. Princeton Gamma-Tech, 1993.

23. Johnson, N. L., Kotz, S., and Balakrishnan, N, 1994, *Continuous Univariate Distributions,* Vol. 1, 2nd Ed., John Wiley & Sons, Inc., pp. 220-222.

24. Johnson, Richard. A., 1994, *Miller & Freund's Probability & Statistics For Engineers,* 5th Ed., Prentice-Hall, Inc., p. 147.

25. Bowles, C. Q., and Schijve, J., 1973, "The Role of Inclusions in Fatigue Crack Initiation in an Aluminum Alloy," *International Journal of Fracture,* Vol. 9, No. 2, pp. 171-179.

26. Gao, Ming, Pao, P. S., and Wei, R. P., 1988, "Chemical and Metallurgical Aspects of Environmentally Assisted Fatigue Crack Growth in 7075-T651 Aluminum Alloy," *Metallurgical Transactions A*, Vol. 19A, pp. 1739-1750.

27. Lankford, J., 1983, "The Effect of Environment On The Growth of Small Fatigue Cracks," *Fatigue of Engineering Materials and Structures,* Vol. 6, No. 1, pp. 15-31.

Acknowledgments

CHARACTERIZATION OF FATIGUE CRACK NUCLEATION SITES IN 2024-T3 ALUMINUM ALLOY

E.A. DeBartolo[*] and B.M. Hillberry[*]

In 2024-T3 aluminum constituent particles are dominant nucleation sites for fatigue cracks. A fatigue life distribution can be generated based on the distribution of constituent particles in the material. The aim of this work is to characterize nucleation sites and determine if a random constituent particle sample is representative of nucleation sites. For this study, the damage state (i.e., cracked, debonded, etc.) and location to nearest grain boundary will be examined. A better representation of the population of nucleating defects would lead to better fatigue life predictions.

BACKGROUND

The objective of this study is to characterize nucleation sites in 2024-T3 aluminum to determine if a general population sample accurately represents the population of nucleating defects. If a particle is damaged (cracked, debonded, etc.) or located near microstructural barriers such as grain boundaries or other constituent particles, the likelihood of that particle being a nucleation site could be affected. This could be critical for fatigue life prediction models that generate a distribution of fatigue lives based on an initial constituent particle distribution (Laz and Hillberry (1)).

Crack nucleation sites have been characterized to some extent by several researchers (Zabett and Plumtree (2), Newman and Edwards, (3), Grosskreutz and Shaw (4), DeBartolo and Hillberry (5)). In general, the nucleation sites in 2024 aluminum alloys (sheet and plate) tend to be cracked or debonded constituent particles or holes where particles have fallen out of the matrix. Analyses in the literature of stress and strain distributions around non-metallic inclusions (Trantina and Barishpolsky (6), Melander (7)) support these observations. Comparisons between cracked or debonded particle configurations and pores in the material indicated that a cracked inclusion could increase the crack driving force by as much as 15% compared with a void and that a debonded inclusion could decrease the

* School of Mechanical Engineering, Purdue University, USA

crack driving force by as much as 10% compared with a void (6). An uncracked, undebonded particle was shown to have lower crack formation driving forces than these other configurations (7).

In another study on the material used in this work (5), microstructural orientation effects were investigated. Fatigue specimens were tested in three different orientations: Cracks forming on the ST face, cracks forming on the LT face with the crack growth direction aligned with the rolling direction, and cracks forming on the LT face with the crack growth direction perpendicular to the rolling direction. In all specimens, no cracks were observed to nucleate at solid particles which were rigidly bonded to the aluminum matrix. All cracks formed at either debonded or cracked constituent particles, or holes where particles had once been. In addition, the two sets of tests with cracks forming on the LT face could be used to compare directly the effects of microstructure. The only two differences between the specimens were constituent particle alignment and grain shape. It was found that having the crack growth direction aligned with the rolling direction resulted in significantly longer fatigue lives. This study also showed that multiple cracking and coalescence early in the fatigue process would have little impact on the fatigue life, which leaves the grain orientation as a leading possible explanation.

There is enough evidence in the literature to suggest that both the particle damage state and the grain boundary distance could influence fatigue life and crack-forming potential of constituent particles. This work will determine if there is a difference between the general population characteristics and the nucleation site characteristics. If there is a significant difference, constituent particle-based fatigue life prediction models may give more accurate results if they use a nucleation site-based particle distribution.

MATERIAL AND METHODS

Microstructural Characterization

The material used in this study was 2024-T3 aluminum alloy sheet which had been rolled to 2.54 mm thickness. The microstructure is shown in Figure 1. It is clear that the constituent particle relative locations and spatial distributions are dependent on the rolled microstructure. The grain sizes also reflect the effects of rolling. Average dimensions were 57.80 μm, 40.82 μm, and 19.58 μm in the longitudinal, transverse, and short directions, respectively (5).

Test Specimens and Methods

The samples used in this study are single edge notch tension (SENT) specimens which were originally tested as part of a previous study on fatigue life prediction (1). The specimens were nominally 203 mm x 45 mm, with a 2.79 mm radius notch machined into the LS face. The notch had a stress concentration of $K_t=3.17$. The notch was machined using a series of decreasing depths of cut, in order to minimize remaining residual stresses. After machining, all specimens were polished in an acid bath (Newman, et al. (8)) which removed machining marks as well as the remaining residual stress layer.

Tests were run at R=0.01 and σ=120 MPa. Replicas of the notch surface had been taken periodically during testing. After testing, the specimens were lightly etched with Keller's etch (10 seconds). After etching the grain boundaries were visible, but the fracture surface and notch surface were not damaged. Fracture surfaces and replicas from the six test specimens were examined after testing and etching to locate the nucleation sites and measure grain boundary distances. Once the nucleating defect was identified and located on the fracture surface, it was found on the pre-test replica. This made it fairly easy to determine whether or not the inclusion was cracked, debonded, or otherwise flawed before the specimen was loaded.

Finally, 100 constituent particles on the LS face were examined at random to generate characteristics of the general particle population. This was done on material that had been polished and etched the same way as the fatigue specimens. The same 100 particles were used to measure grain boundary distances and to record the particle damage state.

RESULTS

The majority of the nucleating defects were found to be cracked particles. Out of 12 observed nucleation sites, 10 were cracked particles. One of the remaining two uncracked nucleating defects, as well as one of the cracked nucleation sites, had debonded from the aluminum matrix. The final uncracked nucleation site, as well as one of the cracked nucleation sites, had a part of the particle missing. All of the cracked nucleation sites were cracked on the pre-test replica, indicating that the particle cracking did not take place as a result of the fatigue loading. Figure 1 shows examples of each of these damage states.

Of the 100 general population particles, 5 were cracked, 15 were debonded from the surrounding matrix, and 28 sites were missing either all or part of the particle (i.e., a hole in the aluminum where a particle had fallen out or a solid particle with an end missing). The few cracked particles were very large relative to most of the examined particles. It is likely that the larger particles may have been broken when the material was rolled to its desired thickness. Figure 2 compares the damage characteristics of nucleation sites with the general population.

Grain boundary measurements could be made on all but two of the nucleation sites. In another case, the distance to the nearest grain boundary could be determined on one side of the nucleating particle, but not on the other side. Of the ten sites the were measured, four were particles which were either directly on a grain boundary or large enough to span an entire grain and, in effect, sat on two grain boundaries (Figure 2). For the ten measured sites, the average distance to the nearest grain boundary was 20.6 μm. This was determined by measuring the distances to the nearest neighboring grains on both sides of each particle (i.e., two data points were obtained for each particle). The average total distance to grain boundaries (treating left side+right side as a single case) was 42.9 μm. Figure 3 shows a box plot of the grain measurements.

For the 100 general population particles, the mean distance from a given particle to the nearest grain boundaries was found to be 8.8 μm (treating each side of each particle as a separate case). In addition, the mean of the total distance to a

grain boundary (right side + left side) was computed as 17.7 μm. These results are also shown in Figure 3. Four particles were located on grain boundaries (Figure 2), and the distances in these cases were measured across each of the two grains containing part of the particle.

DISCUSSION

As expected, the types of particles at which cracks formed were either cracked, debonded, or partially missing particles. This is in agreement with what has been suggested in the literature. It is clear that, while the majority of particles present in the material are undamaged particles that are rigidly bonded to the aluminum matrix, the crack-nucleating particles are overwhelmingly cracked or otherwise damaged. If these cracked or debonded particles are damaged during the rolling process, they would not be nearly as numerous in plate material which has not been rolled as much. This would explain the lack of cracked particles as nucleating defects in studies on aluminum plate (3). Also, the fact that the cracked particles in the general distribution were large relative to the rest of the particles may be a means to finding a material-based threshold for small crack growth.

The grain boundary measurements around nucleating particles showed two differences from the general particle population. First, as shown in Figure 2, a much higher proportion of nucleating defects were located on grain boundaries than was found in the general population. Second, the average distances to neighboring grain boundaries for the nucleation sites that could be measured were over twice the average distance measured for the general population (Figure 3). This would appear to indicate that particles located in the largest grains and/or farthest away from grain boundaries would be most likely to nucleate cracks. The box plots in Figure 3 also shows that there is a large degree of scatter in the data, particularly for the nucleation site measurements. While there is a significant difference between the grain boundary distance measurements of nucleating defects and the general population, more nucleation sites need to be examined to confirm this result.

CONCLUSIONS

The damage state of constituent particles clearly influences their ability to nucleate cracks. An overwhelmingly large percentage of nucleating defects were damaged in some way, mostly cracked. Conversely, the majority of particles in the general population were undamaged particles which were rigidly bonded to the aluminum matrix. It also appears that the location of a particle relative to neighboring grain boundaries is important. Using particle distributions which more closely match these nucleation site characteristics would help particle-based fatigue life models give better life distribution estimates.

REFERENCES

(1) Laz, P.J. and Hillberry, B.M., "Fatigue Life Prediction from Inclusion Initiated Cracks," *International Journal of Fatigue*, v. 20, pp 263-270, 1998.
(2) Zabett, A. and Plumtree, A., "Microstructural Effects on the Small Fatigue Crack Behaviour of an Aluminum Alloy Plate," *Fatigue and Fracture of Engineering Materials and Structures*, v.18, pp 801-809, 1995.

(3) Newman, J.C. and Edwards, P.R., "Short-Crack Growth Behaviour in an Aluminum Alloy - An AGARD Cooperative Test Programme," AGARD 732, December 1988.

(4) Grosskreutz, J.C and Shaw, G.G., "Critical Mechanisms in the Development of Fatigue Cracks in 2024-T4 Aluminum," in *Fatigue 69*, 1969.

(5) DeBartolo, E.A. and Hillberry, B.M., "Effects of Constituent Particle Clusters on Fatigue Behavior of 2024-T3 Aluminum Alloy", *International Journal of Fatigue*, v. 20, pp 727-735, 1998.

(6) Trantina, G.G. and Barishpolsky, M., "Elastic-Plastic Analysis of Small Defects - Voids and Inclusions," *Engineering Fracture Mechanics*, v. 20, pp 1-10, 1984.

(7) Melander, Arne "A Finite Element Study of Short Cracks with Different Inclusion Types under Rolling Contact Fatigue Load," *International Journal of Fatigue*, v. 19, pp 13-24, 1997.

(8) Newman, J.C., Wu, X.R., Venneri, S.L., and Li, C.G., "Small-Crack Effects in High-Strength Aluminum Alloys," NASA/CAE, Reference Publication 1309, May, 1994.

Figure 1. Examples of a (a) cracked particle, (b) a debonded particle, and (c) a particle which is partly missing.
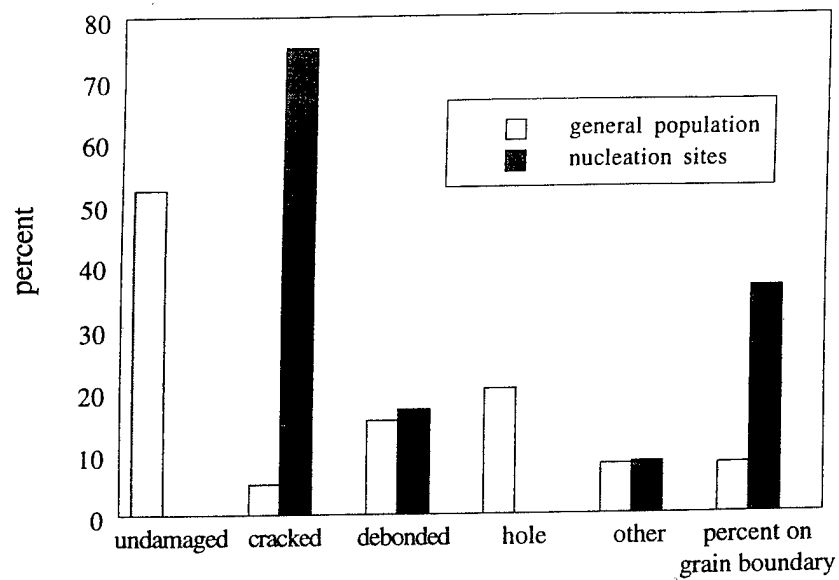
Figure 2. Comparison between characteristics of particles in the general population and characteristics of nucleation sites.
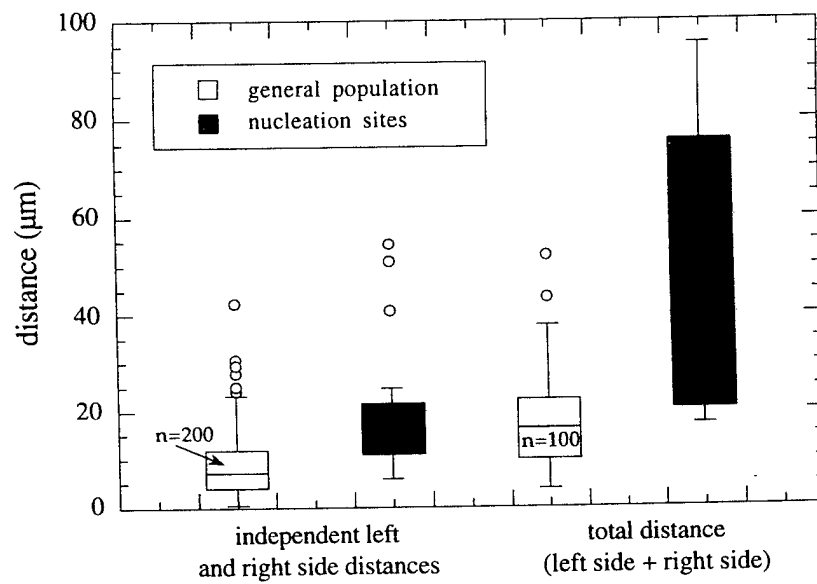
Figure 3. Comparison of distances to neighboring grain boundaries for the general particle population and for nucleation sites. Sample sizes are indicated.

COPYRIGHT AGREEMENT

AGREEMENT made this....29th....day of ...October....19..98........between

NAME _E. A. DeBartolo_   NAME _B. M. Hillberry_

ADRESS _Purdue University_   ADRESS _Purdue University_

School of Mechanical Engineering, Bldg 1288   _School of Mechanical Engineering, Bldg 1288_

West Lafayette, IN 47907-1288 USA   _West Lafayette, IN 47907-1288 USA_

(Please attach a separate sheet for additional names and addresses)

(hereinafter called the AUTHOR(S)) of the one part, and Engineering Materials Advisory Services Ltd, whose Registered Offices is at 339, Halesowen Road, Cradley Heath, West Midlands, B64 6PH, U.K. (hereinafter called EMAS) and Higher Education Press, whose Registered Office is at 55 Shatan Houjie, Beijing, 100009, P. R. China (hereinafter called HEP) of the other part.

EMAS/HEP has undertaken to prepare for publication a book under the title: **Fatigue'99**. The Editor(s) for the publication of this book will be: **X. R. Wu and Z. G. Wang**.

EMAS/HEP has invited the AUTHOR(S) to write a manuscript (which with its drawings, diagrams and photographs is hereinafter called "The Manuscript") to be included as part of the publication and it is intended that EMAS/HEP will also invite other authors to make contributions. Please complete the title of your manuscript:

NOW IT IS HEREBY AGREED as follows:

1. The manuscript will produced in accordance with the instructions using the master sheets provided and sent to the EDITOR(S) no later than 31st October, 1998.

2. EMAS/HEP shall have entire control over the publications, paper, binding, cover and embellishments of the book. EMAS/HEP shall also have entire control over the price and the terms of sale of the book, the manner and extent of advertisements, and the manner and distribution of free copies.

3. EMAS/HEP acquires the sole and exclusive right to print and publish the manuscript and the sole and exclusive copyright. EMAS/HEP will use its endeavors to prevent reproduction and/or re-sale by any third party. The AUTHOR(S) agrees to obtain prior written permission from EMAS/HEP to quote passages from the above publication and to reproduce illustrations, tables and diagrams.

2 LIANG

THE DEVELOPMENT OF A TOTAL FATIGUE LIFE APPROACH ACCOUNTING FOR NUCLEATION AND PROPAGATION

P.J. Laz[*], B.A. Craig[†], S.M. Rohrbaugh[*] and B.M. Hillberry[*]

A fatigue life prediction model has been developed in this study which incorporates crack nucleation and crack propagation. Fatigue life is commonly modeled entirely as crack propagation using fracture mechanics concepts. During experimental testing, however, the life for fatigue crack nucleation was observed to represent a significant portion of the total life. The total life model developed in this study uses a probabilistic Monte Carlo method, where the distribution parameters are obtained from experimental data. The nucleation life distribution is represented as a Weibull distribution, which is fit to the experimentally measured nucleation lives. The propagation life distribution was predicted using the distribution of experimentally measured crack nucleating inclusion sizes and Newman's FASTRAN II life prediction model. The total life model represents the observed fatigue mechanisms and predicts the distribution of fatigue lives better than previous efforts made using only crack growth.

INTRODUCTION

Fatigue crack formation has commonly been observed to occur at inclusions in thin sheet aluminum alloys (Newman and Edwards (1), Laz and Hillberry (2,3)). Previous research on aluminum 2024-T3 (2,3) has shown that fatigue cracks originated at inclusions and that the inclusions that started cracks tended to come from the tail of the distribution of inclusions. Accordingly, the distribution of inclusion sizes were used as the primary input into a probabilistic model, which in conjunction with Newman's FASTRAN II (4) was able to predict the fatigue lives of single edge notch tension (SENT) specimens under constant amplitude loading (2,3). The probabilistic model, using a Monte Carlo simulation, was able to predict the critical shortest fatigue lives and the overall range of values for several loading conditions, but failed to match the shape of the cumulative distribution function (CDF) of experimental fatigue lives.

The original probabilistic model (2,3) and many other models make fatigue life predictions entirely based on crack propagation. Experimental results (2,3, Rohrbaugh (5)), however, have shown that nucleation lives are often significant (sometimes exceeding the propagation life) and therefore, should be included in life prediction models. When using a deterministic model, the assumption to neglect nucleation life results in a conservative result. The present trends of designing for reliability and extending the design life of existing components (i.e. aging aircraft)

[*] School of Mechanical Engineering, Purdue University, West Lafayette, Indiana 47907, USA
[†] Department of Statistics, Purdue University, West Lafayette, Indiana 47907, USA

have led to an emphasis on distributions of results using standard deviation and probability of failure concepts over the traditional mean results. Accordingly, the total life prediction model presented in this paper is total in the sense that it accounts for the mechanisms observed during experimental testing (nucleation and propagation) and that it predicts the distribution of fatigue lives for a stress level (including the critical shortest life, the mean life, and potential runouts), instead of a mean result.

METHODS

Experimental testing was conducted on single and double edge notch tension (SENT and DENT) specimens of 2.54 mm thick aluminum 2024-T3 under constant amplitude loading (R = 0.01 and ΔS = 120 MPa). The experimental data from two studies (2,3;5) have been collected. The SENT specimens in the first study were cycled to breakthrough (through-thickness crack) (2,3), while the DENT specimens from the second study were cycled to a specified lifetime (90,000 cycles) and pulled to failure (5). The SENT tests resulted in a distribution of fatigue lives corresponding to breakthrough, and the DENT tests resulted in a distribution of crack sizes at 90,000 cycles. In both cases, acetate replicas of the notch surface were made at cyclic intervals. The replicas served a dual purpose: to determine the nucleation life and to monitor the growth and coalescence of fatigue cracks.

Crack Nucleation Life

Acetate replicas were taken according to the method developed in Swain (6). By examining the series of replicas under the optical and scanning electron microscopes, a life range (corresponding to the replica increment) containing the nucleation of a crack was determined for each specimen. The lower bound of the range is defined as the longest fatigue life where no fatigue crack was observed on the replica and the upper bound is defined as the life where the first fatigue crack was observed. The size of the range corresponds to the replica measurement increment (e.g. 10,000 cycles).

A Weibull distribution was fit to the nucleation range data from all of the tests using an iterative maximum likelihood estimation technique. The Weibull distribution has a cumulative distribution function F(x) of the form:

$$F(x) = 1 - \exp\left[-\left(\frac{x}{\gamma}\right)^{\phi}\right] \qquad (1)$$

where γ and ϕ are the shape and scale parameters. The fitting technique in this case is complicated by the data being interval censored, containing ranges of fatigue lives instead of specific life values. The γ and ϕ parameters are determined by maximizing the following likelihood function:

$$L(\gamma, \phi) = \prod_{i}\left[F\left(x_{i,upper}; \gamma, \phi,\right) - F\left(x_{i,lower}; \gamma, \phi\right)\right] \qquad (2)$$

which is the product of the terms where $F(x, \gamma, \phi)$ is the Weibull CDF with $x_{i,upper}$ and $x_{i,lower}$ equal to the upper and lower bounds for each of the i nucleation life ranges. In the event that no cracks were observed to form (i.e. a runout or specified life of

90,000 cycles reached), the lower bound was represented by the life when the final replica was taken and the upper bound was assumed equal to infinity (F(x) = 1.0).

Crack Nucleation Sites

Nucleation site data (width, depth, area) were collected from the replicas and fracture surfaces of each specimen using the optical and scanning electron microscopes. Since cracks were observed to grow in the ST plane - perpendicular to the loading and rolling directions, the dimensions and area of the crack nucleating particle were measured from the fracture surfaces in this plane. A log-normal distribution was then fit to the crack nucleating areas. The log-normal distribution was selected because it had provided a good fit to the overall distribution of inclusion sizes (2,3) and the crack nucleating inclusions represent a subset of the overall distribution.

In previous work (2,3), the distribution of all inclusion sizes was used as the initial crack size distribution. A threshold ΔK value was used to determine the critical crack-nucleating inclusion size for the probabilistic model (2,3). However, many microstructural factors (inclusion size and shape, grain orientation, and proximity to grain boundaries) influence crack formation. Although the inclusions that nucleated cracks were located in the tail of the distribution, the observation that the largest inclusion did not always start a crack is evidence that factors other than size are significant. The distribution of actual crack nucleation sites, a subset of the overall distribution, is used in this study and eliminates the speculation over which inclusions nucleate cracks and the need to fit a ΔK threshold value.

Total Life Prediction Model:

The total life prediction model uses a Monte Carlo simulation with the experimentally obtained nucleation life and cracked nucleating inclusion size distributions. In each trial, a nucleation life is selected from the Weibull nucleation life distribution. Additionally, a crack nucleation site is selected from the distribution of crack nucleating inclusion areas. The selected nucleating area is transformed to an equivalent semi-circular crack size, which is then grown to breakthrough using FASTRAN II (4). FASTRAN II is a crack-closure based life prediction model which accounts for crack growth in the short and long crack growth regimes (4). The da/dN versus ΔK effective crack growth rate curve from Newman *et al.* (7) and a threshold ΔK value of 1.05 MPa$\sqrt{m}$ (1) were used in this study. The nucleation life and resulting propagation life were summed to obtain the total fatigue life for each trial. The model was conducted for 2000 trials, which appeared sufficient for convergence.

RESULTS AND DISCUSSION

The experimental nucleation life ranges and the fit Weibull distribution are shown in Figure 1. The Weibull parameters determined from the maximum likelihood estimation technique described in the Methods section are $\gamma = 0.265$ and $\phi = 25976$.

Two typical crack nucleation sites observed on fracture surfaces are shown in Figure 2. The nucleation site is often larger below the surface than it appears on the surface. The distribution of crack nucleating inclusion areas (Figure 3) contains 33 inclusions taken from 7 SENT and 10 DENT specimens tested at the R = 0.01 and ΔS = 120 MPa stress level. A log-normal distribution (Figure 3), with the parameters $\mu = 4.205$ and $\sigma = 0.805$, was fit to the crack nucleating inclusion areas.

TABLE 1 - Comparison of Experimental Fatigue Lives and Total Life Model Results.

Fatigue Lives	Samples	Minimum	Mean	Median	Std. Dev.
Experimental	23	68525	201837	134500	148580
Total Life Model	2000	65503	545050	139142	2526819

The cumulative distribution function for total life is compared in Figure 4 to experimental fatigue life data from the AGARD (1) and SENT (2,3) studies. By examining the contributions of nucleation life and propagation life to breakthrough, Figure 4 shows that the shorter fatigue lives $F(x < 0.5)$ can be modeled accurately using only propagation life. The longer experimental fatigue lives, however, are best modeled as a combination of nucleation and propagation lives. The total life model results in a more accurate prediction of the overall shape of the experimental fatigue life distribution and can be used to predict the presence of runouts. Table 1 presents a statistical comparison between the combined experimental fatigue lives (1,2,3) and the results predicted by the total life model. The model closely predicted the critical shortest total life (Table 1). The median is likely a better method of comparison than the mean and standard deviation, because the presence of long 'infinite' fatigue lives skews the mean and standard deviations predicted by the model. The median (50%) fatigue lives compared well (Table 1).

It is important to note that the nucleation life and crack nucleating inclusion size distributions are stress level dependent. In this study, a relatively large amount of data (7 SENT and 10 DENT specimens) were collected for the $R = 0.01$ and $\Delta S = 120$ MPa stress level. Because of the intensive nature of the experimental testing and data collection, large sample sizes of nucleation lives and crack nucleating inclusions are difficult to obtain. Fitting of distributions to small sample sizes can result in uncertainty. Additionally, the transferability of the distribution functions to other stress levels is presently being investigated.

SUMMARY

In this study, the development of a total fatigue life prediction model accounting for nucleation and propagation is outlined. The model uses experimentally measured nucleation life and crack nucleating inclusion size distributions in conjunction with the FASTRAN II crack closure model to predict fatigue lives. The total life model better reproduces the observed mechanisms and results in a better prediction of the CDF of experimental fatigue lives than previous efforts using only propagation.

REFERENCES

(1) Newman, J.C., Jr. and Edwards, P.R., "Short Crack Growth Behaviour in an Aluminum Alloy", AGARD-R-732, 1988.
(2) Laz, P.J. and Hillberry, B.M., "Fatigue Life Prediction from Inclusion Initiated Cracks", Int. J. Fatigue, Vol. 20-4, 1998.
(3) Laz, P.J., and Hillberry, B.M., "The Role of Inclusions in Fatigue Crack Formation in Aluminum 2024-T3", Fatigue '96, Berlin, Germany, May, 1996.
(4) Newman, J.C., Jr., "FASTRAN II - A Fatigue Crack Growth Structural Analysis Program", NASA-TM-104159, 1992.
(5) Rohrbaugh, S.M., "Probabilistic Fatigue Damage Model for a 2024-T3 Aluminum Alloy", Master's Thesis, Purdue University, 1996.
(6) Swain, M.H., "Monitoring Small-Crack Growth by the Replication Method", Small Crack Test Methods, ASTM STP 1149, Larsen, J. and Allison, J., Ed., 1992.
(7) Newman, J.C., Jr., Phillips, E.P. and Swain, M.H., "Fatigue-Life Prediction Methodology using Small-Crack Theory...", DOT/FAA/AR-97/2, II, July 1997.
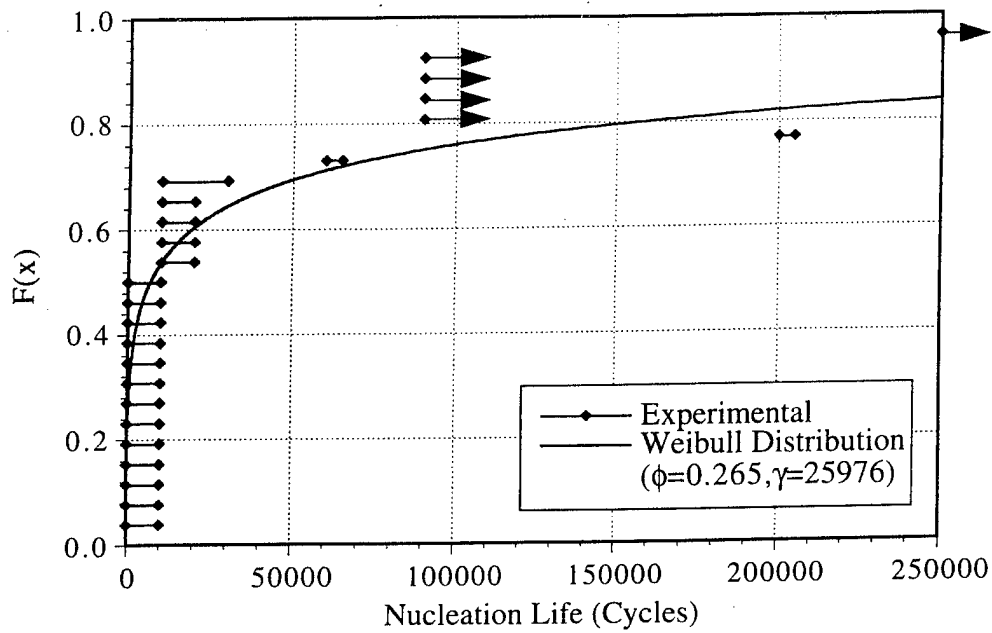
Figure 1. Cumulative distribution function (CDF) of nucleation lives showing the experimental data and the fit Weibull distribution.
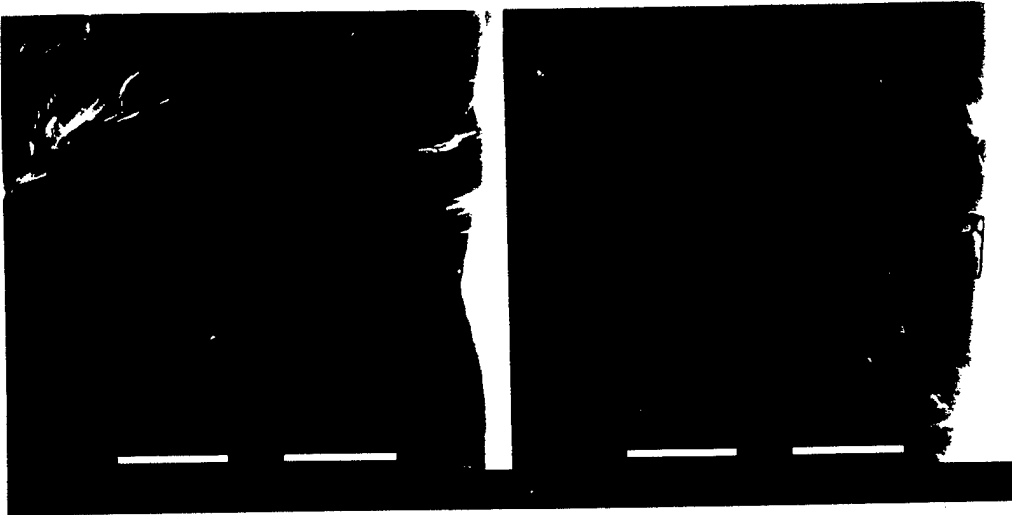

Figure 2. Typical crack nucleation sites (shown outlined) from the fracture surfaces of aluminum 2024-T3 specimens at 2500X.
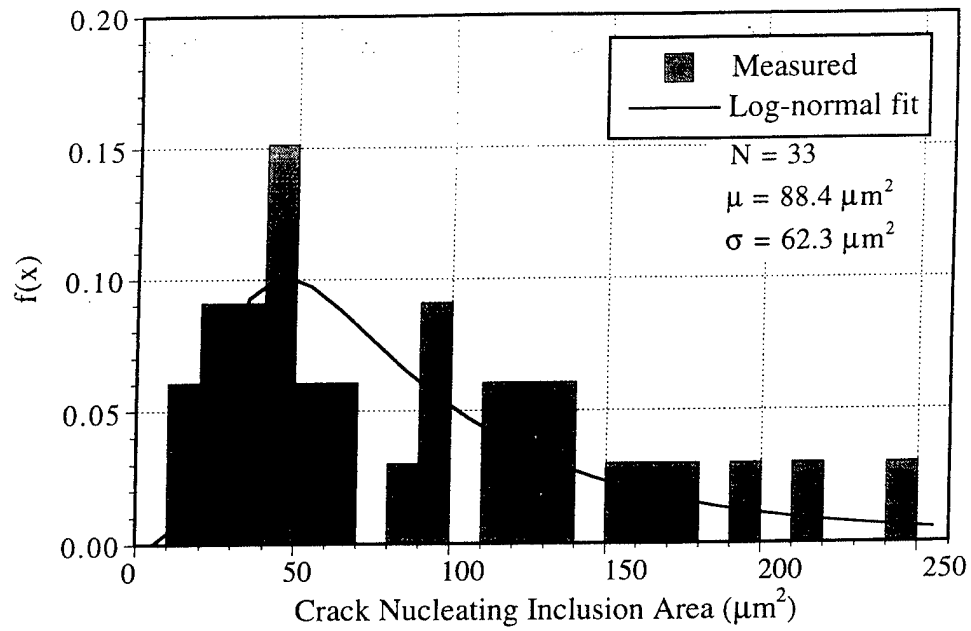
Figure 3. Distribution of experimentally measured crack nucleating inclusion areas and the fit log-normal distribution.
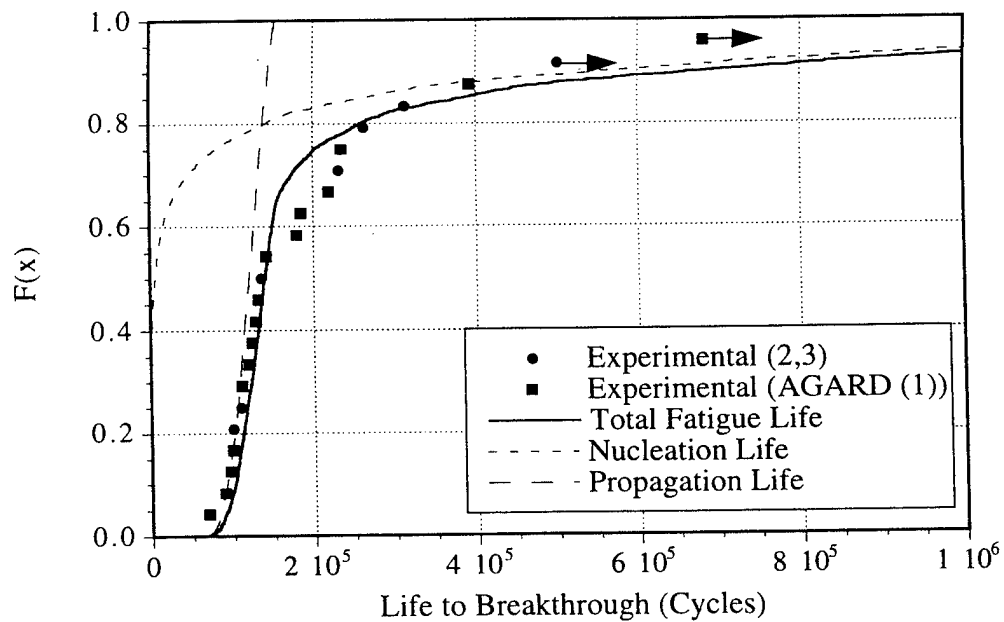

Figure 4. Fatigue life (CDF) comparison between experimental data (1,2,3) and the total life model, showing the contributions of nucleation and propagation.

COPYRIGHT AGREEMENT

AGREEMENT made this.....29.....day of ...OCTOBER..19.98...........between
NAME___P.J. LAZ , S.M. ROHRBAUGH,___NAME__BRUCE CRAIG___
ADRESS___B.M. HILLBERRY___ADRESS_1399 MATHEMATICAL SCIENCES___
_1288 MECHANICAL ENGINEERING___PURDUE UNIVERSITY___
_PURDUE UNIVERSITY___W LAFAYETTE, IN 47907___
WEST LAFAYETTE, IN 47907
(Please attach a separate sheet for additional names and addresses)

(hereinafter called the AUTHOR(S)) of the one part, and Engineering Materials Advisory Services Ltd, whose Registered Offices is at 339, Halesowen Road, Cradley Heath, West Midlands, B64 6PH, U.K. (hereinafter called EMAS) and Higher Education Press, whose Registered Office is at 55 Shatan Houjie, Beijing, 100009, P. R. China (hereinafter called HEP) of the other part.

EMAS/HEP has undertaken to prepare for publication a book under the title: **Fatigue'99**. The Editor(s) for the publication of this book will be: **X. R. Wu and Z. G. Wang**.

EMAS/HEP has invited the AUTHOR(S) to write a manuscript (which with its drawings, diagrams and photographs is hereinafter called "The Manuscript") to be included as part of the publication and it is intended that EMAS/HEP will also invite other authors to make contributions. Please complete the title of your manuscript:

NOW IT IS HEREBY AGREED as follows:

1. The manuscript will produced in accordance with the instructions using the master sheets provided and sent to the EDITOR(S) no later than 31st October, 1998.

2. EMAS/HEP shall have entire control over the publications, paper, binding, cover and embellishments of the book. EMAS/HEP shall also have entire control over the price and the terms of sale of the book, the manner and extent of advertisements, and the manner and distribution of free copies.

3. EMAS/HEP acquires the sole and exclusive right to print and publish the manuscript and the sole and exclusive copyright. EMAS/HEP will use its endeavors to prevent reproduction and/or re-sale by any third party. The AUTHOR(S) agrees to obtain prior written permission from EMAS/HEP to quote passages from the above publication and to reproduce illustrations, tables and diagrams.

ZHANG

4. Illustrations, tables and diagrams will be supplied to EMAS/HEP free of all copyright charges. The AUTHOR(S) warrant that his/her (their) manuscript will in no way whatever violate any existing copyright and that it contains nothing of a libelous or scandalous character and undertake to indemnify EMAS/HEP in respect of any such materials. The AUTHOR(S) undertakes to obtain prior written permission from author and publisher to quote passages from books or journals and to reproduce illustrations, tables and diagrams for which a copyright exists.

Signed by the AUTHOR(S)

DATED 29 Oct. 1998

DATED 29 Oct 1998

DATED 29, Oct 1998

DATED 29 Oct 1998

Signed by a Director for and on behalf of EMAS

DATED 12TH AUG 98

Signed by a Director for and on behalf of HEP

ZHANG ZENG SHUN   1998-7-16

DATED

INHERENT MATERIAL BEHAVIOR AND WIDESPREAD FATIGUE

B.M. Hillberry[*], P. Laz[*], K.M. Gruenberg[*], E.A. DeBartolo[*], and B.A. Craig[†]

In aging aircraft, large flaws and defects have most likely already been discovered. However, fatigue cracks can form at inherent material defects and contribute to widespread fatigue damage, particularly for structures having accumulated a large number of cycles. We have developed a probabilistic life prediction model based on fatigue cracks forming at the inclusion particles inherent to rolled aluminum sheet. Using the particle size distribution as the flaw size distribution and a deterministic crack growth model, good agreement between experimental and predicted fatigue lives was observed for notched test specimens of 2024-T3 and 7075-T6 aluminum alloys. The model predicts the distribution of the fatigue lives. It can also be directly incorporated into risk analysis programs.

INTRODUCTION

Widespread fatigue damage is among the major concerns in aging aircraft especially for the airframe structure. In aging aircraft structures, fatigue cracks forming at the larger defects early in the life have most likely already occurred and been repaired. In the stabilized crack growth regime fatigue damage can be accumulating with use, leading to the development of multiple fatigue cracks in the structure, i.e., widespread fatigue. Development of widespread fatigue in a structure with a large number of flight hours is likely due to the inherent fatigue crack formation mechanisms in the material. It is generally observed in aluminum alloys that fatigue cracks form at inhomogenities inherent in the material (1-5). These inhomogenities include constituent particles and micropores. In aging aircraft, damage induced flaws such as machining scratches and corrosion pits are assumed to have already created cracks and have been repaired. In this work we are investigating thin rolled sheet for which the rolling process has eliminated the microporosity. This leaves the material inclusions as the remaining constituent particles influencing the crack formation. The AGARD studies showed cracks formed at the inclusions very early in the life and that this formation life was small relative to the crack propagation life and could be neglected (6). Therefore, the total life can be considered to be the fatigue crack propagation life.

[*] School of Mechanical Engineering, Purdue University, West Lafayette, IN 47907
[†] Department of Statistics, Purdue University, West Lafayette, IN 47907

A small crack forming at an inclusion located on the surface will become a semi-circular crack very early in life. This geometry approaches that of a small crack emanating around the particle which can be characterized as a fracture mechanics crack with a known stress intensity factor. It has been observed that LEFM is applicable in the small crack regime (6). Since the life is based on the crack growth and the initial crack is small, both short and long crack growth behavior must be considered. Using these observations, we have developed a probabilistic model for predicting the total fatigue life and its variability

DISTRIBUTION OF PARTICLE SIZES

To quantify the particle size effect on the life, it is assumed that the initial flaw is semicircular with an area equal to the cross-sectional area of an inclusion particle in the plane of the crack growth. The distribution of the flaw size then becomes the distribution of the cross-sectional area of the particle which is measured from scanning electron images of the crack plane using IMIX[R] measurement analysis software. With a determini$_\text{s}$tic crack growth model, the variability in fatigue life will be due to the variability of the initial flaw size, as given by the particle area distribution.

The aluminum alloys that we have investigated are 2024-T3[1] and 7075-T6[2] both of 1970's vintage and common to the aging aircraft fleet. To measure the particle sizes with the SEM, small coupon samples were cut and polished on the ST plane, which is the plane of the fatigue cracks in the test specimens. To determine the particle size distributions 3799 particles were measured for 2024-T3 alloy, and 1282 particles for 7075-T6. A log-normal distribution was fit to the particle size distributions for each of the alloys (7,8) (Figure 1).

LIFE PREDICTION

For comparison, we used the single edge, semi-circular notch specimen which is the same geometry as used in the AGARD Studies (9,11). This specimen was designed to simulate an open hole in a panel. Measured fatigue life was the life to grow a crack to a through thickness crack. For the life prediction, the crack was assumed to form in the center of the notch width. A deterministic crack growth model, FASTRAN II (10), that accounts for short and long crack growth behavior is used to grow the cracks to a defined failure. A Monte Carlo simulation is used to predict the life by selecting a particle size from the distribution, growing the crack to break-through and then repeating this 1000 times. At a fixed stress level, the largest particle will yield the shortest life as expected. The life can be represented by the cumulative distribution function, CDF, and compared directly with the AGARD results for both the 2024 and 7075 alloys (7,8) since the geometry of the specimen was used in the crack growth model.

EXPERIMENTAL STUDY

In addition to the AGARD data, we tested several specimens very similar in geometry to the AGARD specimens for both 2024 and 7075, such that the data could be compared directly with the AGARD results. The semi-circular notch was carefully machined and chemically polished to remove residual stresses due to machining. Periodically throughout each test, replicas were taken to monitor when the cracks formed. The results of these tests are included with the AGARD data. In this study

---

[1] Virkler's material
[2] Material used in AGARD study, donated by NASA Langley Research Center

particles that initiated fatigue cracks were located and measured by examining the fracture surfaces with an SEM. Our experimental lives for the 2024 alloy were determined statistically to be from the same distribution as the AGARD data.

INFLUENCE OF THE THRESHOLD

The long life portion of the CDF is determined by the smallest particles to start a crack. Infinite life would indicate that the stress intensity level was below the threshold, and, therefore, the longest observed life at a given stress level was used to calculate ΔK_{th} for that stress level. In the 2024-T3, ΔK_{th} was found to be 1.36 ksi$\sqrt{in}$ for each of the three stress levels, 110, 120 and 145 MPa, used in the AGARD tests. This ΔK_{th} is then used to terminate the distribution function on the small particle end. This ΔK_{th} is based on the entire spread of the data and also indicates it is a true ΔK_{th}, because there were no other failures with longer lives observed experimentally at that stress level. As the stress is increased more of the smaller particles can initiate a crack because ΔK_{th} is constant with varying stress. With decreasing ΔK_{th} smaller particles can initiate cracks which increases the probability of more long life particles being selected and extending the life on the CDF curve.

RESULTS AND DISCUSSION

The short life portion of the CDF prediction agrees very well with the AGARD data, and with our data for both alloys and the different stress levels as illustrated by the CDF (Figures 2 and 3). This is also confirmed in our study with the particles that initiated the flaws being in the tail of the large particle end of the distribution (7) (Figure 4). The earliest failure portion of the life is the critical region. The periodic replicas made it possible to determine the crack formation lives. More cycles to crack formation occurred in the long life region of the CDF.

In the rolled sheet materials, the particles tend to break up into clusters of smaller particles. We expected crack formation and crack coalescence within the clusters could affect the short crack growth behavior. Investigating this, DeBartolo (13) found that crack coalescence seldom occurred. She also modeled crack coalescence and found that in the short crack region even if coalescence occurs the overall life reduction would be small for the ST and LT planes, the most common loaded conditions for thin sheet.

The Monte Carlo simulation can be computer intense especially when analyzing multi-site damage with numerous cracks growing. However, conditional probability can be used to give a direct integration of the CDF and eliminate the iterative Monte Carlo method. The conditional probability determines the probability of selecting a particle from the distribution given that the particle is greater than ΔK_{th}. This significantly reduces analysis time and is particularly helpful when examining low probabilities of failure. The Monte Carlo and conditional probability are compared in Figure 4 and conditional probability is seen to be more exact.

The good correlation with the experimental results indicates that the particle size distribution is describing the initiating flaw distribution quite well. However, in the high stress area of the notch, there are over 10,000 particles on the surface that can initiate a crack. The actual distribution initiating the flaw could be a subset of the overall particle distribution. It could be cracked particles and/or debonded particles that could likely be of the same distribution as the total particle distribution.

The model can be directly implemented into risk analyses and multi-site damage models. An MSD open hole model with ten holes has been investigated using the Monte Carlo simulation with an initiating particle size selected from the distribution for each side of each hole. The cracks are grown to failure using Swift's plastic zone model for crack link-up. Ten thousand trials were run to obtain four nine's reliability. The CDF also showed that, at very low probabilities of failure, there was still an infinite life region.

REFERENCES

(1) Suresh, S., "Fatigue of Materials," Cambridge University Press, Cambridge, 1991.

(2) Tanaka, K. and Mura, T., Metallurgical Transactions A, 1982, 13A, 117-123.

(3) Grosskreutz, J.C. and Shaw, C. G., 2nd International Conference on Fracture, Brighton, UK, 1969.

(4) Bowles, C. Q. and Schijve, J., International Journal of Fracture, 1973, 9, 171-179.

(5) Kung, C. Y. and Fine, M.E, Metallurgical Transactions A, 1979, 10A, 603-610.

(6) Newman, J.C., Jr., Phillips, E. P., Swain, M. H. and Everett, R.A., Jr., ASTM STP 1122, American Society for Testing and Materials, Philadelphia, 1992, pp. 5-27.

(7) Laz, P.J. and Hillberry, B.M., Int. J. of Fatigue, Vol. 20, No. 4, 1998, pp. 263-270.

(8) Gruenberg, K.M., Craig, B.A., and Hillberry, B.M., Proceedings, 39th Structural Dynamics and Materials Conference, AIAA, No. 98-2055, April 1998.

(9) Newman, J.C., Jr., and Edwards, P.R., AGARD R-732, 1988.

(10) Newman, J.C., Jr., NASA-TM-104159, NASA Langley Research Center, 1992.

(11) Edwards, P.R., and Newman, J.C., Jr., AGARD R-767, 1990.

(12) Newman, J.C., JR., Wu, X.R., Venneri, S.L., Li, C.G., NASA/CAE Reference Publication 1309, 1994.

(13) DeBartolo, E.A., and Hillberry, B.M., Int. J. of Fatigue, Vol. 20, No. 10, 1998, pp. 727-735.
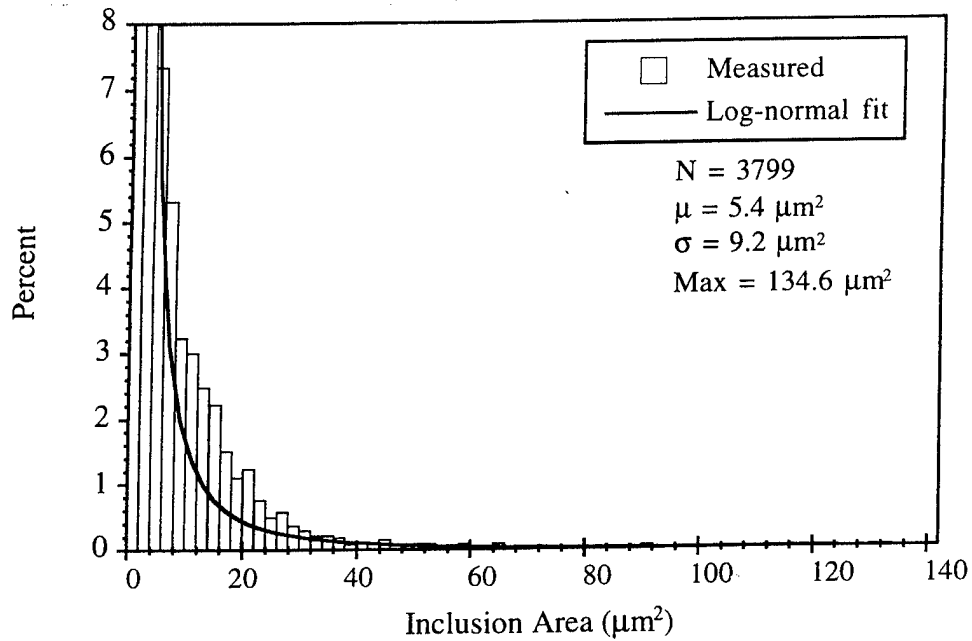
Figure 1. Particle area distribution for aluminum 2024-T3 alloy with log-normal dsitribution function fit.
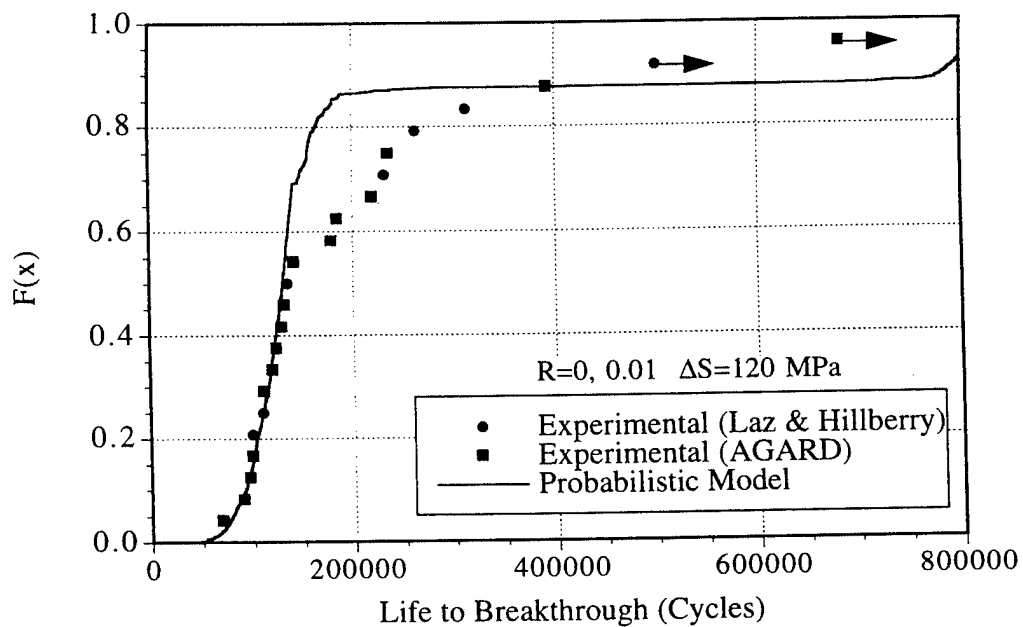
Figure 2. Predicted cumulative distribution function of fatigure lives of 2024-T3 compared with experimental data from AGARD studies and these studies.
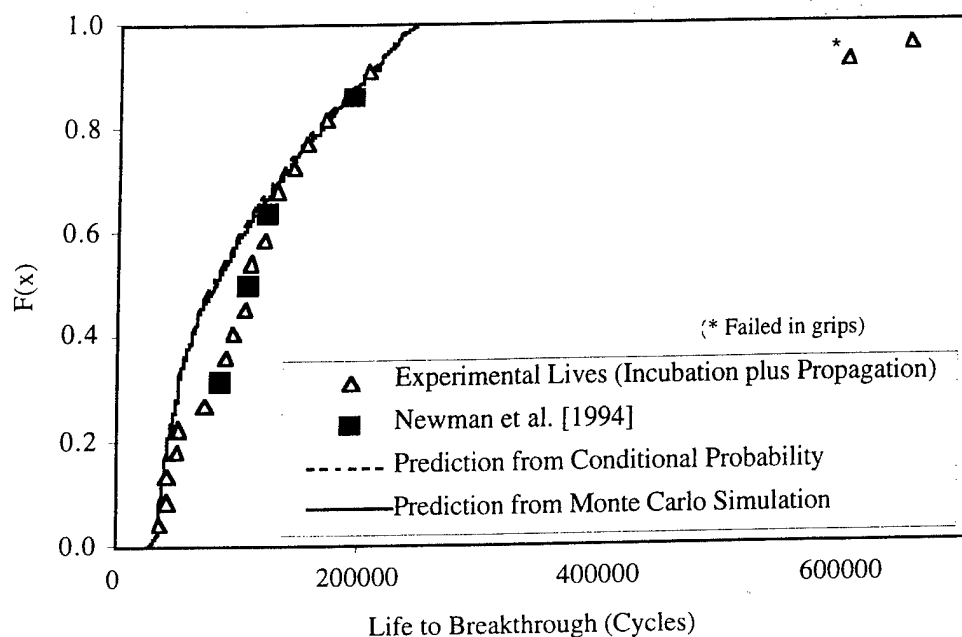
Figure 3. Predicted cumulative distribution function of fatigure lives of 7075-T6 compared with experimental data from AGARD studies and these studies.
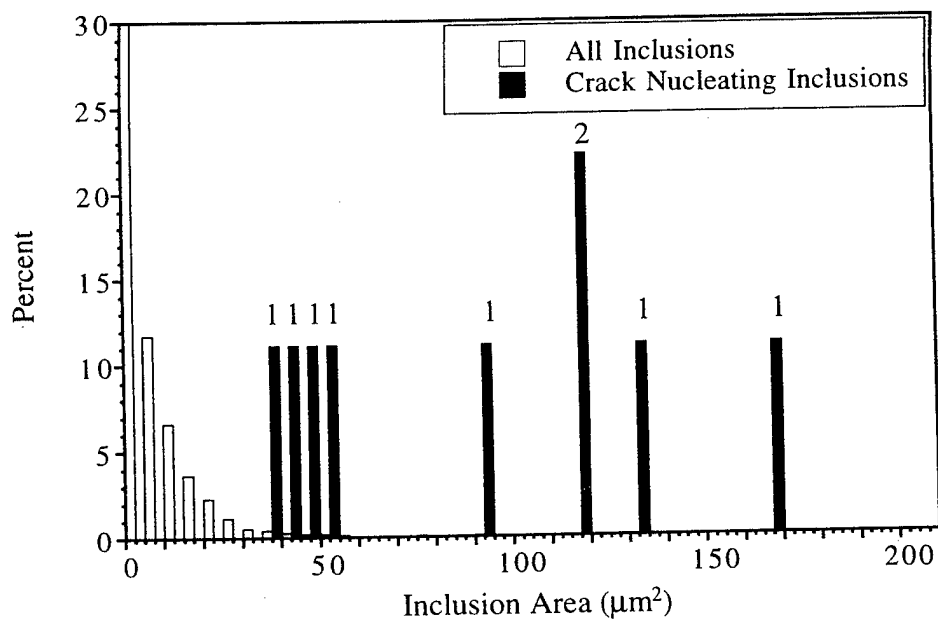
Figure 4. Measured sizes of particles that initiated fatigue cracks (shown as solid bars) compared with particle area distribution.

COPYRIGHT AGREEMENT

AGREEMENT made this...2.9......day of ..*October*..19..*98*.........between
NAME___*B. M. Hillberry*___ NAME___*P.J. Laz*_____
ADRESS___*School of Mech.Engr.* ~~ADDRESS~~ *K.M. Gruenberg*_____
_____*Purdue University*_____ *E.A. DeBartolo*_____
_____*W. Lafayette, IN 47906*___ *B.A. Craig*_____
_____ *Same address*

(Please attach a separate sheet for additional names and addresses)

(hereinafter called the AUTHOR(S)) of the one part, and Engineering Materials Advisory Services Ltd, whose Registered Offices is at 339, Halesowen Road, Cradley Heath, West Midlands, B64 6PH, U.K. (hereinafter called EMAS) and Higher Education Press, whose Registered Office is at 55 Shatan Houjie, Beijing, 100009, P. R. China (hereinafter called HEP) of the other part.

EMAS/HEP has undertaken to prepare for publication a book under the title: **Fatigue'99**. The Editor(s) for the publication of this book will be: **X. R. Wu and Z. G. Wang**.

EMAS/HEP has invited the AUTHOR(S) to write a manuscript (which with its drawings, diagrams and photographs is hereinafter called "The Manuscript") to be included as part of the publication and it is intended that EMAS/HEP will also invite other authors to make contributions. Please complete the title of your manuscript:

NOW IT IS HEREBY AGREED as follows:

1. The manuscript will produced in accordance with the instructions using the master sheets provided and sent to the EDITOR(S) no later than 31st October, 1998.

2. EMAS/HEP shall have entire control over the publications, paper, binding, cover and embellishments of the book. EMAS/HEP shall also have entire control over the price and the terms of sale of the book, the manner and extent of advertisements, and the manner and distribution of free copies.

3. EMAS/HEP acquires the sole and exclusive right to print and publish the manuscript and the sole and exclusive copyright. EMAS/HEP will use its endeavors to prevent reproduction and/or re-sale by any third party. The AUTHOR(S) agrees to obtain prior written permission from EMAS/HEP to quote passages from the above publication and to reproduce illustrations, tables and diagrams.

4. Illustrations, tables and diagrams will be supplied to EMAS/HEP free of all copyright charges. The AUTHOR(S) warrant that his/her (their) manuscript will in no way whatever violate any existing copyright and that it contains nothing of a libelous or scandalous character and undertake to indemnify EMAS/HEP in respect of any such materials. The AUTHOR(S) undertakes to obtain prior written permission from author and publisher to quote passages from books or journals and to reproduce illustrations, tables and diagrams for which a copyright exists.

Signed by the AUTHOR(S)

B. M. Hallberry DATED _29 Oct 1998_

23 Oct. 1998

R. M. Bruenberg DATED _29 Oct 1998_

25 Oct 1998

DATED _29 OCT 1998_

Signed by a Director for and on behalf of EMAS

C Minclary DATED _12 TH AUG 98_

Signed by a Director for and on behalf of HEP

ZHANG ZENG SHUN _1998-7-16_

DATED

Shell Modeling of Fretting in Riveted Lap Joints

G. Harish and T. N. Farris

Shell Modeling of Fretting in Riveted Lap Joints

G. Harish* and T. N. Farris[†]

Purdue University, West Lafayette, Indiana 47907-1282

Fretting is a contact damage mechanism arising from microslip associated with small-scale oscillatory motion of nominally clamped structural members. Fretting has been observed near aircraft skin fastener holes. Shell finite elements are used to model the contact at a typical skin/rivet interface, with emphasis on fretting as a crack nucleation mechanism. Contact elements implementing the Coulomb friction law keep track of contact status between interacting surfaces. The model accounts for bending, contact between the skin panels, and rivet head clamping pressure. Elastic supports control the load transferred and simulate various rivet configurations. No interference is considered, leading to loss of contact between the skin and rivet on loading. The distinct stick-slip zones, combined with high tensile stresses at the edge of contact, are indicative of fretting, resulting in crack nucleation at the edge of contact. Away from the edge of contact, the tensile stress decays rapidly. The slip displacement has values typically associated with fretting fatigue. The interface between the two skin panels is also a region of fretting damage. Crack nucleation lives are predicted using a multiaxial fatigue theory. The top row of rivets has the smallest predicted life. For low remote stresses, increase in friction coefficient increases life, whereas for high remote stresses, life decreases with increase in coefficient of friction. Increasing rivet head clamping pressure increases the life. Plasticity blunts the effects of friction coefficient and clamping pressure. An approximate solution that does not require finite element analysis estimates the crack nucleation life for any rivet configuration quickly.

Introduction

FRETTING is a damage phenomenon occurring between contacting bodies nominally at rest but having oscillatory motion of small amplitude. Fretting is characterized by high contact stresses and microslip at the surface. Corrosion, wear, and fatigue all form part of the damage mechanism, which leads to acceleration of near-surface crack nucleation. Fretting has been well documented for flange joints, lap joints, dovetail notches in engine blades, roller bearings, and other locations exhibiting high contact stresses and small-scale oscillations.[1,2]

The fretting damage process can be divided into three stages.[3] In the first few cycles, the thin oxide layer resident on the material surface is removed through wear caused by the microslip. Then the material underneath the oxide layer forms microwelds through an adhesive process, accumulating wear debris between the contact surfaces.[4] Finally, the plastic deformation near the surface accumulates, and the wear process forms more oxide, which promotes the nucleation of microcracks. The coefficient of friction also increases during the first few hundred cycles and reaches a stable value.[5-7] Fretting fatigue results when one or more of these microcracks penetrate the bulk of the material. Fretting fatigue can reduce the crack nucleation life by an order of magnitude.

Because of various constraining factors, the U.S. Air Force is looking to extend the lives of some of its aging fleets of KC-135 and C-141. Also, some of the fleets are operating at loads higher than the design loads.[8] This has necessitated the periodic inspection of aircraft, both old and new. Particular emphasis is being laid on the effect of multiple site damage (MSD), which is characterized by a multitude of small cracks, which, although individually not catastrophic, can cause premature failure by their combined effects. Farris et al.[9] have discussed fretting as a mechanism for formation of MSD at fastener holes. The teardown inspections of KC-135, C-5A, and C-141 have revealed the existence of MSD cracks at fastener holes. This makes the understanding of various crack nucleation and propagation mechanisms very important. Figure 1 shows a typical

lap joint and the local contact at a fastener location with the fretting locations highlighted. The nature of the contact between the skin and rivet, as well as between the two skin panels, is conducive to fretting damage, thus requiring a careful study of the parameters involved in fretting and the development of an appropriate theory applicable to actual structural members. In the recent past, various researchers have studied the fretting of lap joints in the laboratory.[10-12] Ghosh et al.[13] used an inverse method to study the load transfer from a smooth elastic pin onto an infinite sheet. Sundarraj et al.[14] used an axisymmetric model to study a double lap joint with no contact separation. Fung and Smart[15] analyzed a single-rivet lap joint. The current work investigates a typical lap splice with emphasis on fretting and an estimation of the effect of the fretting contact stresses on crack nucleation life.

Finite Element Model

Any theory must satisfy two criteria: It must agree with experimental results and must have a good physical basis. Although experiments simulating field behavior provide a framework for evaluating the theory, the physical basis involves the identification and proper modeling of the various parameters that govern the field phenomenon whose understanding is sought. The study of crack nucleation in lap joints is governed by the stress and strain state in the joint as well as the material properties of the components. The present work concentrates on the estimation of the stresses and strains and their effect on the crack nucleation behavior for a joint made of 2024-T351 aluminum with a Young's modulus of 73 GPa and a Poisson's ratio of 0.33. A bilinear kinematic hardening model is used to model plasticity, with an initial yield stress of 330 MPa and a hardening modulus E_t of 1.55 GPa. Because the state of stress is influenced by the complex phenomena of contact and plasticity (and their interactions with each other), closed-form solutions are not available. The finite element method (FEM) is a numerical approach to such problems.

The finite element approach involves the following steps: identification of the skin/rivet configurations to be studied, reduction to a discrete model with necessary assumptions, solution of the discrete model for various loading patterns, and interpretation of the results within the framework of assumptions.

The model consists of one-half rivet and the skin around it. A finite number of rivet rows, with a large number of rivets in each row, is assumed. The section of the plate near the lap joint may be considered equivalent to a collection of unit structures, each of which is similar to the model, comprising half a rivet and the adjacent skin around it.

*Research Assistant, School of Aeronautics and Astronautics, 1282 Grissom Hall #350.

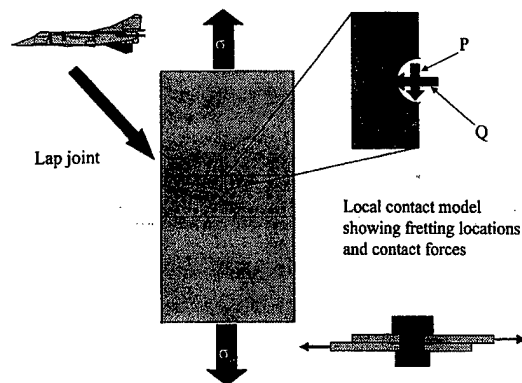[†]Professor, School of Aeronautics and Astronautics, 1282 Grissom Hall #350. Senior Member AIAA.

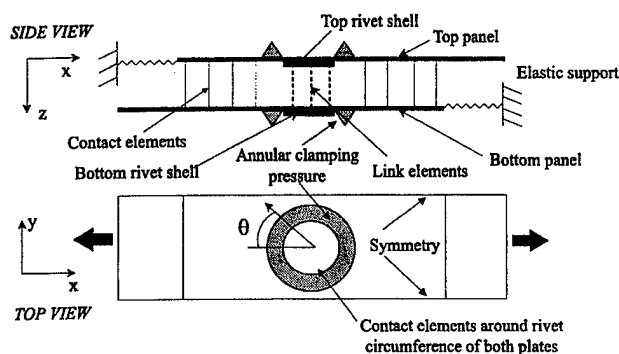**Fig. 1 Fretting and aircraft.**

Fig. 2 Schematic of shell model.

The remote load seen by each rivet is uniformly distributed on the model boundaries. Appropriate boundary conditions and spring elements allow for the modeling of any particular rivet with arbitrary load transfer. The results in this work refer to a three-row lap joint containing rivets of diameter 0.51 cm with a spacing of 2.54 cm. The effect of rivet head clamping is accounted for by applying an annular pressure on the skin around the rivet. The contact regions comprise the skin/rivet interface and the skin/skin interface.

The dimensions of aircraft skin panels are characteristic of the realm of validity of shell theory. The two skin panels are modeled as shells. To ensure consistency of the model, the rivet too is modeled as two shells initially aligned with the skin shells. These two shells are subjected to constraint conditions to link them together. Each skin panel is 7.62 cm in length and 1.27 cm in width. The thickness of each panel is 1.78 mm. Figure 2 shows a schematic of the model. Considering the effect of local contact stresses to be negligible at a distance of five radii (of the rivet) from the contact, the remote load is distributed uniformly along the edges of the two panels. Both of the panels have symmetry conditions along the edges parallel to the applied remote loading, which follows from the assumption of an infinite number of rivets in each row. Consequently, a nonuniform traction, orthogonal to the applied remote load, results on the application of the remote traction. There are elastic supports on one side of either panel. By varying the stiffness of the support, the amount of load being transferred by the rivet assembly can be controlled. This, coupled with the magnitude of the applied remote traction, enables the simulation of any configuration having an arbitrary number of rows of rivets. The elastic supports model the effect of the subsequent rows of rivets, whereas the magnitude of the applied traction takes into account the load transferred in the rows ahead of the rivet being analyzed.

The sum of the applied traction and the support reaction must be the same for both of the shells. Hence, the support stiffnesses are not arbitrary but must be found iteratively. The clamping pressure due to the rivet head on the skin panels is modeled by applying pressure on an annular region bounded by the rivet hole and an outer circle with radius 1.3 times the radius of the rivet.[16] The pressure goes to zero on either end to ensure a smooth profile. The total force acting on the top and bottom shell is equal. Note that this is the clamping

pressure that remains after the removal of the forces applied during the installation of the rivet.

To enable the two distinct shells composing the rivet to behave as a single body, link elements and constraint equations are used. The link elements link the corresponding nodes of the top and bottom shells. The nodes are located in the midplane of the shells. Both of the shells have identical meshes for this purpose. The two nodes on either shell are connected by a rod element that has a stiffness determined by the stiffnesses of each of the elements that contain the two nodes that form the rod element. Each shell element would contribute a stiffness, the value of which depends on the element volume and the number of nodes in the element, to each of the nodes that compose it. The stiffnesses are summed at each node, and the stiffness of the rod element is then determined. For identical meshes of the two shells with the same thickness, the equation for the stiffness can be expressed as

$$K = \frac{1}{t} \sum \frac{A_i E_i}{n_i} \tag{1}$$

where K is the stiffness, t is the thickness, A_i and E_i are, respectively, the area and the Young's modulus of the elements that are connected to the node, and n_i is the number of nodes in the element. Note that only one of the link element nodes needs to be considered for the preceding equation, and the summation is over all of the elements containing the node.

The bottom of the top rivet shell and the top of the bottom rivet shell correspond to the same point in physical space. Hence, constraint equations are imposed to ensure continuity at this plane, the center plane of the rivet itself. The constraint equations account for translation and bending of the shell as well as any shear deformation. The two equations at each node pair corresponding to the two in-plane directions can be expressed as

$$(u_i + 0.5\theta_i t)_{\text{bottom}} = (u_i - 0.5\theta_i t)_{\text{top}} \tag{2}$$

where t is the thickness of each of the shells forming the rivet, u_i is the translational displacement in the i direction, and θ_i is the angular displacement (in the i direction) of the normal section to the midplane of the shell.

Contact Modeling

Contact elements are used to keep track of the contact between the various surfaces. Contact elements exhibit a nonlinear relationship between force and displacement. They have zero stiffness in tension and a high stiffness in compression. In the present model, contact elements are used to keep track of the contact between the skin and rivet as well as between the two skin panels themselves. Point-to-point contact elements are used for both contacts. Even though the problem is three dimensional, the nature of contact is roughly the same over the entire loading spectrum. Also, the sliding is expected to be small. Hence, because the contact area can be estimated a priori, the point-to-point contact elements are the most appropriate.

The contact elements between the two shells have a soft contact stiffness. This allows the two nodes composing the contact element to move toward each other in compression, simulating the compression of the two skin panels in the transverse direction. The contact stiffness is calculated using the method used to calculate the stiffness for the link elements connecting the rivet shells. The contact stiffness for the contact elements between the plate and rivet is kept high in comparison to the stiffness of the adjacent shell elements.

The shell element has only one node through the thickness. Hence, contact can be resolved only at the midplane of the shell. Partial contact through the thickness cannot be resolved. Bending effects are not considered as part of the contact forces. Figure 3 shows an example of a possible contact state and the finite element implementation of the same.

Finite Element Mesh

The commercial finite element package, ANSYS version 5.3, provided to Purdue University on an academic license, is used for the solution of the problem. The skin panels and the rivet shells are modeled by four-noded Mindlin shell elements (SHELL43). The contact
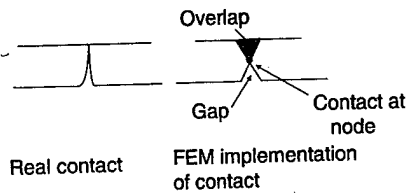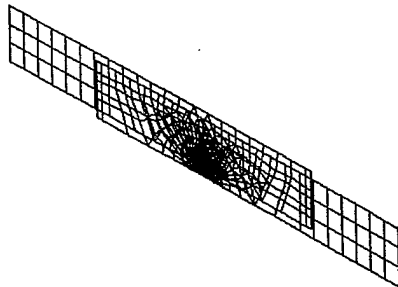
Fig. 3 Implementation of contact in FEM.

Fig. 4 Finite element mesh (on top) with side view of deformed mesh: $\sigma_o = 96.5$ MPa, $\mu = 0.65$, maximum clamping pressure = 83 MPa, and LTR = 0.38.

elements are three-dimensional, point-to-point elements (CONTAC52). The two rivet shells are linked by rod elements (LINK4). The finite element mesh is shown in Fig. 4. There are 852 nodes composing 768 shell elements. There are 24 elements around the circumference of the rivet. The contact is tracked through 267 contact elements. There are 50 contact elements between the panel and rivet shells and 217 contact elements between the two panels. There is a row of elements on each panel shell that acts as the elastic support modeling the effects of the subsequent rows of rivets. These provide both axial and bending stiffness. There are symmetry conditions on the boundaries parallel to the x axis. Tractions are applied along one edge of each of the two panels parallel to the y axis. Displacement compatibility is imposed on the rivet shells using Eq. (2).

Five remote stresses from 55 to 110 MPa, three coefficients of friction (0.2, 0.4, and 0.65), and two values of maximum clamping pressures (55 and 83 MPa) were investigated. These analyzes were performed assuming the joint of interest to be the first row of a three-lap joint with 38% of applied remote load transferred through the rivet. Also, the corresponding configuration of the second row with 24% load transfer was studied.

Verification of Mesh Adequacy

The first step in the analysis is to verify that the mesh is able to resolve the contact and other issues accurately. The problem was solved with zero load transfer and no friction. The symmetry condition modeling the infinite number of rivets is replaced by an applied traction. Because the boundaries are far away from the rivet, their effect is small. The results were compared with the solution for a frictionless inclusion in an infinite matrix. Note that this is a receding contact problem. The analytical solution is due to Keer et al.[17] The results are shown in Fig. 5 for two ratios of the tractions along the two directions. The finite element results agree well with the analytical solution, demonstrating the adequacy of the mesh.

Results

The displacement profile is shown in Fig. 6, and a side view of a typical displacement profile is shown at the bottom of Fig. 4. The contact is centered around $\theta = 0$ deg with the half-contact angle calculated to be approximately 90 deg. The dominant contact mechanism is seen to be the global motion of the skin into the rivet. Another mechanism is the tendency of the skin panel hole to
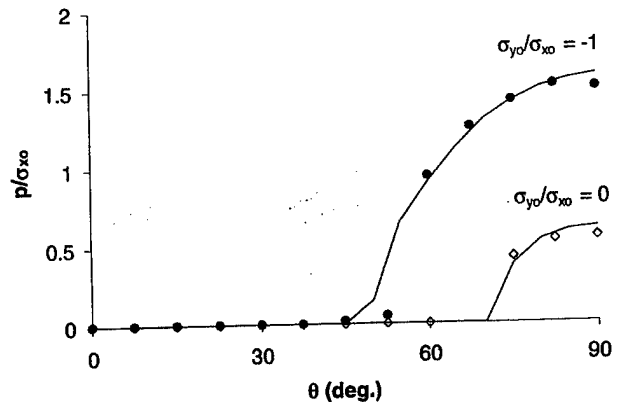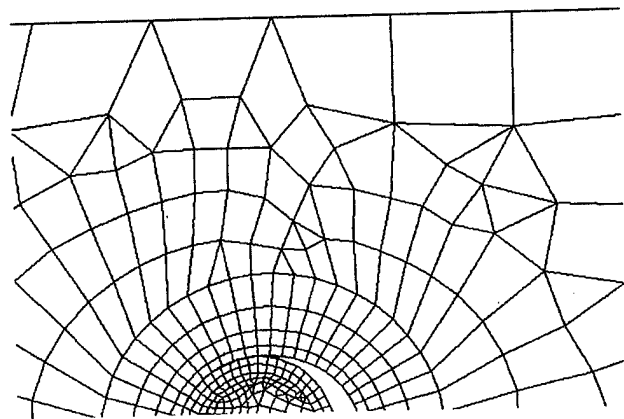

Fig. 5 Comparison of results for 0 LTR case with analytical solution.

Fig. 6 Top view of deformed mesh (only a portion of the mesh is shown for clarity): $\sigma_o = 96.5$ MPa, $\mu = 0.65$, maximum clamping pressure = 83 MPa, and LTR = 0.38.

deform into a elliptical shape under loading, which contributes to the contact around $\theta = 90$ deg. The observed contact area is in agreement with the results of Narayana and Dayananda.[18] The contact area is observed to be nearly constant for all values of the applied load, especially with little or no plasticity. This surprising result can be explained by considering the nature of the skin/rivet contact. Because the final contact area is less than the initial contact area (with no load), this problem is a receding contact problem. It can be shown that, for such problems, the contact area is independent of the actual magnitudes of the applied loads.[19] Whereas the preceding result assumes elastic behavior, the present problem has little plasticity, and hence the contact area remains constant.

The load transferred through the rivet assembly is transferred through the skin/skin interface and between the skin/plate interface. The partition of load between the rivet and skin/skin interface is shown schematically in Fig. 7. When the loading is applied for the first time, initially nearly all of the load is taken up by the interfacial friction as the panels have to overcome this interfacial friction to move into the rivet and initiate contact at the rivet/skin interface. Thus, the rivet begins to take up load only after the two panels slip with respect to each other. The rivet absorbs the subsequent loading. When unloading begins, once again the panels need to slip in the opposite direction to relieve the load on the rivet. This necessitates the reversal of the interfacial frictional load. During this phase of unloading, the rivet itself does not experience significant change in load. When the unloading is complete, there is a frictional load between the two panels and a balancing load on the rivet. When reloading begins, once again the interfacial friction accounts for the initial part and the rivet absorbs the subsequent loading. This mechanism now continues in a cyclic fashion. The amount of interfacial friction depends on the clamping pressure on the rivet. Also, the presence of high slip amplitudes in conjunction with any high stresses can cause extensive damage to the faying surfaces and nucleate cracks.
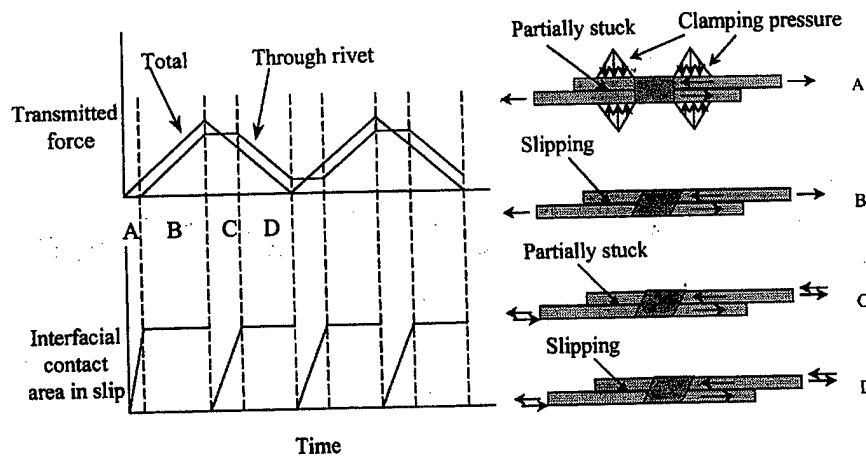
Fig. 7 Partition of load between rivet and interfacial friction between panels.

Fig. 8 Contact stresses, elastic regime: $\sigma_o = 83$ MPa, $\mu = 0.4$, maximum clamping pressure = 83 MPa, and LTR = 0.38.
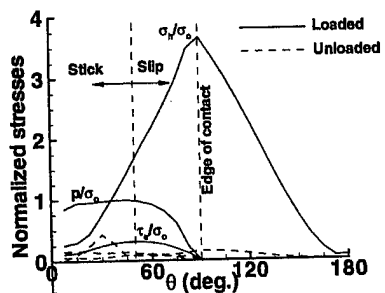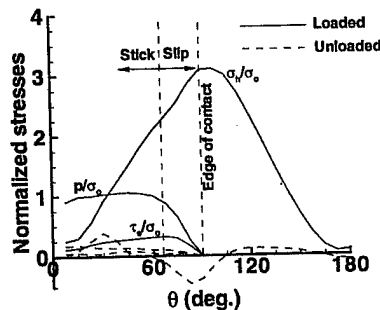
Fig. 9 Contact stresses, plastic regime: $\sigma_o = 110$ MPa, $\mu = 0.4$, maximum clamping pressure = 83 MPa, and LTR = 0.38.

Fig. 10 Hysteresis diagram over two and a half cycles; A, B, and C are consecutive peak loadings: $\sigma_o = 96.5$ MPa, $\mu = 0.65$, and maximum clamping pressure = 83 MPa. Data are plotted for top panel, first row.

Evidence of Fretting

The most severe stress conditions occur at the skin/rivet interface for the parameters considered in the present study. Figure 8 shows the results, expressed in the form of stress distribution around the rivet hole, for a typical configuration. Figure 9 shows similar results for a loading configuration that produces plastic deformation. The normal pressure p, the equivalent shear stress τ_{eq} at the interface, and the hoop stress on the panel surface are plotted as functions of the angular coordinate θ, which is defined in Fig. 2. The stresses, plotted at the midplane of the shell (without bending effects), are made nondimensional by dividing by the remote tensile load σ_o. The loaded and unloaded configurations are plotted. The stick/slip nature of the contact is observed, where slip is characterized by the frictional contact force being equal to the coefficient of friction times the normal contact force. Note that, because the contact algorithm uses only forces, the effective coefficient of friction when comparing shear and normal stresses in the slip zone might be different. This effective coefficient of friction is referred to as μ_{eff}. The stick/slip nature is also verified by checking the nature of the contact elements. Wherever the contact elements report no contact, the pressure and shear traction are assumed to be zero.

The pressure distribution is nearly semielliptic in nature and resembles the Hertzian pressure distribution. However, at higher load transfer ratios (LTR; the ratio of transferred load to applied remote load), the pressure reaches a maximum at a value of θ other than zero, an effect of the aforementioned effect of the local tendency of the panel hole to deform into an ellipse. This causes the region around $\theta = 0$ deg to move away from the rivet, with a resulting drop
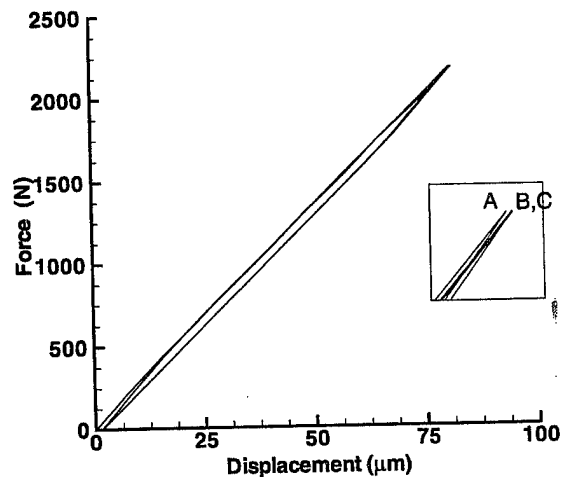
in the contact pressure. The effective shear stress, which is the vector sum of the two interfacial shear stresses $\tau_{r\theta}$, and τ_{rz}, follows the pressure distribution in the slip region, where τ_{eq} equals $\mu_{eff}p$. In the stick region, the effective shear stress decreases as θ goes to zero. The region of slip varies from 60 to 15 deg of arc as the coefficient of friction varies from 0.2 to 0.65. Experiments indicate that for 2024-T351 aluminum the coefficient of friction is about 0.2 initially and under fretting conditions increases to a stable value of about 0.65 after a few hundred cycles.

The hoop stress σ_h has a peak at the edge of contact, i.e., $\theta = 0$ deg, and decays rapidly away from the edge of contact. However, it seems to stabilize in the stick region. The hoop stress is derived from three sources: the stress concentration due to the panel hole, the normal pressure, and the shear traction. The latter two result from contact.

In Fig. 9 the same features mentioned earlier are observed, except that plasticity causes the hoop stress distribution around the edge of contact to be flatter as the load gets redistributed. The pressure distribution is also flatter and no longer resembles the Hertzian distribution. The plasticity is very localized and is observed only in the first cycle. Owing to the small strain hardening, the peak value of stress remains close to the nominal yield stress. Additionally, the adjacent elastic material constrains the plastic deformation. Subsequent loading cycles are elastic, cycling between the two states shown in Fig. 9. Figure 10 shows a hysteresis plot of the applied remote load against the displacement in the direction of the load at the loading edge of the top panel. The first cycle includes plastic energy dissipation in addition to the frictional energy dissipation. The subsequent cycles marked B and C are identical, indicating that there is no further plastic energy dissipation. The area enclosed by the hysteresis curve over one cycle gives the energy dissipation for that cycle.
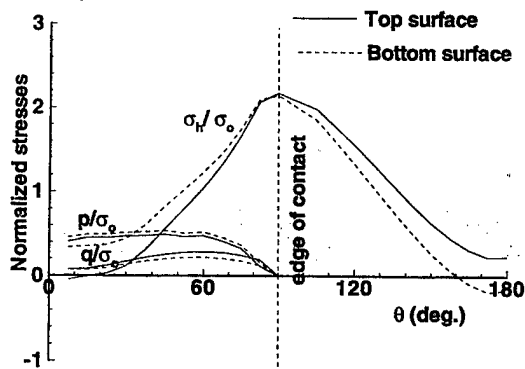
Fig. 11 Contact stresses, bending effects: $\sigma_o = 96.5$ MPa, $\mu = 0.65$, maximum clamping pressure = 83 MPa, and LTR = 0.24 (middle row).
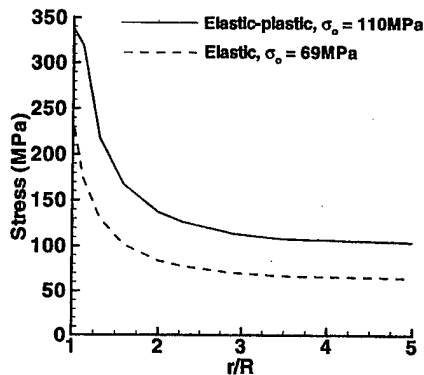

Fig. 12 Decay of σ_h in radial direction; R is the radius of the rivet: $\mu = 0.2$ and LTR = 0.38.

Fig. 13 Relative displacements between skin and rivet: $\sigma_o = 96.5$ MPa, $\mu = 0.65$, maximum clamping pressure = 83 MPa, and LTR = 0.38 Data are plotted for top panel, first row.

Fig. 14 Crack nucleation lives at various remote stresses and clamping pressures.

As mentioned earlier, on unloading, the pressure and other stresses do not go to zero. In the presence of plasticity, the hoop stress at the edge of contact is compressive on unloading. The cyclic stress in the rivet is the difference between the stable loaded and unloaded configurations. The presence of distinct stick-slip zones in the contact area, coupled with the high tensile hoop stress at the edge of contact, is indicative of fretting behavior.

Figure 11 shows the effect of local bending on the contact stresses between the rivet and skin. Although bending affects all three contact stresses, the effect on the hoop stress is minimal at the edge of contact, which is the critical location. Hence, stress severity at the critical location is unaffected by local bending. In the slip region, τ_{eq} is not equal to $\mu_{eff}p$, as the contact algorithm uses the contact force at discrete nodes and does not account for the bending forces, in contrast to the stress-based approach more suitable for continuum bodies.

The rapid decay of the hoop stress away from the contact interface is shown in Fig. 12 . Both the contact stresses and the stress concentration decay rapidly away from the hole. The gradient is quite steep even when plasticity sets in. Thus, this problem involves high stress gradients in addition to contact, frictional dissipation, and plasticity. The decay of the stresses along the 0-deg direction is steep as well, resulting in a nearly uniform state of stress at the elastic supports. This indicates that rivet interaction is primarily through stress shielding, which is simulated through the use of appropriate boundary conditions.

Fretting fatigue occurs when slip displacements between the panels and the rivet are small. Figure 13 shows the relative displacements between the top panel and the corresponding rivet shell. The gap displacement refers to the relative normal displacements between the plate and rivet. This is zero in the contact region. The gap is positive elsewhere, indicating loss of contact. The slip displacement refers to the relative motion between the plate and rivet in the hoop direction. The slip in the transverse direction is also brought out in the model. The transverse slip is small in the presence of clamping pressure on the rivet head, in part due to the consequent
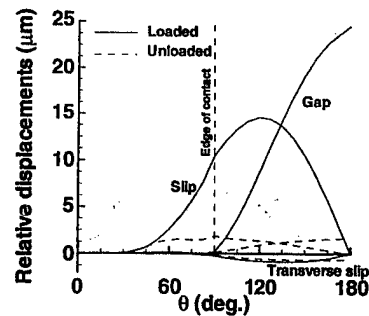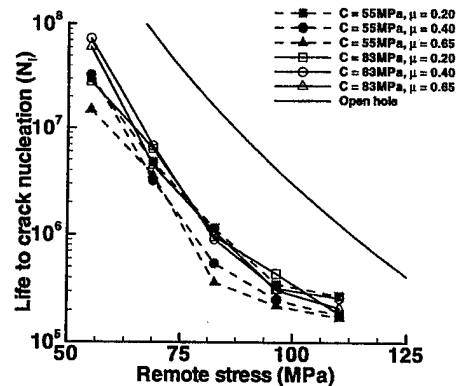
restriction on the motion of the plate in the thickness direction. The slip displacements are zero in the stick region and indicate the amount of slip in the slip region. Once again the stable value of the slip is nonzero in the unloaded state. The slip displacement plot has no particular significance beyond the contact area. The maximum slip displacement occurs at the edge and typically is nearly 14 μm. This is consistent with the values reported for a lap joint.[20] This small slip causes wear that nucleates a crack at the edge of contact, which is then driven by the tensile hoop stress. Thus, this is the critical location for a crack to nucleate. The slip between the two panels reaches a maximum of 1.5 μm at $\theta = 135$ deg and a radial distance of 1.6 from the center of the hole, where R is the hole radius. This slip may be related to the formation of cracks at the skin/skin interface away from the skin/rivet contact.

Application to Fretting Crack Nucleation

The multiaxial theory proposed by Socie[21] has been used by Szolwinski and Farris[22] to predict fretting crack nucleation in a controlled fretting test. Their predictions are in good agreement with the experiments of Nowell and Hills[23] and data collected at Purdue University.[24] The number of cycles N_i to nucleate a crack of length 1 mm is given by

$$\Gamma = \sigma_{max}(\Delta\epsilon/2) = (\sigma_f'^2/E)(2N_i)^{2b} + \sigma_f'\epsilon_f(2N_i)^{b+c} \quad (3)$$

where the fatigue constants σ_f', ϵ_f, b, and c are 1013.5 MPa, 0.22, −0.12, and −0.52. The critical parameter is identified as Γ, the maximum value of the product of the maximum stress and the normal strain amplitude. This always occurs near the edge of contact for lap joints without interference. Note that, for uniaxial loading, Eq. (3) becomes the Smith–Watson–Topper equation.[25] The predicted lives to crack nucleation are shown in Fig. 14. Any other life prediction theory would give similar qualitative results with possible scale changes. For the middle row of rivets, the stress level is much lower than that for the first row of rivets. Only the first row results are plotted, as the middle row data fall above the open hole data. The load transfer ratio is kept at 0.38. The open hole data are for a plate with no hole subjected to the same remote loading. The effects of friction, clamping pressure, and plasticity are discussed next.

Effects of Coefficient of Friction

As the coefficient of friction increases, the region of stick becomes larger and results in more shear traction, which increases the hoop stress at the edge of contact. For a given load transfer ratio of the rivet assembly, as the coefficient of friction increases, there is more load taken up by the interfacial friction between the two skin panels, resulting in less load being transferred through the rivet itself. The tradeoff is that the higher coefficient of friction increases the severity of the local stresses at the skin/rivet contact for a given load. For small remote loads, the load reduction is more than that required to compensate for the increased stress severity, resulting in lower stress values overall. As the remote load increases, the load relief provided by the increased interfacial friction is insufficient to offset the high stress severity. Also, as the coefficient of friction increases for a given remote stress, the interfacial frictional load once again cannot compensate for increased stress severity. There is an optimum coefficient of friction for a given configuration. In a lap joint, the coefficient of friction is expected to stabilize after a few cycles, and hence the application of the preceding phenomenon lies in using coatings to reduce friction. It might be more beneficial to reduce friction at the skin/rivet interface but let the friction develop between the two panels.

At low remote loads, an increased coefficient of friction is beneficial in increasing the crack nucleation life. This beneficial effect becomes less pronounced either as the remote stress increases or as the coefficient of friction becomes very high. At high remote loads, plasticity sets in and constrains the value of peak stress, causing any effects of friction to be blunted.

Effects of Clamping Force

As seen from Fig. 7, the clamping pressure determines the load taken up by interfacial friction between the panels, which reduces the load taken up by the rivet and hence the stress severity at the skin/rivet interface. The two clamping conditions considered correspond to a clamping force of 930 and 1400 N. The clamping pressure diffuses through the thickness and encompasses a larger area at the interface of the two panels. The interfacial friction needs to be overcome before any change in the load transferred through the rivet takes place. The higher the clamping pressure, the greater the interfacial frictional load, and, hence, the less the load on the rivet. This results in lower peak stress values leading to higher nucleation lives as shown in Fig. 14. Again, this effect is less significant in the presence of plasticity.

Effects of Plasticity

The observed plasticity is restricted to a small zone near the edge of contact. The sharp peak in the hoop stress initiates plastic deformation in the first loading cycle. The constraining effect of the surrounding elastic material coupled with the small strain hardening of aluminum causes the plastic deformation to remain small with any additional load being redistributed. The peak stress values remain close to the nominal yield stress. There is no change in the contact area. On unloading, the hoop stress becomes negative close to the edge of contact, and subsequent cycles oscillate between this state and the stress state on reloading. This is demonstrated by the hysteresis plot (Fig. 10). However, the strain amplitude is still comparable to the values obtained in a purely elastic analysis. Hence, as Eq. (3) uses the maximum stress as a parameter, plasticity reduces the value of Γ and hence the crack nucleation life curve flattens out at high remote stresses. In addition, plasticity blunts the effects of increased coefficient of friction and clamping force. However, if a pure-strain-amplitude-based theory is used, plasticity will not have such a significant effect.

Approximate Model

The origin of the stress concentration at the skin/rivet contact can be identified as the combination of the stress concentration due to the rivet hole and the contact stresses. For the purpose of an approximate solution, it may be assumed that the two contributions can be superposed. Whereas the stress concentration can be approximated as a plate with a hole under tension with symmetry boundary conditions along the edges parallel to the tensile traction, the
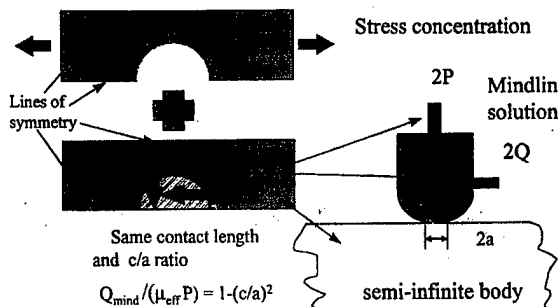

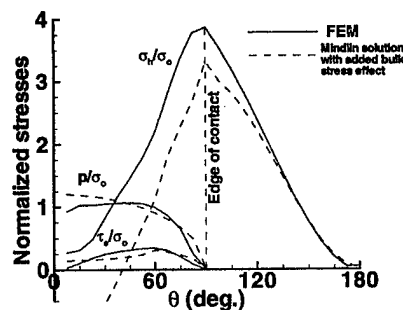Fig. 15 Analytical equivalent of skin/rivet contact.

Fig. 16 Comparison of FEM and analytical contact stresses: $\sigma_o = 83$ MPa, $\mu = 0.4$, maximum clamping pressure = 55 MPa, and LTR = 0.38 (top panel, first row).

contact problem is symmetric about $\theta = 0$ deg and does not have a closed-form solution. However, the corresponding antisymmetric problem (Mindlin problem) has a closed-form solution.[26] The presence of an antisymmetric boundary condition as opposed to a symmetric boundary condition has a small effect at the edge of contact. McVeigh and Farris[27] have shown that the Mindlin solution can be used to approximate more complicated situations involving stress due to other sources in addition to contact stresses. Hence, the preceding approach is appropriate to estimate the stress (and strain) at the edge of contact. Figure 15 shows the schematic decomposition of the problem into a stress concentration and Mindlin problem with the same contact area, normal force, and slip zone. Bending is neglected as it has little effect at the edge of contact. The interfacial friction is assumed to take up a load of $\mu_{eff}F$, where F is the clamping force.

Figure 16 shows the comparison of the finite element solution and the analytical approximation for a particular loading case. The agreement is best near the edge of contact, and the analytical solution degrades as we move away. Whereas the Mindlin solution assumes a Hertzian pressure distribution, the tendency of the hole to deform into an ellipse forces the actual pressure distribution to look different. Also, for the Mindlin problem, the shear stress does not go to zero at $\theta = 0$ deg.

Because a finite element analysis cannot be done for every possible configuration, the parameter governing crack nucleation Γ is quickly estimated as follows. The load transfer ratio, remote stress, clamping pressure, and coefficient of friction are assumed to be known. The interfacial frictional force is calculated, and the load taken up by the rivet is obtained. The ratio of stick zone length to total contact length is assumed to be equal to the coefficient of friction itself. The normal force and the frictional force can be calculated from the remote stress, the load transfer ratio, and the rivet dimensions. The stress concentration (including the symmetry tractions) and the contact stress can now be estimated. A perfectly plastic material is assumed, and the strain amplitude is calculated as if the material were elastic. The details of this implementation can be found in Ref. 28. Figure 17 shows the comparison of the finite element and analytical values of Γ for all of the cases studied. The correlation is good considering the approximations made in the theoretical model. This approximation may be used with Eq. (3) to predict crack nucleation quickly.
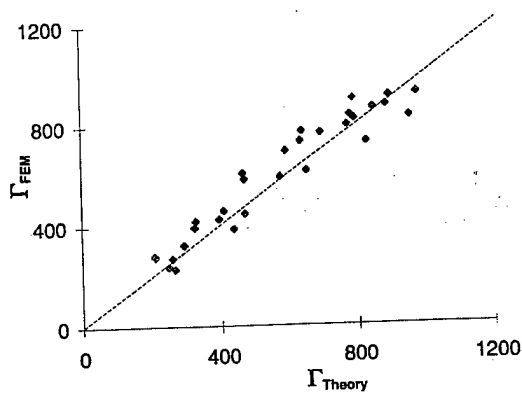
Fig. 17 Comparison of Γ: FEM and theory.

Conclusions

Fretting is one of the causes of crack nucleation in riveted lap joints. For riveted lap joints with no interference, fretting damage can occur at the skin/rivet interface as well as at the interface between the two skin panels. The finite element method has been used to demonstrate the prevalence of conditions conducive to fretting damage. The effects of friction, rivet head clamping pressure, and plasticity are accounted for in a shell model. Higher clamping force causes more load to be taken up at the skin/skin interface, thereby reducing the load on the rivet itself. This also causes the rivet to have some residual load on unloading. A higher coefficient of friction causes more severe contact stresses at the skin/rivet interface but also increases the frictional load-bearing capacity of the skin/skin interface, causing some relief in the load seen by the rivet. There is an optimum coefficient of friction at which the stress severity for a given configuration is minimum. Plasticity constrains the peak value of the stresses at the edge of contact, which is the primary location for the cracks nucleated by the relative slip between the skin and rivet and propagated by the high stresses at the edge of contact. A multiaxial fatigue model based on the Smith–Watson–Topper equation is used to predict the number of cycles to nucleate a fretting crack at the edge of contact. The first row of rivets in a multirow lap joint are the most susceptible to fretting crack nucleation as they transfer more load and are subject to higher stress concentration. A simple model is used to quickly estimate the crack nucleation life for an arbitrary lap joint.

Acknowledgment

References

[1]Kalb, B. J., "Friction Stresses Between Blade and Disk Dovetail Possible Cause of Numerous Dovetail Problems," *Proceedings of the 1991 USAF Structural Integrity Program Conference*, Wright Lab., Wright–Patterson AFB, OH, 1991, pp. 585–601.

[2]Waterhouse, R. B., "Fretting Fatigue in Aqueous Electrolytes," *Fretting Fatigue*, Applied Science, London, 1981, pp. 159–176.

[3]Hurricks, P. L., "Mechanism of Fretting," *Wear*, Vol. 15, 1970, pp. 389–409.

[4]Waterhouse, R. B., and Taylor, D. E., "The Initiation of Fatigue Cracks in a 0.7% Carbon Steel by Fretting," *Wear*, Vol. 17, 1971, pp. 139–147.

[5]Hills, D. A., Nowell, D., and O'Connor, J. J., "On the Mechanics of Fretting Fatigue," *Wear*, Vol. 125, 1988, pp. 129–146.

[6]Nishioka, K., and Hirakawa, K., "Fundamental Investigations of Fretting Fatigue, Part 2," *Bulletin of the Japan Society of Mechanical Engineers*, Vol. 12, No. 50, 1969, pp. 180–187.

[7]Endo, K., and Goto, H., "Initiation and Propagation of Fretting Fatigue Cracks," *Wear*, Vol. 38, 1976, pp. 311–324.

[8]Lincoln, J., "USAF Aging Aircraft Program," *Aerospace Engineering*, Vol. 34, No. 10, 1994, pp. 11–13.

[9]Farris, T. N., Grandt, A. F., Harish, G., and Wang, H. L., "Analysis of Widespread Fatigue Damage in Structural Joints," *41st International SAMPE Symposium and Exhibition*, Society for the Advancement of Material and Process Engineering, Covina, CA, 1996, pp. 65–79.

[10]Iyer, K., Hahn, G. T., Bastias, P. C., and Rubin, C. A., "Analysis of Fretting Conditions in Pinned Connections," *Wear*, Vol. 181, 1995, pp. 524–530.

[11]Petiot, C., Vincent, L., Dang Van, K., Maouche, N., Foulquier, J., and Journet, B., "An Analysis of Fretting–Fatigue Failure Combined with Numerical Calculations to Predict Crack Nucleation," *Wear*, Vol. 181, 1995, pp. 101–111.

[12]Müller, R. P. G., "An Experimental and Analytical Investigation on the Fatigue Behavior of Fuselage Riveted Lap Joints," Ph.D. Thesis, Dept. of Aerospace Engineering, Delft Univ. of Technology, Delft, The Netherlands, 1995.

[13]Ghosh, S. P., Dattaguru, B., and Rao, A. K., "Load Transfer from a Smooth Elastic Pin to a Large Sheet," *AIAA Journal*, Vol. 19, No. 5, 1981, pp. 619–625.

[14]Sundarraj, N., Dattaguru, B., and Ramamurthy, T. S., "Analysis of a Double Shear Lap Joint with Interference Fit Pin," *Computers and Structures*, Vol. 55, No. 2, 1995, pp. 357–363.

[15]Fung, C. P., and Smart, J., "An Experimental and Numerical Analysis of Riveted Single Lap Joints," *Proceedings of the Institution of Mechanical Engineers, Journal of Aerospace Engineering*, Vol. 208, 1994, pp. 79–90.

[16]Reithmaier, L. (ed), *Standard Aircraft Handbook*, 4th ed., Tab Books, Blue Ridge Summit, PA, 1986, Chap. 1.

[17]Keer, L. M., Dundurs, J., and Kiattikomol, K., "Separation of a Smooth Circular Inclusion," *International Journal of Engineering Science*, Vol. 11, No. 11, 1973, pp. 1221–1233.

[18]Narayana, K. B., Dayananda, T. S., Dattaguru, B., Ramamurthy, T. S., and Vijayakumar, K., "Cracks Emanating from Pin-Loaded Lugs," *Engineering Fracture Mechanics*, Vol. 47, No. 1, 1994, pp. 29–38.

[19]Dundurs, J., "Properties of Elastic Bodies in Contact," *Proceedings of the Symposium of the International Union of Theoretical and Applied Mechanics*, edited by A. D. de Pater and J. J. Kalker, Delft Univ. Press, Delft, The Netherlands, 1974, pp. 54–66.

[20]Harris, W. J., *Metallic Fatigue*, Pergamon, New York, 1961, pp. 166–204.

[21]Socie, D., "Critical Plane Approaches for Multiaxial Fatigue Damage Assessment," *Advances in Multiaxial Fatigue*, ASTM STP 1191, American Society for Testing and Materials, Philadelphia, PA, 1993, pp. 7–36.

[22]Szolwinski, M. P., and Farris, T. N., "Mechanics of Fretting Fatigue Crack Nucleation," *Wear*, Vol. 198, 1996, pp. 93–107.

[23]Nowell, D., and Hills, D. A., "Crack Initiation Criteria in Fretting Fatigue," *Wear*, Vol. 136, 1990, pp. 329–343.

[24]Szolwinski, M. P., Harish, G., McVeigh, P. A., and Farris, T. N., "The Role of Fretting Crack Nucleation in the Onset of Widespread Fatigue Damage: Analysis and Experiments," *Proceedings of the FAA–NASA Symposium on the Continued Airworthiness of Aircraft Structures* (Atlanta, GA), Office of Aviation Research, Washington, DC, 1996, pp. 585–596.

[25]Smith, K. N., Watson, P., and Topper, T. H., "A Stress–Strain Function for the Fatigue of Metals," *Journal of Materials*, Vol. 5, No. 4, 1970, pp. 767–778.

[26]Mindlin, R. D., and Deresiewicz, H., "Elastic Spheres in Contact Under Oblique Forces," *Journal of Applied Mechanics*, Vol. 75, Sept. 1953, pp. 327–344.

[27]McVeigh, P. A., and Farris, T. N., "Finite Element Analysis of Fretting Stresses," *Journal of Tribology*, Vol. 119, 1997, pp. 797–801.

[28]Harish, G., and Farris, T. N., "Modeling of Skin/Rivet Contact: Application to Fretting Fatigue," *A Collection of Technical Papers, AIAA/ASME/ASCE 38th Structures, Structural Dynamics, and Materials Conference*, Vol. 4, AIAA, Reston, VA, 1997, pp. 2761–2771.

R. K. Kapania
Associate Editor

WEAR

Observation, analysis and prediction of fretting fatigue in 2024-T351 aluminum alloy

Matthew P. Szolwinski [*], Thomas N. Farris

1282 Grissom Hall, School of Aeronautics and Astronautics, Purdue University, West Lafayette, IN 47907-1282 USA

Aims and Scope

This international journal is dedicated to the rapid publication of high quality papers on the important subjects of wear and friction, together with papers on closely related aspects of lubrication, contact phenomena or surface characterization. The scope includes all aspects of physics, chemistry, materials science and mechanical engineering which relate directly to the subjects of wear and friction; papers may approach the subject from a fundamental or technological viewpoint. Thorough refereeing of all papers, in accordance with normal procedures for international journals in science and engineering, ensures that *Wear* provides an international forum of high quality for multidisciplinary communications on topics which include:

- the fundamental understanding of wear and frictional phenomena, including nanometre and atomic scale aspects of tribology;
- interactions between chemical processes (e.g. corrosion) and wear, and chemical aspects of lubrication (e.g. boundary lubrication);
- design and materials selection for the control of wear and friction;
- tribology of natural biological and artificial implanted materials;
- contact phenomena in the context of friction and wear;
- new materials and their tribological behaviour;
- wear and friction in cutting and forming processes;
- lubricants and mechanisms of lubrication in the context of wear and friction control;
- topics in surface physics and chemistry related to wear and friction

Papers concerned with these Fields may be submitted. Facilities also exist for the prompt publication of Research reports and Letters, subject to editorial approval.

Publication Information

Orders, Claims and Product Enquiries

(no manuscript enquiries)
Please contact the Customer Support Department at the Regional Sales Office nearest you:

WEAR

Observation, analysis and prediction of fretting fatigue in 2024-T351 aluminum alloy

Matthew P. Szolwinski *, Thomas N. Farris

1282 Grissom Hall, School of Aeronautics and Astronautics, Purdue University, West Lafayette, IN 47907-1282 USA

Abstract

Fretting is associated with microslip at the interface of contacts experiencing oscillatory loads. One consequence of fretting is the formation and subsequent growth of cracks at the edge of contact, a phenomenon known as fretting fatigue. Fretting fatigue is an important fatigue failure mechanism in aircraft structural lap joints and turbine blade/disk contacts. A well-characterized, integrated fretting test system has been developed in which both normal and cyclic tangential fretting loads are applied and monitored in conjunction with a bulk load on the specimen. The experimental data includes histories of the three applied forces and a detailed record of the evolution of interfacial friction coefficient, an evolution driven by surface microslip. The experimental system has been exercised to observe fretting crack nucleation and growth under a wide range of loading conditions in the context of a statistically-designed test matrix. An extensive multiaxial fatigue analysis based on the stress–strain cycle experienced by each point of the bodies subjected to the fretting loads reveals that the critical location for crack formation is the trailing edge of contact, consistent with observations made in the laboratory. The resulting stress–strain cycles are coupled with strain-life theory and literature values of uniaxial fatigue constants to predict fretting fatigue crack nucleation. The data collected for 2024-T351 aluminum alloy correlates very well with this prediction. © 1998 Published by Elsevier Science S.A. All rights reserved.

1. Introduction

Fretting, the interfacial damage process that arises from a tripartite interaction among wear, corrosion and fatigue phenomena, is experienced by nominally-clamped surfaces subjected to oscillatory loads or vibrations. With nearly every mechanical system witnessing such requisite contact conditions and in light of the potential componential degradation driven by the highly-localized contact stresses and surface microslip associated with the frictional fretting tractions, those responsible for the design, manufacturing and subsequent maintenance of systems must be able to assess quantitatively the severity of the impact fretting can have on product life.

* Corresponding author. 2046 Jonsson Engineering Center, Department of Mechanical Engineering, Aeronautical Engineering and Mechanics, Rensselaer Polytechnic Institute, 110 8th Street, Troy, NY 12180-3590. Tel.: + 1-518-276-2024; Fax: + 1-518-276-6025; E-mail: szolwin@rpi.edu

The role of fretting in the degradation of one particular class of complex systems—civilian and military aircraft—has been highlighted recently during teardown analyses of riveted joint structures from both in-service aircraft and laboratory specimens [16,22]. Reports correlating initiation sites of widespread fatigue damage (WFD) and localized fretting damage at and around the rivet/hole interfaces have been made by Refs. [27,30]. Acute attention has also been given to the nucleation of fatigue cracks over a large number of cycles in the so-called high cycle fatigue regime by fretting contact between turbine blades and discs at the dovetail joint in aircraft engines.

The complete characterization and control of the parameters influencing fretting in a seemingly-simple structure such as a riveted lap joint is a daunting one, however. Dobromirski [8] suggests there may be as many as fifty process variables influencing fretting damage, including contact pressure, slip amplitude, hardness of contacting surfaces and temperature. Any efforts targeted at elucidating the parameters critical to fretting damage must be able

to (1) control consistently and monitor continuously the requisite conditions for characterization of the contact, (2) develop a metric based on these parameters allowing for objective quantification (and perhaps prediction) of the damage process, and (3) validate the quantitative investigation with a detailed statistical analysis of the observations. The current effort, framed within a statistically-designed experimental grid and supported by a well-characterized and controlled experimental setup seeks to assess quantitatively the effects of fretting on crack nucleation in an aluminum alloy common to aircraft structures, 2024-T351.

The following will present an overview of the experimental setup employed in the investigation and offer succinctly the details of the mechanics of fretting contact present in such a configuration, motivating an interpretation of the results with regard to a simple analytical model for the prediction of fretting crack nucleation.

2. Experimental setup

Any fretting fatigue test apparatus must be designed for application of both a clamping or normal load (P) to establish contact between two surfaces and a subsequent shearing or tangential loading (Q) to induce relative motion of the contact interface, as shown in Fig. 1. And while the terms 'fretting' and 'fretting fatigue' are most often used synonymously, it is important to note that 'fretting fatigue' implies an oscillatory tangential loading of the contacting bodies with subsequent nucleation and growth of fatigue cracks.

The distribution and amplitude of the relative displacement between the contact surfaces depends intimately on

the amplitude of the applied tangential force. From consideration of an Amontons or Coulomb friction law on a global scale, it is clear that relative motion of the bodies can occur only when the ratio of the applied tangential force to normal force, Q/P, reaches the average coefficient of friction at the contact surface, $\mu_{average}$. (The distinction 'average' is made here as the nomenclature μ is used to refer to the coefficient of friction in the slip zones elsewhere.) Only under such a tangential load is gross sliding generated over the entire contact interface. Under the influence of any conditions in which $|Q| < \mu_{average}P$, a kinematic condition of partial stick or no relative displacement must exist across some portion of the interface.

2.1. Fretting test fixture

While experimental research into fretting fatigue has been conduced for decades [24,33], the debate over a standard for fretting fatigue testing continues unabated, as summarized by Waterhouse [32]. Driving this discord is the difficulty in devising a single test or apparatus to capture the complex mechanical and environmental conditions driving fretting damage present in even seemingly basic mechanical systems. However, most fretting fatigue test fixtures involve the application of a cyclic tangential load to a pad or pads pressed into contact against a usually-flat specimen. The geometry of the pads can vary, ranging from spherical [5], to cylindrical [25] to flat [23]. In many configurations, an additional cyclic bulk stress is induced in the specimen under the influence of oscillatory torsional [9], bending [33] or axial [26] loading.

One of the more common styles of fixtures used for investigations of fretting fatigue is pictured schematically in Fig. 1. After establishing contact between either a cylindrical or flat pad and a flat specimen face, a tangential force can be induced on the pads by the application of an axial bulk load to the specimen fixed at one end. The 'spring' attached to the pad resists motion of the pad along with the specimen, resulting in a tangential load that varies in phase with the bulk axial loading (for a dual-actuator setup allowing for out-of-phase tangential and bulk loading, see work by Hills [14]).

A configuration relying on a single actuator is attractive, though, as it can be implemented with the integration of additional fixturing onto a standard uniaxial servohydraulic fatigue test frame, as pictured in Fig. 2. A chassis capturing the fretting pads is connected to two beam structures and then mounted on a set of uprights bolted to the load frame platform. This chassis/beam structure serves as the 'spring' referenced in Fig. 1. Varying the thickness of the beam members allows for generation of larger tangential forces with the same bulk loading. A set of drawbars passed through the chassis serve as a proving ring structure for application of normal load to the pads. Tightening a set of nuts on the drawbars produces the
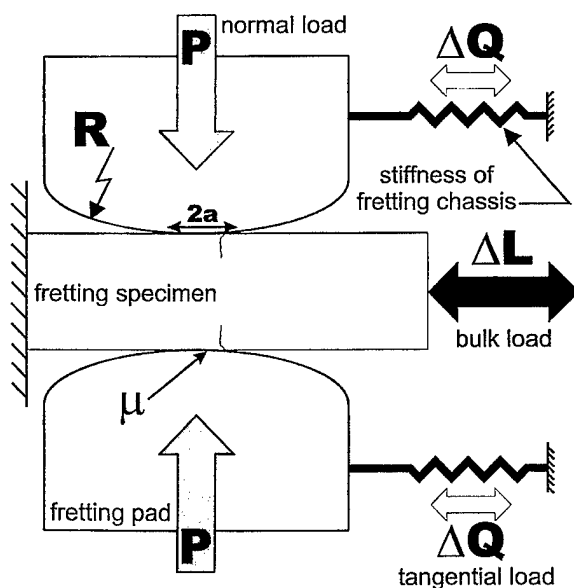
Fig. 1. A schematic of a single-actuator fretting fatigue fixture, highlighting loading, geometric and contact parameters. For a condition of partial slip at the contact interface, $|Q| < \mu_{average}P$.
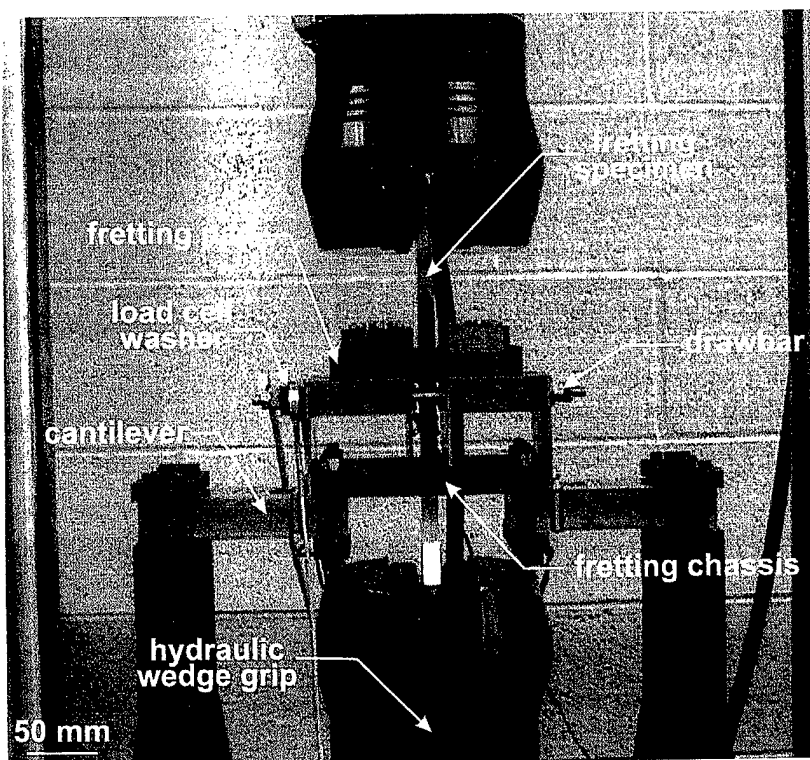
Fig. 2. A photograph of the fretting fatigue test fixture. Note that the schematic in Fig. 1 is rotated by 90° from the actual experimental configuration.

normal load responsible for establishing contact between the pads and the faces of the fretting specimen mounted in hydraulic wedge grips attached to the upper and lower halves of the load train.

The current study, which relies on such a setup, focuses on fretting fatigue crack nucleation in an aluminum alloy common to aircraft structures, 2024-T351. The fretting specimen geometry (Fig. 3) conforms to currently-accepted standards for uniaxial fatigue test specimens (ASTM E 466-82). These specimens were machined from as-received 2024-T351 rolled stock with cross-section 1.5-in. by 0.5-in. (38.1 mm by 12.7 mm). The geometry of a typical fretting
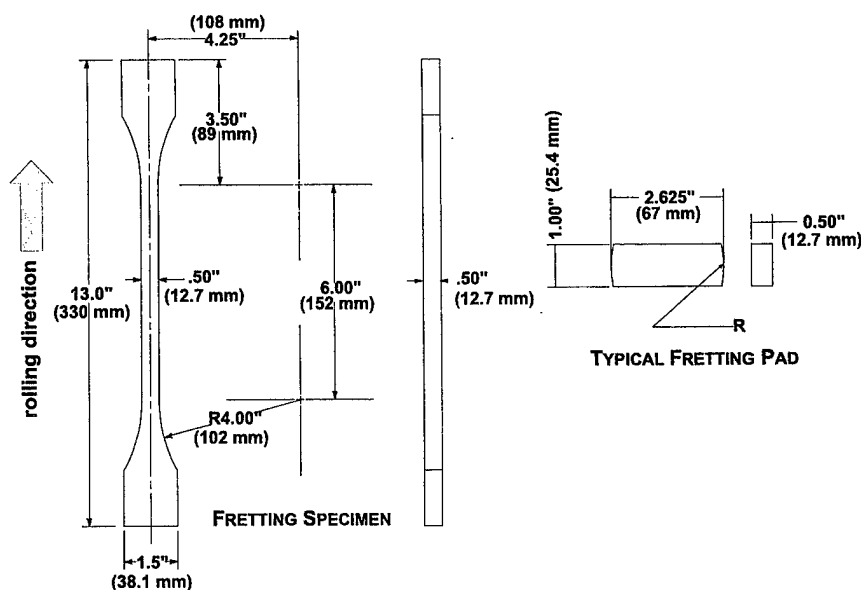
Fig. 3. Dimensioned design drawings for the fretting specimens and a typical fretting pad.

pad is also presented in Fig. 3. The pads were manufactured by machining a cylindrical profile of desired radius on both ends of sections cut from as-received 2024-T351 rolled stock with a 1-in. × 0.5-in. cross-section (25.4 mm by 12.7 mm).

Before establishing contact between the as-received rolled surface of the specimens and milled face of the pads, the regions of contact were polished lightly first with sandcloth (300 grit followed by 600 grit) and followed with a pass by a cloth wheel treated with wax-based rouge. Each of these polishing actions was made along the direction of subsequent tangential loading. The surfaces were then wiped thoroughly with acetone to remove all residual traces of debris remaining from this preparation process.

Traces with a Talysurf contacting surface profilometer revealed that arithmetic average roughness (R_a) values transverse to the polishing direction were in the range of 8 to 12 μin. (0.2 to 0.3 μm). While no standard for fretting tests exists currently, these values of surface roughness for the pads and specimen surfaces fall near the range mandated by the American Society for Testing and Materials (ASTM) standard for sliding wear tests (ASTM G 115-93).

2.2. Transducer array and data acquisition

Inherent to characterizing the fretting contact present at the pad specimen interface and subsequently quantifying the fatigue damage process is accurate control and monitoring of: (1) the applied normal load, P, (2) the oscillatory tangential load, Q, and (3) the bulk stress, σ_o, applied by the actuator to the portion of the specimen below the contact. Concomitant with this monitoring is the need for automated test control and data acquisition. This fact is emphasized by Attia [1] in a summary of a series of papers aimed at developing a fretting fatigue test standard. Attia [1] notes that measurement of contact parameters and automation of the testing procedure and data acquisition are still areas to be addressed adequately by the fretting fatigue test community.

Real-time measurement of the contact parameters is accomplished in the current setup with an array of analog sensors integrated into both the fixture and load train. The total normal force is determined from the calibrated output of a load cell washer slipped over each drawbar assembly. The total tangential force can be measured in two ways: as the difference between the calibrated output from strain gages placed on the specimen below the contact point and the load cell mounted in the load train; and as the calibrated output of a Wheatstone bridge composed of four strain gages bonded on each of the beam members. With the first approach, global static equilibrium of the rig/specimen combination is considered: the load transmitted by the rig is calculated as the difference between the load applied by the actuator to the portion of the specimen below the contact and the reaction load detected by the load cell above the contact. This measurement is

also used to determine a calibration relationship between the tangential force, Q, and deflection of the beams, as measured by strain gages mounted on the beams. Such a calibration provides not only a redundant monitoring system for the tangential force, but also the ability for measuring independently the tangential force at each pad/specimen interface.

As with any fatigue test involving a large number of cycles, automated testing and data acquisition is important. Braun [4] assesses the past, current and future directions of automated fatigue and fracture testing, identifying the characteristics of a next-generation test setup. These characteristics include: (1) a digital control system that implements the control loop and function generation for the waveform applied by the servo-hydraulic loadframe via software, (2) a flexible data acquisition scheme allowing for a wide variety of experimental configurations, and (3) an intuitive software system that relies on a graphical-user interface (GUI). Several diversified approaches have been taken to realize such a system, including use of a UNIX-based workstation and analog controller [17] and general purpose fatigue testing software [7] with a digital controller. Each of these approaches required a significant investment of time and effort for constructing the base code for efficient communication between the myriad of components in the test system.

The current experimental setup relies exclusively on commercially-available hardware components and software packages to achieve a single, flexible, graphically-oriented, personal computer (PC) based system for control, data acquisition (DAQ) and on-line data processing. A schematic of the system is presented in Fig. 4. The requisite control signals corresponding to a given set of frequency, waveform and amplitude parameters are sent to the servo-valves by an Instron 8500 digital controller. The controller can operate either stand-alone through an attached panel-style user interface or remotely through a digital input/output (I/O) line that relies on a standardized general-purpose interface bus (GPIB). This GPIB connection allows for integration of the controller with standard PC bus architecture.

The excitation of each of the analog transducers (Wheatstone bridges and load washers) and subsequent conditioning of the analog signals from the sensors is achieved with a general-purpose Signal Conditioning eXtensions for Instrumentation (SCXI) chassis manufactured by National Instruments. The module allows for user-definable excitation voltages (3.333 or 10 V), two-stage signal gains (from 1 to 1000) and two-stage filters (4 Hz or 10 kHz). The current configuration offers up to eight channels, with the potential for expansion to twelve.

The preconditioned analog signals from the array of sensors are then read from the SCXI chassis in either a multiplexed or parallel mode by a 16-bit analog-to-digital (A/D) data acquisition card in the PC. This card, an AT-MIO-16XE-50 card also manufactured by National
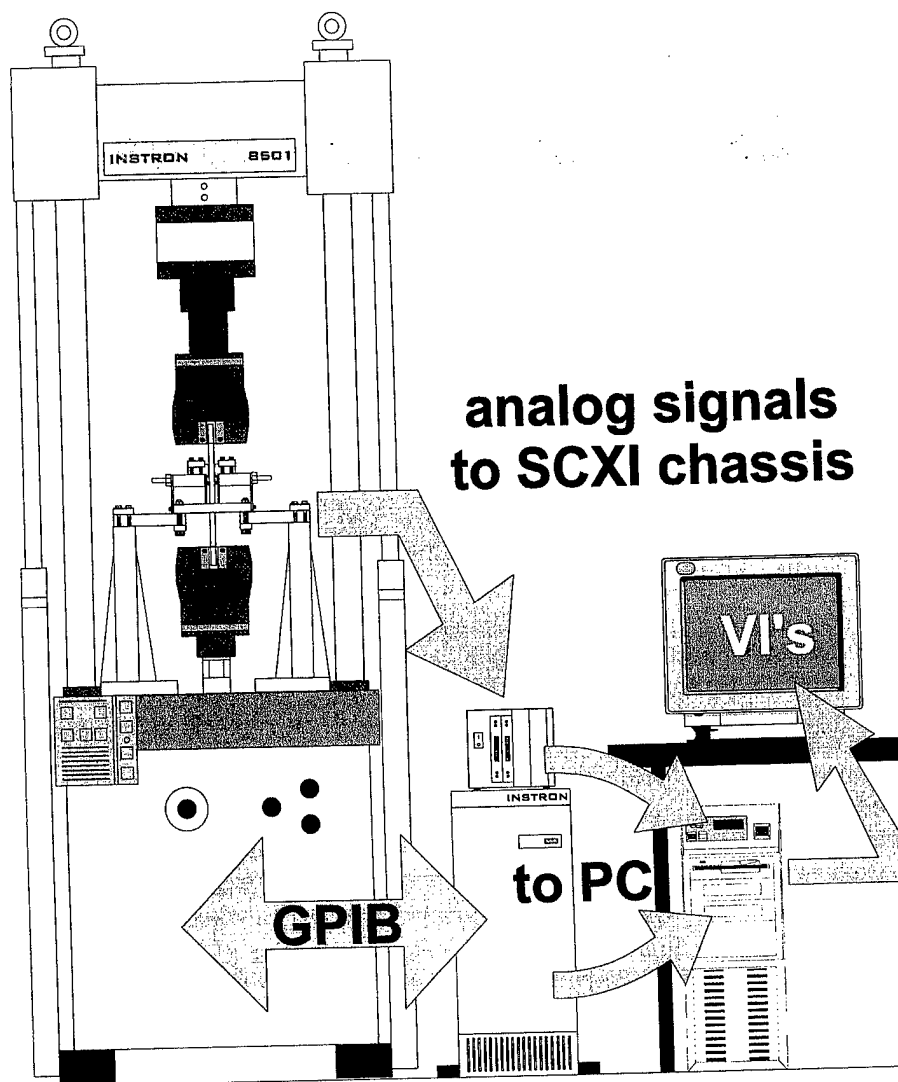
Fig. 4. An illustration of the data acquisition system, including hardware and software, used in the fretting fatigue tests.

Instruments, can read up to 16 single-ended or 8 differential channels at a maximum of 20 kilosamples/s with a maximum resolution of 3 μV.

The real strength of this DAQ system lies not necessarily in the performance and flexibility of its hardware, but in the ability for the hardware to be integrated into a single suite of user-friendly GUI panels that allow for the on-line control, monitoring and analysis of each fatigue experiment. This software platform was developed using National Instrument's LabVIEW (the *Lab*oratory *V*irtual *In*strument *E*ngineering *W*orkbench), a general purpose graphical 'language' that allows the user to develop virtual instruments (VI) for interfacing with a myriad of DAQ entities. Since many of the base level operations such as direct communication with hardware, generation of complex GUI's and data file creation and management are inherent parts of the language constructs, the time required to develop the flexible and versatile software used in the fretting fatigue tests was slashed.

The current experimental effort relies on an integrated suite of custom-designed virtual instruments to control, monitor and analyze the fretting fatigue tests. An initial panel serves as an interface to the 8500 digital controller for the load frame. The user configures parameters such as control channel (load or position), waveform type, amplitude, frequency, and any limit values from a collection of dialog boxes. Complete remote operation of the load frame is possible from this GUI. Two other GUI panels serve to configure, control and monitor graphically the data acquisition of both the load and position digital signals from the 8500 and multiple channels of analog signals from the array of sensors on the fretting rig. The user can configure the number of channels collected, the frequency of data collection and the number of points collected per cycle.

Once this data is collected from the various sources, it can be manipulated in several ways: presented in real-time on screen in graphical format, processed on-line with a wide variety of mathematical functions, or written in bi-

nary or ASCII format to a storage device at user-defined cycle numbers for subsequent automated post-processing by a separate suite of Visual Basic spreadsheet macros.

3. Experimental observations and analysis of results

The main focus of the experimental effort was to identify quantitatively the effects of fretting contact parameters on crack nucleation. To this end, four independent and controllable factors were selected to characterize the fretting contact at the pad/specimen interfaces. The factors of interest were normal load, P, pad radius of curvature, R, specimen bulk or remote stress, σ_o, and ratio of applied tangential force (Q) to bulk axial load (L), denoted symbolically as Q/L. (Changing the beam members or 'spring stiffness' of the fretting fixture effected control of this last factor.) Three levels for each factor were targeted, as summarized in Table 1, with these levels selected to simulate fretting conditions similar to those present at and around the rivet/hole interface of riveted lap joints [13].

3.1. Design of experiments

One approach to studying the interaction effects between two or more factors in an experimental program is known as factorial design. This efficient experimental strategy, which often falls under the more generic term 'design of experiments,' calls for the variation of factors together with a final aim of relating the change in experimental response to the change in the factors. Often used in industrial research and development or process improvement [21], factorial design and subsequent statistical analysis of the experimental results can provide a method for quantitative identification of not only main effects of factors, but also any potential interaction between factors. This method allows for conclusions to be drawn that are valid over a range of experimental conditions.

A complete factorial design that would allow for estimation of all main effects and factor interactions would require 3^4 or 81 experiments. Making an a priori assumption that higher order interactions between factors in Table 1 were negligible, a one-third fractional factorial design involving only 27 experiments was selected. This approach enabled estimation of all the main and first order factor interactions. Generation of a randomized grid ordering the

Table 1
A summary of the factors and their targeted levels for the series of fretting fatigue tests on 2024-T351 aluminum alloy

Factor	Level 1	Level 2	Level 3
P, lb$_f$ (kN)	1200 (5.4)	1400 (6.2)	1600 (7.1)
R, in. (mm)	5 (127)	7 (178)	9 (229)
σ_o, ksi (MPa)	12 (82.7)	14 (96.5)	16 (110.2)
Q/L	0.1	0.124	0.134

27 experiments was performed using a commercially-available statistical analysis software package, SAS, a registered trademark of the SAS Institute, Cary, NC. The experimental parameters for this grid (denoted as 'MAF' experiments) are presented in Table 2.

3.2. Experimental observations

The fretting fatigue tests were conducted under constant-amplitude load control at a frequency of 10 Hz with R-ratio $= L_{min}/L_{max}$ ranging from -0.98 to -1. The testing environment consisted of standard laboratory conditions—temperature between 70–75°F (21–24°C) and relative humidity between 65–75%. Each of the experiments was run to failure, defined as complete fracture of the specimen. Failure was never observed in the pads. Fig. 5 displays macroscopic photographs of a typical fretting wear scar on the face of a pad and a fracture surface of a fretting specimen. The fretting wear scar on the face of the pad is mirrored on the corresponding contact face of the specimen.

Failure was caused in every test by a crack that nucleated at the trailing edge of contact—the edge of contact closest to the actuator end of the specimen. Coincident with this failure site was a deposit of black wear debris (see Fig. 5), a buildup of particles worn from the contact surfaces by interfacial microslip. This location is the trailing edge of contact when bulk applied load L is tensile in nature. To characterize further the details of the nucleation process, a fretting test was carried out for 150,000 cycles (before complete specimen failure) under controlled and monitored conditions ($P = 6.76$ kN (1520 lb$_f$) $R = 178$ mm (7 in.), $\sigma_o = 98.5$ MPa (14.3 ksi) and $Q/L = 0.13$). After the prescribed number of cycles, the specimen was removed and sectioned for a metallographic analysis. The bakelite-mounted sections represented 6.35 mm by 12.7 mm (0.25 in. by 0.50 in.) portions of the TL metallographic plane (see Fig. 3). The faces of these sections were then polished and etched using Keller's reagent (a solution of HF, HCl and HNO$_3$) per standard practices suggested for microstructural analysis of 2XXX series aluminum alloys [19].

Fig. 6 presents a photomicrograph of the near-surface area of one section around the trailing edge of contact. A crack of about 300 μm in length at the trailing edge of contact is clearly visible. Further scrutiny of the crack morphology reveals a short ligament (~ 25 μm) at the surface that nucleated oblique to the horizontal contact surface and turned quickly to grow in an orientation nearly perpendicular to the contact interface. This characteristic initiation site and crack morphology are consistent with observations reported by Nowell and Hills [26] for similar experimental configuration. Also note the presence of a potentially-arrested near-surface oblique crack approximately 425 μm to the left of the trailing edge crack

Table 2
A summary of the parameters and observed failures lives for each of the fretting fatigue experiments conducted as part of the current study, in SI units

Experiment	P (kN)	R (mm)	σ_0 (MPa)	Q/P	p_0 (MPa)	a (mm)	c (mm)	σ_{max} (MPa)	$N_{propagation}$ (cycles)	$N_{failure}$ (cycles)
P001c	7.562	127	110.3	0.22	246.0	1.54	1.25	296.3	26,864	314,000
P004x	4.893	127	84.7	0.28	197.8	1.24	0.94	252.0	65,828	422,000
P006x	5.427	127	110.3	0.31	208.4	1.31	0.94	297.4	26,864	241,475
P008x	4.880	121	100.7	0.35	202.7	1.21	0.82	293.5	36,632	241,016
P011b	6.316	121	110.3	0.31	230.6	1.37	0.99	317.4	26,864	217,061
MAF1a	5.454	229	111.7	0.43	155.7	1.76	1.02	276.2	25,757	238,000
MAF1b	5.427	229	112.9	0.37	155.3	1.75	1.15	265.5	24,863	249,574
MAF2x	6.228	127	84.8	0.23	223.2	1.40	1.12	257.6	65,467	668,277
MAF3a	6.268	178	100.0	0.27	189.2	1.66	1.27	258.1	37,458	349,520
MAF3b	6.263	178	100.0	0.27	189.2	1.66	1.27	258.1	37,458	433,780
MAF4x	5.370	127	88.4	0.35	207.3	1.30	0.89	285.3	56,849	563,946
MAF5a	7.226	127	101.9	0.31	240.4	1.51	1.10	316.1	35,140	545,489
MAF5b	7.226	127	101.9	0.31	240.4	1.51	1.10	316.1	35,140	337,934
MAF6x	5.310	178	85.8	0.38	174.2	1.53	0.99	258.5	62,959	582,922
MAF7x	6.223	229	97.0	0.32	166.3	1.88	1.34	247.8	41,528	739,250
MAF8x	6.994	178	113.1	0.34	199.9	1.75	1.22	300.1	24,697	455,759
MAF9x	6.268	229	85.4	0.32	166.9	1.88	1.33	238.6	63,903	856,524
MAF10x	5.201	127	115.8	0.52	204.0	1.28	0.58	352.1	22,774	465,000
MAF11a	7.085	178	85.2	0.21	201.2	1.77	1.45	234.2	64,435	665,073
MAF11b	7.085	178	85.2	0.21	201.2	1.77	1.45	234.2	64,435	749,093
MAF12a	7.072	229	81.8	0.24	177.3	2.00	1.59	221.5	74,060	747,135
MAF12b	7.073	229	81.8	0.25	177.3	2.00	1.56	225.9	74,060	729,715
MAF13x	6.215	127	109.2	0.35	223.0	1.40	0.96	320.7	27,779	302,804
MAF14x	5.293	229	81.0	0.31	153.4	1.73	1.24	219.7	76,466	867,330
MAF15x	5.325	229	82.9	0.26	153.8	1.74	1.34	210.3	70,799	768,364
MAF16x	7.251	178	99.4	0.31	203.6	1.79	1.29	283.0	38,265	552,250
MAF17x	7.002	229	109.5	0.34	176.4	1.99	1.36	276.5	27,583	320,864
MAF18x	7.070	127	108.8	0.27	237.8	1.49	1.13	309.2	28,151	253,883
MAF19x	6.187	229	110.8	0.33	165.8	1.87	1.31	264.7	26,460	479,540
MAF20x	6.275	127	98.2	0.36	224.0	1.40	0.93	316.1	39,871	464,166
MAF21x	7.153	229	97.9	0.24	178.3	2.01	1.60	237.7	40,273	463,324
MAF22x	6.176	178	84.7	0.27	187.9	1.65	1.27	241.2	65,612	621,442
MAF23x	5.319	178	97.4	0.36	174.3	1.53	1.02	266.3	40,971	459,882
MAF24x	6.460	178	106.4	0.34	192.1	1.69	1.16	287.6	30,335	225,535
MAF25x	5.351	178	110.6	0.38	174.9	1.53	0.98	285.3	26,665	330,695
MAF26x	5.462	127	97.1	0.33	209.0	1.31	0.92	291.5	41,385	311,516
MAF27x	7.118	127	85.4	0.27	238.6	1.50	1.14	286.5	63,881	381,535

The 'MAF' experiments were part of the partial factorial grid, while the 'P0XXx' data were generated during a separate preliminary series of experiments.

nearly coincident with the border of stick and slip (Fig. 6). For the applied loads, pad geometry and $\mu = 0.65$, the associated contact halfwidth, a, is 1.72 mm and stick zone halfwidth, c, is 1.25 mm.

3.3. Analysis of results

With some qualitative understanding of the mechanics of fretting fatigue crack nucleation, focused steps toward
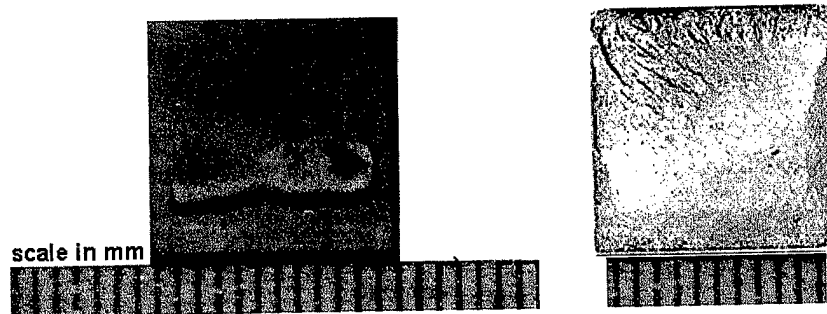

Fig. 5. Photographs of a fretting wear scar on a pad surface (left) and the fracture surface of a failed fretting fatigue specimen (right). The theoretical contact width, $2a$, is 3.4 mm (0.136 in.) as given from Hertzian contact theory using the following load, material and geometric parameters: $P = 6.76$ kN (1520 lb$_f$), $R = 178$ mm (7 in.), $E = 74.1$ GPa (10.7×10^6 psi), $v = 0.33$.
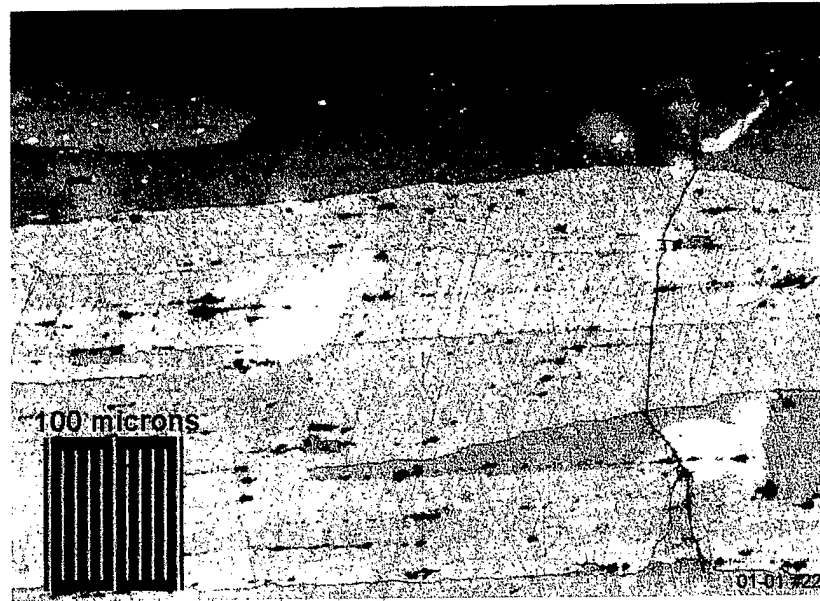
Fig. 6. A photomicrograph at 20 × of the TL plane from a fretting specimen subjected to 150,000 cycles. Note the nearly-perpendicular growth of t crack at the trailing edge of contact (right side). Also notice the seemingly-arrested near-surface oblique crack approximately 425 μm to the left of t trailing edge, corresponding to the border between stick and slip regions.

quantifying the effects of contact parameters on this process can be taken. A graphical summary of the fretting fatigue lives from not only the fractional factorial grid of experiments, but also an earlier series of tests and results present in the literature [26] is offered in Fig. 7. The plot presents life to failure vs. applied bulk or remote stress, σ_0. No effect of the contact is accounted for in this value of stress. Two S–N curves (unnotched specimen and notched specimen with $K_t = 2.0$) for 2024-T3 sheet (MIL-HDBK-5G, 1994) are included on the plot as comparative references. Since the applied bulk stresses are well below the 20 ksi (138 MPa) runout stress amplitude for the unnotched specimen tests, incorporating the fretting contact stress field into a metric for fretting crack nucleation is imperative.

Szolwinski and Farris [31] have proposed coupling an analytical, mechanics-based assessment of the cyclic stresses and strains induced by the fretting interfacial tractions (see Fig. 8) with a multiaxial fatigue life parameter relying on uniaxial strain-life constants. This approach identified the trailing edge of contact ($x = -a$, $z = 0$ in Fig. 8) as the critical location of crack nucleation for the state of stress present in the current experimental configuration. While approaches for correlating fretting contact conditions and crack nucleation have been proposed by several workers, including Dang Van et al. [6] and Fouvry et al. [10], none of the models have the ability to provide a quantitative estimate of the nucleation process relying on closed-form analytical expressions and readily-available material data (see Ref. [31] for a more in-depth treatment of efforts engendered to correlate fretting contact conditions and fretting crack nucleation).

Closed-form solutions for the subsurface elastic stress strains and surface displacements associated with giv normal and tangential loads (P and Q) and coefficient friction in the slip zones (μ) are available [31]. T addition of the bulk tension in the specimen leads to non-symmetric stick zone [18]. Finite element results fr a model of fretting contact for a wide range of loadi parameters point toward the source of crack nucleation d to fretting: a sharp tensile peak in the tangential stre σ_{xx}, at the edge of the contact zone, $x = +a$ (see Fig. !

The observed crack morphology reported earlier is cc sistent with this highly-localized region of tensile tange

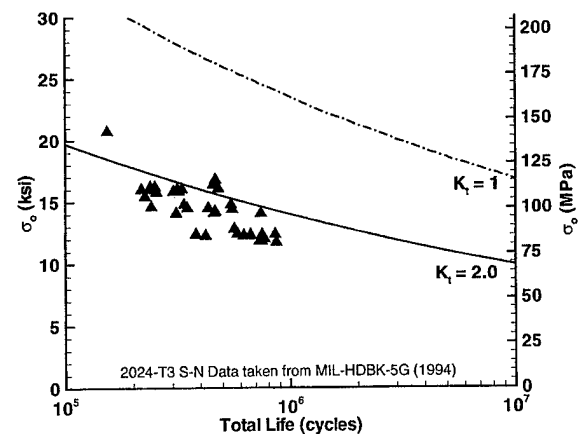Fig. 7. Observed cycles to failure for fretting fatigue specimens plot against bulk applied stress amplitude (no contact stresses). S–N cur estimated from published data (MIL-HDBK-5G, 1994) for notched (K 2.0) and unnotched ($K_t = 1$) specimens.
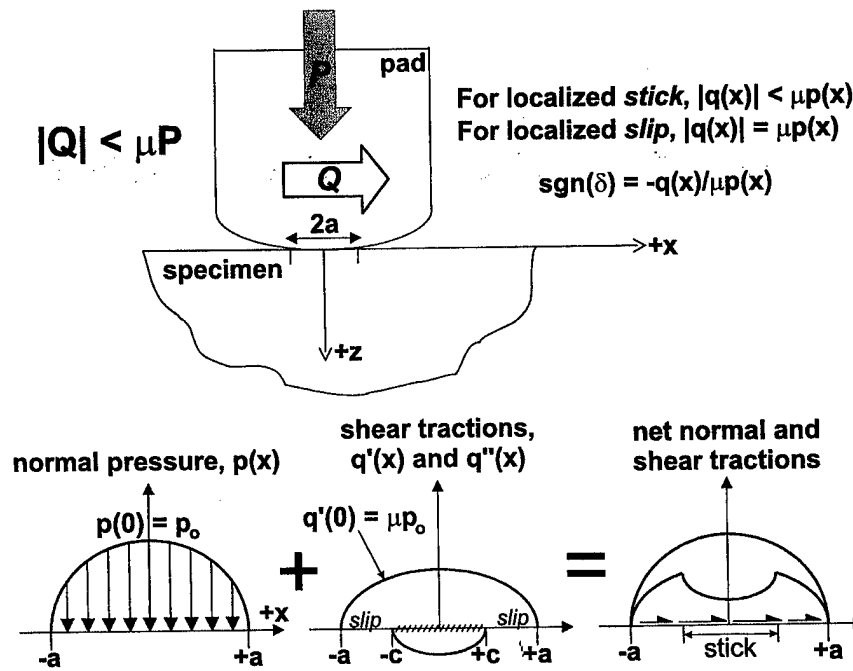
Fig. 8. A summary of the surface tractions associated with fretting fatigue, ignoring the effect of σ_0 on the distribution of partial slip.

tial stress at the trailing edge of contact. Also note the compressive nature of the tangential stress at the boundary of the stick and slip zones, in light of the arrested near-surface oblique crack observed at this location.

The analytical expression for the component of σ_{xx} at this location due to the fretting alone reduces conveniently to [15]:

$$(\sigma_{xx})_{\text{fretting}} = 2p_0\sqrt{\mu Q/P} \tag{1}$$

where p_0 is the maximum Hertzian pressure and μ is the coefficient of friction in the slip zones. This solution corresponds to a symmetric distribution of slip zones in which slip occurs in the same direction. The application of bulk stress serves to generate slip in opposite directions, causing an unsymmetrical distribution of slip. However, McVeigh and Farris [18] have shown that a modification of Eq. (1) that includes the effect of the bulk stress estimates accurately the peak stress for this case as well. Thus, the total tangential stress at the trailing edge of contact can be approximated as a superposition of the fretting contact stresses and the applied bulk stress, according to:

$$(\sigma_{xx})_{\text{total}} \equiv \sigma_{\text{max}} = (\sigma_{xx})_{\text{fretting}} + \sigma_0 = 2p_0\sqrt{\mu Q/P} + \sigma_0 \tag{2}$$

It should be noted that at the edges of contact, $|x| = a$, $z = 0$, both the pressure and shear tractions are identically zero, leading to a 'quasi-uniaxial' state of stress at this point, an observation also made by Fouvry et al. [10]. Thus, for contact pressures in the range of 25 to 30 ksi (172 to 207 MPa), bulk stresses on the order of 12 to 14 ksi (83 to 96 MPa), a nominal value of $Q/P = 0.3$

(representative of the experimental grid) and $\mu_{\text{slip}} = 0.65$ as determined by Szolwinski [30], the fretting contact provides a stress concentration $\sigma_{\text{max}}/\sigma_0$ between approximately 2.5 and 3.0.

Furthermore, for plane-strain, elastic contact (assumed for the range of loads and contact parameters present in the
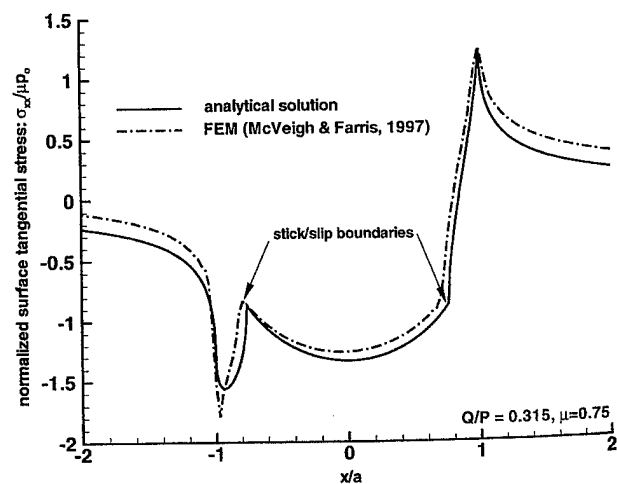

Fig. 9. Plots of normalized tangential stress, $\sigma_{xx}/\mu p_0$, from both analytical [31] and finite element [18] models of fretting contact between a cylindrical pad and flat specimen. For the case presented, $Q/P = 0.315$, $\mu = 0.75$ and $\sigma_0 = 0$. For this distribution, Q is oriented from $x = +a$ toward $x = -a$, making $x = +a$ the critical location for crack nucleation.

experiments), the corresponding strain at the trailing edge of contact is simply:

$$\epsilon_{xx} = \frac{1 - \nu^2}{E} \sigma_{xx}$$ (3)

As the ratio of the tangential load to normal load, Q/P, changes with an oscillatory tangential load, the cyclic stresses and strains are non-proportional in nature, leading to a state of cyclic multiaxial stress beneath the contact. Any attempt to predict nucleation of fatigue cracks due to the influence of fretting must account for this fact. Based on the hypothesis that the peak in tensile stress at the trailing edge of contact drives the observed nucleation of fretting cracks perpendicular to the contact, the proposed relationship between reversals to nucleation (1 cycles = 2 reversals) and the product of strain amplitude and maximum stress during a complete loading cycle normal to the principal plane (the plane of the nucleated crack) is:

$$\sigma_{max}\left(\frac{\Delta\epsilon}{2}\right) = \frac{(\sigma_{f'})^2}{E}(2N_f)^{2b} + \sigma_{f'}\epsilon_{f'}(2N_f)^{b+c}$$ (4)

The form of this parameter is simply the familiar Smith–Watson–Topper equation [2], which relates the product of maximum stress and strain amplitude to uniaxial fatigue test data. Socie [28] applied successfully the Smith–Watson–Topper model to correlate crack nucleation observations in strain-controlled tension and torsion tests of AISI Type 304 stainless steel tubular specimens. In the torsion tests, cracks were observed to nucleate initially on shear planes (classical Stage I behavior). The majority of the life, though, was consumed by further growth in a classical mode I manner under the influence of the applied tensile stress. No evidence of shear cracking was detected in the tension tests, with cracks nucleating in a pure mode I manner. Discussion of this approach is presented in more detail elsewhere [31].

Combining Eqs. (2) and (3) allows for the iterative solution of Eq. (4) and an estimate of cycles to nucleation of a crack under the influence of fretting contact. Uniaxial strain-life constants generated by Blatt [3] for 2024-T351 smooth-bar specimens and elastic constants for the same alloy [20] are summarized in Table 3.

3.4. Fretting crack nucleation predictions

The application of a strain-life approach to fatigue crack nucleation requires the definition of either a failure criterion or a 'nucleated' crack. Fuchs and Stephens [11] note that common definitions include life to a certain percentage decrease in load amplitude, life to a small detectable crack or life to fracture. In the fretting fatigue tests, direct in-situ visual observation of a crack was impossible, with cracks initiating at the contact interface. Thus the approach taken was to separate the total specimen life into cycles to nucleate a crack of 1 mm and cycles to propagate this

Table 3
A summary of 2024-T351 aluminum alloy material constants used in the fretting fatigue crack nucleation analysis

$\sigma_{f'}$	fatigue strength coefficient	103.6 ksi (714 MPa)
b	fatigue strength exponent	−0.078
$\epsilon_{f'}$	fatigue ductility coefficient	0.166
c	fatigue ductility exponent	−0.538
E	Young's modulus	10.7×10^6 psi (74.1 GPa)
ν	Poisson's ratio	0.33
C	Paris law coefficient	3.59×10^{-9} for in., ksi, cycles
m	Paris law exponent	3.387

The strain-life constants are taken from Blatt (1990), the elastic constants from MIL-HDBK-5G (1994), and the crack-growth constants from Gallagher [12].

crack to cause complete fracture of the specimen. This approach is not arbitrary, as will be presented: it is based on both an understanding of the nature of the near-surface contact stress field and fractographic evidence from failed specimens.

A review of contours of the subsurface stress field associated with fretting contact [25,18,31] reveals that the contact stresses decay rapidly beneath the contact surface. Typically, the effect of the contact is negligible one or two contact halfwidths (a or $2a$) beneath the interface. It follows then that any effect of the fretting contact on a crack longer than a or $2a$ would also be negligible. With the majority of the contact halfwidth values for the fretting experiments on the order of 1.5 mm, a length of 1 mm was chosen to define a nucleated crack. This definition is also consistent with work by Socie [29].

With a definition of cycles to nucleation, an estimate of the propagation phase of total life is required. While it is clear that this phase of life is controlled entirely by the bulk applied stress in the specimen, an assumption about crack morphology must be made for application of fracture mechanics to estimate a propagation life. Fig. 10 provides insight into this assumption. The low-magnification scanning electron microscope image of a fracture surface from a failed fretting test specimen shows a portion of a semi-elliptical crack emanating from the contact surface and propagating toward the middle of the specimen.

The mode I stress intensity factor, K_I, for a semi-elliptical surface crack at its deepest point in a thick plate is approximated as [11]:

$$K_I = \frac{1.12 \sigma_o \sqrt{\pi a}}{\Phi}$$ (5)

where a and c now refer to the minor and major semi-axis lengths and Φ is a tabulated function of (a/c).

Using this stress intensity factor and a Paris-type crack growth model (with constants presented in Table 3), a propagation life was estimated for each of the fretting fatigue tests as the time for a 1 mm semi-elliptical crack to grow under the influence of the bulk applied stress amplitude to a depth of 6.35 mm (the midplane of the specimen).
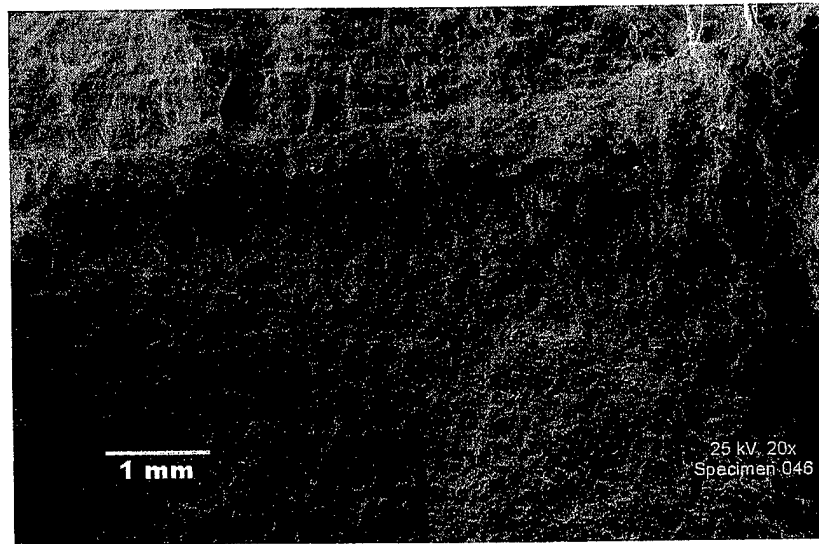
Fig. 10. A scanning electron microscope image at 20 × of a portion of the fracture surface near the contact interface of a fretting fatigue test specimen. The shape of the crack is semi-elliptical in nature, with the major axis of the ellipse spanning across the entire specimen width.

Note that no interaction between crack fronts was considered. An 'experimental' nucleation life was then defined as the difference between the observed failure life and the estimated propagation life. That is:

$$\left(N_{\text{nucleation}}\right)_{\text{experiment}} = \left(N_{\text{failure}}\right)_{\text{observed}} - N_{\text{propagation}} \quad (6)$$

Since the propagation life estimates ranged from only 10–15% of total life (see Table 2), effort extended toward more accurate modeling of the propagation behavior under the influence of the bulk applied stress would seem to provide only minimal added insight into the nucleation process.

The estimated nucleation lives are plotted in Fig. 11 against the calculated amplitude of stress at the trailing edge of contact, σ_{max}, as given by Eq. (2). Recall that for the nominally-elastic stress ranges and fully-reversed loading involved in the experiments, σ_{max} can be related to strain amplitude using Eq. (3). The Smith–Watson to Topper expression, Eq. (4), at the trailing edge of contact then becomes:

$$\frac{1-\nu^2}{E}\left(\sigma_{\text{max}}\right)^2 = \frac{\left(\sigma_{f'}\right)^2}{E}\left(2N_f\right)^{2b} + \sigma_{f'}\epsilon_{f'}\left(2N_f\right)^{b+c} \quad (7)$$

or by using Eq. (2) to express σ_{max} in terms of the applied loads, maximum Hertzian contact pressure and bulk stress amplitude:

$$\frac{1-\nu^2}{E}\left(2p_0\sqrt{\mu Q/P} + \sigma_0\right)^2 = \frac{\left(\sigma_{f'}\right)^2}{E}\left(2N_f\right)^{2b}$$
$$+ \sigma_{f'}\epsilon_{f'}\left(2N_f\right)^{b+c} \quad (8)$$

The predicted value of nucleation life as given from Eq. (4) is plotted as a solid line on the graph. Upper and lower bounds on this prediction are also displayed. Comparison between the data points (including data from a fretting

study on a 4% copper aluminum alloy in the literature for which the requisite loading information was included [26]) and the predictions establish confidence in the predictive capability of this approach. It should be noted that the strength of the agreement between the data and predictions wanes near the initial yield strength of the material (310 MPa (45 ksi)). This result is not surprising, though, as the estimate of σ_{max} (and $\Delta\varepsilon/2$) assumed purely elastic behavior.

Finally, note that Fig. 6 provides a single point of data from an interrupted fretting fatigue test. For the applied
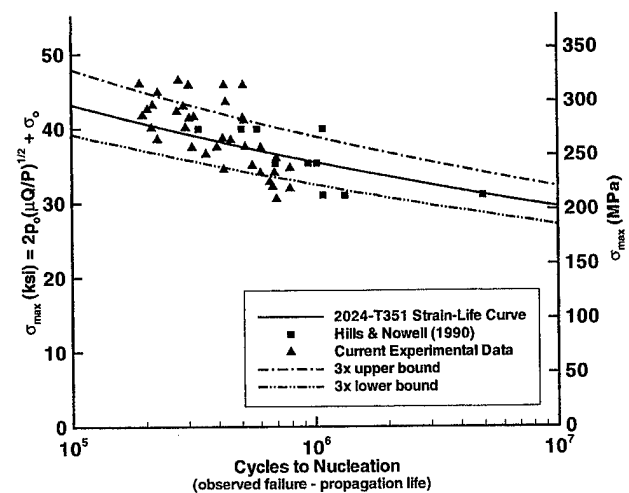

Fig. 11. A plot of maximum tangential stress amplitude at the trailing edge of contact versus cycles to nucleation. Note cycles to nucleation is defined as observed failure cycles minus an estimated propagation life. The solid line represented the predicted values from Eq. (4) and strain-life constants for 2024-T351 aluminum.

loads and interfacial friction associated with the test, the multiaxial fatigue life parameter predicts approximately 300,000 cycles for the nucleation of a 1 mm crack. As stated, the specimen presented in the figure was removed after 150,000 cycles, at which time a trailing-edge crack of over 300 μm was present. While a more complete set of interrupted fretting tests following the approach adopted in the current investigation would further strengthen the confidence in the predictive method, this single observation does offer qualitative support.

4. Conclusions and future directions

The highly-localized nature of the contact stresses, strains and surface microslip associated with fretting contact play a critical role in the nucleation of fatigue cracks. For the experimental configuration employed in this study, a configuration designed to simulate the fretting conditions in aluminum aircraft structural components, a characteristic mode of fretting fatigue crack nucleation was observed. Failures occurred without exception in the test specimens at the trailing edge of contact.

Characterization of the surface and subsurface stresses associated with the fretting interfacial tractions and microslip revealed a region of high tensile stress tangential to the surface at the trailing edge of contact, consistent with the morphology of the nucleated crack. Estimates of this stress along with a crack nucleation criterion rooted in multiaxial fatigue theory were used to predict fretting crack nucleation. Comparison with estimated nucleation lives from a statistically-designed set of fretting fatigue experiments provided confidence in the predictive capability of this approach. Work on application of the approach to fretting fatigue in titanium alloys for aircraft engine and turbine blade applications is also in progress.

5. Biographies

Matthew P. Szolwinski completed his PhD in the School of Aeronautics and Astronautics at Purdue University in 1998, after earning his MS degree from the same program in 1995. In support of his academic pursuits, he has been awarded fellowships by the Mercury 7 foundation, the National Science Foundation and the Department of Defense through the National Defense Science and Engineering Graduate (NDSEG) fellowship program. His current research interests include both experimental and numerical work on fretting fatigue and its impact on aircraft structures and jet engine components; and the mechanics of manufacturing processes. He plans to seek a position in academia beginning in the fall of 1998.

Professor Thomas N. Farris obtained a PhD at Northwestern University in Theoretical and Applied Mechanics in 1986 at which time he joined Purdue University where he is now professor of Aeronautics and Astronautics. He won a 1990 National Science Foundation Presidential Young Investigator Award and the 1992 ASME Burt L. Newkirk Award. He spent the summer of 1991 on a Japan Society for the Promotion of Science Fellowship and the fall of 1991 as a sabbatical visitor to the Cambridge University Engineering Department. He has made contributions in using fracture mechanics to explain the material removal mechanism in the fine finishing of ceramic materials and various aspects of contact fatigue. This research has led to more than 60 journal papers and book chapters, seven PhD theses, and fifteen MS theses. Prof. Farris supervises presently five PhD and four MS students. Current research interests include manufacturing processes and fretting fatigue with particular regard to the fatigue of jet engine components.

Acknowledgements

References

[1] M.H. Attia, Fretting fatigue testing: Current practice and future prospects for standardization, in: M.H. Attia, R.B. Waterhouse, (Eds.), Standardization of Fretting Fatigue Test Methods and Equipment, ASTM STP 1159, American Society for Testing and Materials, Philadelphia, PA (1992), pp. 263–275.

[2] J.A. Bannantine, J.J. Comer, J.L. Handrock, Fundamentals of Metal Fatigue Analysis, Prentice-Hall, Englewood Cliffs, NJ (1990).

[3] P.A. Blatt, Evaluation of fatigue crack initiation behavior of an experimental ternary aluminum–lithium alloy, Master's thesis, School of Aeronautics and Astronautics, Purdue University, West Lafayette, IN (1990).

[4] A.A. Braun, A historical overview and discussion of computer-aided materials testing, in Automation in Fatigue and Fracture, ASTM STP 1231, American Society for Testing and Materials, Philadelphia, PA (1994), pp. 5–17.

[5] R.A. Burton, J.C. Tyler, P.M. Ku, Thermal effects in contact fatigue under oscillatory normal load, J. Basic Engng. 87 (1965) 177–184.

[6] K. Dang Van, B. Griveau, O. Message, On a new multiaxial fatigue limit criterion: Theory and application, in Biaxial and Multiaxial Fatigue, American Society for Testing and Materials, Philadelphia, PA (1985), pp. 479–496.

[7] S. Dharmavasan, S.M.C. Peers, General purpose software for fatigue testing, in: C. Amzallag (Ed.), Automation in Fatigue and Fracture —ASTM STP 1231, American Society for Testing and Materials, Philadelphia, PA (1994) pp. 52–67.

[8] J.M. Dobromirski, Variables of fretting process: are there 50 of them? in: M.H. Attia, R.B. Waterhouse (Eds.), Standardization of Fretting Fatigue Test Methods and Equipment—ASTM STP 1159, American Society for Testing and Materials, Philadelphia, PA (1992), pp. 60–66.

[9] K. Endo, H. Goto, T. Fukunaga, Behaviors of frictional force in fretting fatigue, Bulletin of the JSME 17 (108) (1974) 647–654.

[10] S. Fouvry, P. Kapsa, L. Vincent, K. Dang Van, Theoretical analysis of fatigue cracking under dry friction for fretting loading conditions, Wear 195 (1996) 21–34.

[11] H.O. Fuchs, R.I. Stephens, Metal Fatigue in Engineering, Wiley, New York (1980).

[12] J. Gallagher, Damage tolerant design handbook, Technical Report MCIC-HB-01R, Metals and Ceramics Information Center, Vol. 3, Battelle Columbus Laboratories (1983).

[13] G. Harish, T.N. Farris, Shell modeling of fretting in riveted lapjoints, AIAA Journal 36 (1998) 1087–1093.

[14] D.A. Hills, Mechanics of fretting fatigue, Wear 175 (1994) 107–113.

[15] D.A. Hills, D. Nowell, A. Sackfield, Surface fatigue considerations in fretting, in: D. Dowson, C.M. Taylor, M. Godet, D. Berthe (Eds.), Interface Dynamics, Elsevier (1988), pp. 129–156.

[16] D.W. Hoeppner, C.B.I. Elliot, M.W. Moesser, The role of fretting fatigue on aircraft rivet hole cracking, Technical Report DOT/FAA/AR-96/10, FAA, 1996.

[17] P.C. McKeighan, R.D. Evans, B.M. Hillberry,Fatigue and fracture testing using a multitasking minicomputer workstation, in: A.A. Braun, N.E. Ashbaugh, F.M. Smith (Eds.), Applications of Automation Technology to Fatigue and Fracture Testing-ASTM STP 1092, American Society for Testing and Materials, Philadelphia, PA (1990), pp. 52–67.

[18] P.A. McVeigh, T.N. Farris, Finite element analysis of fretting stresses, Journal of Tribology 119 (4) (1997) 797–801.

[19] Metals Handbook, ASM Metals Handbook, Desk Edition, American Society for Metals, Metals Park, OH (1985).

[20] MIL-HDBK-5G, Metallic Material and Elements for Aerospace Vehicle Structures, Vol. 1, Defense Printing Service Detachment Office, Philadelphia, PA (1994).

[21] D.C. Montgomery, Design and Analysis of Experiments, 4th edn., Wiley, New York (1997).

[22] R.P.G. Müller, An Experimental and Analytical Investigation on the Fatigue Behavior of Fuselage Riveted Lap Joints, PhD thesis, Delft University of Technology, the Netherlands (1995).

[23] K. Nakazawa, M. Sumita, N. Maruyama, Effect of contact pressure on fretting fatigue of high strength steel and titanium alloy, in: M.H. Attia, R.B. Waterhouse (Eds.), Standardization of Fretting Fatigue Test Methods and Equipment, ASTM STP 1159, American Society for Testing and Materials, Philadelphia, PA (1992), pp. 115–125.

[24] K. Nishioka, S. Nishimura, K. Hirakawa, Fundamental investigations of fretting fatigue: Part 1, Bulletin of JSME 11 (45) (1968) 437–445.

[25] D. Nowell, D.A. Hills, Mechanics of fretting fatigue tests, Int. J. Mech. Sci. 29 (5) (1987) 355–365.

[26] D. Nowell, D.A. Hills, Crack initiation criteria in fretting fatigue, Wear 136 (1990) 329–343.

[27] R.S. Piascik, S.A. Willard, The characteristics of fatigue damage in the fuselage riveted lap splice joint, Technical Report NASA/TP-97-206257, NASA Langley Research Center (1997).

[28] D. Socie, Multiaxial fatigue damage models, Journal of Engineering Materials and Technology 109 (1987) 292–298.

[29] D. Socie, Critical plane approaches for multiaxial fatigue damage assessment, in Advances in Multiaxial Fatigue-ASTM STP 1191, American Society for Testing and Materials, Philadelphia, PA (1993), pp. 7–36.

[30] M.P. Szolwinski, The Mechanics and Tribology of Fretting fatigue with Application to Riveted Lap Joints, PhD thesis, School of Aeronautics and Astronautics, Purdue University (1998).

[31] M.P. Szolwinski, T.N. Farris, Mechanics of fretting fatigue crack formation, Wear 198 (1996) 93–107.

[32] R.B. Waterhouse, The problems of fretting fatigue testing, in: M.H. Attia, R.B. Waterhouse (Eds.), Standardization of Fretting Fatigue Test Methods and Equipment, ASTM STP 1159, American Society for Testing and Materials, Philadelphia, PA (1992), pp. 13–19.

[33] R.B. Waterhouse, D.E. Taylor, The initiation of fatigue cracks in a 0.7% carbon steel by fretting, Wear 17 (1971) 139–147.

Instructions to Authors

Submission of papers

Authors are requested to submit **THREE** copies of their articles (complete in **ALL** respects) to the appropriate editors mentioned below. For the **final version**, in addition to the original and two copies, authors should submit an electronic version of their manuscript on **disk**.

Contributions are accepted on the understanding that the authors have obtained the necessary authority for publication. Submission of a manuscript implies that it is not under consideration for publication elsewhere. Upon acceptance of an article by the Journal, the author(s) will be asked to transfer copyright of the article to the publisher. This transfer will ensure the widest possible dissemination.

Types of contributions

Full-length, or regular papers describing original research work previously unpublished.

Reviews of specialized topics within the scope of the Journal (prospective authors should obtain preliminary approval of the Editor before preparing such an article).

Case studies providing accounts of the application of tribological knowledge to the solution of engineering problems. Such studies could include failure analysis and accounts of materials selection development and modification.

Short communications ('Letters') for rapid publication (no more than 500 words plus diagram).

Research Reports and Technical Notes giving a complete description of a limited investigation, which will not be included in a later paper. They should be as completely documented, both by reference to the literature and by descriptions of the experimental procedures employed, as a full-length paper.

Book reviews.

Preparation of manuscripts

Manuscripts should be typed in double spacing throughout on consecutively numbered pages of uniform size with a wide margin on the left. Papers should be headed by a concise but informative title. This should be followed by the name(s) of the author(s) and by the name and address of the laboratory where the work was carried out. If the address of the author(s) at the time when the paper will appear is other than the institution in which the work was carried out, this may be stated in a footnote. The name and complete address of the person to whom proofs are to be sent must be given. Telephone, telefax and e-mail address should be included if possible. Recognition of financial support should not be made by a footnote to the title or name(s) of the author(s), but should be included in "Acknowledgments" at the end of the paper.

Languages

Papers may be written in English, French or German. Authors should remember that the Journal is international and is widely read by those whose first language is other than that in which the paper is written. Clarity and precision are best achieved by the use of short words and simple sentences. Authors who write in a language other than their mother tongue are urged to seek assistance in style, syntax and grammar.

Authors in Japan

Authors in Japan please note that information about how to have the English of your article checked, corrected and improved (*before submission*) is available from Elsevier Science K.K., Higashi Azabu 1-chome Building 4F, 1-9-15 Higashi Azabu Minato-ku, Tokyo 106-0044 Tel: +81 (03) 5561 5032; Fax: +81 (03) 5561 5045; E-mail: info@elsevier.co.jp

Abstract

An abstract of 50–200 words should be included at the beginning of a full-lenght paper. Authors of papers in French or German should supply in addition a translation in English of the Résumé or Zusammenfassung. No abstract is required for a Research Report or a Technical Note. Abstracts should be understandable in isolation, and reference to formulea and equations in the main text is thus not permissible.

Some flexibility of presentation will be allowed but authors are urged to arrange the subject matter clearly under such headings as Introduction, Experimental details, Results, Discussion etc.

References

The references should be listed at the end of the article, and numbered in the order of their appearance in the text. Footnotes should not include bibliographic material. Authors should check whether every reference in the text appears in the list of references and vice versa. Numerals for references are given in square brackets [ ]; equations should be numbered (1), (2) etc. In the text the authors' names are given without initials. When reference is made to publication written by more than two authors, it is preferable to give only the first author's name in the text followed by "et all.". However, in the list of references the names and initials of all authors must be given. In the reference list, periodicals [1], books [2], and multi-author books [3] should be cited in accordance with the following examples:

[1] R.L. Howard, A. Ball, Wear, 205 (1997) 11–14.
[2] G.P. Shparkov, Friction Surface Phenomena, Tribology Series 29, Elsevier Science, Amsterdam, 1995, 343 p.
[3] C.J. Hooke, in: D. Dowson (ed), Elastohydrodynamics-'96: Proceedings of the 23rd Leeds–Lyon Symposium on Tribology, Tribology Series 32, Elsevier Science, Amsterdam, 1997, 185–197.

Each reference should be complete, thus the use of *ibid.*, *idem.*, *et al.* etc. is not permitted.

Abbreviations for the titles of journals should follow the system used by Chemicals Abstracts Service Source Index, 1970 edition, and supplements. Articles not yet published should be given as "in press", "submitted for publication", "in preparation" or "personal communication, 19xx". Years should be given for all references.

Tables

Tables should be typed in double spacing on separate sheets and provided with a suitable heading. Tables should be clearly referred to in the text using Arabic numerals. Considerable thought should be given to laying out the tables (and figures) so that the significance of the results can be most readily and quickly grasped by the busy reader. It is sometimes surprising how much more easily a table of results can be understood if columns and lines are interchanged. Each table should have a title which makes the general meaning understandable without reference to the text.

Illustrations

Line drawings and cyclic or aromatic chemical formulae should be in a form suitable for direct reproduction, drawn in Indian ink on drawing or tracing paper or in the form of high-contrast black and white glossy prints (letter height 3–5 mm). Legends to illustrations should be typed in sequence on a separate page or pages and should be understandable without reference to the text. They should begin with a title followed by any other necessary material describing the points or lines on the figure. Photographs, autoradiographs and electron micrographs should be black and white glossy prints and as rich in contrast as possible. Magnifications should be indicated as scale bars on the photographs and not adjacent to them.

Units and nomenclature

IUPAC-IUB nomenclature and use of SI units are preferred. Scientific abbrevi-ations may be used, and special abbreviations should be defined the first time they occur.

Submission of electronic text

Articles prepared using of the more popular word-processing packages are acceptable, but please note the following points.

● Submissions should be made on a double-density of high-density 3.5˝ diskette or 5.25˝ floppy disk. Take care to ensure that the disk is formatted to its physical specification.

● The disk must always be accompanied by a hard-copy version of the paper, and the two must be identical.

● Disks formatted for either MS-DOS or Apple Macintosh compatibility are acceptable. If you can provide either of these, our preference is for the former.

● The text must be saved in the native format of the word processor used, *e.g.* WordPerfect, Microsoft Word, etc.

● Although most popular word processor file formats are acceptable, we cannot guarantee the usability of all formats. If the disk you send us proves to be unusable, we will publish your paper from the hard copy.

● If you send ASCII files, it is helpful to adhere to the following guidelines:
®matter to be subscripted or superscripted should be placed between curly brackets, and preceded by an underscore ( ) in the case of subscripts or a hat symbol (^) for subscripts. For example: H_{2}O codes H_2O, T^{3} codes T^3. ®matter to be italicized should be preceded by the string *and succeeded by*.
Use **before and** after matter to be emboldened.

● The disk format, word-processor format, file name(s) and the title and authors of the paper must be indicated on the disk.

● There is no need to spend time formatting your paper so that the printout is visually attractive (*e.g.* by making headings bold or creating a page layout with figures), as most formatting instructions will be removed upon processing.

● Leave a blank line between each paragraph and between each entry in the list of bibliographic references.

Proofs

Authors will receive proofs, which they are requested to correct and return as soon as possible. No new material may be inserted in the text after the acceptance of the paper.

Further Information

All questions arising after the acceptance of manuscripts, especially those relating to proofs, should be directed to Elsevier Science Ireland Limited, Bay 15 K, Shannon Industrial Estate, Shannon, County Clare, Ireland; Tel.: +353(61) 471 944; fax: +353(61) 472 144; e-mail: postmaster@elsevier.ie

Offprints

A total of 25 reprints of each paper will be supplied free of charge to the author(s). Additional reprints can be ordered at prices shown on the reprint order form which will accompany the proofs. This order form should be returned promptly since the price of offprints ordered after publication is substantially higher.

There are no page charges.